

Reliability of Three-dimensional Ultrasound Parameters and Their Correlation with the Progression of Adolescent Idiopathic Scoliosis

by

Quang Nhat Vo

A thesis submitted in partial fulfillment of the requirements for the degree of

Doctor of Philosophy

Department of Biomedical Engineering
University of Alberta

© Quang Nhat Vo, 2016

Abstract

Adolescent idiopathic scoliosis (AIS) is a three-dimensional (3D) spinal deformity with unknown causes and with prevalence of 1.5 - 3% of adolescents. If AIS is left untreated, it may progress, leading to back pain, cardiopulmonary problems, and psychosocial concerns, and eventually resulting in surgical intervention. Four types of scoliosis treatment exist and the selection of management depends on the severity and the risk of progression.

Currently, the Cobb angle is the gold standard to measure the severity of the spinal curvature on a two-dimensional (2D) postero-anterior (PA) radiograph. However, this 2D measurement may underestimate the true severity of scoliosis, which affects treatment decisions. To report the actual severity, the Cobb angle on the plane of maximum curvature (PMC) must be measured, requiring a 3D spinal image. Although X-ray based imaging modalities such as computed tomography (CT) and multi-planar radiography provide good 3D images of the spine, the cumulative amount of ionizing radiation increases the risk of cancer. Therefore, 3D ultrasound was proposed in this PhD research as an alternative imaging method to measure spinal severity. In addition to the Cobb angle, the axial vertebral rotation (AVR) and the lateral deviation were also measured from the ultrasound images.

To reconstruct 3D spinal images from 2D B-scans (B-mode images), a software was developed using the voxel-based reconstruction method with bi-linear interpolation. This software could also measure the AVR, the Cobb angle and the lateral deviation on the PA plane and the PMC.

In order to obtain an optimal reconstructed image, *in-vitro* and *in-vivo* experiments were performed to investigate the optimal ultrasound configurations that consisted of the ultrasound

frequency, the minimum spacing between two adjacent B-scans, and the reconstruction resolution. From both *in-vitro* and *in-vivo* studies, it was recommended that the frequency of 2.5 MHz, the spacing of 0.2 mm, and the reconstruction resolution of 0.6 mm constituted the best results.

To measure the AVR, the Cobb angle and the lateral deviation on the PA plane and the PMC, the centre-of-lamina method was used. *In-vitro* and *in-vivo* studies were performed and the results demonstrated that the intra- and inter-rater reliabilities were high for all five parameters (ICC > 0.90). In addition, the Cobb angle measurements from the PA ultrasound images agreed well with the Cobb angle measurements from scoliosis clinics with a small variation (MAD < 3°) and high correlation (ICC > 0.90). The measurements of the lateral deviations also showed high reliabilities (ICC > 0.90 and MAD < 7 mm). Furthermore, the average difference between the PMC Cobb angle and the PA Cobb angle was $1.0^\circ \pm 1.0^\circ$ within the range of 0° and 7°. This result agreed with reports from literature. In addition, the AVR from the *in-vitro* study showed a strong correlation and high agreement between the ultrasound and CT images (ICC > 0.90, MAD < 2°). Unfortunately, the *in-vivo* intervertebral rotations reported from the EOS system did not match to the ultrasound measurements. Further studies will be required to understand the reasons for the discrepancies.

Since the 3D ultrasound was able to provide true spinal deformity information, a study to investigate which demographic and 3D ultrasound parameters correlated with the progression of AIS was conducted. A preliminary predictive model was developed using multi-linear regression and 23 retrospective subjects' data. The results demonstrated the PMC Cobb angle and the number of vertebrae within the largest curve were the most reliable predictors. A preliminary validation using 6 subjects was performed. The variation between the measured

and the predicted Cobb angles was $2.9^\circ \pm 1.3^\circ$. The adjusted r^2 was 0.87, indicating a good fit of data to the model.

In conclusion, this PhD thesis demonstrated that the 3D freehand ultrasound method could be used to reconstruct 3D images of the scoliotic spine. The AVR, the PMC Cobb angle and lateral deviation could be measure reliably to assess the true severity of AIS. The PMC Cobb angle and the number of vertebrae within the largest curve were the potential parameters that could be used to predict the progression of AIS.

Preface

This thesis is an original intellectual product of the author, Quang N. Vo. The research described in this thesis received ethics approval from the Health Research Ethics Board of the University of Alberta with the project name: “Using ultrasound to assess spinal deformity for AIS”, reference number: Pro00005707, starting January 22, 2010.

Portions of the material in this thesis have been published in the following papers:

- VO, Q.N. LOU, E. LE, L.H. 2014. Investigation of the optimal freehand three-dimensional ultrasound configuration to image scoliosis: An *in-vitro* study. In: Vo, T. V. & Tran, P. H. L., eds. The fifth international conference on the development of biomedical engineering in Vietnam, Ho Chi Minh City, Vietnam. Springer, 226-229.
The materials described in this conference paper are reported in Chapter 4. I perceived, executed, and composed the manuscript of the work described in the paper. Dr. Lou endorsed technical advice and direction, and assisted with manuscript preparation. Dr. Le edited the manuscript.
- VO, Q.N. LOU, E. LE, L.H. 2015. Measurement of axial vertebral rotation using three-dimensional ultrasound images. *Scoliosis and Spinal Disorders*, 10, 1-4.
The materials from this journal article are also reported in Chapter 4. I was responsible for conducting the experiment, acquiring data, developing the software, performing measurements, and analyzing the results. I also composed the manuscript with assistance from Dr. Lou and Dr. Le.
- VO, Q.N. LOU, E. LE, L.H. 2014. Reconstruction of a scoliotic spine using a three-dimensional medical ultrasound system. The 10th meeting of the International Research Society of Spinal Deformities, Sapporo, Japan, June 29 – July 2 2014.
Part of the materials from this conference abstract is included in Chapter 4 of this thesis. I conceived of and executed the work from designing and conducting the experiment, collecting data, developing the software, performing measurements, and analyzing the results. I composed the abstract with assistance from Dr. Lou and Dr. Le.

- VO, Q.N. LOU, E. LE, L.H. 2015. 3D ultrasound imaging method to assess the true spinal deformity. The 37th annual international conference of the IEEE Engineering in Medicine and Biology Society, Milan, Italy, August 25-29 2015, 1540-3.
The materials from this conference paper are reported in Chapter 4. I contributed to design the experiment, collecting data, developing the software, performing measurements, and analyzing the results. I composed the manuscript with assistance from all co-authors.
- VO, Q.N. LOU, E. LE, L.H. Prediction of scoliosis progression using three-dimensional ultrasound images: A pilot study. The first combined meeting of the International Research Society of Spinal Deformities and the Society on Scoliosis Orthopaedic and Rehabilitation Treatment, Banff, Canada, May 25-28 2016, 22.
Part of the materials from this conference abstract is included in Chapter 7 of this thesis. I conceived of and executed the work from collecting data, performing measurements, analyzing the results, and developing the predictive model. I composed the abstract with assistance from Dr. Lou and Dr. Le.
- Submission of additional papers is planned related to Chapters 4, 5, 6, and 7.

Acknowledgements

This thesis is made as a completion of the PhD education in Biomedical Engineering. Many persons and organizations have contributed academically, financially, and practically to the completion of this PhD thesis.

I would firstly like to acknowledge my supervisor Dr. Edmond Lou and co-supervisor Dr. Lawrence H. Le for their time, guidance, valuable input and support throughout my entire PhD period. My gratitude also goes to Doug Hill, Jim Raso, Dr. Hong Zhao, and Dr. Rui Zheng, to name a few, for their encouragement, advice or support. I am grateful to Dr. Douglas Hedden, Dr. Marc Moreau, and Dr. James Mahood for supporting the recruitment of patients during their scoliosis clinics.

I would also like to appreciate the financial supports from the Vietnam International Education Development (VIED), the Natural Sciences and Engineering Research Council of Canada (NSERC), the Scoliosis Research Society (SRS), the Woman and Children's Health Research Institute (WCHRI), and the University of Alberta Graduate Students' Association (GSA). I would have not been able to pursue this PhD work and spread it out internationally without these supports.

Finally, I would like to thank my family, especially my wife Tran, for their love, patience, and support during my time studying at the University of Alberta.

Table of Contents

Abstract.....	ii
Preface	v
Acknowledgements	vii
List of Figures.....	xii
List of Tables.....	xviii
List of Abbreviations	xx
Chapter 1. Introduction	1
1.1 Motivation	1
1.2 Objectives	2
1.3 Thesis overview	2
Chapter 2. Background	4
2.1 Anatomy of the spine.....	4
2.1.1 Anatomical planes of the human body	4
2.1.2 Structures of the human spine	5
2.1.3 Structures of the human vertebrae.....	6
2.2 Scoliosis.....	9
2.2.1 Definition.....	9
2.2.2 Classification	12
2.2.3 Treatments	14
2.3 Summary.....	16
Chapter 3. Literature review on imaging modalities and the prediction of AIS progression	17
3.1 Imaging modalities to assess the severity of scoliosis.....	17
3.1.1 Radiography	17
3.1.2 Computed tomography (CT)	22
3.1.3 Magnetic resonance imaging (MRI).....	25
3.1.4 Multi-planar radiography (MPR)	26
3.1.5 Ultrasonography	34
3.1.6 Surface topography.....	49

3.2 Prediction of progression in patients who have AIS	52
3.3 Summary.....	57
Chapter 4. Development of 3D freehand ultrasound reconstruction and determination of the optimal configuration.....	58
4.1 The ultrasound system	58
4.1.1 Ultrasound scanner	59
4.1.2 Transducers.....	59
4.1.3 Position and orientation tracking system.....	62
4.2 Computer hardware and software.....	62
4.3 Three-dimensional ultrasound reconstruction method	62
4.3.1 Step a: Three-dimensional freehand ultrasound data acquisition.....	63
4.3.2 Step b: Image processing.....	63
4.3.3 Step c: Formation of a regular volume	69
4.3.4 Step d: Volume visualization.....	72
4.4 Determination of the optimal ultrasound configuration to image a cadaveric vertebra: An <i>in-vitro</i> study	73
4.4.1 Experimental setup and scanning procedures.....	74
4.4.2 Methods	74
4.4.3 Results	76
4.4.4 Discussion.....	82
4.4.5 Conclusion.....	83
4.5 Determination of the optimal ultrasound configuration to image scoliotic spines: An <i>in-vivo</i> study.....	83
4.5.1. Subject recruitment and scanning procedure.....	84
4.5.2 Methods	85
4.5.3 Results	85
4.5.4 Discussion.....	88
4.6 Summary.....	90
Chapter 5. <i>In-vitro</i> validation of the optimal configuration in imaging AIS	92
5.1 Statistical analysis	92
5.2 Accuracy of the 3D reconstruction of individual cadaveric vertebrae	95

5.2.1 Methods	95
5.2.2 Results	96
5.2.3 Discussion.....	97
5.2.4 Conclusion.....	99
5.3 Measurement of the AVR of cadaveric vertebrae	99
5.3.1 Methods	100
5.3.2 Results	101
5.3.3 Discussion.....	103
5.3.4 Conclusion.....	104
5.4 Accuracy and reliability of the measurement of the AVR, the tilt angle, and the Cobb angle on the spine phantoms	104
5.4.1 The experimental setup and scanning procedures	104
5.4.2 Methods	106
5.4.3 Results	109
5.4.4 Discussion.....	113
5.4.5 Conclusion.....	114
5.5 Summary.....	114
Chapter 6. <i>In-vivo</i> repeatability of the ultrasound method, reliability of the ultrasound measurements, and validity of the PA Cobb angle and AVR measurements	115
6.1 Repeatability of the 3D ultrasound method in imaging scoliosis.....	115
6.1.1 Subject recruitment and scanning procedure.....	116
6.1.2 Methods	116
6.1.3 Results	121
6.1.4 Discussion.....	129
6.1.5 Conclusion.....	130
6.2 Reliability of the measurement of the AVR, the Cobb angles, and the lateral deviations	131
6.2.1 Methods	131
6.2.2 Results	133
6.2.3 Discussion.....	147
6.2.4 Conclusion.....	149
6.3 Validity of the measurements of the PA Cobb angle	149

6.3.1 Methods	149
6.3.2 Results	150
6.3.3 Discussion.....	152
6.3.4 Conclusion.....	153
6.4 Validity of the measurement of the AVR.....	153
6.4.1 EOS imaging system	153
6.4.2 Methods	154
6.4.3 Results	155
6.4.4 Discussion.....	157
6.4.5 Conclusion.....	158
6.5 Summary.....	158
Chapter 7. The correlation of 3D ultrasound parameters with the progression of AIS: A pilot study	159
7.1 Introduction	159
7.2 Methods	160
7.2.1 Recruitment of patient data	160
7.2.3 Selection of predictors (independent variables)	161
7.2.4 Development of the PMC Cobb angle predictive model.....	163
7.2.5 Validation method	163
7.3 Results	164
7.4 Discussion.....	170
7.5 Conclusion.....	172
Chapter 8. Conclusions, limitations, and recommendations	173
8.1 Summary of the work	173
8.2 Contributions	175
8.3 Limitations and recommendations for future work	175
References.....	177
Appendices	198

List of Figures

Figure 2.1 Planes of human anatomy (Modified from (Interactive Biology, 2016)).	5
Figure 2.2 The anatomy of the spine (Martini et al., 2003).	6
Figure 2.3 Vertebral anatomy: (a) The lateral and inferior view of a vertebra; (b) The inferior view of a vertebra; (c) The posterior view of three vertebrae stacked together; (d) The lateral view of three vertebrae stacked together	8
Figure 2.4 The illustration of (a) The AVR; (b) The Cobb angle.	10
Figure 2.5 The illustration of the PMC in scoliosis (b) via the projection of a vector in physics (a).	11
Figure 3.1 An example of a spinal radiograph showing the shadows of the vertebral body, the spinous process and the pedicle.	18
Figure 3.2 The Cobb method of determining the AVR: (a) Normal vertebra without rotation; (b) A vertebra with rotation. If the spinous process is at a, b, c, d, and beyond d, the vertebral rotation is neutral, +, ++, +++, and +++, respectively	19
Figure 3.3 The pedicle method of determining vertebral rotation (Nash and Moe, 1969).	20
Figure 3.4 The Aaro-Dahlborn’s methods to measure the AVR on the CT image.	22
Figure 3.5 The Ho’s methods to measure the AVR on the CT image.	23
Figure 3.6 The Krismer’s methods to measure the AVR on the CT image.	24
Figure 3.7 The illustration of SCPs and NSCPs of a 6-vertex object. Vertices 1 and 3 are SCPs while vertices 2, 4, 5, and 6 are NSCPs.	27
Figure 3.8 The Direct linear transformation with stereo corresponding points.	28
Figure 3.9 The pulse-echo technique.	35
Figure 3.10 3D ultrasound scanning configurations (a) Dedicated 3D tilt scanning; (b) Dedicated 3D linear scanning; (c) Dedicated 3D rotational scanning; (d) Freehand 3D scanning.	38
Figure 3.11 The Voxel Nearest Neighbor (VNN) method. The square grid is the cross section of the volume and the intersections of the vertical and horizontal lines are the centers of voxels; The tilt lines are the cross sections of B-scans; The dots are pixels on each B-scan (for example, numbered from 1 to 7); P1 and P2 are projection points on B-scan A and B-scan B, respectively.	42

Figure 3.12 Bilinear interpolation of two B-scans in the VBMI.	43
Figure 3.13 The Pixel Nearest Neighbor (PNN) method. The square grid is the cross section of the volume and the intersections of the vertical and horizontal lines are the centers of voxels; The tilt lines are the cross sections of B-scans; The dots are pixels on each B-scan (for example, numbered from 1 to 7); P1 and P2 are projection points on B-scan A and B-scan B, respectively.	46
Figure 4.1 The medical Ultrasonix SonixTablet ultrasound system.	59
Figure 4.2 Scan conversion from the transducer grid to the display grid.	60
Figure 4.3 A flow chart of the voxel-based reconstruction method.	64
Figure 4.4 A fuzzy interference system.	66
Figure 4.5 Examples of the common triangular-shaped, trapezoidal-shaped, bell-shaped, gaussian, sigmoidal, and S-shaped membership functions.	68
Figure 4.6 The voxel-based technique with bilinear interpolation.	70
Figure 4.7 The illustration of the search region for the j^{th} voxel of the i^{th} volume section i^{th} VS. An example with $n_s = 3$	72
Figure 4.8 The relationship among frequency, resolution and penetration (Otto, 2000).	73
Figure 4.9 Cadaveric vertebra T7 and the in-vitro experimental setup.	74
Figure 4.10 The four distance parameters on the cadaveric vertebra T7: 1. Left superior articular process - right superior articular process, 2. Left transverse process - right transverse process, 3. Left superior articular process - spinous process, 4. Right superior articular process - spinous process.	76
Figure 4.11 The best reconstructed images and the corresponding configurations for the penetration depth of 9 cm.	80
Figure 4.12 The best reconstructed images and the corresponding configurations for the penetration depth of 6 cm.	81
Figure 4.13 The subject scanning procedure.	84
Figure 4.14 Three-dimensional reconstructed image provided by: (a) The convex probe (2.5 MHz), and (b) The linear probe (6.6 MHz).	88
Figure 4.15 Examples of two B-scans acquired with frequencies 2.5 MHz and 6.6 MHz at the same depth of 6 cm.	89

Figure 5.1 Five distances to be measured on lumbar vertebrae L1 and L3: (1) left superior articular process - right superior articular process, (2) left transverse process - right transverse process, (3) left inferior articular process - right inferior articular process, (4) left superior articular process - left inferior articular process, and (5) right superior articular process - right inferior articular process.....	95
Figure 5.2 Cadaveric vertebrae T7, L1, and L3 and their corresponding 3D reconstructed images.....	96
Figure 5.3 The limitation to imaging the vertebral body due to the lack of ultrasound energy penetrating through bone.....	99
Figure 5.4 (a) - The frontal view (left) and (b) - The transverse view (right) of the 3D reconstructed T7 vertebra for AVR measurement (a) The COLs (red dots) or transverse processes (blue dots) were manually located by using the computer mouse pointer. (b) The rotation of each reconstructed vertebra was automatically determined by the angle between the line going through either the COLs (L-L) or the centres of transverse processes (TP-TP) and a reference vertical plane (xz).....	100
Figure 5.5 The top view (left) and the frontal view (right) of the 3D reconstructed L3 vertebra for the lamina data missing due to ultrasound blocking.....	101
Figure 5.6 The in-vitro experimental setup: (a) Spine phantom 1 (scoliotic); (b) Spine phantom 2 (straight); (c) The spine phantom was immersed into a tank of water that mimicked the body setting.....	105
Figure 5.7 The spine phantom was CT scanned in the lying position.....	106
Figure 5.8 The determination of a pixel of the PA image from a voxel of the 3D spinal volume.....	107
Figure 5.9 The determination of the PMC.....	108
Figure 5.10 The phantom, the ultrasound reconstructed image, and the CT reconstructed image of: (a) Spine 1 (curved), and (b) Spine 2 (straight).....	110
Figure 5.11 The US and CT PA images of the two spine phantoms.....	111
Figure 6.1 Measurement of the AVR: (a) PA view, (b) Transverse view, and (c) 3D coordinate system.....	118

Figure 6.2 (a) The determination of vertebra T12, and (b) The determination of the AVR and the Cobb angle: color magenta represents the upper and lower end vertebrae while color yellow represents the apex..... 121

Figure 6.3 a) 3D reconstructed spinal image with emulated spinous processes; b) The determination of end vertebrae, apex, the AVR, the Cobb angles, and the lateral deviation on the PA view; c) The determination of end vertebrae, apex, the AVR, the Cobb angles, and the lateral deviation on the PMC view. 123

Figure 6.4 The correlation of the AVR measurements between the scan and the rescan..... 124

Figure 6.5 The correlation of the PA Cobb angle measurements between the scan and the rescan. 124

Figure 6.6 The correlation of the PMC Cobb angle measurements between the scan and the rescan. 125

Figure 6.7 The correlation of the PA lateral deviation measurements between the scan and the rescan. 125

Figure 6.8 The correlation of the PMC lateral deviation measurements between the scan and the rescan. 126

Figure 6.9 The Bland-Altman plot - A comparison of the AVR measurements between the scan and the rescan. 127

Figure 6.10 The Bland-Altman plot - A comparison of the PA Cobb angle measurements between the scan and the rescan. 127

Figure 6.11 The Bland-Altman plot - A comparison of the PMC Cobb angle measurements between the scan and the rescan. 128

Figure 6.12 The Bland-Altman plot - A comparison of the PA lateral deviation measurements between the scan and the rescan. 128

Figure 6.13 The Bland-Altman plot - A comparison of the PMC lateral deviation measurements between the scan and the rescan. 129

Figure 6.14 A flowchart of the procedure to select the measurements from Rater 1 and Rater 2 for comparisons. 132

Figure 6.15 The intra-rater correlation of the AVR measurements (Rater 1). 134

Figure 6.16 The intra-rater correlation of the PA Cobb angle measurements (Rater 1). 135

Figure 6.17 The intra-rater correlation of the PMC Cobb angle measurements (Rater 1). 135

Figure 6.18	The intra-rater correlation of the PA lateral deviation measurements (Rater 1).	136
Figure 6.19	The intra-rater correlation of the PMC lateral deviation measurements (Rater 1).	136
Figure 6.20	The intra-rater correlation of the AVR measurements (Rater 2).	137
Figure 6.21	The intra-rater correlation of the PA Cobb angle measurements (Rater 2).	137
Figure 6.22	The intra-rater correlation of the PMC Cobb angle measurements (Rater 2).	138
Figure 6.23	The intra-rater correlation of the PA lateral deviation measurements (Rater 2).	138
Figure 6.24	The intra-rater correlation of the PMC lateral deviation measurements (Rater 2).	139
Figure 6.25	The inter-rater correlation of the AVR measurements between Rater 1 and Rater 2.	141
Figure 6.26	The inter-rater correlation of the PA Cobb angle measurements between Rater 1 and Rater 2.	141
Figure 6.27	The inter-rater correlation of the PMC Cobb angle measurements between Rater 1 and Rater 2.	142
Figure 6.28	The inter-rater correlation of the PA lateral deviation measurements between Rater 1 and Rater 2.	142
Figure 6.29	The inter-rater correlation of the PMC lateral deviation measurements between Rater 1 and Rater 2.	143
Figure 6.30	The Bland-Altman plot - A comparison of the AVR measurements between Rater 1 and Rater 2.	144
Figure 6.31	The Bland-Altman plot - A comparison of the PA Cobb angle measurements between Rater 1 and Rater 2.	144
Figure 6.32	The Bland-Altman plot - A comparison of the PMC Cobb angle measurements between Rater 1 and Rater 2.	145
Figure 6.33	The Bland-Altman plot - A comparison of the PA lateral deviation measurements between Rater 1 and Rater 2.	145
Figure 6.34	The Bland-Altman plot - A comparison of the PMC lateral deviation measurements between Rater 1 and Rater 2.	146
Figure 6.35	The Bland-Altman plot - A comparison of the ultrasound and radiograph PA Cobb angle measurements by Rater 1.	151

Figure 6.36 The Bland-Altman plot - A comparison of the ultrasound and radiograph PA Cobb angle measurements by Rater 2. 151

Figure 6.37 The EOS imaging system and its working principle (modified from (Illes and Somoskeoy, 2012)). 154

Figure 6.38 The Bland-Altman plot - A comparison of the AIR measurements between the ultrasound and the EOS images by Rater 1. 156

Figure 6.39 The Bland-Altman plot - A comparison of the AIR measurements between the ultrasound and EOS images by Rater 2. 156

Figure 7.1 The flowchart of selecting the significant predictors. 162

Figure 7.2 Multiple linear regression output shown for the range of the 1st PMC Cobb angle and the number of vertebrae. The color map indicates the magnitude of the predicted PMC Cobb angle (degrees). 167

Figure 7.3 The normal probability plot of the residuals. 167

Figure 7.4 The difference between the measured and predicted Cobb angles. 169

Figure 7.5 Bland-Altman plot – A comparison of the predicted and measured PMC Cobb angles 170

List of Tables

Table 4.1 The penetration depth versus the converted B-scan resolution on a convex transducer.....	61
Table 4.2 The penetration depth versus the converted B-scan resolution on a linear transducer.	61
Table 4.3 Acoustic impedance, Z , for selected tissues.	65
Table 4.4 The MAD and r values for the 45 configurations with the penetration depth of 9 cm.	78
Table 4.5 The MAD and r values for the 45 configurations with the penetration depth of 6 cm.	79
Table 4.6 The maximum absolute and relative errors.	82
Table 4.7 Rankings of the best five coded images from the volunteer selected by six raters.	86
Table 4.8 Scores of the selected coded images from the volunteer selected by six raters.	86
Table 4.9 Rankings of the best five coded images selected for the two patients by five raters.	86
Table 4.10 Scores of the selected coded images from the two patients selected by five raters.	87
Table 4.11 the ranking of the 3D reconstructed images from the first to the fifth quality for the volunteer and the two patients.	87
Table 4.12 The scan time and the number of B-scans acquired with five frequencies from the volunteer.	90
Table 5.1 The mean absolute difference and Pearson correlation between two sessions of measurements on the reconstructed image and between the image and cadaveric vertebra.	97
Table 5.2 The intra-rater reliabilities for three raters.....	102
Table 5.3 The inter-rater reliability between two raters.	102
Table 5.4 The mean absolute difference [absolute (mean measured value - actual value)]. ...	102
Table 5.5 The range of absolute difference [absolute (mean measured value - actual value)].	102
Table 5.6 The mean absolute difference between two raters.....	103

Table 5.7 Intra-rater reliabilities of the AVR between CT and US measurements for the two raters.	112
Table 5.8 Intra-rater reliabilities of the PMC tilt angle between CT and US measurements for the two raters.	112
Table 5.9 Inter-rater reliabilities of the ultrasound measurements of the AVR and the PMC tilt angle.	112
Table 5.10 The Cobb angle on the PA and PMC view between CT and US measurements for the two raters.	113
Table 6.1 Reliabilities of the measurements of the five parameters.	122
Table 6.2 Intra-rater reliabilities of the 5 parameters by Rater 1.	133
Table 6.3 Intra-rater reliabilities of the 5 parameters by Rater 2.	134
Table 6.4 The Pearson's r and the difference between the PA and PMC Cobb angles by Rater 1 and Rater 2.	139
Table 6.5 Inter-rater reliability of the 5 parameter between Rater 1 and Rater 2.	140
Table 6.6 End vertebrae difference between individual raters and between Rater 1 and Rater 2.	146
Table 6.7 Comparison of the PA Cobb angle measurements between the radiograph and ultrasound methods by two raters.	150
Table 7.1 Collinearity among all initial predictors.	164
Table 7.2 Statistical analysis for all initial predictors.	165
Table 7.3 Measurements considered as selected predictors in the multiple linear regression.	165
Table 7.4 Statistical analysis for the two final predictors.	166
Table 7.5 Measurements of selected predictors used to validate multiple linear regression.	168
Table 7.6 The measurements of the first clinical visit and the predicted Cobb angle.	168
Table 7.7 The statistical analysis of the validation.	169
Appendix Table 1 Training data	198
Appendix Table 2 Test data	199

List of Abbreviations

2D	Two-dimensional
3D	Three-dimensional
3DSA	Three-Dimensional Scoliosis Analysis
AIR	Axial Intervertebral Rotation
AIS	Adolescent Idiopathic Scoliosis
AVR	Axial Vertebral Rotation
BMI	Body Mass Index
CI	Confidence Interval
COL	Centre Of Lamina
CPU	Central Processing Unit
CT	Computed Tomography
CTLSSO	Cervico-Thoraco-Lumbo-Sacral Orthosis
DLT	Direct Linear Transformation
EI	Error Index
FBM	Function Based Method
GPS	Global Positioning System
ICC	Intraclass Correlation Coefficient
ISIS	Integrated Shape Imaging System
LCD	Liquid Crystal Display
LEV	Lower End Vertebra
L-L	Lamina-Lamina
MAD	Mean Absolute Difference
MD	Minimum Distance
MPR	Multi-Planar Radiography
MRI	Magnetic Resonance Imaging
NSCP	Non-Stereo Corresponding Point
PA	Postero-anterior
PA-Cobb	Cobb angle on the PA view
PA-LD	Lateral Deviation on the PA view

PBM	Pixel Based Method
PMC	Plane of Maximum Curvature
PMC-Cobb	Cobb angle on the PMC
PMC-LD	Lateral Deviation on the PMC
PMC-TA	Tilt Angle on the PMC
PNN	Pixel Nearest Neighbor
RBF	Radial Basis Function
RD	Range of Difference
RR	Reconstruction Resolution
SB	Stack of B-scans
SCP	Stereo Corresponding Point
SD	Standard Deviation
SEM	Standard Error of Measurement
SPV	Subject Per Variable
TLSO	Thoraco-Lumbar-Sacral Orthosis
TP-TP	Transverse Process - Transverse Process
UEV	Upper End Vertebra
URI	Ultrasound Research Interface
US	Ultrasound
VBM	Voxel Based Method
VNN	Voxel Nearest Neighbor
VS	Volume Section

Introduction

1.1 Motivation

Scoliosis is a three-dimensional (3D) deformity of the spine with axial vertebral rotation (AVR). Adolescent idiopathic scoliosis (AIS) is defined as scoliosis whose etiology remains unknown and occurs in children who are 11 - 17 years old. It affects 1.5 - 3% of the adolescent population (Lonstein, 1994). Curve progression, back pain, cardiopulmonary problems, and psychosocial concerns are the most common long-term consequences in untreated AIS patients (Asher and Burton, 2006, Weinstein *et al.*, 2008). There are four types of scoliosis treatment including observation, exercises, bracing and surgery, and the selection of management depends on the severity and the risk of progression.

Current clinical practice uses the Cobb angle as the gold standard to measure the spinal curvature on a two-dimensional (2D) PA radiograph. This 2D method may underestimate the true severity of scoliosis, which may affect treatment decisions. To report the actual severity, Stagnara *et al.* (Stagnara *et al.*, 1965) proposed measuring the Cobb angle on the PMC. The PMC generally occurs near the maximum axial vertebral rotation plane. To determine the PMC, a 3D spinal image is required. Although computed tomography and multi-planar radiography provide good 3D images of the spine, exposing children to ionizing radiation increases the risk of cancer (Miller, 1999, Doody *et al.*, 2000, Ronckers *et al.*, 2010, McKenna *et al.*, 2012). Therefore, an innovative 3D ultrasound spinal imaging method is proposed and developed in this research to measure the spine severity. In addition to the Cobb angle measurements, the AVR and the lateral deviation were also measured from the ultrasound images to understand better the 3D deformity of the spine.

To provide the most effective management, a good prediction of curve progression is important. From literature, researchers have been using patients' demographics information and measurements from radiographs to develop models to predict the progression of scoliosis. The 2D radiography parameters' model is lack of accuracy (Yamauchi *et al.*, 1988). Although the 3D radiography parameters' models are quite accurate (Wu *et al.*, 2005, Wu *et al.*, 2010, Parent *et al.*, 2014), the approaches expose growing children to ionizing radiation. Therefore, this research is also to determine which demographic and 3D ultrasound parameters correlate with the progression of AIS.

1.2 Objectives

The objectives of this research are to:

1. determine the optimal ultrasound configuration to reconstruct 3D spinal images,
2. investigate if 3D ultrasound images of the spine can be reconstructed within a clinic time (less than 20 minutes),
3. determine the repeatability of the ultrasound scanning method and measurements,
4. determine the reliability and the validity of the ultrasound measurements on the AVR, the Cobb angle, and the lateral deviation from ultrasound images, and
5. study which 3D ultrasound parameters can be used to predict the progression of scoliosis.

1.3 Thesis overview

This thesis contains 8 chapters. In this chapter, the motivation and the objectives of this research are described. The remaining chapters are organized as follows.

Chapter 2 introduces the background of scoliosis, the anatomy of the spine and vertebrae, and the anatomical planes of the human body. It also reports the three important parameters that are commonly used to assess scoliosis severity.

Chapter 3 reports a comprehensive literature review on different imaging modalities for scoliosis and predictive models to estimate the progression of scoliosis.

Chapter 4 describes different 3D ultrasound reconstruction methods and the developed method on using 3D ultrasound data to reconstruct a 3D spine. Based on both the *in-vitro* and

in-vivo studies, the optimal ultrasound configuration to reconstruct 3D vertebral and spinal images are reported.

In Chapter 5, there is analysis of the optimal configuration through variations in the measurements of the AVR, the Cobb angle and the lateral deviation on the PA plane and the PMC. The methods to measure these five parameters are described in the *in-vitro* studies.

Chapter 6 contains the *in-vivo* repeatability and reliability studies on the measurements of the AVR, the Cobb angle and the lateral deviation on the PA plane and the PMC from the 3D ultrasound images. The measurements of the PA Cobb angle and the AVR on ultrasound images are compared with that measured on the corresponding radiographs and 3D spinal images from the EOS system, respectively.

Chapter 7 describes a retrospective study to develop a preliminary predictive model that can be used to estimate the future PMC Cobb angle from the current ultrasound measurements using multiple linear regression.

Finally, in Chapter 8, the conclusion, the limitations of this research work are discussed and the recommendations for future studies are described.

Background

This chapter introduces the background of scoliosis and its related definitions. In section 2.1, the anatomy of the spine is described, emphasizing on the major anatomical planes of the human body, the structure of the spine, and the structure of vertebrae. In addition, section 2.2 mainly focuses on three important parameters to assess the severity of scoliosis: the coronal curvature, the AVR, and the lateral deviation. The classification and treatment options of scoliosis are also mentioned in this chapter.

2.1 Anatomy of the spine

2.1.1 Anatomical planes of the human body

The human body is a 3D object. Any slice or plane that cuts through a 3D object can be described with reference to three major planes: the transverse plane, the coronal plane and the sagittal plane (Figure 2.1). These planes are useful as they produce a common method of communication for physicians to describe the location of structures or the direction of movements.

The *transverse plane* (or the *axial plane*) is a horizontal plane that is perpendicular to the long axis of the body and divides it into superior (upper) and inferior (lower) sections. A division along this plane is called a transverse section, or cross section. Meanwhile, the *coronal plane* (or the *frontal plane*) is a vertical plane that parallels the longitudinal axis of the body and splits the body into anterior (front) and posterior (back) sections. The *sagittal plane* (or the *lateral plane*) is also a vertical plane that parallels the longitudinal axis of the body. It extends from anterior to posterior, separating the body into left and right sections. This plane can also move from a medial position (closer to the midline of the body) to a lateral position

(further from the midline of the body). A plane that passes along the midline of the body and divides it into left and right halves is a midsagittal plane, or a median sagittal plane. A plane that is parallel to the midsagittal line is a parasagittal plane.

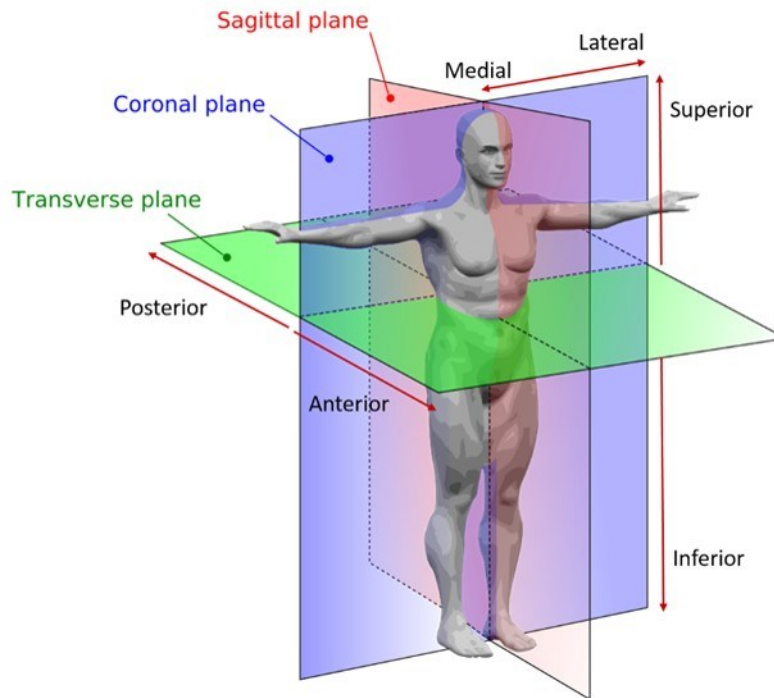


Figure 2.1 *Planes of human anatomy (Modified from (Interactive Biology, 2016)).*

2.1.2 Structures of the human spine

The spine (also known as the vertebral column) of an adult comprises of 26 bones, 24 of which are vertebrae followed by the sacrum and the coccyx (Figure 2.2). The vertebrae provide a passageway to protect the spinal cord. They also support the head, the neck, the trunk, as well as maintain the body in the sitting or standing position.

The spine is divided into five sections including cervical, thoracic, lumbar, sacral, and coccygeal sections. The cervical section consists of 7 vertebrae and connects the neck to the trunk. Twelve thoracic vertebrae constitute the thoracic section that is the longest section of the spine. Each thoracic vertebra articulates with one or more pairs of ribs to form the rib cage that functions as a guard to protect the internal organs. The twelfth thoracic vertebra

articulates with a pair of half ribs and is adjacent to the lumbar region. The lumbar region is comprised of five lumbar vertebrae. The first lumbar vertebra is connected to the twelfth thoracic vertebra while the fifth lumbar vertebra is joined with the sacrum. The coccyx ends the vertebral column. In adults, the average spinal length is 71 cm or 28 inches (Martini *et al.*, 2003). The normal spine looks straight on the coronal plane; however, it has a certain curvature on the sagittal plane as shown in Figure 2.2.

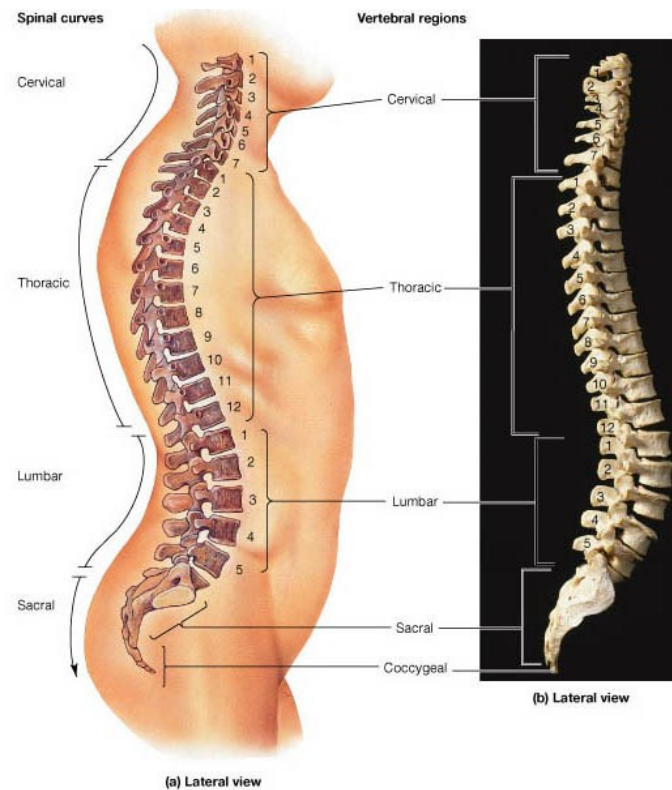


Figure 2.2 The anatomy of the spine (Martini *et al.*, 2003)

2.1.3 Structures of the human vertebrae

Generally, all twenty-four vertebrae have four parts in common: the vertebral body, the vertebral arch, the articular processes, and the vertebral articulation (Figure 2.3).

The *vertebral body* (also known as the *centrum*) is the thick oval front segment of a vertebra that transfers weight along the axis of the vertebral column (Figure 2.3a, b). Each

vertebral body is connected with neighboring bodies by ligaments and separated by the inter-vertebral discs. Inter-vertebral discs are pads of fibrocartilage that absorb spinal compression while permitting slight movements of the vertebrae. Their function is to spread loading evenly on the vertebral bodies no matter what the spine is under compression or flexion.

The *vertebral arch* (also known as the *neural arch*) is formed by the laminae, pedicles, and processes. Two pedicles arise along the sides of the vertebral body to connect the vertebral body to the vertebral arch. The laminae project dorsally and medially to join and complete the vertebral arch. The fusion of the laminae forms the spinous process that projects dorsally and posteriorly from the junction of the laminae. Muscles and ligaments are attached to the spinous processes. The spinous processes can be visualized and recognized on the back. There are also two transverse processes, each of which arises from either side of the vertebral body at the point where the lamina and the pedicle are joined. These processes also serve to attach muscles and ligaments.

The *articular processes* also project at the pedicle - laminae junction. Each side of the vertebra locates a superior and inferior articular process. The superior articular processes project toward the head or superior end of the body (cranially) while the inferior articular processes arise toward the inferior end of the body (caudally).

Vertebral articulation links the inferior articular processes of one vertebra with the superior articular processes of the lower vertebra. Each articular process has an articular facet that is a polished surface. The superior processes have articular facets on their dorsal surfaces, whereas the inferior processes articulate along their ventral surfaces.

Although the vertebrae share some common features, some others distinguish the cervical, thoracic, and lumbar vertebrae from each other.

The *cervical vertebrae* (named C1 - C7) reside right below the skull and are the thinnest and most delicate vertebrae as compared to the thoracic and lumbar vertebrae. The oval-shaped cervical vertebral body is relative small with respect to the size of the triangular vertebral foramen. Their spinous processes are generally short with the exception of C2 and C7.

The *thoracic vertebrae* (named T1 - T12) are located in the middle region of the spine with vertebra T1 being adjacent to vertebra C7. The body of a thoracic vertebra has a distinctive heart-shape and weighs more than a cervical vertebra. Nevertheless, the vertebral foramen of the former is rounder and relative smaller than that of the latter. The thoracic vertebra has transverse processes with surfaces articulating with the ribs, and the long, slender spinous process projecting postero-caudally. The spinous processes of vertebrae T10, T11, and T12 increasingly resemble those of the lumbar vertebrae due to a transition between the thoracic and the lumbar curvatures.

The *lumbar vertebrae* (named L1 - L5) reside between the ribcage and the pelvis and are the largest vertebrae of the spine. They do not articulate with the ribs and have sturdy construction since they need to bear more weight than the others do. The body of a typical lumbar vertebra is thicker than that of a thoracic vertebra. In addition, the superior and inferior surfaces are oval rather than heart-shaped. The spinous processes are stumpy and project dorsally while the slender transverse processes project dorsally and laterally.

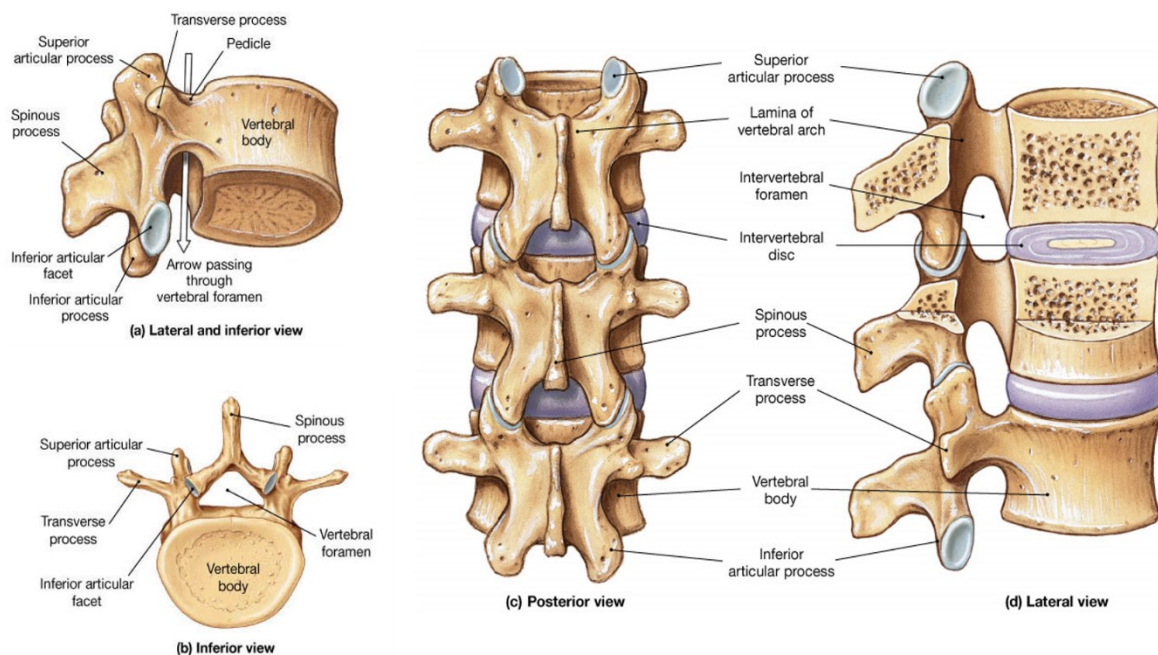


Figure 2.3 Vertebral anatomy: (a) The lateral and inferior view of a vertebra; (b) The inferior view of a vertebra; (c) The posterior view of three vertebrae stacked together; (d) The lateral view of three vertebrae stacked together (Martini et al., 2003).

2.2 Scoliosis

2.2.1 Definition

There are several abnormal spinal curvature, of which scoliosis is the most common type (Martini *et al.*, 2003). Originally, scoliosis was a Greek term meaning curved or bent. Although ancient works described people with spinal deformities since 3500 BC, it was not until the fifth century BC that Hippocrates (460 - 370 BC) was the first to explicitly describe scoliosis (Vasiliadis *et al.*, 2009). Concepts such as the magnitude of deformity and knowledge of curve progression were mentioned in his works. The term 'scoliosis' used in his works has a general meaning and applies to almost all kinds of spinal curvature. Consequently, little information can be derived from the Hippocratic texts when the term is placed in its contemporary context (Marketos and Skiadas, 1999).

Today, even though scoliosis is described as a complex 3D deformity of the spine characterized by the AVR and the lateral spinal curvature (Deacon *et al.*, 1984), it is defined as a lateral spinal curvature of the spine that is 10° or greater measured on a standing frontal radiograph (Figure 2.4). Currently, the Cobb angle (Cobb, 1948) is the gold standard to quantify the spinal curvature of each curve on PA radiographs. It is defined as the angle between the line going through the top endplate and the bottom endplate of the two most tilted vertebrae (the upper end vertebra and the lower end vertebra) of the curve (Figure 2.4b). If the spinal curvature (or the Cobb angle) is less than 10° , it is considered spinal asymmetry; otherwise, it refers to scoliosis (Van Goethem *et al.*, 2007). Scoliosis is considered mild if the curvature is between 10 and 25° , moderate if the curvature is from 26° to 45° , and severe if the curvature is greater than 45° . It is common in healthy children to have chest and trunk asymmetry. From a study conducted on a thousand physically mature high school students, Bunnell (Bunnell, 1993) found that only 1.6% of the students had a clinically determined straight spine (scoliometer reading of 0° at all three levels of the spine). According to the Hueter - Volkmann law (Mehlman *et al.*, 1997), after a critical degree of coronal curvature has developed, a vicious mechanical cycle drives the progression of scoliosis which accelerates during periods of rapid spinal growth. Therefore, the Scoliosis Research Society has recommended that all children aged 10 - 14 years should be annually screened for scoliosis (Scoliosis Research Society, 1986). The Adam's forward bend test (Adams, 1882) with the

use of a scoliometer is most often used in school screening for scoliosis (Bunnell, 2005). During this test, children take off their shirts to expose the spines. They are requested to bend over at the waist until the back comes parallel to the floor. Their feet are together with the arms hanging and the knees in extension as if they were touching their toes. The examiner stands and looks from behind the children, levels his or her eyes with the back, and searches for one side being higher than the other, or any asymmetry of the back. In addition, the examiner may use a scoliometer to measure the rotation of the trunk in this position. If a rotational deformity of the trunk exists, the examiner gently places the scoliometer along the thoracic, thoracolumbar, and lumbar spine and records measurements. The largest measurement is used for assessment of scoliosis (Bunnell, 1984). The axial trunk rotation threshold for referral to hospital should be 7° at any level of the spine (Bunnell, 1993).

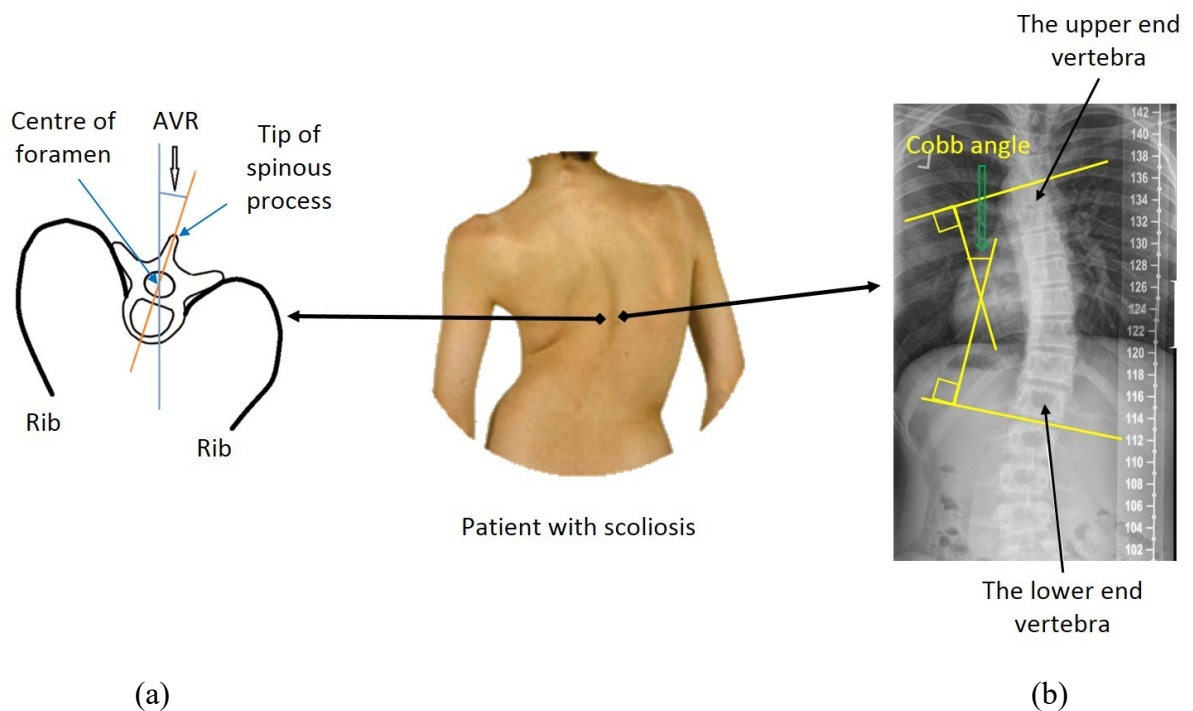


Figure 2.4 The illustration of (a) The AVR; (b) The Cobb angle.

Despite the 3D nature of scoliosis, the Cobb angle cannot quantitatively correlate to the AVR. The axial rotation of the vertebra is another parameter that produces the asymmetry of the rib cage and the flank muscle. It is determined by the angle between the vertical line and the line going through the tip of spinous process and the center of foramen (Figure 2.4a).

According to Stokes' theory (Stokes, 2002), the abnormal spinal asymmetry is initiated by a vertebral rotation in the axial plane. There is an influence of rotation over frontal plane deformity and it is more apparent at curves with the AVR greater than 30° ; therefore, the actual Cobb angle might be 20% greater than the one measured on the PA radiographs (Gocen and Havitcioglu, 2001). For the actual measurement of the severity, the PMC was proposed by Stagnara *et al.* (Stagnara *et al.*, 1965) as the vertical plane rotated around the gravitational axis where the projected Cobb angle is maximum. The illustration of the PMC in scoliosis via the projection of a vector is described in Figure 2.5. In physics, the projection of vector AB on a plane that is parallel to it provides its greatest length (Figure 2.5a). In this case, the projection of vector AB on a parallel plane (A1B1) is longer than that on any other arbitrary plane (A2B2). Similarly, the PMC is considered parallel to the curve and the projection of the curve on this plane provides the greatest spinal curvature (Figure 2.5b). The PMC can be acquired when a 3D spinal image is available.

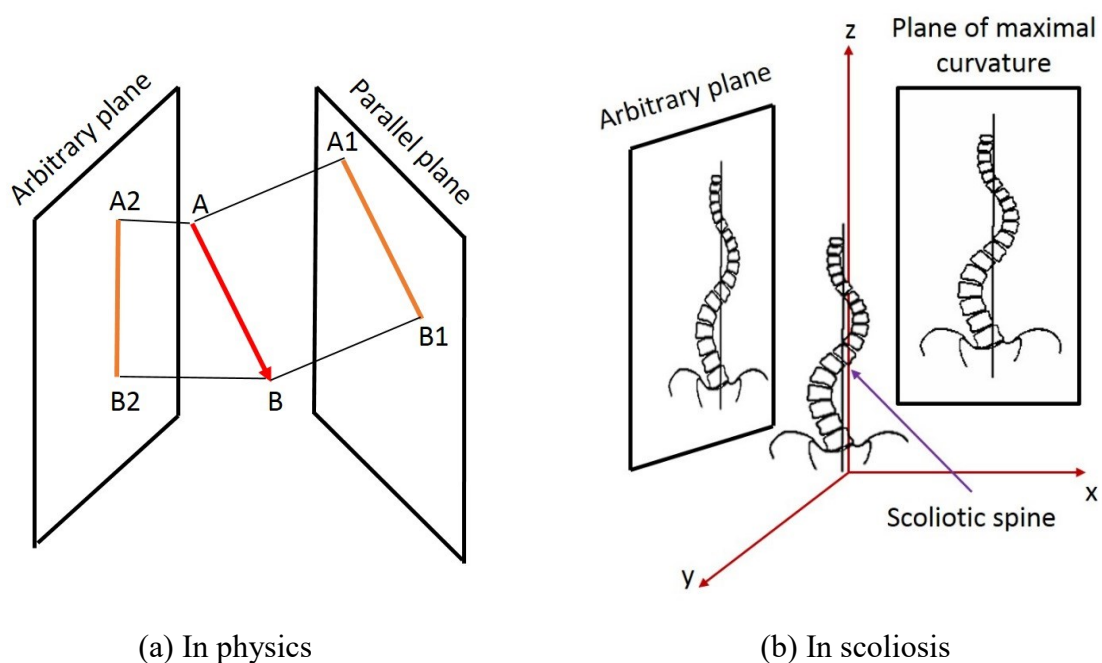


Figure 2.5 The illustration of the PMC in scoliosis (b) via the projection of a vector in physics (a).

In scoliosis, there are some other general definitions, which are helpful in the discussion of this medical condition throughout this thesis. The *apex* (or the apical vertebra) is defined as the vertebra that has the largest AVR and furthest lateral deviation from the centre of the vertebral column. The *end vertebrae* are those with the largest tilt, but the least displacement and rotation. Each curve has two end vertebrae: the upper end and the lower end vertebrae. The *neutral vertebra* has no rotation and may be at the same level as end vertebrae, either above or below the end vertebra. The *stable vertebra* is the most proximal vertebra that is bisected or closely bisected by the central sacral vertical line. The central sacral vertical line bisects the sacrum vertically and is perpendicular to a tangential line drawn across the top of the iliac crests on PA radiographs. The *lateral deviation* is the horizontal distance from the centre of the apical vertebra to the central sacral vertical line.

2.2.2 Classification

Scoliosis is typically classified according to etiology, curve location, age at onset, and curve type (Van Goethem *et al.*, 2007).

Etiology

In the ancient time when scoliosis was first described, Hippocrates mentioned two possible causes of this medical condition in his works entitled “*On Joints*”: “There are some in whom the vertebrae are curved laterally to one side or the other. All such affections, or most of them, are due to gatherings on the inner side of the spine, while in some cases the positions the patients are accustomed to take in bed are accessory to the malady” (Hippocrates, 1927). Today, scoliosis is more clearly understood; some causes could be explained. As a result, scoliosis is sub-categorized as congenital, idiopathic, generalized disease and syndrome-related, traumatic, and degenerative scoliosis.

Congenital scoliosis is a type of scoliosis, which occurs due to a defective formation or separation of vertebrae during the embryologic stage. Its progression depends on the types of improper development of the vertebra. The deviation develops from 1 to 2.5° per year if hemi-vertebra exists; meanwhile, this deviation ranges from 2° to 5° per year in case of double hemi-vertebra (Van Goethem *et al.*, 2007). Hemi-vertebra refers to the incomplete development of one side of a vertebra.

Idiopathic scoliosis is the most common type and accounts for about 80% of all scoliotic cases, and its potential causes are still unknown since the evidence of underlying physical or radiographic pathology does not exist. Some experts relate it to genetic factors (Alden *et al.*, 2006), an earlier growth spurt (Stokes and Windisch, 2006), and vertebral growth anomalies (Guo *et al.*, 2003).

Generalized disease and syndrome related scoliosis is caused by neuromuscular disorders. Marfan's syndrome, neurofibromatosis, rheumatoid disease, or bone dysplasia are other causes. In addition, some people with Down syndrome also show an appearance of scoliosis.

Traumatic scoliosis is another type of scoliosis caused by bony lesions such as fractures and dislocations or by soft tissue lesions resulted by burns or post-empyema.

Finally, *degenerative scoliosis* occurs due to degeneration of the whole body and the spine deviates laterally after the age of 50. This type of scoliosis normally appears at the lumbar region because of a disc or facet joint arthritics, a progression of adolescent scoliosis during adulthood, or osteoporosis.

Curve location

It is classified according to the position of the apex of a curve, which is defined as the most laterally deviated vertebra of the curve. There are six types of scoliosis in terms of curve location. It is considered cervical scoliosis if the apex is between C2 and C6, cervicothoracic scoliosis between C7 and T1, thoracic scoliosis between T2 and T11, thoracolumbar scoliosis between T12 and L1, lumbar scoliosis between L2 and L4, and lumbosacral between L5 and below (Van Goethem *et al.*, 2007). Typically, over 90% of idiopathic scoliosis patients will develop a right thoracic or left lumbar curvature (Hresko, 2013).

Age at onset

Age at onset is the age at which scoliosis commences to occur and develop. Scoliosis can appear at four stages of age. Scoliosis can be sub-classified as infantile scoliosis if deformity occurs before or at three years old, juvenile scoliosis if it occurs during four to ten years of age, adolescent scoliosis in children between eleven to seventeen years of age, and adult scoliosis occurs when the patient is at or older than 18 years (Van Goethem *et al.*, 2007).

Spinal deformity that occurs before the adolescent stage is more likely due to an underlying spinal cord abnormality. The prevalence of this condition is approximately 20% in infantile and juvenile patients (Gupta *et al.*, 1998, Dobbs *et al.*, 2002).

Curve type

The scoliotic spine can contain one or more curves, of which the largest one is known as the primary or major curve, whereas the smaller one if any is classified as secondary or minor curvature. The primary curve develops first and the secondary curve develop afterward to compensate for the unbalance that results from the progression of major curves by repositioning the head and trunk over the pelvis to maintain balance (Van Goethem *et al.*, 2007, Malfair *et al.*, 2010).

Although there are many types of scoliosis, AIS is the most common type. AIS affects 0.47 - 5.2% of the population, and its incidence is 1.5 - 3 times higher in females than in males in the moderate and severe cases. This ratio increases significantly with increasing age (Konieczny *et al.*, 2013).

2.2.3 Treatments

There are long-term complications if AIS is left untreated. The most common complications include back pain, physical disability, compromised self-image, pulmonary symptoms and early mortality (Asher and Burton, 2006). The treatment goals are to prevent progression and correct the existing curve. The treatment of idiopathic scoliosis depends on the severity of the curvature (the Cobb angle) at onset and the risk of progression. There are a variety of treatment including observation only, exercises, bracing, and surgery.

Observation and/or physical exercise therapy

Observation can only be applied to patients with mild idiopathic scoliosis (coronal curvature between 10° and 25°) when they have a little or no discomfort and show no progression. In this case, patients need to be monitored every four to twelve months (Van Goethem *et al.*, 2007). However, if the curve is greater than 30°, monitoring for progression after skeletal maturity is required every five years (Van Goethem *et al.*, 2007). Sometimes, patients are prescribed special physical exercises that can help to correct their spines.

Bracing

Brace treatment (orthosis) is recommended for skeletally immature patients whose spines have curves ranging from 25° to 45° during their growth phase (Weinstein *et al.*, 2008). The purpose of bracing is to prevent the curve from progression until the patient reaches skeletal maturity. Three main types of braces are widely used for scoliosis treatment. The first type is called a TLSO that stands for Thoraco-Lumbar-Sacral Orthosis. A TLSO is usually custom molded from plastic and covers the front and the back of the patient starting the pelvis to under the armpit. A three-point pressure from the brace is applied to the curvature to prevent its progression. This type of brace is generally for thoracic with an apex at or below T8, thoraco-lumbar, and lumbar curves (Canavese and Kaelin, 2011). Therefore, it is the most commonly prescribed. The second type is a CTLSO that stands for Cervico-Thoraco-Lumbo-Sacral Orthosis. It is similar to the aforementioned TLSO, but a neck ring is included and held in place by vertical bars attached to the body of the brace. This type of brace is often prescribed for thoracic curves that have an apex at or above T8 (Canavese and Kaelin, 2011). Meanwhile, the third type is the nighttime bending brace and the most common one is the Charleston bending brace that is only worn while the patient is sleeping. It is molded to the patient while the patient is bent to the side, thus applying more pressure and bending the patient against the curve. This bending pressure overcorrects the curve while the patient is wearing his or her brace. In AIS patients, Weinstein *et al.* (Weinstein *et al.*, 2013) found a positively strong correlation between the reduction in the progression of high-risk curves to the threshold for surgery and the hours of brace wear. The success rate of the treatment was 72% and 48% for the bracing group and the observation group, respectively. The success rate was also higher (75%) in the group of patients randomly assigned to bracing than that of patients randomly assigned to observation (42%). The success rate could increase up to 93% if brace wear was over 12.9 hours per day. Morton *et al.* recommended bracing for 18 to 20 hours a day since full-day adherence is hardly possible (Morton *et al.*, 2008). However, in a recent study (Katz *et al.*, 2010), Katz *et al.* reported that there was no significant difference between twenty-three hours and sixteen hours of brace wear. The patients who wore braces between school and bedtime and during school hours had the most successful treatment outcomes. The effectiveness of brace treatment for AIS was also confirmed with 76% of the curves being stabilized by Maruyama *et al.* (Maruyama *et al.*, 2015). However, this

management is not always effective and not recommended for congenital scoliosis as most congenital scoliotic curves are not flexible, and therefore resilient to bracing (Kaspiris *et al.*, 2011).

Surgery

Surgery is a final option to improve spinal alignment and balance. It can help to prevent curves from further progression. This method is indicated when spinal curvature is greater than 45° while still growing (Weinstein *et al.*, 2008). It can also be suggested when associated pain occurs after skeletal maturity. All scoliosis surgery approaches use modern instrumentation systems including hooks and screws to anchor long rods to the spine. The rod's functions are to reduce the curvature and hold the spine, which are fused with bone to prevent further changes after surgery. Once the bone fuses, spinal fusion eliminates motion between vertebrae, thus ending the progression of the curve. The stainless steel Harrington rod was first introduced in the 1960s to provide a spinal fusion and internal fixation to maintain a straighter spine. Although complications and outcomes have been improved over years, the current techniques and implants still involve spinal fusion; thus, the correction of curvature is obtained at a cost of losing spinal motion. For that reason, a dual rod, segmental spinal fixation system is preferable since it yields multiple anchor points for attachment to the scoliotic spine (Hresko, 2013).

2.3 Summary

This chapter provided some background information on the structure of the spine in general, and vertebrae in particular. Scoliosis, and its types as well as treatment were also discussed. Although there are a variety of scoliosis, AIS is the most common type that accounts for 80% of all cases.

Literature review on imaging modalities and the prediction of AIS progression

The treatment of scoliosis depends on the conditions of severity and the risk of progression. This chapter reports the literature review on the imaging modalities used to assess the severity of scoliosis and to predict the progression of scoliosis. In section 3.1, the working principles and utilities of the common imaging modalities, namely radiography, computed tomography, magnetic resonance imaging, multi-planar radiography, surface topography, and ultrasonography are extensively described in the context of scoliosis imaging. Section 3.2 provides information on predictive models of the progression of scoliosis based on demographic and imaging parameters. Section 3.3 summarizes the aforementioned imaging modalities and predictive models through which the motivation of this PhD thesis is presented.

3.1 Imaging modalities to assess the severity of scoliosis

3.1.1 Radiography

Radiography is an imaging technique that utilizes X-rays to view the internal structure of an object such as a human body. To create an X-ray image or radiograph, an X-ray tube generates a heterogeneous beam of X-rays upon the object. X-ray absorption, scattering, and transmission occur when the X-ray photons interact with the object. A certain amount of X-ray energy is absorbed by the object while the remaining photons are transmitted through the object and captured by a detector (either photographic film in analog radiography or a digital detector in digital radiography) that is placed at the other side of the object. The detector then provides a superimposed 2D image displaying the internal structures of the object. Coronal

and lateral radiographs are usually taken during the initial scoliosis clinic visit. The Cobb angle is measured on the coronal radiograph. However, in order to reflect the 3D nature of scoliosis, the AVR should be measured.

Figure 3.1 illustrates the shadows of the vertebral body, the spinous process, and the pedicles on a spinal radiograph. These landmarks were used in the following methods to measure the AVR.

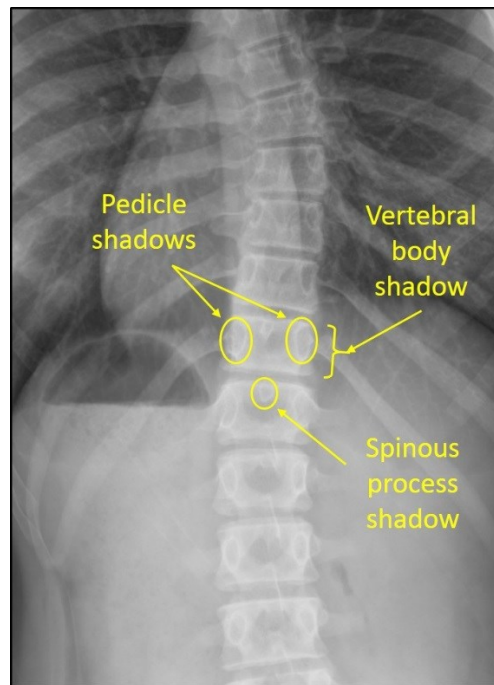


Figure 3.1 An example of a spinal radiograph showing the shadows of the vertebral body, the spinous process and the pedicle.

In addition to the introduction of the Cobb angle, Dr. John Robert Cobb also introduced a method for measuring the AVR on radiographs (Cobb, 1948). His method is to use the width of the vertebral body on a PA radiograph to estimate the AVR. The vertebral body width is divided into six equal sections by seven vertical lines with the spinous process located at the central line (the fourth line) for a normal vertebra (Figure 3.2a). Depending on the position of the spinous process, the level of rotation is determined as neutral, +, ++, +++, or +++++, respectively (Figure 3.2b). This method is simple to use; however, it has some disadvantages.

The grading system is merely divided into 5 grades, which does not allow the quantification of the degree of the rotation angle.

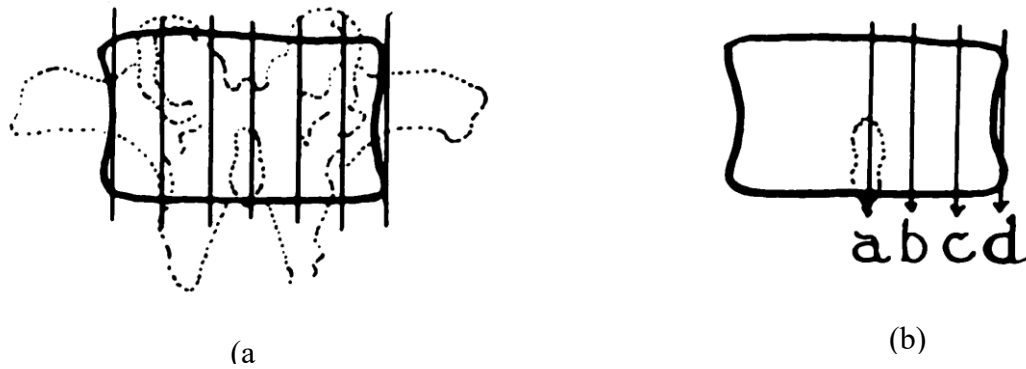


Figure 3.2 The Cobb method of determining the AVR: (a) Normal vertebra without rotation; (b) A vertebra with rotation. If the spinous process is at a, b, c, d, and beyond d, the vertebral rotation is neutral, +, ++, +++, and +++++, respectively (Cobb, 1948).

The spinous process was reported to have a limited visibility on coronal radiographs (Nash and Moe, 1969), leading to the development of the Nash - Moe method (Nash and Moe, 1969) to measure the AVR. Figure 3.3 demonstrates the Nash - Moe method. This technique is similar to the previous Cobb's method; nevertheless, the pedicles are used as landmarks instead of the tip of the spinous process. Since the pedicle shadow on the concave side of the curve disappears earlier in rotation than the pedicle shadow on the convex side, the latter was used as the standard landmark. The half width of the vertebral body on the convex side of a curve on a PA radiograph is divided into three equal segments. Grading the vertebral rotation from 0 to 4+ depends on the location of the pedicle within these segments. This method showed a better visibility of the selected anatomical landmark; therefore, it could investigate the rotation of the pedicle on the convex side up to 90°. Furthermore, the pedicles are less deformed in severe scoliosis than the spinous process; therefore, symmetry remains unchanged. Yet, this method also shows the same disadvantage as the previous one when the percentage of pedicle displacement (0% - 100%) was used to approximate the degree of vertebral rotation (0° - 100°). Moreover, this method does not account for the width of the vertebral body; therefore, the approximation of the vertebral rotation varies among vertebrae due to a difference in their sizes.

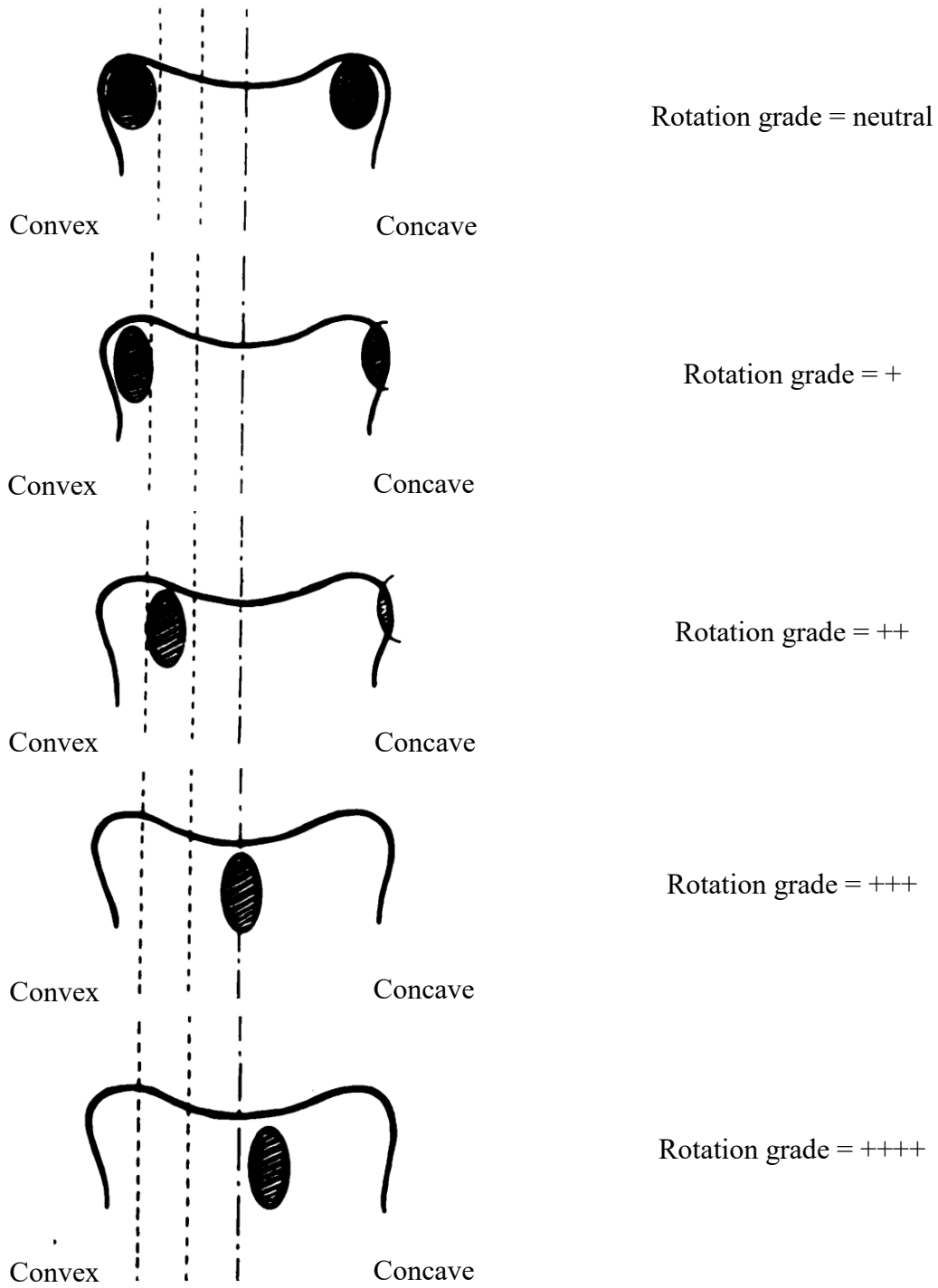


Figure 3.3 The pedicle method of determining vertebral rotation (Nash and Moe, 1969).

In order to overcome the disadvantages of the aforementioned methods in quantifying the degree of vertebral rotation, Perdriolle (Perdriolle and Vidal, 1985) proposed a torsion meter, which facilitated the process of measurement on anteroposterior radiographs. The torsion meter is placed over the radiograph such that the lateral borders of the vertebral body are aligned with the outer margins of the torsion meter. The AVR is then measured by a vertical line of the torsion meter going through the convex pedicle. This method shows an advantage over the Cobb and Nash - Moe methods in providing the quantification of the vertebral rotation with a $\pm 5^\circ$ accuracy (Barsanti *et al.*, 1990, Omeroğlu *et al.*, 1996). Although it can be applied to mild or moderate scoliotic cases, one drawback of the previous methods is still unsolved in using the torsion meter is the inability of accounting for the sizes of vertebra in different locations (cervical, thoracic, and lumbar) are still not accounted for. Hence, the measurements of lumbar vertebral rotations are very accurate, but there is bigger difference between the measurement of thoracic vertebrae and that of the real rotation (Cerny *et al.*, 2014).

In another study, Stokes *et al.* (Stokes *et al.*, 1986) developed the measurement technique based on pedicle offset by accounting for the vertebral asymmetry and size differences of vertebrae from T4 to L4. The centers of the vertebral endplates, and the upper and the lower margins of the pedicles on each vertebra are used as landmarks. The vertebral rotation, θ , is denoted by

$$\tan\theta = \left(\frac{a-b}{a+b}\right) \times \frac{w}{2d} \quad (3.1)$$

where a and b are the distances from the centres of pedicles to the vertebral body axis (the line connecting the endplate centres, and w/d is the width-to-depth ratio of each vertebra in the region T4 to L4. These ratios were experimentally determined from a 99 AIS patient dataset. The Stokes's method produces errors of approximate $\pm 1\text{mm}$ in identifying landmarks, thus yielding an error of 2.7° in vertebral rotation. Even though this method has a simple measuring procedure, it creates a greater random error in comparison to methods involving marking of vertebral edges (Lam *et al.*, 2008).

Recently, Cerny *et al.* proposed another radiographic method to measure the vertebral rotation based on the pedicle shadows, the properties of the geometric shape of vertebrae, and their dimensional proportions (Cerny *et al.*, 2014). The method takes the difference in the sizes of vertebrae in various locations into consideration, and does not require any special devices. Although the Cerny's method provides similar measurements to the Perdriolle's method, it has some limitations. When the vertebral rotation exceeds 30° , the pedicle on the concave side of the curve becomes invisible; therefore, the method is not applicable. In addition, if the vertebra is noticeably deformed, the rotation is less accurate.

3.1.2 Computed tomography (CT)

Computed tomography is one of the most promising methods to reconstruct the 3D images of the bony structures. It uses multiple views sampled at regular angular spacing to produce tomographic images. An X-ray source and detectors are located at opposite orientation. During data acquisition, the source and detectors rotate around the patient. X-rays transmitting through the body are recorded by the detectors. A high-speed computer processes the data to provide a cross sectional image. Modern multi-slice CT scanners provide sub-millimeter helical and volumetric scanning in few seconds.

Aaro and Dahlborn developed a technique to measure the AVR, spinal deformity, and rib cage deformity based on CT images (Aaro and Dahlborn, 1981). The AVR was defined as the angle between the vertical line and the line going through the most posterior part of the spinal canal (point A) and the middle of the vertebral body (point B) (Figure 3.4).

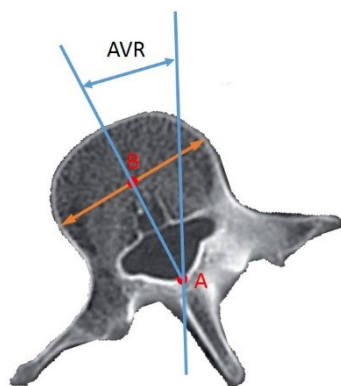


Figure 3.4 The Aaro-Dahlborn's methods to measure the AVR on the CT image.

However, inaccuracy increases if the measured vertebra were tilted greater than 20° in both the coronal and sagittal planes. Aaro and Dahlborn also stated that the larger the distance between the dorsal central aspect of the vertebral foramen and the true axis for vertebral longitudinal rotation, the larger was the error.

According to Ho *et al.* study (Ho *et al.*, 1993), several methods could be used to measure the AVR on spinal CT images. However, one of the difficulties was to select the datum points that can be used to draw the reference axes reliably. Ho *et al.* proposed reliable datum points as illustrated in Figure 3.5. Their first proposed method to determine the AVR was by drawing a line through the junction of the inner surface of laminae (point A) and the center of posterior surface of the vertebral body (point B) relative to a vertical line. The reference points can also be the junction of inner surface laminae (point A) and the inner junctions between laminae and pedicles (points C). The AVR is determined by the angle between the line bisecting angle CAC and the vertical line (method 2). There are reliable referential points; these methods have an advantage of reducing errors, so require less experienced readers. However, in method 1, the midpoint is not easily identified and reading difference appeared; meanwhile, method 2 showed no difference.

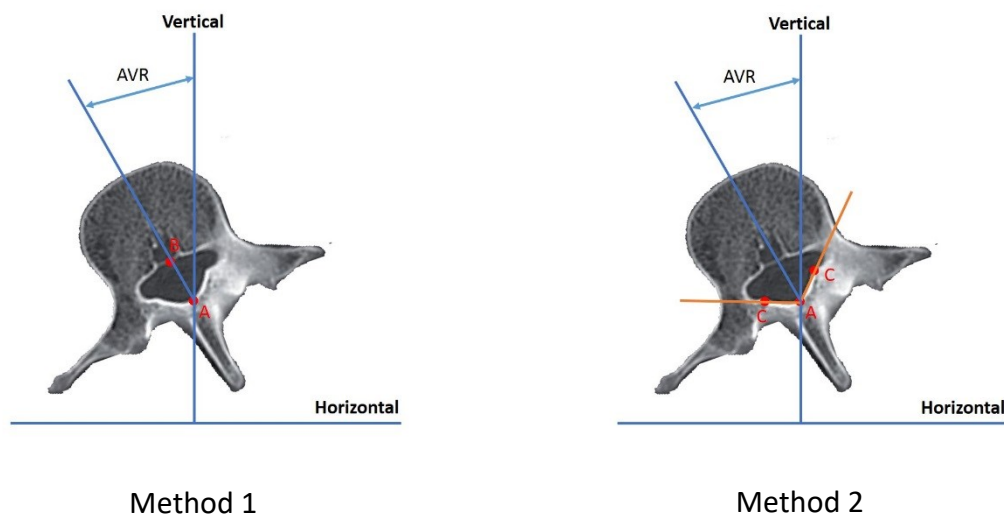


Figure 3.5 The Ho's methods to measure the AVR on the CT image.

Krismer *et al.* proposed another CT method to measure the AVR of a scoliotic vertebra using different reference points. Figure 3.6 illustrates how the AVR is measured. Point A is the centre of the segment connecting two laminae. Point B is the most anterior part of the spinal canal. Point C is the centre of the longest diameter through the vertebral body. The AVR is the angle between AB and BC.

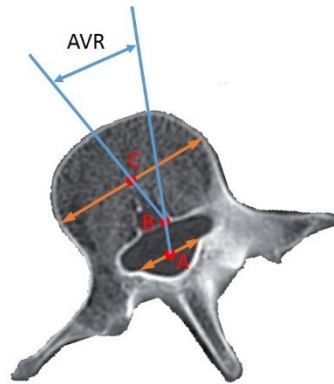


Figure 3.6 The Krismer's methods to measure the AVR on the CT image.

Gocen *et al.* performed a clinical intra- and inter-rater analysis to compare three aforementioned CT measurement methods (Gocen *et al.*, 1998). There was no correlation between the Krismer's method and the other two ($p > 0.05$) while there was a significant correlation between the Aaro-Dahlborn's method and the Ho's method ($p < 0.02$). The study also demonstrated that the Ho's method was the most reliably and clinically useful method to measure the AVR in AIS.

Although CT can provide clear 3D bone structures, it is relatively expensive and requires patients in the supine position when comparing with plain radiography. The supine position eliminates the gravitational effect, which makes the spinal curvature appear smaller (Torell *et al.*, 1985, Yazici *et al.*, 2001, Forsberg *et al.*, 2013). Torell *et al.* attempted to compare data on standing and supine Cobb angle measurements in lateral curves in girls with idiopathic scoliosis (Torell *et al.*, 1985). The mean difference in the Cobb measurements was 8.9° and the standard deviation was 6.2° . Yazici *et al.* (Yazici *et al.*, 2001) compared the AVR values

measured by the Perdriolle's method (Perdriolle and Vidal, 1985) with those obtained by the Aaro-Dahlborn's method (Aaro *et al.*, 1978). The standing vertebral rotation angles were measured using the torsion meter while the supine vertebral rotation angles were obtained using the Aaro-Dahlborn's method on the CT scans. Their result also showed a large difference in measurements between standing and supine position even measured by the same method. The discrepancy in the average apical vertebral rotation angle between standing and supine position was approximately 6°, whereas the disparity in the average Cobb angle was about 16°. As a result, CT scans were primarily used to provide a high quality 3D image of a section of spine to identify the underlying causes of scoliosis. The use of CT for scoliosis is limited due to high radiation exposure to patients. Although dose-reduction technology has been implemented in recent CT scanners, radiation dosage is still significant (Illes *et al.*, 2011). Recently, Kalra *et al.* attempted to use the sub-milliSievert scanning protocol to scan the whole spine for pediatric patients (Kalra *et al.*, 2013). However, the dosages were found to be two to three times higher than plain radiography reported in the Chamberlain's study (Chamberlain *et al.*, 2000). Therefore, CT scans are still used only for surgical planning or assessing post-operative complications of scoliosis (Imagama *et al.*, 2011, Kim *et al.*, 2010).

3.1.3 Magnetic resonance imaging (MRI)

Another promising 3D imaging modality is MRI, which utilizes the property of nuclear magnetic resonance to image nuclei of atoms inside the body to visualize internal structures. MRI not only generates more detailed images of the human body than the standard X-rays but also provides good contrast between soft tissues and bone structures. The magnets of an MRI scanner generate a strong magnetic field that forces protons (dipole) in the body to align in the same direction. When radiofrequency pulses are transmitted through the patient, the protons are stimulated, and knocked out of alignment. When the radiofrequency waves are turned off, the protons realign with the magnetic field and release the energy as radio signals that are detected by MRI sensors. These output signals provide clinicians with information about the location of the dipoles in the body. They are also used to distinguish different types of internal tissue since the time it takes for the protons to realign with the magnetic field varies with the environment and the chemical nature of the molecules.

There are three types of MRI scanners: closed, open, and upright MRI. A closed system looks like a tube. The restricted space may cause patients discomfort, especially for those with claustrophobia and obesity (Dewey *et al.*, 2007, Brennan *et al.*, 1988, Sarji *et al.*, 1998). Although the open MRI scanner provides more space for patients, the quality of image is lower than that from the closed MRI. It is because the open MRI scanner produces weaker magnetic field than the closed MRI scanner (Chung *et al.*, 2011). Furthermore, both the closed and open models require patients in the supine position, which reduce scoliosis severity by removing gravity effects, thus the MRI imaging method is not suitable to diagnose and monitor the severity of scoliosis. Recently, upright MRI is available allowing images to be obtained in either the standing or sitting position. Unfortunately, this upright system also provides inferior image quality when compared to the closed system (Chung *et al.*, 2011).

The AVR in patients who have AIS can also be measured with MRI images (Birchall *et al.*, 1997). In Birchall *et al.* study, the apex, the two vertebrae above the apex, and the two others below the apex of the scoliotic curve were imaged in the axial plane. The reconstruction was done in the axial plane of each endplate from selected sections passing through superior and inferior endplates of each vertebra. Vertebral rotation was measured in a similar manner to the Ho's method. On one hand, this method yielded small intra-observer and inter-observer variations, and is therefore reproducible. On the other hand, its absolute accuracy depends on reference to a neutrally rotated vertebra.

Unlike CT, MRI is a non-invasive approach but its use for scoliosis remains limited. The operation cost of a MRI machine is much higher than that of a radiographic facility and the scan time is usually longer, which restricts throughput in a clinical setting. Additionally, MRI is not recommended for patients with surgical implants since the non-ferromagnetic metallic implants create artefacts, thus reducing the quality of images. For these reasons, it is mainly used to assess neurological complications and often used for a complementary diagnosis examination. Furthermore, both CT and MRI are not suitable for studying spine mobility since the patient is constrained in a small area.

3.1.4 Multi-planar radiography (MPR)

Apart from the CT and MRI imaging modalities, the 3D spinal images can be reconstructed from multi-planar standing radiography. The principles of 3D reconstruction are based on the

direct linear transformation (DLT) with stereo corresponding points (SCPs), the DLT with non-stereo corresponding points (NSCPs), and the semi-automatic statistics. The SCPs are points that are identifiable in two or more orthogonal radiographs. For example, Figure 3.7 illustrates a six-vertex object with the lateral and antero-posterior images. Vertices 1 and 3 are SCPs because they manifest in both images while vertices 2, 4, 5, and 6 are NSCPs as they appear only in one image.

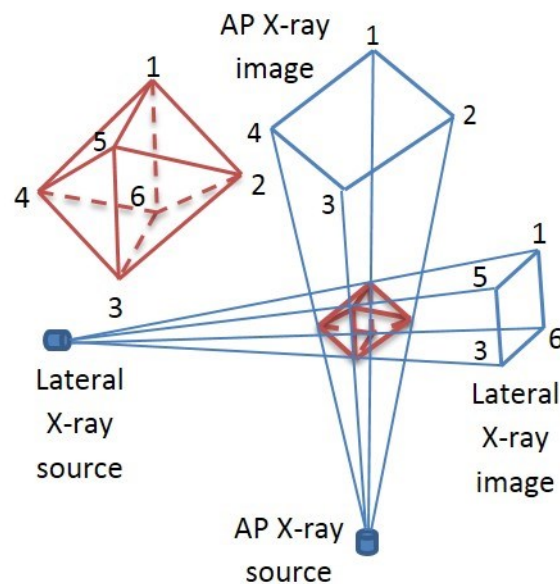


Figure 3.7 The illustration of SCPs and NSCPs of a 6-vertex object. Vertices 1 and 3 are SCPs while vertices 2, 4, 5, and 6 are NSCPs.

Direct linear transformation with stereo corresponding points

The direct linear transformation was proposed by Aziz and Karara and further developed by Marzan (Aziz and Karara, 1971, Marzan, 1976). For 3D spinal reconstruction, two radiographs are obtained at different angles with a minimum of six stereo corresponding anatomical landmarks for each vertebra. To display a complete vertebra, a total of 178 points were required (Trochu, 1993). The kriging interpolation method was used to generate 178 points from the six SCPs. Each vertebra was then reconstructed using either triangles or quadrangles to link the points to form a vertebral surface. However, the accuracy of the

reconstruction image was low. Occasionally, the DLT method had difficulty to identify SCPs in the stereo images (Nyström *et al.*, 1994). If a blur occurred in one of the points, it led to reconstruction errors (Pearcy, 1985). Despite that the dual kriging interpolation method could further smooth the 3D reconstruction surface (Andre *et al.*, 1996), six landmarks for each vertebra were still not adequate. An increased number of landmarks were needed to achieve a better quality of 3D images.

Figure 3.8 illustrates the principle of the DLT, which is explained as follows. Assuming that source S_1 has coordinates (X_0, Y_0, Z_0) in the reference coordinate system (X, Y, Z) of the calibrating frame and (x_0, y_0, z_0) in the reference (X_1, Y_1, Z_1) coordinate system of the image plane. $N(X, Y, Z)$ is an arbitrary point in the calibrating frame. $P_1(x_1, y_1, 0)$ is the projection of N from S_1 on the image plane (X_1, Y_1) .

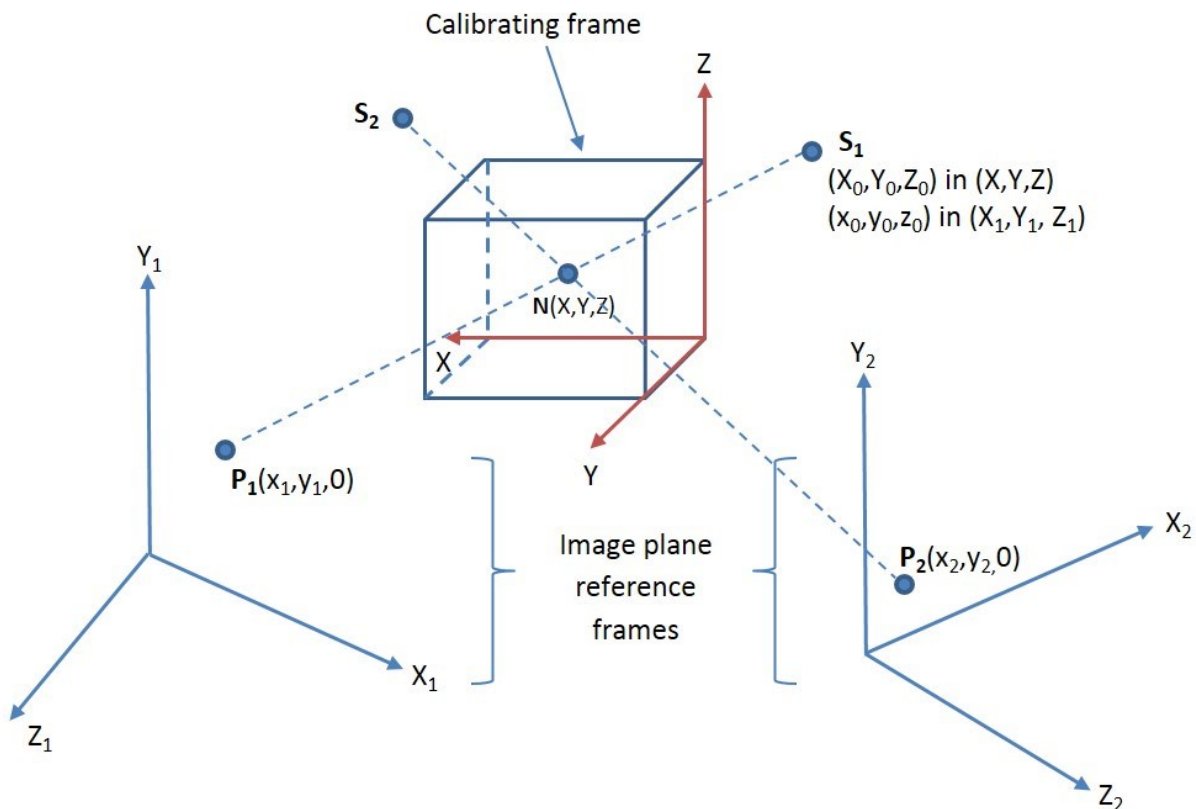


Figure 3.8 The Direct linear transformation with stereo corresponding points.

Since S_1 , N , and P are on the same line, the relationship among them can be expressed in Equation 3.2:

$$\overrightarrow{S_1P_1} = d \cdot \overrightarrow{S_1N} \quad (3.2)$$

where d is a proportional coefficient.

$$\overrightarrow{S_1P_1} = \begin{pmatrix} x_1 - x_0 \\ y_1 - y_0 \\ -z_0 \end{pmatrix} \quad (3.3)$$

and

$$\overrightarrow{S_1N} = \begin{pmatrix} X - X_0 \\ Y - Y_0 \\ Z - Z_0 \end{pmatrix} \quad (3.4)$$

Substitute Equations 3.3 and 3.4 into Equation 3.2, we obtain Equation 3.5:

$$\begin{pmatrix} x_1 - x_0 \\ y_1 - y_0 \\ -z_0 \end{pmatrix} = d \cdot \begin{bmatrix} r_{11} & r_{12} & r_{13} \\ r_{21} & r_{22} & r_{23} \\ r_{31} & r_{32} & r_{33} \end{bmatrix} \cdot \begin{pmatrix} X - X_0 \\ Y - Y_0 \\ Z - Z_0 \end{pmatrix} \quad (3.5)$$

Deploy and simplify Equation 3.5, we achieve:

$$x_1 = \frac{L_1X + L_2Y + L_3Z + L_4}{L_9X + L_{10}Y + L_{11}Z + 1} \quad (3.6)$$

$$y_1 = \frac{L_5X + L_6Y + L_7Z + L_8}{L_9X + L_{10}Y + L_{11}Z + 1} \quad (3.7)$$

where

$$L_1 = \frac{x_0 r_{31} - d \cdot r_{11}}{D}$$

$$L_2 = \frac{x_0 r_{32} - d \cdot r_{12}}{D}$$

$$L_3 = \frac{x_0 r_{33} - d \cdot r_{13}}{D}$$

$$L_5 = \frac{y_0 r_{31} - d \cdot r_{21}}{D}$$

$$\begin{aligned}
L_4 &= \frac{(d.r_{11} - x_0r_{31}).X_0 + (d.r_{12} - x_0r_{32}).Y_0 + (d.r_{13} - x_0r_{33}).Z_0}{D} \\
L_6 &= \frac{y_0r_{32} - d.r_{22}}{D} & L_7 &= \frac{y_0r_{33} - d.r_{23}}{D} \\
L_8 &= \frac{(d.r_{21} - y_0r_{31}).X_0 + (d.r_{22} - y_0r_{32}).Y_0 + (d.r_{23} - y_0r_{33}).Z_0}{D} \\
L_9 &= \frac{r_{31}}{D} & L_{10} &= \frac{r_{32}}{D} \\
L_{11} &= \frac{r_{33}}{D} & D &= -(x_0r_{31} + y_0r_{32} + z_0r_{33})
\end{aligned}$$

$L_1 \dots L_{11}$ are referred to as DLT parameters. As can be seen from Equations 3.1 - 3.6, one calibrated point N generates two equations including five known coordinates (X,Y,Z, x_1 , y_1) and eleven DLT unknown parameters ($L_1 \dots L_{11}$). The first step in the 3D reconstruction procedure is to determine the DLT parameters. In order to determine the DLT parameters, we need to predetermine the coordinates in at least eleven equations. Therefore, six calibrated points are needed to generate twelve equations to solve for the DLT parameters. In the next step, each stereo corresponding point of the object and its 3D reconstruction can be performed based on the DLT parameters and its 2D coordinates in at least two different images.

The application of SCP-DLT for 3D spinal reconstruction is not new. De Smet *et al.* used triangulation to display the top view of a 3D reconstructed spine to predict the progression of scoliosis (De Smet *et al.*, 1983). Aubin *et al.* performed 3D reconstruction of vertebral endplates to measure wedged scoliotic vertebrae and intervertebral disks (Aubin *et al.*, 1997). Jaremko *et al.* used Dansereau's techniques described in (Dansereau *et al.*, 1990) and neural networks to correlate spine and rib deformity in scoliosis (Jaremko *et al.*, 2000). The indices that were commonly extracted from the 3D reconstruction were the Cobb angle, the apex location, the magnitude of vertebral axial rotation for each level, the magnitude of posterior rib rotation, and the orientation of the PMC. Artificial neural networks and linear regression models have been used to predict rib rotation based on these spinal indices. Carpineta and Labelle determined the Cobb angle in the frontal and sagittal planes, in the planes of maximum and minimum deformity, and the orientation of the plane of maximum and

minimum deformity to find evidence of 3D variability in scoliotic curves (Carpineta and Labelle, 2003).

Direct linear transformation with non-stereo corresponding points

Mitton *et al.* and Mitulescu *et al.* improved the 3D reconstruction image quality by increasing the number of 3D reconstructed points (Mitton *et al.*, 2000, Mitulescu *et al.*, 2001). This technique required 25 vertebral landmarks: six SCPs and nineteen NSCPs. The six SCPs were obtained from the DLT and the nineteen NSCPs were extracted from *a priori* knowledge of vertebra anatomy. The principle was based on the deformation of an elastic generic object that respected SCP and NSCP observations available in various projections. The kriging interpolation technique was then applied to the 25 points to obtain a set of 178 points for a single vertebra. Although the image quality was improved, the processing time also increased to the extent that this technique was not suitable as a clinical tool.

Furthermore, there were several studies applying the DLT-NSCP technique to study scoliosis. Dumas *et al.* performed 3D reconstruction on ten patients who had right thoracic curves for surgical treatment outcomes evaluation (Dumas *et al.*, 2003). This group also evaluated the accuracy and precision of the 25-point vertebral model and the basic 6-point model (Dumas *et al.*, 2004). The DLT-NSCP results were close to those obtained using 3D reconstruction from CT scans.

Semi-automated statistical method

Pomero *et al.* reported a semi-automated statistical method which was based on the vertebral body volume (Pomero *et al.*, 2004). This method required a reliable known knowledge of the vertebral shape and used eight measurements from a vertebral body to estimate 21 coordinates of each vertebra. The results showed a similar accuracy of 3D reconstruction between the manual DLT-NSCP technique and the semi-automated statistical method with regard to the CT-scan references. Modifications for the statistical method have been made to improve image quality (Blanchard and Elbaroudi, 2008, Dumas *et al.*, 2008), and reduce user's interactions (Deschenes *et al.*, 2004).

Apart from the aforementioned approaches, other MPR techniques have also been proposed to increase the simplicity, accuracy and implementation speed of 3D reconstruction. The triangulation technique helped to determine the location of any point when the locations of both X-ray sources and the projected images were known (De Smet *et al.*, 1980). A computerized method using three radiographs, or a 3D/2D statistical registration model for a minimization of a cost function for each vertebra were also reported (Cook *et al.*, 1981, Benameur *et al.*, 2003). A single radiograph and prior vertebra models were added to visualize the lateral view of the spine in a lateral bending position when only an anterior–posterior view is available (Novosad *et al.*, 2004). In addition, the hierarchical statistical modelling was proposed to overcome the problem of supervision (Benameur *et al.*, 2005). Involuntary motion occurring between X-ray exposures could be compensated by a novel calibration jacket worn by the patient during imaging and explicit calibration algorithm (Cheriet *et al.*, 2007b). In addition, an estimation from partial 3D spine models and articulated spine model reconstruction from radiographs could be applied in case of missing information (Boisvert *et al.*, 2008). Finally, the application of epipolar geometry could accurately identify the corresponding landmarks, or that of a deformable articulated model could minimize the need for calibration objects (Zhang *et al.*, 2010, Moura, 2010).

Traditional MPR exposes a lower radiation dose than CT while remaining sensitive to bony structures. However, the method also has some drawback. MPR does not exploit all the information contained in the two or more X-ray radiographic projections. The DLT-based stereography allows the 3D reconstruction and requires a small number of stereo corresponding anatomical landmarks (6 points for each vertebra). However, the DLT showed a difficulty to identify corresponding points in images (Nyström *et al.*, 1994, Pearcy, 1985), leading to reconstruction errors. Common radiographic digitization errors of up to 2 mm can cause 3D reconstruction errors of up to 5 mm (Otsu, 1979). In order to achieve higher quality images, researchers proposed increasing the number of 3D reconstructed points to improve the reconstruction accuracy (Mitton *et al.*, 2000, Mitulescu *et al.*, 2001, Pomero *et al.*, 2004, Benameur *et al.*, 2005, Moura *et al.*, 2011, Kadoury *et al.*, 2008). However, the increase in the number of reconstructed points results in longer processing time. Nevertheless, the MPR approaches also require a large database as *a priori* knowledge. They can only be applied to less deformed vertebrae. Also, these methods require a calibrating frame encompassing the

patient's trunk (Aubin *et al.*, 1997, Mitton *et al.*, 2000, Mitulescu *et al.*, 2001, Dumas *et al.*, 2003, Pomero *et al.*, 2004, Benameur *et al.*, 2003, Benameur *et al.*, 2005, Dansereau and Stokes, 1988), a rotatory platform with calibration objects (Cheriet *et al.*, 2007b), or small calibration objects at an expense of more user interaction (Cheriet *et al.*, 1999, Kadoury *et al.*, 2007). The calibration process makes the clinical routine setup complicated, time-consuming, and contributes artefacts to the reconstructed images. The fact that two or more exposures are not taken simultaneously makes the calibrations and 3D position of the spine are not consistent, causing the reconstruction vulnerable to the patient's motion or re-positioning between exposures (Marcil *et al.*, 1995). Furthermore, these techniques require a high level of user interaction by well-trained experts. Therefore, they are mainly used for research purposes. Like CT and MRI, MPR is not appropriate for the lateral bending test; therefore, a novel method was developed (Novosad *et al.*, 2004). In terms of accuracy, a summary of an error analysis from different techniques is carefully described in the Moura's thesis (Moura, 2010).

Recently, an advanced version of MPR (EOS[®] imaging system) can scan the patient in the standing position with two X-ray sources and provides the coronal and lateral radiographs simultaneously. Its radiation dose is at least 9 times lower than computed radiography (Dubousset *et al.*, 2005, Deschenes *et al.*, 2010, Release, 2013), and its 3D reconstruction accuracy is similar to a CT scan (Dubousset *et al.*, 2005, Glaser *et al.*, 2012). In addition, its image quality is claimed to be better than the traditional radiography (McKenna *et al.*, 2012, Wade *et al.*, 2013). The dedicated software combines the details (simultaneity and orthogonality) of several landmarks digitized by the operator on both radiographs and *a priori* statistical knowledge to reconstruct a 3D envelope of the bone structure. The software displays the 3D images within 15 minutes.

The EOS[®] imaging has several advantages. First, the exposures are taken with the patient standing, thus eliminating the effect of gravity. Second, the radiation dose is less with very good image contrast and without the distortion inherent in today's longer length film and digital imaging systems (Dubousset *et al.*, 2005, Deschenes *et al.*, 2010, McKenna *et al.*, 2012, Wade *et al.*, 2013). For the EOS[®], the scale of the subject and the image is considered 1:1, whereas the image is usually larger than the subject for the other radiographies. Third, the

imaging system performs the simultaneous acquisition of the PA and lateral X-ray images. The simultaneous acquisition minimizes the patient motion artifacts between the two radiographs, thus resulting in better image quality. Furthermore, EOS 3D reconstruction depends on landmark digitization and *a priori* database. Better quality images show clearer landmarks, resulting in more accurate landmark digitization and then more accurate reconstruction. The accuracy of the 3D reconstruction obtained from both EOS® and CT was reported to be similar (Dubousset *et al.*, 2005, Glaser *et al.*, 2012). However, the enclosed design of the EOS® system posts limitations on the patient's size as well as the bending test.

Although X-ray based imaging modalities provide good images of bony structures, they raise a concern of radiation-induced cancer risk among the patients and their families. The majority of patients with scoliosis are relatively young, thus being more sensitive to the harmful radiation than adults are. Children are also more likely to manifest radiation-induced effects over their lifetime (Brenner *et al.*, 2001). In general, during the treatment or observation periods, patients with AIS may have repeated radiographs every four to twelve months (Doody *et al.*, 2000); the cumulative amount of ionizing radiation may increase the risk of cancer (McKenna *et al.*, 2012, Doody *et al.*, 2000, Miller, 1999, Ronckers *et al.*, 2010). In the Ronckers *et al.* study (Ronckers *et al.*, 2010), they reported the potential risk of radiography and found that the cancer mortality of scoliotic patients was 8% higher. Miller also claimed that less than 10% of the patients who underwent radiological examinations required treatment (Miller, 1999). This means that more than 90% were exposed to X-ray radiation unnecessarily.

3.1.5 Ultrasonography

Ultrasound is a sound wave with frequency higher than the upper audible limit of human hearing that is approximate 20 kHz. The ultrasound frequencies for most medical applications are usually in the range of 2 MHz to 10 MHz. Ultrasonography or ultrasound imaging is an ultrasound-based diagnostic imaging technique, which has been used to visualize soft tissues. Using ultrasound to image bone has become popular because of increasing concerns with ionizing radiation exposure, especially in growing children. Ultrasonography in imaging bone can be 2D and 3D.

Two-dimensional ultrasonography

In 2D ultrasonography, the pulse-echo technique is used in such a way that a short-duration pulse of mechanical energy is transmitted into the region of interest of tissues at the speed of sound (1,540 m/s), and echo signals reflecting from reflection and scattering return to the source and are detected and displayed. The amount of reflection and scattering energy vary with the changes in the tissue acoustic properties. Images are displayed as cross-sections of the region of interest and are called B-mode images. Due to the difference in acoustic impedances, the reflection of ultrasound energy occurs at the boundary between two different tissues. Figure 3.9 demonstrates the pulse-echo techniques. For instance, at point A as shown in the figure, the reflection coefficient R can be expressed as follows.

$$R = \frac{I_{r1}}{I_{i1}} = \left(\frac{Z_2 - Z_1}{Z_2 + Z_1} \right)^2 \quad (3.8)$$

where I_{r1} and I_{i1} are the reflected and incident intensity in media 1 and 2, respectively, Z_1 and Z_2 are the acoustic impedances of media 1 and 2, respectively.

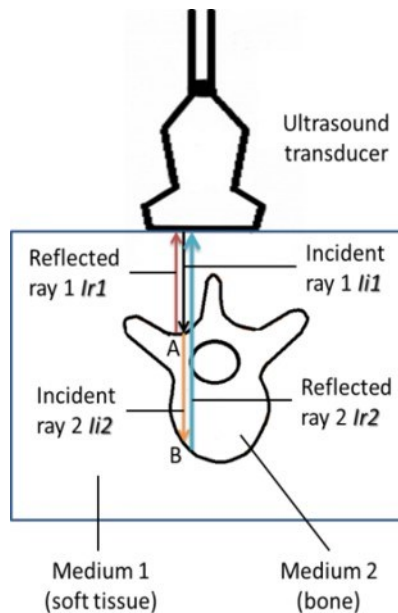


Figure 3.9 The pulse-echo technique.

Suzuki *et al.* were the first to utilize ultrasound technique to scan the back of the patient in the prone position to measure the AVR (Suzuki *et al.*, 1989). At first, an antero-posterior radiograph was taken to determine the inclination of the vertebrae relative to the horizon. Lines were then drawn parallel to the inclination of the vertebrae on patients' back through previously marked spinous processes. The ultrasound probe that was attached with an inclinometer was placed on the spinous process along each line. The screen displayed the transverse processes and the laminae; the transducer was then tilted until the image of the laminae became horizontal on the screen. In this study, laminae were used as landmarks to measure the AVR and the rotation of the laminae were determined by using the inclination of the transducer. The result showed that ultrasound could be used to visualize the spinous process and the laminae, leading to the measurement of the AVR. Ultrasound was also used to measure laminal and rib rotations directly on the back of the patient in the prone position (Burwell *et al.*, 2002). However, prone positioning was reported to reduce all spinal curves (Driscoll *et al.*, 2012).

Years later, Chen *et al.* proposed a method using the centres of lamina (COL) instead of vertebral body endplates as landmarks to measure the proxy Cobb angle (Chen *et al.*, 2012, Chen *et al.*, 2013). The proxy Cobb angle was measured by the angle between two lines going through the COL of the two most tilted vertebrae of each curve. The difference in the Cobb angle between the traditional Cobb and COL methods was quite small ($0.7^\circ \pm 0.5^\circ$), inferring that the latter can replace the former. The measurement of the AVR using the COL on the transverse view demonstrated high intra- and inter-rater reliability for both *in-vitro* and *in-vivo* studies (ICCs > 0.91, MAD < 1.4°) (Chen *et al.*, 2016). The *in-vitro* results also showed good correlation with the Stokes method (ICC = 0.84 - 0.85, MAD = 4.5° - 5.0°); however, poor agreement was for the *in-vivo* study (ICC = 0.49 - 0.54, MAD = 2.7° - 3.5°). This was the pilot study and the validity of the method was not performed.

Many researchers applied the COL method to measure the spinal curvature and the AVR on ultrasound images (Zheng *et al.*, 2015, Vo *et al.*, 2015, Young *et al.*, 2015, Wang *et al.*, 2015, Wang *et al.*, 2016). In the Wang *et al.* study (Wang *et al.*, 2015), the spinal curvature was measured using the COL method on the ultrasound image while using the Cobb method on the MRI image. Their results showed that there was no significant difference ($p < 0.05$) and

high agreement ($r > 0.9$) between the two methods. Wang *et al.* (Wang *et al.*, 2016) determined the validity of the AVR measurement using 3D ultrasound in AIS. The COL method and the Aaro-Dahlborn's method were used to measure the AVR on the ultrasound transverse image and MRI image, respectively. Their *in-vivo* study reported high intra- and inter-rater reliabilities ($ICC(2,k) > 0.978$). In addition, the mean absolute differences between the two methods for the vertebral rotation range of $0^\circ - 5^\circ$, $5^\circ - 10^\circ$, and $> 10^\circ$ were $0.3^\circ \pm 0.3^\circ$, $0.5^\circ \pm 0.3^\circ$, and $1.0^\circ \pm 1.1^\circ$, respectively. In another trend, Young *et al.* and Zheng *et al.* (Young *et al.*, 2015, Zheng *et al.*, 2016) investigated if the reliability and accuracy of the coronal curvature were improved with the aid of previous radiographs in AIS. In these studies, the last pair of ribs was used to determine the vertebra T12 on the ultrasound image. Raters laid the current ultrasound image over the previous radiograph such that the corresponding designated points, laminae on the ultrasound image and pedicles on the radiograph, were lined up. The measurement of spinal curvature was performed on the overlaid images. It was found that the previous radiograph helped to increase the agreement between ultrasound and radiograph measurements ($r^2 = 0.90$, $MAD = 2.8^\circ$). It also helped the user to select the end vertebrae on the ultrasound image more accurately (improved 43%).

Three-dimensional ultrasonography

All internal human organs are 3D objects; therefore, 2D B-mode images cannot present the true shape and structure of the scanned objects. In the past, physicians used their imagination to reconstruct the 3D images in their minds, which may lead to inevitable errors. Thus, 3D ultrasonography is needed. In theory, 3D ultrasound images can be obtained by stacking a series of acquired 2D B-mode images together with their position and orientation information. Reviews of 3D ultrasound imaging techniques can be found in (Fenster *et al.*, 2001, Solberg *et al.*, 2007, Prager *et al.*, 2010). There are two major steps to obtain a 3D ultrasound spinal image: scanning the spine to acquire 3D ultrasound data and reconstructing the acquired data into the 3D spinal image.

In general, there are four 3D ultrasound scanning approaches, which use: a) a dedicated 3D transducer, b) freehand techniques with position tracking, c) freehand techniques without position tracking, and d) a 2D-array transducer.

Scanning using a dedicated 3D transducer

The probe with motorized scanning consists of a linear ultrasound transducer, which is controlled by a mechanical motor to translate or rotate to generate the 3D ultrasound images. There are three types of mechanical scanning: tilt, linear, and rotational (Figure 3.10). For the tilt configuration, the transducer sweeps within a pre-determined angulation and acquires data at a regular angular spacing interval (Figure 3.10a). Meanwhile, B-scans generated by linear scanning are translated within a pre-determined distance and are parallel to each other at a regular spacing (Figure 3.10b). The rotational scanning configuration is similar to the first type; however, it has a wider angulation of 360° (Figure 3.10c). In all configurations, the speed of the motor is steadily controlled to move the transducer array that generates B-scans; therefore, the 3D mechanical scanning technique can provide short-time imaging, high-quality 3D images, and real-time 3D visualization. However, this type of transducer is bulky and heavy with the motorized mechanism, thus inconvenient to be used for scanning long objects like the entire spine.

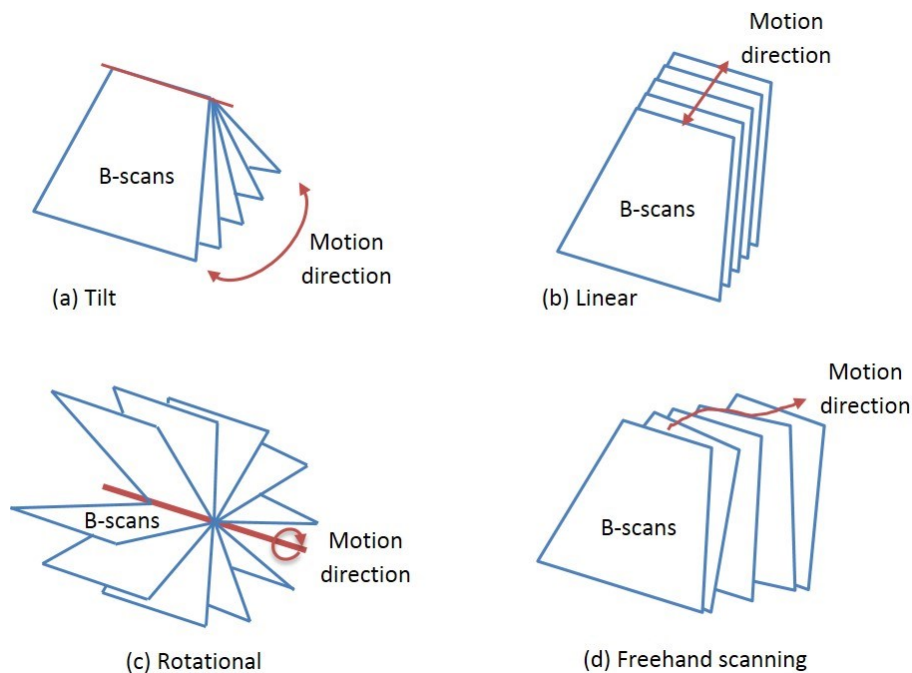


Figure 3.10 3D ultrasound scanning configurations (a) Dedicated 3D tilt scanning; (b) Dedicated 3D linear scanning; (c) Dedicated 3D rotational scanning; (d) Freehand 3D scanning.

Scanning using the freehand technique with position tracking

In order to overcome the clumsiness of the motorized probe, the freehand 3D scanning technique with position sensing has been developed. With this configuration, the operator is free to move the transducer along any arbitrary direction (Figure 3.10d). The conventional 2D ultrasound linear transducer has no mechanical mechanism, but is attached to a position sensor (for example, an electromagnetic sensor) to track the position and the orientation of the transducer when it moves over the object. As the transducer moves along the scanning object, a series of 2D B-mode images can be captured. After the completion of the data acquisition, the 2D B-mode images and their tracking data are used to form a 3D volume. This freehand technique is considered more suitable for imaging the spine due to the flexibility and ease of mobilizing the transducer. Unfortunately, the acquired data are usually irregularly spaced; resampling the data for a regularly spaced data set is a time-consuming process (Figure 3.10d).

Position tracking techniques can be categorized into five major types (Fenster *et al.*, 2001, Cinquin *et al.*, 1995, Mercier *et al.*, 2005): articulated arm, optical sensing, magnetic sensing, acoustic sensing, and speckle decorrelation. Position and orientation sensing can be obtained by attaching the ultrasound probe on a mechanical articulated arm having a minimum of six degrees of freedom. Potentiometers mounted at the joints of the arm provide necessary information to determine the position and orientation of acquired B-scans. Even though the articulated arm has acceptable accuracy, it is bulky and can only track one object at a time. Optical sensing is the most accurate localizer that can be used to track multiple objects. Cameras are used to observe markers on the objects and the position of each marker will be reconstructed by the system. Unfortunately, it requires a line of sight between the cameras and the markers so that the optical signal can be transmitted and received properly. In electromagnetic sensing, a spatially varying magnetic field is produced by a transmitter and its magnetic field strength is sensed by a receiver having three orthogonal coils. The position and orientation of each acquired B-scan can be calculated from the strength of three components of the local magnetic field. Despite being small and not obstructed by an object between the transmitter and the receiver, electromagnetic sensing devices are affected by metal located in the surrounding environment. In acoustic sensing, three sound emitters are attached on the

probe while an array of fixed microphones are placed over the patient. The microphones continuously receive sound pulses from the emitters while the probe is being moved. The position and orientation of each acquired B-scan are calculated based on the information on the speed of sound in air, times from each emitter to each microphone, and the fixed locations of the microphones. Acoustic sensing is affected by variations in temperature, pressure and humidity and it requires a clear space between the speaker and the microphone. In speckle decorrelation, ultrasound image speckle can be used to track the positions and orientations of two adjacent B-scans. If one of the B-scans is moved parallel relative to the other, the degree of decorrelation is proportional to the distance between two B-scans. If the B-scans are tilted or rotated, they are divided into smaller regions. Similar regions in these adjacent B-scans are cross-correlated to generate a decorrelation pattern that determines the relative position and orientation of the two B-scans. Speckle decorrelation techniques for 3D ultrasound imaging are complicated and time-consuming.

Scanning using the freehand technique without position tracking

If spatial accuracy is not required, the freehand scanning technique without position tracking can be used. In this approach, the transducer is manipulated over the body in a predefined and regular scanning geometry. The 2D acquired images are assumed to be uniformly or regularly spaced. In the scanning process, the operator attempts to control the motion speed of the transducer as steadily as possible along the path of the anatomy.

Scanning using a 2D-array transducer

In this approach, a 2D phased array of transducer elements is used to generate a broad beam of ultrasound covering a truncated pyramid shaped volume. The ultrasound signals returning to the 2D-array transducer are processed to display multiple planes from this volume in real time. The limitations of this technique are the high cost and large size of the 2D-array transducer.

3D reconstruction

As previously mentioned, the acquired 2D B-scans need stacking together to form a volume. For the scanning technique using a dedicated 3D probe and the freehand scanning

without position sensing, only a set of B-scans is acquired. The regular spacing or angulation between two adjacent frames is set by the mechanical configuration of the dedicated probe or by the software in case of not using position sensing. For freehand scanning with position sensing, it is obvious that B-scans are irregular and not uniform. In order to more easily render and manipulate the reconstructed volume, these B-scans need to be rearranged in such a way that all of them are regular; that is, the spacing between two consecutive B-scans are equal. There are four distinct reconstruction approaches based on their implementation: feature-based reconstruction, voxel-based reconstruction, pixel-based reconstruction, and function-based reconstruction.

In the feature-based reconstruction method, surfaces of desired anatomical structures are first determined, extracted and then reconstructed into 3D images. This approach generates a smaller size of data because non-featured data is removed; therefore, the reconstruction process takes a shorter time and the manipulation of the reconstructed image can be easily performed using a less powerful computer. However, it is tedious and time-consuming if the feature extraction step is manually performed. Furthermore, this technique only keeps data on the features; data beyond the features are missing, thus leading to an inability to display region data on an arbitrary plane.

The voxel-based reconstruction method (VBM) is more popular than the feature-based method. The voxel-based method is also known as the backward reconstruction method since it traverses each voxel in the reconstructed volume across 2D images and gather information of the corresponding pixel from the acquired 2D images to be assigned for the voxel. The reconstruction process undergoes two major steps. In the first step, the acquired images are stacked into the image volume by placing each 2D pixel coordinates (x',y') to its corresponding 3D coordinates (x,y,z) . In the second step, each voxel value is calculated based on its nearest neighbors. There are several variants of voxel-based methods. If only the closest pixel to the voxel is used without any weighting, the method is then called voxel-nearest-neighbor (VNN) (Sherebrin *et al.*, 1996). It can be done by traversing each volume voxel across the target voxel grid and assigns the value of the nearest image pixel as illustrated in Figure 3.11.

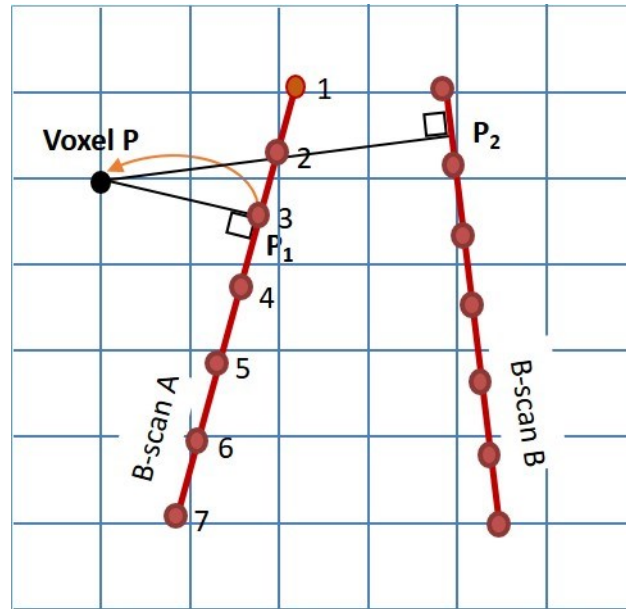


Figure 3.11 The Voxel Nearest Neighbor (VNN) method. The square grid is the cross section of the volume and the intersections of the vertical and horizontal lines are the centers of voxels; The tilt lines are the cross sections of B-scans; The dots are pixels on each B-scan (for example, numbered from 1 to 7); P_1 and P_2 are projection points on B-scan A and B-scan B, respectively.

For simplicity, two B-scans are inserted into the volume: B-scan A and B-scan B. In order to find a value for voxel P, the distances from voxel P to the two B-scans PP_1 and PP_2 are calculated respectively. Intuitively, PP_1 is shorter than PP_2 , which means voxel P is closer to B-scan A than B-scan B. Therefore, the value assigned to voxel P should be situated on B-scan A. In the next step, the pixel closest to projection point P_1 should be found. In this example, pixel 3 is closest to P_1 ; therefore, its intensity value is used to assign to voxel P.

Another variant of the VBM is the Voxel-Based Method with Interpolation (VBMI) that uses one value achieved by the interpolation of several input pixel values for deciding a voxel value. Trobaugh *et al.* proposed an algorithm to decide a voxel value by an interpolation from the two nearest surrounding slices (Trobaugh *et al.*, 1994). This approach traverses the voxel across the target volume grid and finds the two nearest 2D slices on each side of the voxel. An example of bilinear interpolation with the two nearest B-scans is shown in Figure 3.12. We suppose that voxel P finds its two nearest B-scans: B-scan A and B-scan B among many other B-scans in the volume. The projections of the voxel on these two slices are determined by P_1

and P_2 , respectively. The four surrounding pixels of P_1 and P_2 are bi-linearly interpolated in each plane to calculate values of P_1 and P_2 .

$$\begin{aligned} \text{value}P_1 = & BscanA(x_1, y_1)(1 - x_{b1})(1 - y_{b1}) + BscanA(x_1 + 1, y_1)x_{b1}(1 - y_{b1}) \\ & + BscanA(x_1, y_1 + 1)(1 - x_{b1})y_{b1} + BscanA(x_1 + 1, y_1 + 1)x_{b1}y_{b1} \end{aligned} \quad (3.9)$$

Similarly,

$$\begin{aligned} \text{value}P_2 = & BscanB(x_2, y_2)(1 - x_{b2})(1 - y_{b2}) + BscanB(x_2 + 1, y_2)x_{b2}(1 - y_{b2}) \\ & + BscanB(x_2, y_2 + 1)(1 - x_{b2})y_{b2} + BscanB(x_2 + 1, y_2 + 1)x_{b2}y_{b2} \end{aligned} \quad (3.10)$$

The final voxel value is calculated as a weighted sum with interpolated values from the two planes based on the distances d_1 and d_2 from the voxel to the planes.

$$\text{value}_{\text{voxel}P} = \frac{\text{value}P_1 \cdot \frac{1}{d_1} + \text{value}P_2 \cdot \frac{1}{d_2}}{\frac{1}{d_1} + \frac{1}{d_2}} \quad (3.11)$$

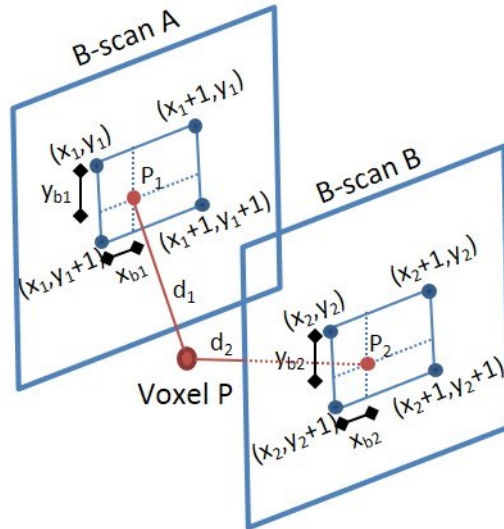


Figure 3.12 Bilinear interpolation of two B-scans in the VBMI.

The interpolated value can be achieved from more B-scans for a higher accuracy. In this case, it is generalized that:

$$value_{voxelP} = \frac{\sum_i (valueP_i \cdot \frac{1}{d_i})}{\sum_i \frac{1}{d_i}} \quad (3.12)$$

where i is the number of B-scans involved in the interpolation.

Coupé *et al.* modified this approach by proposing the probe trajectory method (Coupe *et al.*, 2005). For each voxel, two nearest B-scans also need to be determined. Instead of finding an orthogonal projection of the voxel on each of these slices, a probe trajectory is estimated and used for finding the corresponding pixels in the nearest 2D planes.

The VBM does not leave any holes since all voxels are traversed throughout the target volume and acquire non-empty values from somewhere, no hole filling is necessary. However, this algorithm requires the completion of data acquisition before the reconstruction process can commence; therefore, real-time imaging may be difficult to achieve.

In the pixel-based reconstruction method (PBM), each pixel in the input image is traversed and its value is assigned to one or more voxels (outputs); therefore, the PBM is also referred to as the forward reconstruction. The PBM is implemented in two steps: the distribution step (bin filling) and the hole-filling step. The distribution step traverses each input pixel and assigns its value to one or several voxels. Most PBM methods use the Pixel Nearest Neighbor (PNN) bin filling as shown in Figure 3.13. In the PNN method, the value of the pixel is assigned to the voxel that is closest to that pixel. As can be seen from Figure 3.13, voxel P receives two assignments from pixels 3 and 4 of B-scan B. If there are multiple assignments to a single voxel, the voxel value can be one of the following: the last value (Ohbuchi *et al.*, 1992), the first value (Trobaugh *et al.*, 1994), the maximum value (Nelson and Pretorius, 1997), or the average of all contributions (McCann *et al.*, 1988, Nelson and Pretorius, 1997, Gobbi and Peters, 2002). If the voxel value is updated with the first or the last value, it can be erroneous if the updated value is erroneous due to noise in tracking data or ultrasound sensing. Updating the voxel value with an averaged value of all contributions reduces noise at an

expense of image blurring at that voxel. Therefore, updating the voxel with the maximum value among all contributions can be useful to avoid deleting non-erroneous values by overwriting them with erroneous values. It is also likely that there are voxels existing without any contribution of a pixel value, especially when the object has not been scanned with a dense sampling. Therefore, the second step may be needed to fill the remaining gaps. In (Nelson and Pretorius, 1997), Nelson and Pretorius proposed a method and later applied by Solberg *et al.* (Solberg *et al.*, 2011) in which empty voxels are filled by taking the average of the filled voxels in a $3 \times 3 \times 3$ neighborhood. If there are remaining unfilled voxels, they are then filled by averaging originally filled voxels in a $5 \times 5 \times 5$ neighborhood and so on, until all voxels are filled. The PBM can be implemented along with data acquisition, which enables real-time imaging. Nevertheless, this method may encounter more problems in the determination of holes and finding values in the neighborhood to fill these holes.

Finally, in the function-based reconstruction method (FBM), a function or functions through input pixels are estimated for reconstruction. A particular function (such as a polynomial) is chosen and coefficients are determined to make one or more functions pass through the input pixels. A regular voxel array is created by evaluating the function or functions at regular intervals. Rohling *et al.* proposed the Radial Basis Function interpolation (RBF) which is an approximation with splines using the underlying shape of the data in the volume reconstruction (Rohling *et al.*, 1999). Although the RBF offers more accurate reconstruction than the standard methods, it is computationally expensive.

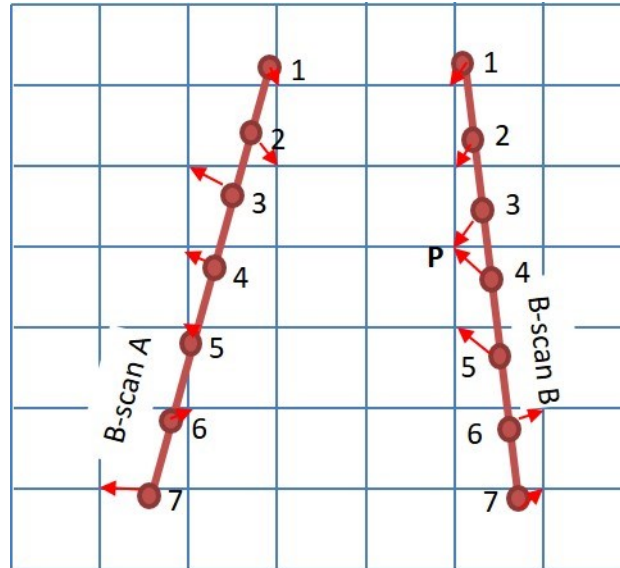


Figure 3.13 The Pixel Nearest Neighbor (PNN) method. The square grid is the cross section of the volume and the intersections of the vertical and horizontal lines are the centers of voxels; The tilt lines are the cross sections of B-scans; The dots are pixels on each B-scan (for example, numbered from 1 to 7); P1 and P2 are projection points on B-scan A and B-scan B, respectively.

3D ultrasound images for scoliosis applications

Unlike MPR, only few studies reported on 3D ultrasound reconstruction of the scoliotic spine. Purnama *et al.* introduced a framework for human spine imaging using a freehand 3D ultrasound system with an optical tracking device (Purnama *et al.*, 2007a). The 3D reconstruction process underwent four stages: bin-filling (VNN), hole-filling, volume segment alignment and volume segment compounding. The AVR and the tilt of each vertebra were calculated based on the centres of mass of the selected vertebral regions that were determined manually and semi-automatically by landmark points. The 3D deformity of the spine was determined by two curves connecting the centres of mass of the left and the right selected regions of each vertebra. The coronal projection of this curve shows lateral deviation whereas the projection on the lateral plane provides information on the magnitude of kyphosis and lordosis of the spine. The thresholding method was proposed to improve the estimation result (Dewi *et al.*, 2009). Purnama *et al.* built a 3D spinal model from a non-scoliotic healthy volunteer (Purnama *et al.*, 2007a), and then validated the model using 5 data sets from

scoliotic patients (Dewi *et al.*, 2009). The validation was not fully proven. In a recent study, the surface rendering technique was applied to display a 3D reconstructed spine from ultrasound data (Nguyen *et al.*, 2015). Nguyen *et al.* used manual digitization method of the vertebral surface from each B-mode image to reconstruct the spine. The 3D reconstruction process was fast but the digitization process was tedious and time-consuming. Furthermore, since the vertebral body could not be identified and reconstructed, the COL method was used to measure the Cobb angle (Chen *et al.*, 2012). Two lines were drawn through the COL of two most tilted vertebrae of each curve. The study reported a good reconstruction of the whole spine with a difference of 4° in the Cobb angle and 2° in the AVR.

Cheung *et al.* designed a system with a freehand 3D ultrasound system and an electromagnetic spatial sensing device for a scoliosis application (Cheung *et al.*, 2015a). After a patient was scanned, a series of B-mode images was collected and displayed in the 3D space according to their corresponding spatial information. The sharpest tips of different bony features (transverse process, superior articular process) were manually identified on the B-mode images and marked with spherical markers using the custom-designed software. All the selected tips were reconstructed into a virtual 3D model of a patient's spine, which was projected to form a coronal image analogous to the PA radiograph. The spinal curvature was the angle between two lines connecting the markers of transverse process or superior articular process of the most tilted vertebrae. The results reported a significant linear correlation ($r^2 = 0.86$, $p < 0.001$) between spinal curvatures measured on ultrasound images and radiographs. The limitations of this study were the time consumption and subjectivity of the manual marking procedure, and the influence of ultrasound image quality on the identification of bony features. In another study (Cheung *et al.*, 2015b), the ultrasound volume data was reconstructed by the squared distance weighted interpolation method. The narrow-band non-planar volume-rendering algorithm was developed to better visualize spine anatomy through coronal images. The coronal image, which was similar to a PA radiograph, was obtained with the consideration of the natural curve of the spine therefore revealed more bony features. The spinal curvature was manually determined using either the spinous column profile or the transverse processes as reference. In the first method, the spinous processes created an ultrasound shadow curve nearby the midline of the spine image. The vertebra located at the curve inflection point could be considered as the most tilted vertebrae. Two short lines going

through the inflection points were manually drawn in the middle of the shadow curve. The angle between these two lines was spinal curvature. The second method used transverse processes as reference features. The spinal curvature was determined by the angle between two lines connecting two pairs of transverse processes of the most tilted vertebrae. The results showed that the intra- and inter-rater variations between two methods were small (1.4° - 2.5°), and the ultrasound methods had good linear correlation with X-ray Cobb method. However, there was a compromise between image quality and implementation speed.

Ungi *et al.* proposed another freehand 3D ultrasound imaging method in which the tips of the transverse processes of each vertebrae were utilized as landmarks to calculate the transverse process angle relative to horizontal of each vertebra (Ungi *et al.*, 2014). Instead of scanning the spine vertically as in the aforementioned approaches, their ultrasound transducer was orientated vertically while scanning from the side toward the midline of the spine. When the acoustic shadow of the transverse process of that side was most clearly visible, the tracked ultrasound image was taken in this position. The procedure was repeated for the other side of the vertebra. For each vertebra, two images of the transverse process were taken. The tips of the transverse processes were manually chosen on these ultrasound images. The line going through two tips of transverse process of each vertebra and the horizontal line formed the transverse process angle of that vertebra. Based on the calculated transverse process angle, upper and lower tilted angle to calculate the proxy Cobb angle could be calculated. This phantom study reported that the discrepancies between the ultrasonographically and radiographically measured transverse process angles were approximately 1° for the two spine phantoms. The limitation of this study was that the phantoms were rigid. Therefore, they did not bear any weight or change the curvature like in scoliosis patients. Furthermore, this study did not propose the measurement of the AVR.

Ultrasonography is an alternative to image the scoliotic spine. It is a non-ionizing, low cost, portable and able to display real-time imaging. Non-ionization makes this imaging modality safe to patients. So far, there is no evidence that medical ultrasound causes any harms to internal organs. In addition, its mobility and configuration do not require a special setup, calibration and dedicated equipment like the other methods. In recent years, ultrasound has been used to characterize bone tissues (Zheng *et al.*, 2007, Tran *et al.*, 2013, Tran *et al.*, 2014,

Nguyen *et al.*, 2013, Le *et al.*, 2010). Although spinous process, laminae, and transverse processes can be visualized and used as landmarks to measure the curvature and rotation (Purnama *et al.*, 2007b, Cheung *et al.*, 2015b, Ungi *et al.*, 2014, Chen *et al.*, 2013, Suzuki *et al.*, 1989, Conversano *et al.*, 2015), a full clinical validation on 3D measurements has not been performed yet. Despite having several advantages, ultrasonography still has limitations due to the characteristics of ultrasound and tissue. The majority of incident ultrasound beams are reflected at the interface between soft tissue and bone. Ultrasound signals are even worse when a patient has thick back muscles due to higher ultrasound attenuation. Thus, it is extremely hard or even impossible to recognize vertebral body on B-mode images, leading to the impossible reconstruction of the vertebral body. As a result, the upper end plate of the superior end vertebra and the bottom end plate of the inferior end vertebra cannot be identified to determine the Cobb angle. Other landmarks such as the COL (Purnama *et al.*, 2007b, Chen *et al.*, 2013, Vo *et al.*, 2015, Vo *et al.*, 2014), or the centres of transverse processes (Purnama *et al.*, 2007b, Cheung *et al.*, 2013, Cheung *et al.*, 2015b, Ungi *et al.*, 2014, Vo *et al.*, 2014) have been proposed. Laminae are resistant to deformation, whereas transverse processes and spinous processes are not. Therefore, measuring the Cobb angle using transverse processes and spinous processes can only be applied to mild and moderate scoliosis. Another limitation is that sonographs include speckle noises. The interface between two different media is blurred, which makes the identification of posterior arch of a vertebra difficult. Hence, image-processing techniques including filtering, edge enhancement, and segmentation are necessary to enhance signal-to-noise ratio prior to the 3D reconstruction. An additional drawback is that this 3D reconstruction is time-consuming. However, real-time or close to real-time reconstruction and visualization of ultrasound could be achieved by the Graphical Processing Unit (GPU)-based technique (Ludvigsen, 2010). Finally, 3D ultrasonography is currently used for AIS, not intentionally for the other types of scoliosis.

3.1.6 Surface topography

In contrast to the aforementioned imaging modalities, surface topography is a non-invasive method that can be used to study the 3D surface of the back. Normally, patients and their parents are more concerned with the cosmetics than the Cobb angle or the AVR. In general, there are several surface topography measurement systems that have been used to digitize the

patient torso to create a 3D model: the Moire fringes, the raster-stereography, the Integrated Shape Imaging System (Oxford Metrics Ltd., Oxford, UK), the Quantec imaging system, and the Inspeck system (Creaform Inc., Lévis, QC, Canada).

The Moiré fringes are created by dark and light lines through interference between a screen and its shadow that falls on an object placed behind. The pattern of the fringes depends on the shape of the illuminated object. Every point on the same fringe has the same distance to the moiré screen. This distance, h , is calculated by:

$$h = \frac{s * l}{d - s} \quad (3.13)$$

where s is the screen intervals (the diameter of a screen wire + the space between two adjacent wires), l is the distance between the light source and the screen, and d is the distance between the light source and the camera.

Since Takasaki used the Moiré fringes to describe the 3D shape of the body (Takasaki, 1970), many researchers have used this method to measure the back morphology based on a change between two halves of the back due to a deformation (Turner-Smith *et al.*, 1988, Sahlstrand, 1986, Weisz *et al.*, 1988, Theologis *et al.*, 1997, Berryman *et al.*, 2008, Willner, 1979b, Willner, 1979a, Daruwalla and Balasubramaniam, 1985, Adair *et al.*, 1977, Ruggerone and Austin, 1986, Kim *et al.*, 2001).

In raster-stereography, a standard slide projector is used to project a regular line raster, a cross raster or a point raster onto the back surface to be measured. A camera records the projected and distorted raster lines. The projector and the camera may be considered as a stereo-photographic system with the raster diapositive and the camera image forming the stereo image pair. However, since the raster diapositive is *a priori* known, only the camera image must be analyzed. The data acquired from the camera image are converted into a conventional stereo image pair to enable conventional photogrammetric calibration and 3D model reconstruction. Raster stereo-photography was used by many researchers (Stokes *et al.*, 1988, Drerup and Hierholzer, 1994, Frobin and Hierholzer, 1982, Hierholzer and Frobin, 1982, Frobin and Hierholzer, 1981).

The Integrated Shape Imaging System (ISIS) was deployed by Weisz *et al.* to investigate if the value of ISIS surface shape measurements can be used to assess the progression of

scoliosis (Weisz *et al.*, 1988). The ISIS is designed to quantify the apparent distortion of a horizontal line of light as it scans vertically over the back of a subject. It comprises an optical scanner and a moving line projector. The former is a stationary television camera producing a plane of light deflected by a mirror. The latter consists of a fixed light projector and a rotating mirror. The mirror is controlled so that it can be accurately positioned to direct the plane of light on different horizontal positions on the patient back. The horizontal line of light is viewed by the camera and light lines on the back are measured by the computer. As the line illuminates a section of non-uniform surface, it will appear to the camera to be distorted. The displacement of each element of the line can be shown to represent the distance of the surface of the object from the optical axis of the projector. Analysis programs convert the raw television data into 3D coordinates from which the clinical parameters are deduced by correlating the topographic findings with the spinal curvature. In Weisz *et al.* study, 51 patients with AIS were recruited to study the correlation of the curve progression with the Cobb angles (initially between 10° and 55°). The follow-up period was more than two years. The results showed that 84% of the patients who had curve progression was identified correctly.

The Quantec imaging system was created by Quantec Image Processing in the United Kingdom in 1995. The Quantec system is based on raster stereography/photography and comprised of a digital camera, a quartz halogen light and booth. The computer software is able to measure the 3D trunk images, record and quantify scoliosis deformity. Scoliosis deformity includes trunk balance, spinal angles, sagittal angles, rib humps and surface asymmetry. This system measures a Quantec angle instead of a Cobb angle to assess the severity of scoliosis. Sakka and Mehta utilized the Quantec system to identify the correlation of the Quantec scanner measurements with the radiographic Cobb angles in scoliosis (Sakka and Mehta, 1997). Their study included 128 patients aged from 2 to 60 years old (27 males and 101 females) and all had the radiographs and the Quantec scans in the same week. The correlation coefficients for the thoracic and thoraco-lumbar regions were 0.91 and 0.92, respectively, indicating strong correlations between the Cobb angles and the Quantec angles. However, this coefficient was lower at the lumbar region (0.85). The mathematical equation relating the Quantec angle and the Cobb angle also reported a high r^2 of 0.801.

The InSpeck system consists of four optical digitizers, skin markers, and a structured light projector that projects a pattern of black and white narrow stripes onto the patient's trunk. Data consists of five data sets acquired from the four digitizers, four with fringes and the fifth without fringes, from each camera. Phase-shifted Moiré projections, an interferometer measuring method and an optical triangulation technique are used to reconstruct 3D models. Cheriet *et al.* used the InSpeck system to create an external 3D structure of a scoliotic trunk (Cheriet *et al.*, 2007a). They studied a simulation tool that would allow clinicians to monitor the progression of adolescent scoliosis. The tool was developed based on information collected on the trunk. The results demonstrated that the proposed tool could estimate the progression of scoliosis if measurements on the external trunk were given. Most recently, Clin *et al.* proposed a method using the InSpeck system that included the gravitational forces in the finite element model of a scoliotic trunk in the standing position (Clin *et al.*, 2011). They concluded that the developed method could study the effects of gravitational forces and the spinal loading in scoliosis biomechanics. This is important to investigate the pathomechanisms and treatment of the spinal deformity.

Regarding surface topography, Bunnell summarized that the standard deviation between clinical deformity and radiographic measurement was so high that the degree of curvature could not be reliably predicted from surface topography in any given patient by any technique (Bunnell, 2005). Furthermore, it was also stated that surface metrics had very little correlation to Cobb angle measurements, and indices measured on different planes do not correlate to each other (Pazos *et al.*, 2005, Patias *et al.*, 2010, Parent *et al.*, 2010). A review of surface topographic system could be found in the study conducted by Liu *et al.* (Liu *et al.*, 2013).

3.2 Prediction of progression in patients who have AIS

Treatment of AIS is mainly dependent on the current severity and the progression of the scoliotic curve. A curve progresses if it shows an increment of 6° or more between the initial clinical visit and the consecutive follow-up clinic. Soucacos *et al.* reported that only a small percentage of those scoliotic curves progressed (14.7%) after prospectively following 1,436 patients with untreated idiopathic scoliosis for approximately three years (Soucacos *et al.*, 1998). Therefore, to provide the most effective treatment in the timeliest manner, a good

prediction to estimate which spinal curve may progress is of importance (Lonstein and Carlson, 1984).

Many researchers have attempted to determine which parametric values can contribute to the evolution of scoliosis. Some of the prognostic factors are measured from radiographic images: **Cobb angle** (Lonstein and Carlson, 1984, Duval-Beaupere and Lamireau, 1985, Weinstein and Ponseti, 1983, Duval-Beaupere, 1992, Duval-Beaupere, 1996, Wu *et al.*, 2005, Tan *et al.*, 2009, Wu *et al.*, 2010, Wu *et al.*, 2011, Lam *et al.*, 2012), **apex location** (Peterson and Nachemson, 1995, Wu *et al.*, 2011), **apex lateral deviation** (Yamauchi *et al.*, 1988, Wu *et al.*, 2005, Wu *et al.*, 2010, Wu *et al.*, 2011), **axial vertebral rotation** (Weinstein and Ponseti, 1983, Yamauchi *et al.*, 1988), **curve pattern** (Weinstein and Ponseti, 1983, Duval-Beaupere and Lamireau, 1985, Soucacos *et al.*, 1998, Lonstein and Carlson, 1984), and **rib hump** (Duval-Beaupere, 1992, Duval-Beaupere, 1996). Others are growth factors: **gender** (Soucacos *et al.*, 1998, Wu *et al.*, 2011), **age** (Lonstein and Carlson, 1984, Peterson and Nachemson, 1995, Lam *et al.*, 2012), **Risser sign** (Lonstein and Carlson, 1984, Yamauchi *et al.*, 1988, Peterson and Nachemson, 1995), **states of maturation** (Lam *et al.*, 2012), **imbalance** (Peterson and Nachemson, 1995), **peak height velocity** (Escalada *et al.*, 2009, Chazono *et al.*, 2015).

In details, Tan *et al.* found that the initial Cobb angle was the strongest predictive factor in predicting long-term scoliosis progression (Tan *et al.*, 2009). The Cobb angle threshold where a curve is likely to progress varies among studies. It was found that curves with a Cobb angle of equal or greater than 25° are likely to develop further to 30° or greater at skeletal maturity (68.4% probability), whereas this probability is 8.1% in case of less than 25° (Tan *et al.*, 2009). In a previous study, Weinstein and Ponseti reported that scoliosis with the curvature (Cobb angle) of less than 30° had no tendency to progress after skeletal maturity regardless of curve patterns (Weinstein and Ponseti, 1983). Meanwhile, Lonstein and Carlson (Lonstein and Carlson, 1984) reported a threefold increase in the percentage of patients with progressive curves when the initial curve was greater than 20°. The average initial Cobb angle was 15° for non-progressive curves while it was 19.7° for progressive curves. Duval-Beaupere found that 95% of the patients who had the supine Cobb angle larger than 17° had progressive curves (Duval-Beaupere, 1996).

The apex location is another prognostic factor. An apical level was found to independently contribute to the progression of scoliosis (Peterson and Nachemson, 1995). Apex locations in the progressive group were reported approximately 1.2 vertebra levels higher than those in the non-progressive group (Wu *et al.*, 2011). Regarding the lateral deviation of the apical vertebra level, Yamauchi *et al.* performed a multiple regression analysis and found that the lateral deviation seemed to have great significance (Yamauchi *et al.*, 1988). Maximal apex lateral deviations were strongly correlated with maximal Cobb angles ($r = 0.77 - 0.85$) in the progressive group, but moderately correlated ($r = 0.33 - 0.78$) in the non-progressive group. (Wu *et al.*, 2011).

In terms of curve pattern, the incidence of progression was different for the different curve patterns. Soucacos *et al.* reported a significant change in the proportion of progression according to the pattern of the curve, with double curves showing a higher incidence of progression (21%), followed by thoracic (16.9%), lumbar (14.3%), and then thoraco-lumbar curves (10.1%) (Soucacos *et al.*, 1998). In addition, the direction of the curve was also a decisive prognostic factor for scoliosis progression. Meanwhile, Lonstein and Carlson determined that double curves was 10% more progressive than single curves (27% versus 17.6%) (Lonstein and Carlson, 1984). This study also showed that among the progressive double curves (thoracic and lumbar), 25% of the curves progressed in the thoracic region, 43% in the lumbar region, and 32% in both regions. Among the progressive double curves (thoracic and thoraco-lumbar), 31% progressed in the thoracic region, 40% in the thoraco-lumbar region, and 29% in both regions. In another trend, Duval-Beaupere and Lamireau investigated the progression rate of scoliosis (Duval-Beaupere and Lamireau, 1985). According to their study, the rate of progression was greater for thoracic and double curves than for the other curves ($5^\circ/\text{year}$ versus $3.5^\circ/\text{year}$). Their results also explained why these two types of curves were often detected earlier than the others (age of detection: 10 years 9 months versus 12 years 2 months).

Rib hump is also used to predict the risk of scoliosis progression. Duval *et al.* measured the rib hump in the sitting position and used it to predict when scoliosis progressed (Duval-Beaupere, 1992). They found that all scoliosis with the rib hump of more than 11 mm would progress. However, they were not sure if scoliosis with a lower rib hump would not progress.

Regarding the gender, Soucacos *et al.* found that there were fewer boys than girls with progressive scoliosis (2.6% versus 12%, respectively), including a remarkable difference in the percentage of progression between boys and girls for double and thoracolumbar curves (double curves: 8.3% versus 23.6% and thoracolumbar curves: 4.9% versus 12.9%, respectively) (Soucacos *et al.*, 1998).

The incidence of progression decreased as the chronological age increased (Lonstein and Carlson, 1984). Peterson and Nachemson developed a prognostic model including the Risser sign, the apical level, the imbalance, and the chronological age to classify a curve as either progressive or non-progressive (Peterson and Nachemson, 1995). This study reported that 81% of the patients who had thoracic or thoracolumbar curves were predicted correctly as either progressive or non-progressive. The chronological age was also put into another logistic regression model from which the *p*-value for the regression coefficient of variable age could derive and was smaller than 0.001 (Lam *et al.*, 2012). This indicated that age contributed significantly to determine whether a curve was progressive or not. In the same study, the menarche status also had the *p*-value smaller than 0.001. Puberty is another important predictive factor in determining whether scoliosis develops or not. Tan *et al.* reported a probability of 82.23% to progress to a curve of 30° or more in a girl less than 12 years old and before her puberty with an initial Cobb angle of equal or greater than 25° (Tan *et al.*, 2009). However, this probability of progression to 25° or more is 2.39% in a post-pubertal boy who is 12 years old or older and has a spinal curvature of less than 25°. Similar to the chronological age, the incidence of curve progression decreased with the increasing initial Risser sign. Thirty-six per cent of the patients with a Risser sign of 0 or 1 developed progression, whereas this figure in the patients whose Risser sign was 2, 3, or 4 was 11% (Lonstein and Carlson, 1984).

The final prognostic factor is the peak height velocity. The peak height velocity and the peak angle velocity occurred simultaneously one year prior to menarche in progressive curves that were managed with a brace in AIS (Escalada *et al.*, 2009). Changes in height growth velocity influenced changes in angle velocity. As of six months after menarche, the height velocity was inversely related to the curve progression in the group of AIS girls with progressive curves managed with a brace. As the height velocity starts decreasing at one year

prior to menarche, this study indicates that at the end of puberty, a risk of progression still exists in this group of girls despite bracing.

The prediction outcomes of most of the aforementioned studies were only qualitative; they only showed the risk of progression. It is not clear how much a curve will progress. For this reason, Yamauchi *et al.* developed an equation to predict quantitatively scoliosis progression with five variables: the initial Cobb angle, the apical AVR, the apical lateral deviation, the maturation index of the iliac apophysis, and the Risser sign with correction. In this study, a curve was considered to progress if its Cobb angle increased 5° or more during more than 2 years. Unfortunately, their prediction outcome was poor and the error was $\pm 10^\circ$ (Yamauchi *et al.*, 1988).

These aforementioned studies only used data acquired from the initial clinical visit and the final follow-up to predict if a curve would progress or not. However, it requires time for a curve to progress or stabilize. The progression or stabilization of different curves may vary. For this reason, Wu *et al.* developed quantitative predictive models for the progression of AIS at 6 or/and 12 month intervals using serial 3D spinal curves and apex lateral deviations (Wu *et al.*, 2005, Wu *et al.*, 2010). The 3D reconstruction of the spine and rib cage was performed by the bi-planar radiography with the direct linear transformation. The 3D spinal curve was represented by a line passing through the centers of pedicles and best fit with the third order Fourier series smoothing function. In (Wu *et al.*, 2005), the combination of fuzzy c-means clustering and artificial neural network was used to establish the predictive model. The accuracy for the test data sets were within $4.40^\circ (\pm 1.86^\circ)$ of Cobb angles and $3.98 (\pm 3.41)$ mm of lateral deviations. In the other study (Wu *et al.*, 2010), the artificial progression surface technique was developed to predict scoliosis future progression. This artificial technique was constructed by three previous 6-month interval consecutive spinal curves (acquired from 11 AIS patients) and the non-uniform rational B-spline surfacing technique. The generalized cross-validation extrapolation technique was applied to align the curves on the artificial progression surface to obtain the future progression. The prediction accuracy at the next 6-month interval were $4.1 \pm 3.3^\circ$ for Cobb angles and 3.6 ± 3.5 mm for apex lateral deviations. Wu *et al.* developed their predictive models using radiographic metrics and the prediction could only start after three or four clinical visits.

Nault *et al.* investigated if 3D morphological parameters of the spine could differentiate which curve would progress after the initial visit. The findings showed that this predictive model could increase the precision of the prediction of the final deformity (Nault *et al.*, 2013, Nault *et al.*, 2014). In their retrospective study (Nault *et al.*, 2013), there were 6 categories of measurements: angle of the PMC, Cobb angles (kyphosis, lordosis), 3D wedging, rotation, torsion, and slenderness. This study reported that 3D morphologic parameters could be used in the prediction of AIS progression as early as the initial visit. Their prospective case-control study confirmed that there were significant differences in 3D morphology in terms of the plane of maximal curvature, torsion and apical intervertebral rotation between non-progressive and progressive AIS even at the initial presentation (Nault *et al.*, 2014). In those two studies, measurements were made on the 3D spine reconstructed using multi-planar radiography that is an expensive and complicated technique.

3.3 Summary

In summary, imaging modalities have been used in the scoliosis domain to diagnose and assess the severity of scoliosis. This chapter summarizes that the X-ray based imaging modalities expose patients to ionizing radiation which increases the risk of cancer. Meanwhile, CT and MRI are costly and require patients in the supine position, which may underestimate the severity of scoliosis. Surface topography is a non-ionizing imaging modality, but surface metrics have very little correlation to Cobb angle measurements. Ultrasonography has shown its ability and feasibility to image scoliosis in the standing position. This imaging modality is cost effective and free of ionizing radiation; therefore, it is safe to patients.

Some works have been done using measurements obtained from the X-ray based imaging modalities to develop a model to predict the progression of scoliosis. The 2D predictive models have been used for few decades but the accuracy is still low. The 3D models due to their adaptiveness to the 3D nature of scoliosis improve the accuracy of the prediction. Unfortunately, all of the models deploy radiographic metrics, which expose patients to radiation. Therefore, it is essential to develop an accurate 3D model from parameters acquired from a non-ionizing radiation imaging modality to predict numerically the progression of scoliosis.

Development of 3D freehand ultrasound reconstruction and determination of the optimal configuration¹

Chapter 3 indicated that sonography could be used to image the spine and monitor the progression of scoliosis. In this chapter, the development of an ultrasound method to reconstruct the 3D spine is reported. The optimal configuration including the operating frequency, the penetration depth, the minimum distance, and the reconstruction resolution is determined to provide optimal reconstructed images. Sections 4.1 and 4.2 introduce the ultrasound system, and the developed software, respectively; they are used throughout this PhD study. Section 4.3 presents the image processing techniques for the 3D freehand ultrasound reconstruction of an object. Section 4.4 describes the *in-vitro* study to determine the optimal configuration to obtain the optimal reconstructed images. Section 4.5, reports the *in-vivo* study to confirm the optimal configuration on human subjects.

4.1 The ultrasound system

The equipment used for data acquisition throughout the study was the Ultrasonix SonixTABLET ultrasound system (Analogic Ltd., USA). This system consists of three components: the main ultrasound scanner (SonixTablet), the transducer (or the probe), and the position and orientation tracking system (SonixGPS) (Figure 4.1).

¹ Part of the materials in this chapter was published in: Vo, Q.N. *et al.* Investigation of the optimal freehand three-dimensional ultrasound configuration to image scoliosis: An *in-vitro* study. *In:* Vo, T. V. & Tran, P. H. L., eds. The fifth international conference on the development of biomedical engineering in Vietnam, 2014 Ho Chi Minh City, Vietnam. Springer, 226-229.



Figure 4.1 The medical Ultrasonix SonixTablet ultrasound system.

4.1.1 Ultrasound scanner

The SonixTablet is a compact medical ultrasound scanner with a built-in 19" touch screen. This machine is designed to be portable. It can be mounted on a cart for ease of transportation. The machine is also equipped with an Ultrasound Research Interface (URI) software that enables raw data acquisition and storage in multiple formats. In addition, the URI enables the retrieval and modification of low-level parameters used to generate ultrasound images.

4.1.2 Transducers

Only two transducers that support the position and orientation tracking function (also known as the global positioning system (GPS)) are provided by the manufacturer: the convex transducer (C5-2/60 GPS), and the linear transducer (L14-5/38 GPS). The convex transducer consists of 128 elements that cover an active scanning area of 60 mm x 15 mm and operates at the ultrasound frequency range 2 - 5 MHz. Three frequencies of 2.5 MHz, 3.3 MHz, and 4.0 MHz can be selected from the control panel, and the penetration depth can be programmed

from 5 to 30 cm. The linear transducer also contains 128 elements covering 38 mm x 9 mm area. It operates at 6.6 MHz and 10 MHz and the penetration depth can be adjusted for 2 - 9 cm. A spatial sensor (GPS receiver) is embedded in both transducers so that they can interact with the GPS transmitter to track or locate the position, and orientation of each acquired B-scan (B-mode image) in the 3D space. Both transducers are one-dimensional array probes and coupled with the tracking system to generate 3D images.

Clinically speaking, it is essential that the B-scan display the exact geometry of the cross-section of the object being imaged. A B-scan is formed by combining all A-lines that are generated by elements in the transducers. As shown in Figure 4.2, a B-scan acquired by simply aligning vertically A-lines and placing them at regular intervals cannot satisfy the geometrical conservation of the cross section. For example, two pixels A and B (the red dots) of the yellow cross section of an object are obtained from A-line 3 (the third A-line from the left) in the transducer grid, but may be misinterpreted as pixels A' and B' (the blue dots) in the display grid. The reason is the formation of this image does not account for the geometry of the transducer. This leads to a distortion of the displayed image. Therefore, scan conversion is necessary to map the acquired data to the actual geometry of the cross-section (Figure 4.2).

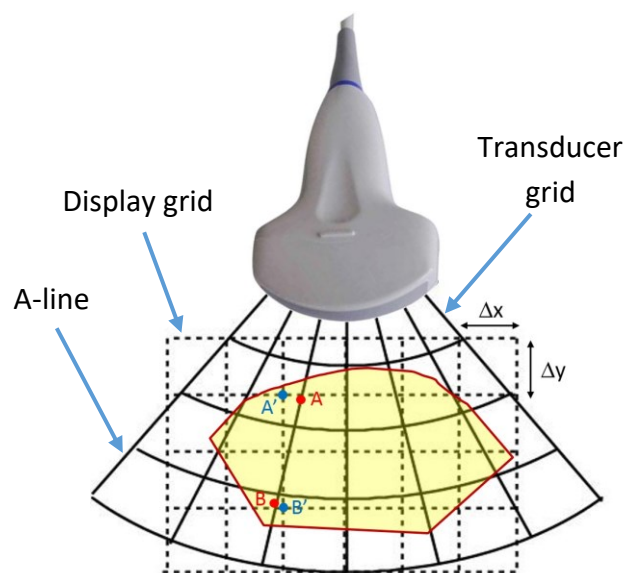


Figure 4.2 Scan conversion from the transducer grid to the display grid.

The B-scan in the transducer grid is called the pre-scan converted B-scan. The scan conversion is an interpolation process in which the pre-scan converted B-scan is interpolated into the display grid, which represents the display pixels on the LCD screen of the system. The resolution of the converted B-scan, which depends on the penetration depth and transducer type, is shown in Table 4.1 and Table 4.2. The Δx and Δy are pixel dimensions. The converted B-scans can be exported from the Ultrasonix system and use throughout this thesis. Each converted B-scan is an 8-bit greyscale digital image with the size of 640 x 480 pixels. Its brightness intensity values range from 0 to 255 with 0 being the darkest intensity and 255 being the brightest intensity.

Table 4.1 *The penetration depth versus the converted B-scan resolution on a convex transducer.*

Penetration depth (cm)	Δx & Δy (mm)	Penetration depth (cm)	Δx & Δy (mm)
5	0.127	15	0.345
6	0.148	16	0.366
7	0.171	17	0.389
8	0.193	18	0.411
9	0.214	20	0.454
10	0.236	22	0.499
11	0.257	24	0.542
12	0.280	26	0.585
13	0.301	28	0.629
14	0.323	30	0.673

Table 4.2 *The penetration depth versus the converted B-scan resolution on a linear transducer.*

Penetration depth (cm)	Δx & Δy (mm)	Penetration depth (cm)	Δx & Δy (mm)
3	0.062	6.5	0.135
3.5	0.072	7	0.145
4	0.083	7.5	0.156
4.5	0.093	8	0.166
5	0.104	8.5	0.177
5.5	0.114	9	0.187
6	0.125		

4.1.3 Position and orientation tracking system

The position and orientation tracking system includes three components: the tracking receiver, the tracking transmitter, and the driving circuit. The interaction between the tracking receiver (GPS receiver) attached to the ultrasound probe and the tracking transmitter (GPS transmitter) via the driving circuit provides the position, and orientation of each B-mode image (B-scan) relative to the transmitter (referred to the global coordinate system).

The transmitter used in this thesis was the mid-range transmitter that offers a flexible set-up; therefore, it can be integrated into scoliosis imaging applications where the tracking volume needs to cover a large anatomical region. As the electromagnetic field is easily distorted or affected by surrounding metals, it is recommended that no metal present within 30 cm around the transmitter. Furthermore, the electromagnetic signal strength is always checked prior to scanning an object to ensure that it is strong within the scanning area.

4.2 Computer hardware and software

Apart from the ultrasound system, a high-end desktop computer was used to process the data obtained from the ultrasound system. The Matlab R2015a v8.5 (Mathworks, U.S.A.) and its toolboxes (image processing toolbox v. 9.2, MATLAB coder v 2.8, MATLAB Compiler v. 6.0, and Parallel Computing Toolbox v. 6.6) were used to develop the “Three-dimensional Scoliosis Analysis (3DSA)” software. The 3DSA software was then used to perform the 3D reconstruction, the determination of the PMC, the measurement of the AVR, the Cobb angle and lateral deviation of each curve on both the PA plane and the PMC.

4.3 Three-dimensional ultrasound reconstruction method

The 3D freehand ultrasound scanning technique was used in this study to acquire data from scanned objects. One drawback of this scanning technique is the result of irregular stack of 2D B-mode images. That means most of the acquired B-scans are not parallel to each other, and the distance between any adjacent B-scans varies. This irregular stack cannot be used by the regular rendering technique; thus, a rearrangement is required so that its 2D images are uniformly spaced. The following paragraphs presents how the original irregular stack is reconstructed. Figure 4.3 illustrates the four major steps, which are used to reconstruct 3D sonographs.

4.3.1 Step a: Three-dimensional freehand ultrasound data acquisition

Figure 4.3a demonstrates how the object was scanned using the 3D freehand ultrasound scanning technique. After the scan was completed, two datasets were simultaneously acquired. Intensity data I in the *.b8* format which consisted of a stack of 2D B-scans obtained when the probe was moved along the surface of an object. Meanwhile, position and orientation data G in the *.gps* format was a pile of data sets corresponding to every B-scan. Both the I and G datasets are 3D matrices. They were first saved inside the ultrasound machine during the acquisition, then exported and loaded into the high-end desktop computer for further image processing.

4.3.2 Step b: Image processing

In order to improve the reconstruction speed and the clarity of the reconstruction image, image processing techniques that include reduction of the overlapping data, removal of speckle noise, increase of image contrast, and segmentation of vertebral features were applied to raw datasets I and G .

Reduction of overlapping data

During the scanning process, duplicated data might be obtained because the transducer could not move smoothly along the object surface. When this situation occurred, it would increase the data size with duplicated data. Hence, some overlapped B-scans in dataset I and their corresponding information in dataset G should be deleted. The number of eliminated B-scans depended on the pre-selected spacing (minimum distance) between two adjacent B-scans by the operator. The optimal spacing value was determined after the study that was described in section 4.4. If the distance between the k^{th} and $(k+2)^{th}$ B-scans in dataset I was smaller than the selected spacing, the $(k+1)^{th}$ B-scan was discarded (k is the order of the B-scan in the dataset).

Removal of speckle noise

Speckle noise is one of the characteristics of sonographs. A median filter is the most effective and widely used technique (Conversano *et al.*, 2015) to remove speckle noises on 2D ultrasound images. The process was implemented by running through the image pixel by pixel

and replacing each pixel with the median of neighboring pixels. In this study, a 9 x 9 neighboring (filtering) windows was chosen as a compromise between the image quality rated by its signal-to-noise ratio and the processing time. Generally, the larger the window is, the better the signal-to-noise ratio is, but the longer the filtering process takes.

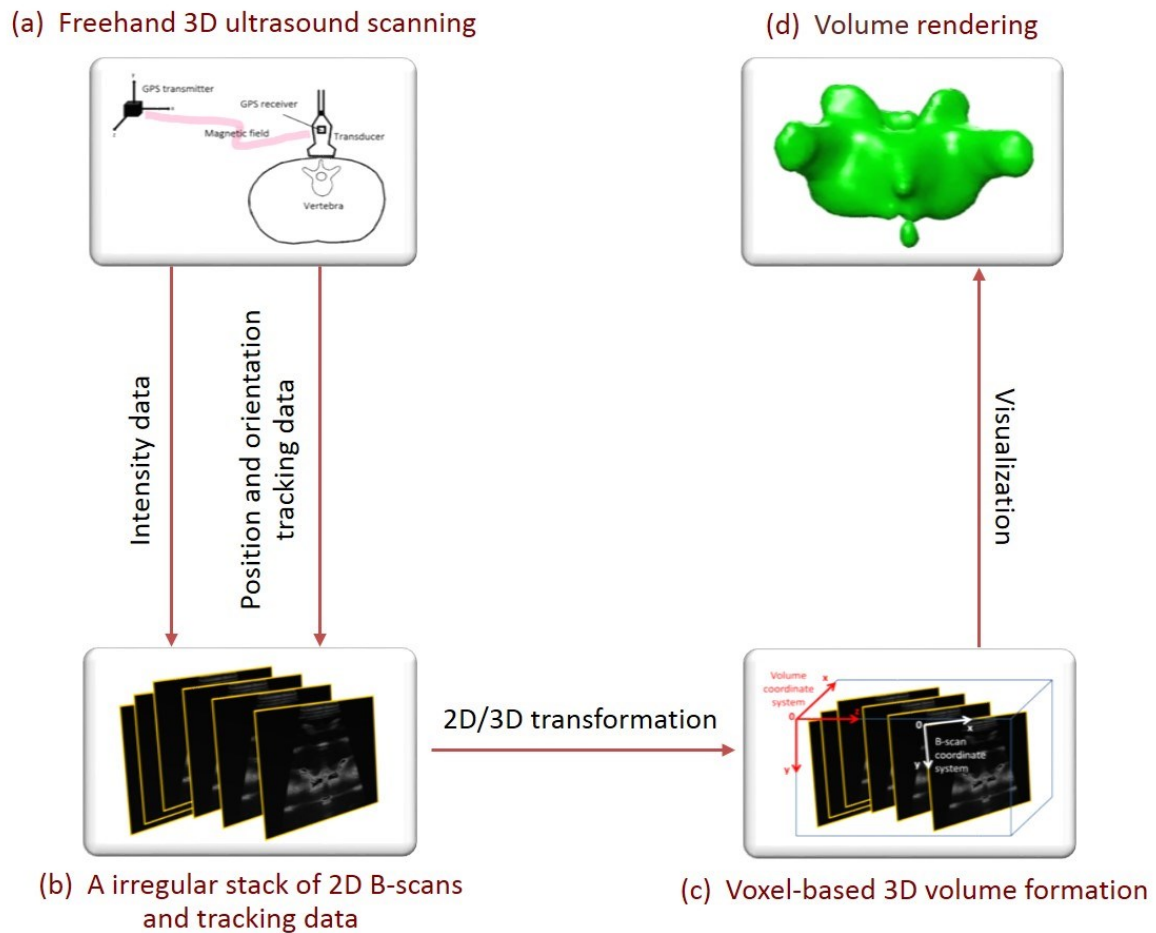


Figure 4.3 A flow chart of the voxel-based reconstruction method.

Contrast stretching

The contrast of an ultrasound image depends on reflection of ultrasound energy at the interface between two media. The stronger reflection signals from a point on the interface are the brighter that point is displayed on the B-scan. The reflect intensity is given by the reflection coefficient, R , which depends on the acoustic contrast of the two media:

$$R = \frac{I_r}{I} = \left[\frac{Z_2 - Z_1}{Z_2 + Z_1} \right]^2 \quad (4.1)$$

where Z_1 and Z_2 are the acoustic impedances of media 1 and 2, respectively, I_r is the reflection intensity at the interface, and I is the original intensity coming out from the transducer.

Acoustic impedances for tissues in the human body are provided in Table 4.3 (Bushberg *et al.*, 2012).

Table 4.3 Acoustic impedance, Z , for selected tissues.

Tissue	Z (Rayls)
Fat	1.34×10^6
Water	1.48×10^6
Kidney	1.63×10^6
Blood	1.65×10^6
Liver	1.65×10^6
Muscle	1.71×10^6
Skull bone	7.8×10^6

From Table 4.3, the acoustic impedance of bone is significantly higher than that of surrounding tissues (muscle, fat, water, etc.), leading to a substantially higher reflection coefficient R at a bone interface when ultrasound penetrates from soft tissue to bone. However, a penetration of ultrasound from bone to soft tissues results in a significantly lower reflection coefficient at the bone interface. As a result, when imaged using the pulse-echo ultrasound technique starting skin, bone features normally have considerably higher image intensity values than their surrounding tissues on the same ultrasound image (B-scan). Contrast stretching was applied to compress the values of darker pixels (lower-level values) in an image while enhancing the brighter pixels (higher-level values). Vertebral bone features, of which brightness intensity values are higher on B-scans, were of interest throughout this thesis. Therefore, the contrast stretching function was aimed to enhance vertebral features, separated them from surrounding tissues for ease of segmentation in the next step.

The contrast stretching output, I_{out} , was calculated as follows:

$$I_{out}(m, n) = \frac{I(m, n) - minValue}{maxValue - minValue} * 255 \quad (4.2)$$

where $minValue$ and $maxValue$ are the non-zero minimum and the maximum intensity values of input image I (B-scan), respectively, m and n are the position of the pixel at row m and column n .

Fuzzy segmentation

In this step, vertebral features should be segmented from their surrounding tissues so that only bone structures could be reconstructed. There are many techniques, which can perform image segmentation. However, the fuzzy segmentation technique is a good choice for this application because it is able to solve the geometrical fuzziness problems when the boundary between two adjacent image segments is unclear.

The fuzzy segmentation technique is based on the IF-THEN rule as follows.

- IF a pixel is dark THEN make it darker.
- IF a pixel is gray THEN keep it gray.
- IF a pixel is bright THEN make it brighter.

This process underwent three steps: image fuzzification, membership modification with the support of expert knowledge and the fuzzy set theory, and image defuzzification as illustrated in Figure 4.4.

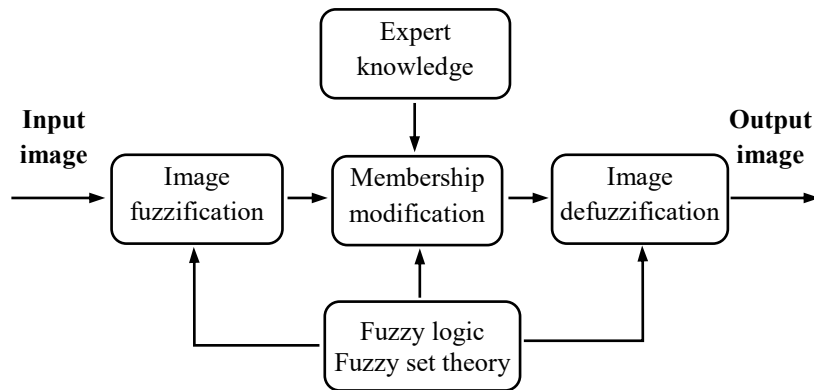


Figure 4.4 *A fuzzy inference system.*

Expert knowledge was based on the physics of the ultrasound imaging as described above and summarized as follows:

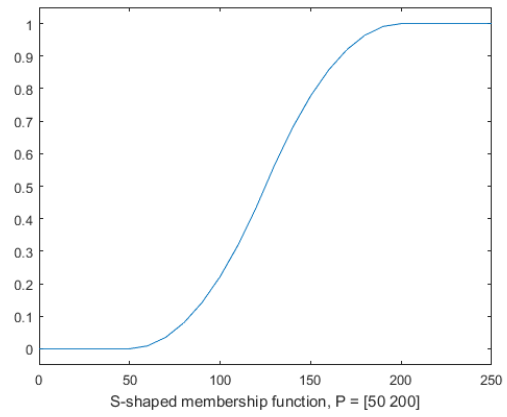
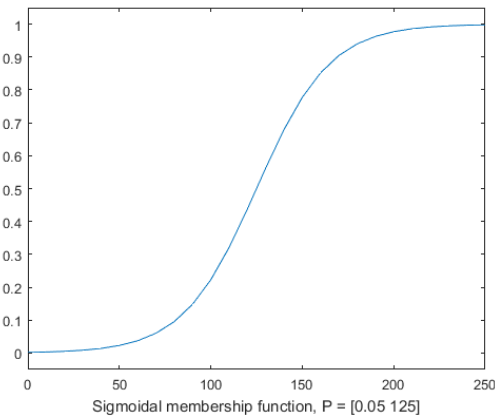
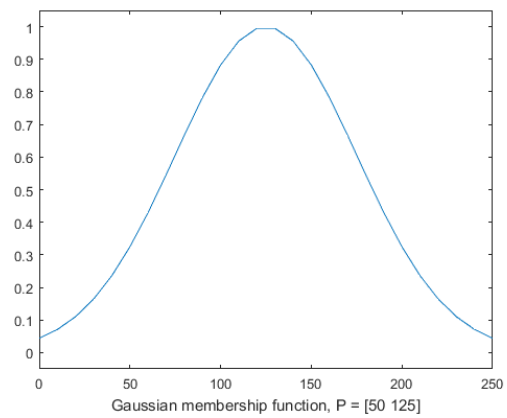
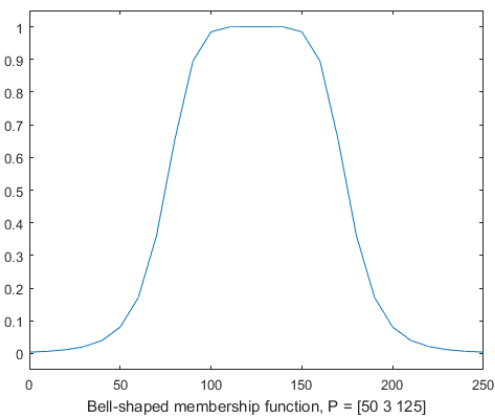
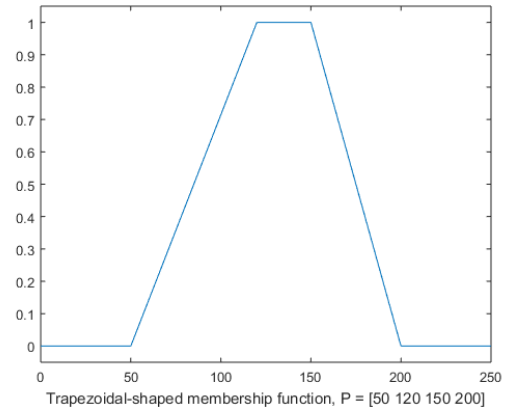
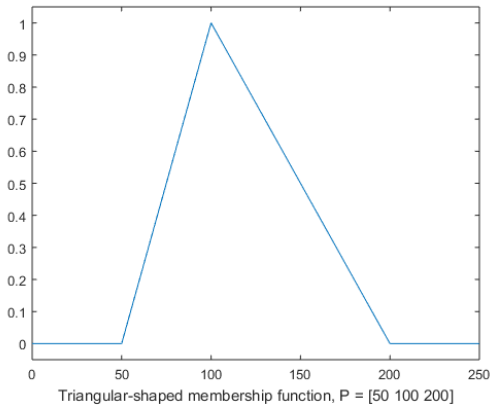
- Vertebral features reflect stronger ultrasound signals than surrounding soft tissues when ultrasound energy penetrates from soft tissue to bone. This phenomenon occurs because bone has higher acoustic impedance. As a result, the vertebral features displayed brighter (higher brightness intensity value) than the surrounding materials in B-scans.
- Vertebral features hardly reflect ultrasound energy at the bone interface when ultrasound energy penetrates from bone to soft tissues; therefore, regions behind the vertebral features appear as black pixels having value 0 in the B-scan.

The first step in the segmentation was the image fuzzification, in which a membership function defined how each point in the input space was mapped to a membership value (or a degree of membership) between 0 and 1. Figure 4.5 illustrates common membership functions such as triangular-shaped, trapezoidal-shaped, bell-shaped, gaussian, sigmoidal, and S-shaped functions. As shown in Figure 4.5, the first four membership functions can be used to enhance gray pixels (for example, brightness intensity range 50 - 200) while suppressing darker and brighter pixels. Meanwhile, the last two membership functions can boost brighter pixels and compress darker pixels. Furthermore, the S-shaped membership function is easier to calculate than the sigmoidal membership function; therefore, it is the most suitable to the aforementioned IF-THEN rule.

The S-shape membership function is given by:

$$\mu_{mn} = \begin{cases} 0, & I_{mn} \leq a \\ 2 \left(\frac{I_{mn} - a}{b - a} \right)^2, & a \leq I_{mn} \leq \frac{a + b}{2} \\ 1 - 2 \left(\frac{I_{mn} - b}{b - a} \right)^2, & \frac{a + b}{2} \leq I_{mn} \leq b \\ 1, & b \leq I_{mn} \end{cases} \quad (4.3)$$

where parameters a and b locate the extremes of the sloped portion of the curve, and μ_{mn} is the membership value of pixel I_{mn} . In this thesis, the S-shaped membership function is used and the non-zero minimum and maximum values of each ultrasound image are chosen as a and b , respectively.



*x-axis (horizontal): brightness intensity values [0 255]
y-axis (vertical): membership values [0 1]*

Figure 4.5 Examples of the common triangular-shaped, trapezoidal-shaped, bell-shaped, gaussian, sigmoidal, and S-shaped membership functions.

The membership modification is the heart of the fuzzy segmentation because it helps to further suppress darker intensity values and enhance brighter intensity values. The membership values are modified using a contrast intensifier. There are two commonly used contrast intensifiers, namely the square operation and the cube operation; however, the latter is used because it provides better contrast than the former. The cubic contrast intensifier operation is written as:

$$\mu'_{mn} = \begin{cases} 4 * \mu_{mn}^3, & \mu_{mn} \leq 0.5 \\ 1 - 4 * (1 - \mu_{mn})^3, & 0.5 \leq \mu_{mn} \leq 1.0 \end{cases} \quad (4.4)$$

where μ'_{mn} is the new value of μ_{mn} .

Image defuzzification is the inverse of the fuzzification process. Its algorithm is to map the fuzzy plane back to gray level intensities within value range [0 255].

4.3.3 Step c: Formation of a regular volume

As previously mentioned, the irregular stack of 2D images (called **SB**) (Figure 4.6a) cannot be used by the regular rendering techniques. Thus, a rearrangement of the images to be uniformly spaced (Figure 4.6b) is necessary. To rearrange, the previously processed vertebral feature data were integrated with corresponding position, and orientation data to form a target volume using the voxel-based method with bi-linear interpolation as proposed by Trobaugh *et al.* (Trobaugh *et al.*, 1994). The voxel-based reconstruction method was applied to a series of acquired 2D images (B-scans) to form a voxel-based 3D image. Initially, target volume grid V of isotropic resolution was created so that it could just cover the **SB** (Figure 4.6c). This approach traversed the voxel across the target volume grid and found the two nearest B-scans on both sides of the voxel. A projection of the voxel on each of these B-scans was determined and its value was calculated by a bi-linear interpolation of its four surrounding pixels in each plane. The final voxel value, $value_{voxelP}$, was then calculated as a weighted sum with interpolated values from the two planes based on the distances from the voxel to the planes (Figure 4.6d).

$$value_{voxelP} = \frac{valueP_1 \cdot \frac{1}{d_1} + valueP_2 \cdot \frac{1}{d_2}}{\frac{1}{d_1} + \frac{1}{d_2}} \quad (4.5)$$

where $valueP_1$ and $valueP_2$ are the interpolated intensity value of the projection of P on the first and second nearest plane, respectively. They are bi-linearly interpolated from their four neighbouring pixel values of projection P_1 and P_2 . d_1 and d_2 are distances from voxel P to the first and second nearest planes, respectively. For those voxels that could not identify the closest B-scans on their both sides, values of NaN (not a number) were assigned.

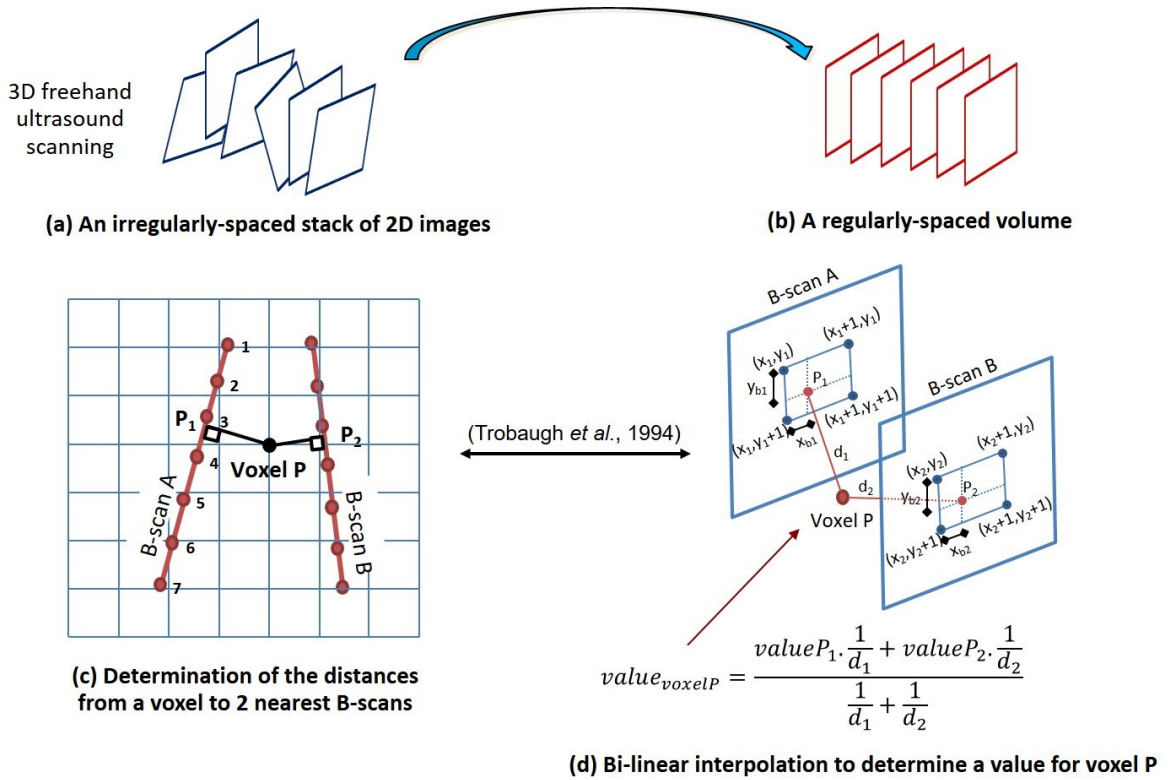


Figure 4.6 The voxel-based technique with bilinear interpolation.

This regular formation step was very time-consuming. To reduce the implementation time, two techniques were applied. The first technique divided target volume V into N equal sections (VS) along its length (z -axis) to take advantage of the multi-core central processing

unit (CPU) in the computer. The number of section N was equal or lesser than that of CPU cores. Each volumetric section VS was assigned to each CPU core so that N sections could be simultaneously executed and then combined into the whole volume. Thus, the processing time was reduced. For example, for an 8-core CPU, the target volume V was divided into 8 volumetric sections VS . The other technique that accelerated the computation process was to limit the search region. Instead of searching the entire B-scans (SB) data to find the two closest B-scans, the search region was limited to a certain number of B-scans. Figure 4.7 shows the process of the limitation of the search region in each of the eight volumetric sections i^{th} VS . The first step of the process was to find the k^{th} B-scan that was approximately at the same level as the j^{th} voxel respective to plane xy . Then, the two nearest B-scans to the j^{th} voxel were expected to be close to the k^{th} B-scan on either sides. If all B-scans were parallel to each other, the two closest B-scans were among the $(k-1)^{th}$, k^{th} , and $(k+1)^{th}$ B-scans. Since B-scans were usually not parallel due to freehand scanning and might cross each other, the two closest B-scans might not be among these three B-scans. For example, one of the closest B-scans to the j^{th} voxel is $(k-2)^{th}$ B-scan, not the $(k-1)^{th}$ B-scan. Therefore, in order to avoid this situation, the search region was expanded from the k^{th} B-scan toward its both sides a number of scans (ns). In order to determine the two closest B-scans of the j^{th} voxel, the distance d from the j^{th} voxel to plane xy was first calculated. Then, the distance d_temp from the centre of the k^{th} B-scan to the xy plane was also calculated. If d_temp was greater than or equal to d , the execution stopped and the search region was formed from $(k-ns)^{th}$ to $(k+ns)^{th}$ B-scans. If not, the execution continued until the condition was reached. In this study, $ns = 25$ was selected by experiment with an assumption that there was no missing data.

The preceding paragraphs presented the method to convert pixel intensity values of B-scans into corresponding voxel intensity values of the reconstructed volume. However, in order to display the reconstructed volume, it was required to determine voxel coordinates with respect to the global coordinate system that depended on pixel coordinates in 3D space. Therefore, there was a requirement for the conversion of all 2D ultrasound image pixels to the global coordinate system (transmitter coordinate system). This coordinate conversion process underwent two steps:

4.4 Determination of the optimal ultrasound configuration to image a cadaveric vertebra: An *in-vitro* study

3D ultrasound imaging technique has been applied to image the scoliotic spine. Researchers used different ultrasound configurations including the type of transducer, the operating frequency, the penetration depth, and the reconstruction resolution (the voxel size) to acquire images (Cheung *et al.*, 2015, Ungi *et al.*, 2014, Nguyen *et al.*, 2015, Young *et al.*, 2015, Zheng *et al.*, 2015, Chen *et al.*, 2013, Purnama *et al.*, 2009, Dewi *et al.*, 2009). Figure 4.8 shows the relationship among the ultrasound frequency, resolution, and penetration depth. The higher the operating frequency, the higher the image resolution, but the lower the penetration depth. Therefore, an *in-vitro* study was conducted to investigate the optimal ultrasound configuration by comparing the results of the reconstructed images based on the visualization of the image quality and the measurement accuracy with a cadaver.

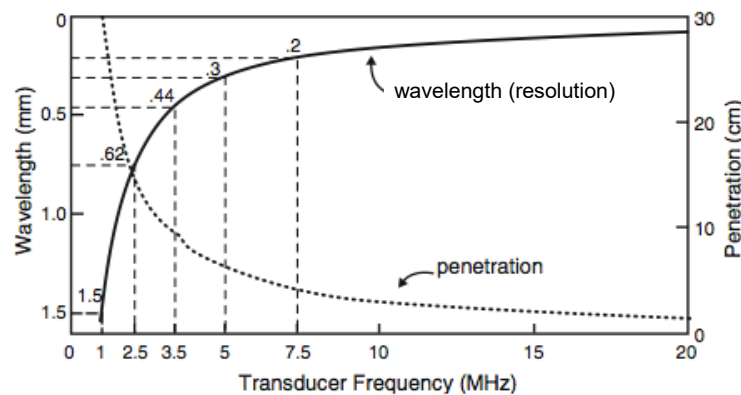


Figure 4.8 The relationship among frequency, resolution and penetration (Otto, 2000).

The following paragraphs present the experimental setup, study method and the results from the *in-vitro* study to determine the optimal ultrasound configuration to image a cadaveric vertebra and reconstruct images in terms of the operating frequency, reconstruction resolution (voxel size), minimum distance between two adjacent B-scans, and penetration depth.

4.4.1 Experimental setup and scanning procedures

For the *in-vitro* study, a cadaveric thoracic T7 vertebra was used. This vertebra was mounted on a plastic bar with a pointer attached to its centre (Figure 4.9a). The plastic bar was then secured on top of a plastic platform that consisted of a protractor to indicate the vertebral rotation. The pivot point was located at the centre of mass of the vertebral body. During experiments, the tested vertebra was submerged into an acrylic water tank with a wall thickness of 4.5 mm. The vertebra was entirely covered by water. This set up was to simulate a body environment as water has a similar acoustic impedance to the soft tissue (1.48×10^6 Rayls to 1.50×10^6 Rayls). The acrylic wall simulated the role of skin and fat. Although the acrylic wall had a higher acoustic impedance (3.26×10^6 Rayls) than skin (1.7×10^6 Rayls) and fat (1.34×10^6 Rayls), the thickness of the wall was similar to skin and fat. Figure 4.9b shows the experimental set up in which the transducer was faced to the posterior arch of the vertebra. The vertebra was set at 0° rotation, which was obtained when the pivot was set at 0° degree position on the protractor and perpendicular to the surface of the water tank. The GPS transmitter was set up within the working range of 5 - 25 cm relative to the GPS receiver (or the ultrasound probe).

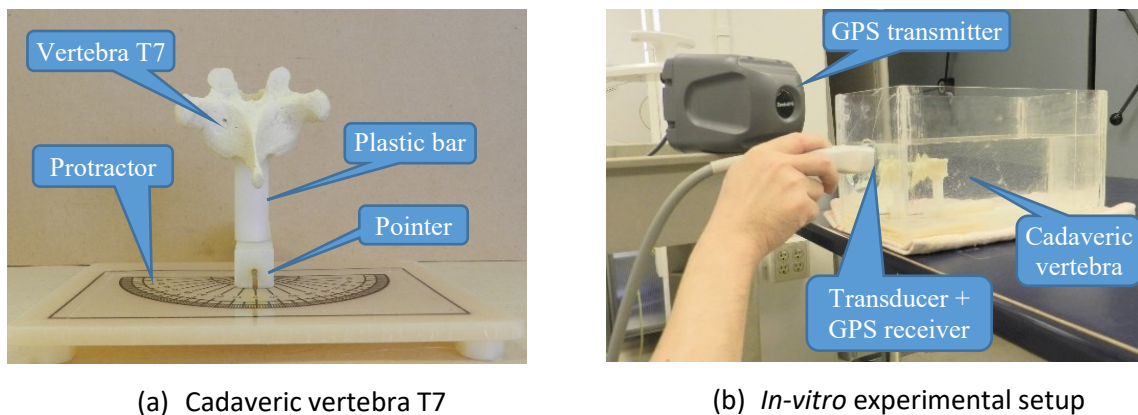


Figure 4.9 Cadaveric vertebra T7 and the *in-vitro* experimental setup.

4.4.2 Methods

Both the convex probe (C5-2/60 GPS) and the linear probe (L14-5/38 GPS) were used in this study. For the convex probe, the following three operating frequencies were tested: 2.5

MHz, 3.3MHz and 4.0 MHz. For the linear probe, the following two frequencies were used: 6.6 MHz and 10.0 MHz. The depth was set at 9 cm and the acquisition frames rate was automatically set by the machine based on the operating frequencies (2.5 MHz, 3.3 MHz, 4.0 MHz, 6.6 MHz, and 10.0 MHz) to 27, 36, 36, 8, and 10 frames per second, respectively. The scanning time was approximate 23 seconds for the convex probe and 46 seconds for the linear one. The five scans at different frequencies were performed, resulting in five datasets for each frequency. After the scanning process, a series of B-scans was acquired, including the intensity data *I* (*.b8*) and GPS data *G* (*.gps*). These two data were then imported into the developed program described in section 4.3, which deployed the voxel-based method to reconstruct the T7 vertebra into a 3D image.

In order to eliminate the overlapping B-scans, the spacing (minimum distance (MD)) between two adjacent B-scans was preliminarily experimented to investigate the limit of spacing. It was found that the spacing that was equal or greater than 0.4 mm eliminated most of B-scans; therefore, the reconstructed image could not be recognized. Hence, three minimum distances (0.1 mm, 0.2 mm, and 0.3 mm) were scrutinized. To investigate the reconstruction resolution, three different voxel sizes (or reconstruction resolution - RR) of 0.2 mm, 0.6 mm, and 1.0 mm were also determined. Each dataset acquired with each operating frequency was reconstructed with each spacing and voxel size. As a result, 45 configurations (3 MD x 3 RR x 5 frequencies) were established, providing 45 reconstructed images.

To evaluate the effects of the ultrasound penetration depth on the image reconstruction accuracy, the entire aforementioned process was repeated with the penetration depth of 6 cm. Another 45 images were also reconstructed.

Evaluation

For each of penetration depth (6 cm or 9 cm), 45 configurations (3 MD x 3 RR x 5 frequencies) were obtained. To determine the reconstruction accuracy, four distance parameters (Figure 4.10) were measured three times on both the images and the cadaver by a rater in one week apart to minimize memory bias. Four distance measurements between a) the left superior articular process and the right superior articular process, b) the left transverse process and the right transverse process, c) the left superior articular process and the spinous process, and d) the right superior articular process and the spinous process were calculated

after the featured landmarks were identified on the developed software (3DSA). The 3DSA software captured the landmark coordinates and provided the measurements. For the cadaver, the rater used a Vanier caliper (Mitutoyo Coporation, Japan) to measure the distances between those landmark points. The averaged measurements that were performed on the image and the cadaver were used to evaluate the accuracy of the 3D reconstruction. The mean absolute difference (MAD) with the standard deviation (SD) and the Pearson correlation coefficient (Pearson's r) were used to evaluate the reconstruction accuracy and linear correlation between two averaged measurements. The reconstructed image for each operating frequency was rated by its accuracy (MAD \pm SD) and intuitive image quality. The smaller the MAD \pm SD was, the better the image. A better intuitive image was judged by the details and the geometrical similarity to the cadaver. Furthermore, a higher r showed a higher linear correlation, indicating a higher agreement between measurements on the cadaver and the image.

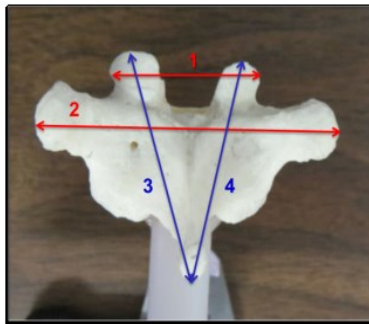


Figure 4.10 The four distance parameters on the cadaveric vertebra T7: 1. Left superior articular process - right superior articular process, 2. Left transverse process - right transverse process, 3. Left superior articular process - spinous process, 4. Right superior articular process - spinous process.

4.4.3 Results

Table 4.4 reports the MAD \pm SD and Pearson's r of the 45 configurations for the penetration depths of 9 cm. For the 9-cm penetration depth, the smallest MADs \pm SDs were 0.9 ± 0.6 mm, 0.6 ± 0.3 mm, and 0.9 ± 0.3 mm for three frequencies 2.5 MHz, 4.0 MHz, and 10.0 MHz, respectively, when the MD was 0.3 mm and the RR was 1.0 mm. Meanwhile, $0.8 \pm$

0.4 mm and 2.0 ± 1.2 mm were the smallest MAD \pm SD obtained at the MD of 0.2 mm and the RR of 1.0 mm for frequencies 3.3 MHz and 6.6 MHz, respectively.

Similarly, Table 4.5 summarizes the MAD \pm SD and Pearson's r of the 45 configurations for the penetration depths of 6 cm. For the 6-cm penetration depth, the results were different with the 0.3 mm/1.0 mm configuration yielding the smallest MAD \pm SD of 0.9 ± 0.6 mm and 0.7 ± 0.8 mm for frequencies 2.5 MHz and 3.3 MHz, respectively. For the 4.0 MHz frequency, the MAD \pm SD at the 0.3 mm/0.6 mm (MD/RR) configuration was smallest and equal to 1.1 ± 0.5 mm. The smallest MAD \pm SDs for frequencies 6.6 MHz and 10.0 MHz occurred at the smaller minimum distances, specifically at the 0.2 mm/1.0 mm and 0.1 mm/0.6 mm configurations, respectively.

In most of the reported configurations, MADs \pm SDs yielded by the linear probe were greater than that by the convex probe. In addition, as can be seen from Table 4.4 and Table 4.5, all Pearson's correlation coefficients are greater than 0.90, ranging from 0.909 (0.3/0.2/10.0 MHz/6 cm) to 0.999 (0.1/1.0/2.5 MHz/6 cm). That means there were high correlations between measurements performed on the cadaver and the images, indicating high reliabilities of measurements.

Based on the above results, the best intuitive quality and the image with the smallest MAD \pm SD for each frequency at the 9 cm and 6 cm penetration depths are illustrated on Figure 4.11 and Figure 4.12, respectively. It was recognized that the convex probe (frequencies 2.5 MHz to 4.0 MHz) provided the images with more details and more similar in shape to the cadaver than those from the linear probe. However, the images from the linear probe showed better spinous process than that from the other. In most of the reported cases, there was a difference between the two selected images (one with the best intuitive image quality and the other with the smallest MAD for the same operating frequency at the same penetration depth). For the 4.0-MHz frequency at the 6-cm penetration depth, the two selected images were the same. Nevertheless, the differences in averaged measurements (MAD \pm SD) between the two images are small, ranging from 0.0 ± 0.0 mm to 1.1 ± 0.7 mm as reported in Figure 4.11 and Figure 4.12.

Table 4.4 The MAD and *r* values for the 45 configurations with the penetration depth of 9 cm.

Frequency (MHz)	MD/RR	0.1/0.2	0.1/0.6	0.1/1.0	0.2/0.2	0.2/0.6	0.2/1.0	0.3/0.2	0.3/0.6	0.3/1.0
2.5	MAD (mm)	1.9 ± 0.8	1.5 ± 0.8	1.0 ± 0.4	1.8 ± 0.9	1.5 ± 1.1	0.9 ± 0.6	1.8 ± 0.7	1.4 ± 0.8	0.9 ± 0.6
	r-value	0.989	0.992	0.998	0.990	0.994	0.997	0.990	0.995	0.998
3.3	MAD (mm)	1.4 ± 0.8	0.9 ± 0.8	0.9 ± 0.7	1.4 ± 1.1	1.0 ± 0.8	0.8 ± 0.4	1.5 ± 1.1	1.0 ± 0.9	0.9 ± 0.5
	r-value	0.997	0.998	0.998	0.997	0.998	0.998	0.996	0.998	0.998
4.0	MAD (mm)	1.7 ± 1.0	1.1 ± 0.4	0.5 ± 0.3	1.6 ± 0.9	1.3 ± 0.6	0.6 ± 0.4	1.7 ± 0.7	1.2 ± 0.5	0.6 ± 0.3
	r-value	0.991	0.994	0.997	0.992	0.991	0.997	0.991	0.994	0.998
6.6	MAD (mm)	2.6 ± 1.4	2.4 ± 1.5	2.2 ± 1.2	2.6 ± 1.5	2.6 ± 1.6	2.0 ± 1.2	2.7 ± 1.6	2.7 ± 1.6	2.1 ± 1.1
	r-value	0.961	0.962	0.964	0.963	0.962	0.967	0.958	0.956	0.967
10.0	MAD (mm)	2.4 ± 1.6	1.8 ± 1.2	1.5 ± 0.9	2.2 ± 1.6	1.7 ± 1.1	1.7 ± 1.0	2.0 ± 1.0	1.7 ± 0.9	0.9 ± 0.3
	r-value	0.972	0.983	0.986	0.976	0.981	0.983	0.981	0.979	0.996

Table 4.5 The MAD and r values for the 45 configurations with the penetration depth of 6 cm.

Frequency (MHz)	MD/RR	0.1/0.2	0.1/0.6	0.1/1.0	0.2/0.2	0.2/0.6	0.2/1.0	0.3/0.2	0.3/0.6	0.3/1.0
2.5	MAD (mm)	1.4 ± 1.4	1.9 ± 1.2	2.2 ± 1.1	1.4 ± 1.3	1.3 ± 1.3	1.6 ± 1.2	1.7 ± 0.7	1.2 ± 0.8	0.9 ± 0.6
	r-value	0.989	0.998	0.999	0.990	0.990	0.998	0.991	0.998	0.998
3.3	MAD (mm)	1.9 ± 0.6	1.9 ± 0.8	1.5 ± 0.6	1.8 ± 0.6	1.4 ± 0.5	1.3 ± 0.6	1.6 ± 0.3	1.1 ± 0.3	0.7 ± 0.8
	r-value	0.980	0.984	0.986	0.984	0.986	0.988	0.989	0.994	0.998
4.0	MAD (mm)	1.1 ± 1.1	1.7 ± 0.7	1.2 ± 0.7	1.3 ± 1.0	1.2 ± 1.0	1.1 ± 0.7	1.3 ± 0.8	1.1 ± 0.5	1.1 ± 0.8
	r-value	0.991	0.985	0.993	0.988	0.994	0.992	0.992	0.995	0.997
6.6	MAD (mm)	2.4 ± 2.1	2.3 ± 2.1	2.0 ± 3.0	2.4 ± 2.1	2.3 ± 2.7	1.9 ± 3.0	2.3 ± 2.3	2.2 ± 2.3	2.5 ± 3.2
	r-value	0.932	0.935	0.948	0.931	0.925	0.944	0.931	0.936	0.945
10.0	MAD (mm)	2.4 ± 2.4	2.2 ± 3.1	3.2 ± 3.6	2.7 ± 2.1	2.4 ± 2.8	3.1 ± 3.5	2.7 ± 2.4	2.4 ± 2.9	3.1 ± 3.4
	r-value	0.924	0.926	0.927	0.920	0.918	0.932	0.909	0.918	0.939

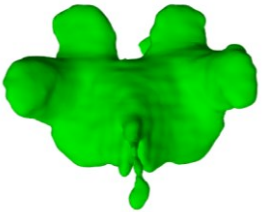
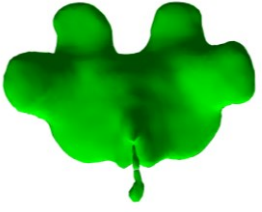
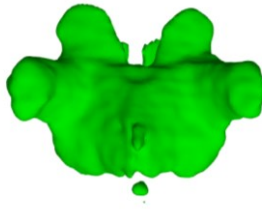
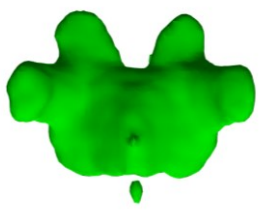
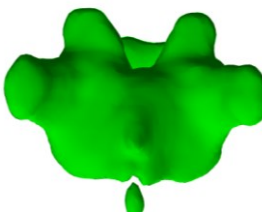
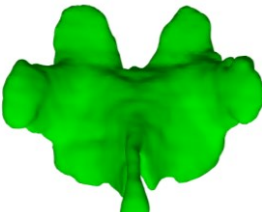
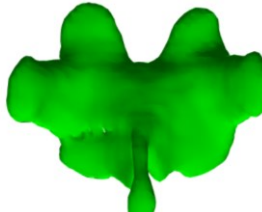
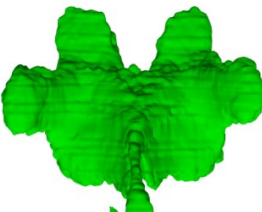
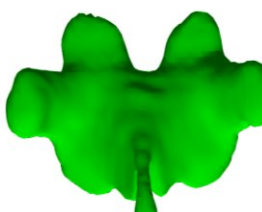
Frequency	Image with the best intuitive quality	Image with the smallest MAD	MAD \pm SD (mm)
2.5 MHz	 MD/RR = 0.2/0.6	 MD/RR = 0.3/1.0	0.7 ± 0.4
3.3 MHz	 MD/RR = 0.2/0.6	 MD/RR = 0.3/1.0	0.5 ± 0.3
4.0 MHz	 MD/RR = 0.2/0.6	 MD/RR = 0.3/1.0	0.8 ± 0.6
6.6 MHz	 MD/RR = 0.2/0.6	 MD/RR = 0.2/1.0	1.0 ± 0.4
10.0 MHz	 MD/RR = 0.2/0.6	 MD/RR = 0.3/1.0	0.9 ± 0.9

Figure 4.11 The best reconstructed images and the corresponding configurations for the penetration depth of 9 cm.

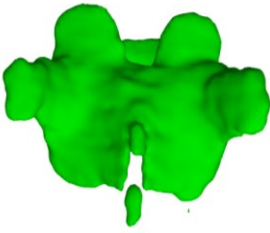
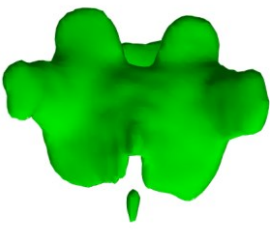
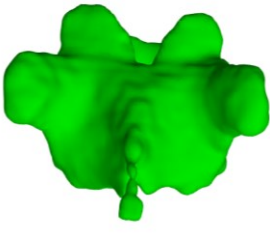
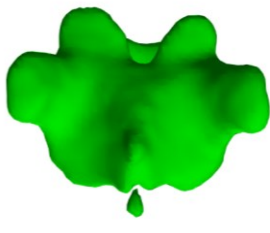
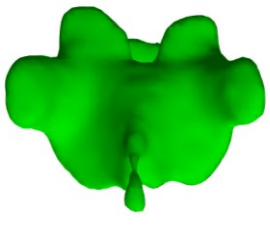
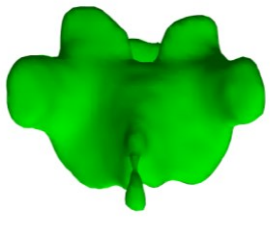
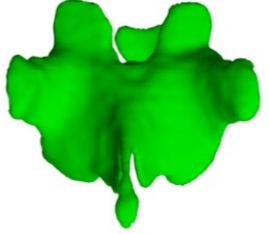
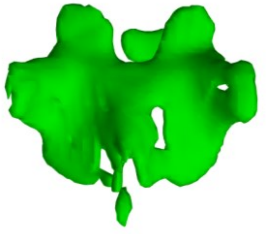
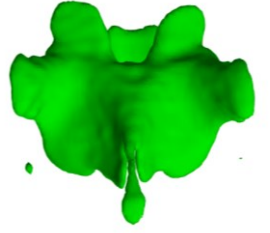
Frequency	Image with the best intuitive quality	Image with the smallest MAD	MAD \pm SD (mm)
2.5 MHz	 MD/RR = 0.2/0.6	 MD/RR = 0.3/1.0	1.0 ± 0.8
3.3 MHz	 MD/RR = 0.2/0.6	 MD/RR = 0.3/1.0	0.9 ± 0.9
4.0 MHz	 MD/RR = 0.3/1.0	 MD/RR = 0.3/1.0	0.0 ± 0.0
6.6 MHz	 MD/RR = 0.1/0.6	 MD/RR = 0.2/1.0	1.1 ± 0.7
10.0 MHz	 MD/RR = 0.2/0.6	 MD/RR = 0.1/0.6	0.5 ± 0.3

Figure 4.12 The best reconstructed images and the corresponding configurations for the penetration depth of 6 cm.

Table 4.6 reports the maximum absolute and relative errors of measurements, which were performed on 45 reconstructed images for the ultrasound penetration depths of 6 cm and 9 cm. It was shown that the errors from the linear probe (6.6 MHz and 10.0 MHz) were higher than that from the convex probe. In particular, the errors from the linear probe were doubled in compared to those from the convex probe for the 6-cm penetration depth. However, the ratios of the errors from the linear probe to those from the convex probe were less than 2 for the 9-cm penetration depth.

Table 4.6 *The maximum absolute and relative errors.*

Frequency	Convex probe						Linear probe			
	2.5 MHz		3.3 MHz		4.0 MHz		6.6 MHz		10.0 MHz	
Depth	6 cm	9 cm	6 cm	9 cm	6 cm	9 cm	6 cm	9 cm	6 cm	9 cm
Max. absolute error (mm)	3.6	2.7	2.7	2.6	2.9	2.8	7.3	4.5	8.6	3.9
Max. relative error (%)	7.1%	6.1%	6.1%	5.9%	5.7%	6.3%	14.5%	10.2%	17.0%	8.8%

4.4.4 Discussion

The convex probe provided better image quality than the linear one in terms of the intuitive image quality and the mean absolute difference for two reasons. Firstly, the acquisition frame rate of the convex probe was greater than that of the latter at the same penetration depth. This resulted in the higher number of B-scans that were available for the 3D reconstruction process. Even though the scanning time of the linear probe doubled that of the convex one to compensate for its lower frame rates, the number of frames acquired with the linear probe was still smaller. At the 9-cm penetration depth, the number of acquired frames at the 2.5MHz, 3.3MHz and 4 MHz were 621, 828, and 828, respectively; at the 6.6MHz and 10.0MHz, the number of acquired frames were 368 and 460 frames, respectively. Furthermore, the reconstruction algorithm applied interpolation to form a regularly spaced volume. According to equation 4.5, a voxel value was proportional to the intensity values of the two projected pixels on the two nearest B-scans of the voxel, but inversely proportional to the distances between the voxel and the two B-scans. If the two B-scans were located far from the voxel due to the low number of acquired B-scans, the interpolated value was then small and would be ignored, leaving a ‘blank’ at the voxel’s position.

Regarding the ultrasound penetration depth, there was an insignificant difference between one configuration at one depth and the same configuration at the other depth. The reason is the resolutions of a converted B-scan provide by the convex and linear probes at the 6-cm penetration depth are 0.148 mm and 0.125 mm, respectively. Meanwhile, these resolutions are 0.214 mm and 0.187 mm at the 9-cm penetration depth (Table 4.1 and Table 4.2). These resolutions are close or even much smaller than the reconstruction resolutions (0.2 mm, 0.6 mm, 1.0 mm). Thus, a change in the penetration depth from 6 cm to 9 cm did not affect the resolution of the reconstructed image.

In most of reported cases, the selected images with the best intuitive quality were obtained at the reconstruction resolution of 0.6 mm while the selected images with the smallest mean absolute difference were obtained at the reconstruction resolution of 1.0 mm. Meanwhile, the difference between the two selected images ranges from 0.0 ± 0.0 mm to 1.1 ± 0.7 mm (Figure 4.11 and Figure 4.12). These errors were close to one voxel size (reconstruction resolution), thus being considered measurement errors rather than reconstruction errors. Therefore, the configuration that provided the image with the best intuitive quality was considered the optimal configuration for the frequency. For example, at the 9-cm penetration depth, the 0.2 mm/0.6 mm configuration is optimal for frequency 2.5 MHz.

4.4.5 Conclusion

This *in-vitro* study concluded that the convex probe generated better images than the linear probe. In addition, the penetration depth, the reconstruction resolution, and the operating frequencies generated by the same probe did not affect substantially the reconstruction of images. The configuration with the frequency of 2.5 MHz, the spacing of 0.2 mm, and the reconstruction resolution of 0.6 mm was chosen as the *in-vitro* optimal configuration.

4.5 Determination of the optimal ultrasound configuration to image scoliotic spines: An *in-vivo* study

The *in-vitro* study reported that the convex probe provided better images with smaller MADs and higher Pearson's correlation r values between measurements performed on the images and on the cadaver than the linear probe. However, in an *in-vivo* situation, the media that surround the vertebrae are inhomogeneous materials, which include soft tissues, fat, and

muscle. Therefore, the image quality may be different. The purpose of this *in-vivo* study was to confirm that the *in-vitro* optimal ultrasound configuration could be applied.

4.5.1. Subject recruitment and scanning procedure

To confirm the optimal ultrasound configuration could be applied on subjects, one healthy volunteer and two patients with AIS were recruited. The healthy volunteer was an adult male while the patients were a 16-year-old girl and a 13-year-old boy. Both patients were recruited from the local scoliosis clinics with inclusion criteria of: i) diagnosed with AIS, ii) had no previous treatment, iii) had out-of-brace radiographs taken on the same day; and iv) had Cobb angle less than 45°. The ethics was approved by the University of Alberta ethics board, and both patients signed the consents before participating in the study.

Figure 4.13 illustrates how the subject was scanned using the ultrasound system. Each subject was scanned in the standing position similar to the posture that the corresponding standing radiograph was taken. The scanning process started from thoracic vertebra C7 and ended at lumbar vertebra L5. The subject wore a gown with an opening at the back and stood with both hand touching to a wall. The operator used her finger to identify the C7 spinous process and put a red sticker at that level. Each scan took less than one minute. The penetration depth of the ultrasound beam was set at 6 cm. However, the penetration depth could be adjusted based on the operator's experience to estimate the thickness of the subject's muscle. The aim of the adjustment was to optimize the image quality.



Figure 4.13 The subject scanning procedure.

4.5.2 Methods

Unlike the *in-vitro* study, the 3D *in-vivo* images were usually not available on subjects due to extra imaging modality requirement (computed tomography or magnetic resonance imaging). Therefore, references were not available for comparisons between measurements on the reconstructed images. Thus, the reconstructed images could only be initially assessed by their intuitive image quality in this pilot study.

The healthy subject was scanned with five operating frequencies: 2.5 MHz, 3.3 MHz, 4.0 MHz, 6.6 MHz, and 10.0 MHz. However, the two patients were scanned with 2.5 MHz and 4.0 MHz only to reduce extra scanning time, which might slow down the clinic. At each of the operating frequency, images were reconstructed with three different minimum distances (MDs) (0.1 mm, 0.2 mm, and 0.3 mm) and three different reconstruction resolutions (RRs) (0.2 mm, 0.4 mm, and 0.6 mm). As a result, 45 images (3 MDs x 3 RRs x 5 frequencies) for the healthy volunteer and 18 images (3 MDs x 3 RRs x 2 frequencies) for each of the two patients were obtained. These images were then evaluated individually by a panel of six raters who were blinded with the ultrasound configurations and patients' information. Each rater selected five best images on each subject group to select visually the five best ones, ranking from the first to the fifth. The selection criteria were dependent on the clarity of the image as well as the details of the vertebra. The details included the appearance of the lamina, the transverse processes, and the ribs on each reconstructed image. All images were displayed on the monitors with the resolution of 1920 x 1080 pixels. Each selected image was scored with 1.0, 0.8, 0.6, 0.4, or 0.2 depending on its ranking from the first to the fifth positions, respectively. The total scores of each selected image was the sum of the raters' scores in which the highest score image was selected as the best image. The configurations that produced the best image corresponded as the optimal configurations.

4.5.3 Results

Forty-five images obtained from the volunteer were randomly rearranged and labelled from 1 to 45. Six raters judged these coded images according to the clarity and the details of the vertebra. Table 4.7 summarizes the best five coded images from the volunteer selected by the six raters. Their scores are reported in Table 4.8. The two coded images with the highest

scores of 3.2 and 2.6 are 29 and 41, respectively, followed by images 5, 21, and 31, having the same score of 1.8.

Table 4.7 *Rankings of the best five coded images from the volunteer selected by six raters.*

Rater	Ranking				
	1 st	2 nd	3 rd	4 th	5 th
1	5	29	41	9	31
2	20	26	24	5	9
3	41	31	29	21	7
4	7	14	21	5	29
5	29	21	30	39	14
6	41	31	29	8	10

Table 4.8 *Scores of the selected coded images from the volunteer selected by six raters.*

Image	5	7	8	9	10	14	20	21	24	26	29	30	31	39	41
Score	1.8	1.2	0.4	0.6	0.2	1.0	1.0	1.8	0.6	0.8	3.2	0.6	1.8	0.4	2.6

Similarly, eighteen images obtained from each patient were also randomly rearranged and coded from 1 to 18. One rater of the panel could not participate in this study; hence, five remaining raters judged these coded images according to the same selection criteria. Table 4.9 illustrates the best five coded images from the two patients selected by the five raters. The total score for each image is reported in Table 4.10. For patient 1 (P1), images 17, 8, 9, 19, and 7 had the highest scores of 3.4, 3.0, 2.2, 2.2, and 1.8, respectively, and were ranked from the first to the fifth. For patient 2 (P2), the five raters selected images 17, 16, 8, 14, and 9 as the best ones with the highest scores of 3.0, 2.4, 2.4, 1.8, and 1.4, respectively.

Table 4.9 *Rankings of the best five coded images selected for the two patients by five raters.*

Rater	Ranking									
	1 st		2 nd		3 rd		4 th		5 th	
	P1	P2								
1	7	7	9	9	14	14	8	8	17	17
2	9	14	7	13	17	18	8	10	15	7
3	17	17	8	8	16	16	9	9	14	14
4	8	17	17	16	16	8	5	5	12	13
5	16	16	17	17	9	8	8	3	1	9

Table 4.10 Scores of the selected coded images from the two patients selected by five raters.

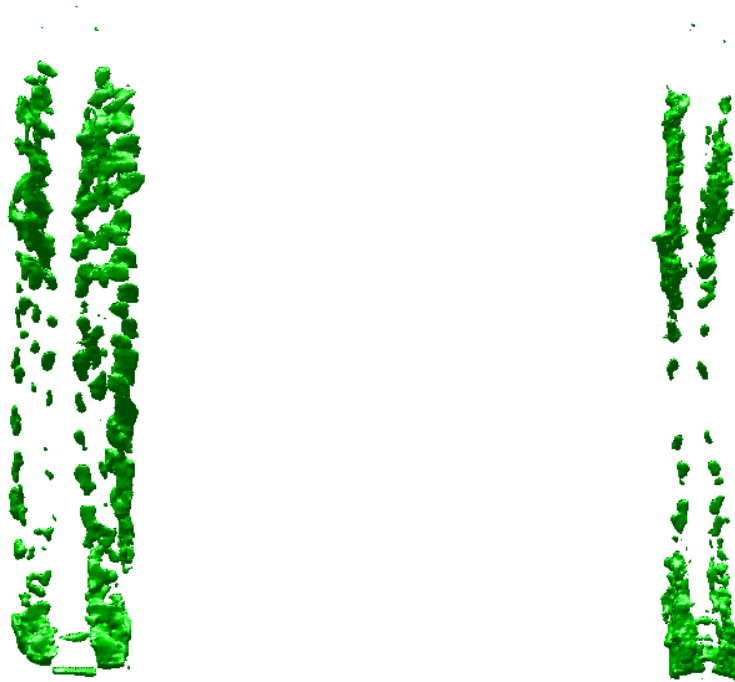
<i>Patient 1</i>										
Image	1	5	7	8	9	12	14	15	16	17
Score	0.2	0.4	1.8	3.0	2.2	0.2	0.8	0.2	2.2	3.4
<i>Patient 2</i>										
Image	3	5	7	8	9	13	14	16	17	18
Score	0.4	0.4	0.2	2.4	1.4	1.0	1.8	2.4	3.0	0.6

Table 4.11 lists the configurations from which the five best images for each subject were selected. The configuration is presented in the form of spacing (minimum distance) - voxel size - frequency. The spacing ranges from 0.1 mm to 0.3 mm while the voxel size changes between 0.6 mm and 1.0 mm. The three first ranked images for the three subjects report the spacing of 0.1mm and the voxel size of 1.0 mm with a compromise between 2.5 MHz and 4.0 MHz. Furthermore, five listed images for the healthy volunteer were reconstructed from datasets acquired with 2.5 MHz and 3.3 MHz with a domination of the former. That means the convex probe provided better images than the linear one on the volunteer, who was scanned with all five frequencies. However, the results from the two patients reports that 4.0 MHz was slightly better than 2.5 MHz.

Table 4.11 The ranking of the 3D reconstructed images from the first to the fifth quality for the volunteer and the two patients.

	1 st	2 nd	3 rd	4 th	5 th
Volunteer	0.1-1.0-2.5	0.3-1.0-2.5	0.2-1.0-2.5	0.3-0.6-2.5	0.1-0.6-3.3
Patient 1	0.1-1.0-4.0	0.3-1.0-4.0	0.1-1.0-2.5	0.2-1.0-4.0	0.3-1.0-2.5
Patient 2	0.1-1.0-4.0	0.2-1.0-4.0	0.3-1.0-4.0	0.2-1.0-2.5	0.1-1.0-2.5

Figure 4.14 demonstrates an example of two reconstructed images provided by the convex probe and the linear probe. The two images were reconstructed with the same minimum distance of 0.2 mm and the same reconstruction resolution of 1.0 mm from two datasets acquired from the same subject but different frequencies of 2.5 MHz and 6.6 MHz. The convex probe yielded the image with more details than the linear probe did. The convex-probe image can show laminae and portions of ribs while the linear-probe image can only show laminae.



(a) Convex-probe image (2.5 MHz)

(b) Linear-probe image (6.6 MHz)

Figure 4.14 Three-dimensional reconstructed image provided by: (a) The convex probe (2.5 MHz), and (b) The linear probe (6.6 MHz).

4.5.4 Discussion

The convex probe was confirmed to provide better images than the linear probe. The convex-probe images showed laminae, transverse processes, and ribs while the linear-probe images could only display laminae. This can be explained by the following reasons. Firstly, the geometry of the convex probe provides wider scanning field than the linear one, which acquires more data. A larger field of view captures more vertebral data and the ribs information assists the determination of the vertebral level. Secondly, the convex probe operates in lower frequency than the linear probe. Ultrasound attenuation is approximately proportional to frequency as denoted in the following equation:

$$\text{Attenuation} = \mu * l * f \quad (4.6)$$

where μ is the ultrasound attenuation coefficient [dB/cm/MHz], l is the distance through the imaging medium [cm], and f is the ultrasound frequency [MHz].

Unlike the *in-vitro* study, the soft tissue in the *in-vivo* study attenuated 2,500 times more than the water; the soft tissue attenuation coefficient is 0.5 dB/cm/MHz (Bushberg *et al.*, 2012) while the water attenuation coefficient is 0.0002 dB/cm/MHz. Consequently, for the same propagation media (soft tissue) and travel distance (from the back skin to the vertebra), a higher ultrasound frequency signal loses more energy than the lower ultrasound frequency. In other words, higher frequency (6.6 MHz and 10.0 MHz) ultrasound loses more features of interest or generates lower brightness intensities on B-scans, leading to missing the details on the 3D reconstructed images. One more feature that should be taken into account is that the convex probe was found to adapt more easily to the scoliotic back than that of the linear probe. A good contact with the convex probe would lead to good datasets and minimize attenuation. Furthermore, higher frequency provides higher resolution sonographs; that is, there are more tiny particles present in the images. Figure 4.15 illustrates two examples of B-scan, one of which was acquired with frequency 2.5 MHz, and the other was acquired with frequency 6.6 MHz at the same penetration depth of 6 cm. In the 2.5 MHz B-scan, vertebral features such as laminae, transverse process, and ribs distinguish from other features were easily segmented and reconstructed with less chance of data missing. In contrast, the 6.6 MHz B-scan shows many features that have similar brightness to vertebral features, leading to a difficulty in the vertebral segmentation. Consequently, missing information of interest was inevitable.

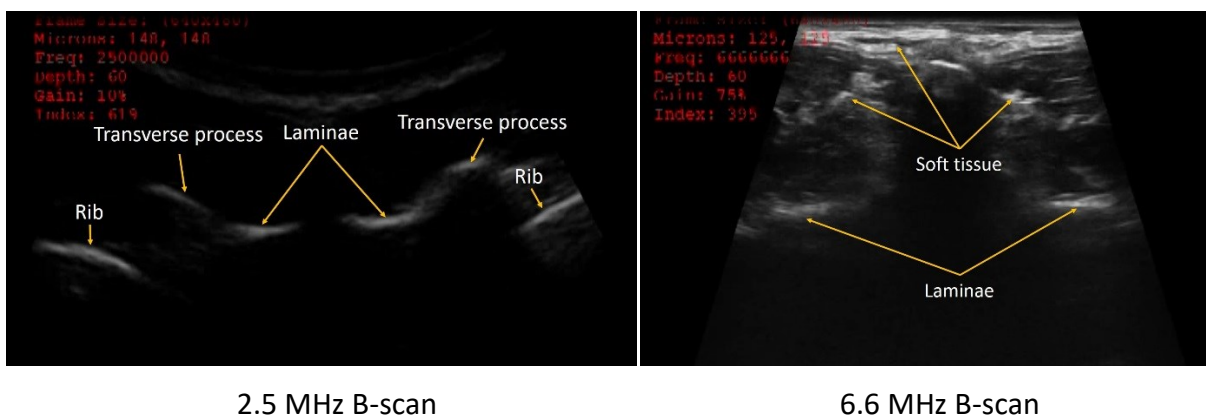


Figure 4.15 Examples of two B-scans acquired with frequencies 2.5 MHz and 6.6 MHz at the same depth of 6 cm.

The last reason was the acquisition frame rate of the convex probe was greater than that of the linear probe at the same penetration depth, which was explained in details in section 4.4.4. Table 4.12 reports the scan time and the number of B-scans acquired with five frequencies from the volunteer. The number of B-scans acquired with 6.6 MHz and 10.0 MHz were substantially less than the other three frequencies, even though the scan time for 10.0 MHz was the longest. The distances between a voxel to its closest B-scans are longer in case of less B-scans, leading to a smaller value assigned to that voxel. This value might be too small to be displayed in the 3D reconstructed image.

Table 4.12 The scan time and the number of B-scans acquired with five frequencies from the volunteer.

Frequency	2.5 MHz	3.3 MHz	4.0 MHz	6.6 MHz	10.0 MHz
Scan time	43 s	40 s	39 s	34 s	54 s
No. of B-scans	1407	1599	1581	478	884

The healthy volunteer was scanned with five frequencies and 2.5 MHz was present in four top best configurations followed by 3.3 MHz. For the two patients, 2.5 MHz contributed to generate 4 out of the 10 best images. By combining these two results, 2.5 MHz was selected and used in *in-vivo* studies as the optimal frequency. In addition, although the images were ranked from the first to the fifth for each subject, the raters found insignificant differences among those five images. Thus, the minimum distance of 0.2 mm and the reconstruction resolution of 0.6 mm were chosen as the optimal default reconstruction parameters. However, these values could be changed between 0.1 mm and 0.3 mm and between 0.2 mm and 1.0 mm, respectively.

4.6 Summary

This chapter has demonstrated that 3D freehand ultrasonography was feasible to image the cadaveric vertebra as well as the human scoliotic spine. The *in-vitro* experiment demonstrated that the dimensional error between the reconstructed image and the cadaver was quite small, encouraging further studies. Furthermore, the effect of the reconstruction configuration on the quality of the reconstructed images was investigated and identified. From both *in-vitro* and *in-vivo* studies, it was decided that the convex probe 2.5 MHz operating frequency, 0.2 mm

spacing, and 0.6 mm reconstruction resolution constituted the optimal configuration and will be used throughout the rest of the thesis.

***In-vitro* validation of the optimal configuration in imaging AIS²**

In this chapter, the optimal configuration is used to reconstructed 3D images from which scoliosis-related parameters are measured and validated. Section 5.1 presents the statistics analysis definition and theory that are used in this thesis. Section 5.2 reports an extension of the *in-vitro* study to determine the accuracy and correlation of the 3D reconstruction images compared to the CT images. Section 5.3 describes the method to measure the AVR of the three cadaveric vertebrae. Section 5.4 investigates the study to determine the PMC on which the maximum Cobb angle is measured using two spine phantoms. Then, AIS patients are recruited to investigate the repeatability and reliability of the proposed ultrasound method. The method to measure the Cobb angle and the lateral deviation on the PA plane and the PMC, and the AVR are proposed in section 5.5. The intra- and inter-rater reliabilities are reported in section 5.6.

5.1 Statistical analysis

Statistical analysis is a method to analyze, evaluate and explore the collecting data to discover underlying patterns and trends and to answer some scientific decisions that the proposed method is applicable to a specific application. The reliability or the repeatability measurements are usually evaluated by the intraclass correlation coefficient (ICC) and the standard error of measurement (SEM) with 95% confidence interval. Meanwhile, the Pearson correlation coefficient is widely used as a measure of the degree of linear dependence between

² Part of this chapter was published in: VO, Q. N. *et al.* 2014. Measurement of axial vertebral rotation using three-dimensional ultrasound images. *Scoliosis*, 10, 1-4, VO, Q. N. *et al.* 2015. 3D ultrasound imaging method to assess the true spinal deformity. *Conf Proc IEEE Eng Med Biol Soc*, 2015, 1540-3.

two variables. The accuracy analysis is more relied on the mean absolute difference (MAD) and the standard deviation (SD). The following paragraphs briefly describe these statistical concepts.

The Pearson correlation coefficient or the Pearson's r is a measure of the strength of the linear relationship between two variables X and Y . This coefficient can range from -1 to 1. An r of 1 indicates perfectly positive correlation while 0 indicates no relationship, and -1 is perfectly negative correlation. The Pearson's r can be calculated as

$$r = \frac{N \sum(XY) - (\sum X)(\sum Y)}{\sqrt{[N \sum X^2 - (\sum X)^2][N \sum Y^2 - (\sum Y)^2]}} \quad (5.1)$$

where N is the number of pairs (x,y) . $x \in X$ and $y \in Y$.

The ICC is a descriptive statistic that is a relative measure of the reliability of measurements. It describes how strongly member in the same group resemble each other. In this context, reliability or relative consistency is formally defined as follows (Baumgartner, 1969):

$$Reliability = \frac{\textit{variability between subjects}}{\textit{variability between subjects} + \textit{error}} \quad (5.2)$$

Therefore, the reliability (ICC) can theoretically vary between 0 and 1.0, where an ICC of 0 indicates no agreement, whereas an ICC of 1.0 indicates perfect agreement. According to Currier (Currier, 1984), the ICC of 0.90 - 0.99 reflects a high reliability, whereas 0.80 - 0.89 indicates a good reliability, and 0.70 - 0.79 a fair reliability. An ICC that is equal or lesser than 0.69 denotes a poor reliability. The intra-class correlation coefficient refers to a comparison between two groups of measurements performed by one rater. Meanwhile, the inter-class correlation coefficient requires two or preferably more raters involving in the study, and refers comparisons between measurements performed by different raters. In this thesis, ICCs with a two-way random model and an absolute agreement (ICC(2,1)) are used.

All measurements are inaccurate as they contain some amount of error. An obtained measurement consists of both true measurement and measurement error. True measurements and error measurements are always unknown quantities. However, these quantities can be estimated through the SEM. While the ICC is a relative measure of reliability, the SEM provides an absolute index of reliability. The ICC has no unit, whereas the SEM has the same units as the measurement of interest. The interpretation of the SEM centers on the assessment of reliability within individual subjects. The SEM is estimated by most references as follows (Weir, 2005):

$$SEM = SD\sqrt{1 - ICC} \quad (5.3)$$

where SD is the standard deviation of the measurements from all subjects.

As can be seen from Equation (5.3), the standard error of measurement is inversely proportional to the reliability. The higher the reliability is, the smaller the standard error of measurement, and vice versa.

Another concept in statistical analyses is confidence bands that are often used in measurement reports. A confidence band represents the uncertainty about the value of a new data-point relative to the trend. A 95% confidence interval (95% CI) is used throughout this thesis. The last concept is the mean absolute difference (MAD) that is defined as the average of the absolute difference of two sets of measurements. It is reported with the standard deviation (SD).

For visualization, the Bland-Altman plot (Bland and Altman, 1999), or the difference plot, is used to compare two quantitative measurements, based on the quantification of agreement between them to construct limits of agreement. These limits are calculated by using the mean and the standard deviation of the differences between two measurements. That is, these limits are equal to the mean difference plus and minus two times the standard deviation of the differences. In this Bland-Altman plot, the differences between the two measurements are plotted against the averages of the two measurement. Three horizontal lines are drawn: one at the mean difference, and two at the limits of agreement. The graphical method can also be used to compare a new measurement method with a gold standard. In this PhD thesis, the Bland-Altman plot is drawn using the Matlab software.

5.2 Accuracy of the 3D reconstruction of individual cadaveric vertebrae

In the preceding chapter, the optimal configuration was determined based on the intuitive image quality of the thoracic T7 vertebra. This *in-vitro* study extends the previous study to validate further if the optimal configuration could be applied to the T7, L1, and L3 vertebrae, which represent three different dimensions and shapes of vertebrae. The goals are to determine the accuracy of the 3D reconstruction of the various single cadaveric vertebrae.

5.2.1 Methods

Thoracic vertebra T7 was scanned and measured in section 4.4. Its measurements were then used in this section. Two other cadaveric vertebrae L1 and L3 were scanned as described in Section 4.2.3 at 0° vertebral rotations. Three acquired ultrasound datasets were then reconstructed into three reconstructed images using the 3DSA software with the optimal configuration (frequency = 2.5 MHz, spacing (MD) = 0.2 mm, reconstruction resolution (RR) = 0.6 mm). The measurement methods performed on the images and the cadavers were described in section 4.4.2. The same procedure was applied to the lumbar vertebrae L1 and L3, but with five distance parameters. Figure 5.1 illustrates how to measure these five parameters including left superior process - right superior process (1), left transverse process - right transverse process (2), left inferior process - right inferior process (3), left superior process - left inferior process (4), and right superior process - right inferior process (5).

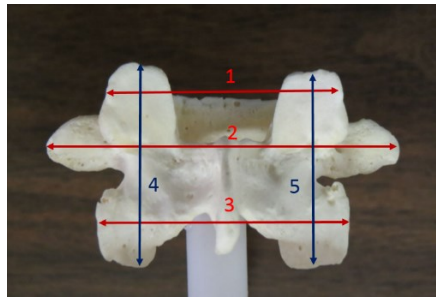


Figure 5.1 Five distances to be measured on lumbar vertebrae L1 and L3: (1) left superior articular process - right superior articular process, (2) left transverse process - right transverse process, (3) left inferior articular process - right inferior articular process, (4) left superior articular process - left inferior articular process, and (5) right superior articular process - right inferior articular process.

For the lumbar vertebrae, it was more reliable to select two points between the superior and inferior processes than two points between the superior process and the spinous process. The mean absolute differences (MAD) and the standard deviations (SD) of the five distance parameters from the cadavers and images were used to investigate the accuracy of the reconstruction. The Pearson correlation coefficients were also used to determine the agreement between the measurements from the cadavers and images.

5.2.2 Results

The three cadaveric vertebrae were successfully reconstructed. Figure 5.2 illustrates the three cadaveric vertebrae and their corresponding reconstructed images. From the figure, the geometric shapes of the reconstructed images are visually similar to that of the corresponding cadaveric vertebrae. However, the vertebral body of the vertebrae could not be imaged completely, except a portion of the interface between the vertebral foramen and the vertebral body.

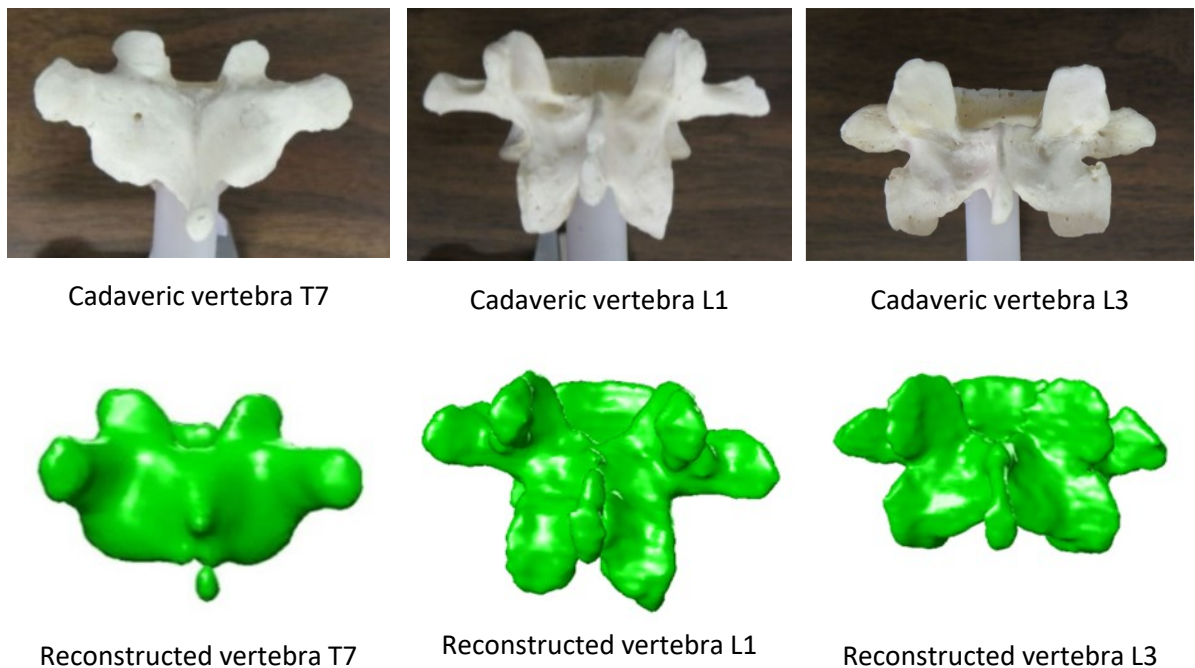


Figure 5.2 Cadaveric vertebrae T7, L1, and L3 and their corresponding 3D reconstructed images.

Table 5.1 reports the mean absolute differences (MAD \pm SD) and Pearson correlation coefficients r between two sessions of measurements on the reconstructed image and between the averaged measurements on the image and cadaveric vertebra. The MAD of the intra-rater measurements performed on the reconstructed images were 0.8 ± 0.7 mm, 0.5 ± 0.4 mm, and 0.4 ± 0.2 mm for vertebrae T7, L1, and L3, respectively; whereas, the MAD of the averaged measurements between the reconstructed images and the cadaver vertebrae were 1.5 ± 1.1 mm, 1.8 ± 0.5 mm, and 2.9 ± 1.5 mm, respectively. The larger the vertebra, the greater the difference (MAD \pm SD) between the image and the cadaver. Furthermore, all Pearson correlation coefficients are very high, very close to 1, indicating high agreement between two corresponding measurements.

Table 5.1 The mean absolute difference and Pearson correlation between two sessions of measurements on the reconstructed image and between the image and cadaveric vertebra.

	Reconstructed image			Image vs. Cadaveric vertebra		
	T7	L1	L3	T7	L1	L3
MAD \pm SD (mm)	0.8 ± 0.7	0.5 ± 0.4	0.4 ± 0.2	1.5 ± 1.1	1.8 ± 0.5	2.9 ± 1.5
r	0.9993	0.9998	0.9996	0.994	0.999	0.994

5.2.3 Discussion

Regarding the accuracy of the measurement, the maximum MAD between the two measurements on the same reconstructed image was small (0.8 mm), which was close to the reconstruction resolution (0.6 mm). However, the difference between the reconstructed image and the cadaver augmented with an increase in the size and the structural complexity of the vertebra. Vertebra T7 which was the smallest and the least complex had the smallest MAD between the reconstructed image and the cadaver (1.5 ± 1.0 mm). Meanwhile, vertebra L3 with its largest and most complex structure had the highest MAD (2.9 ± 1.5 mm). Locating precisely the same landmarks on a larger and more complicated area of both the image and the cadaver was more difficult, leading to a higher error.

The three reconstructed images look geometrically similar to the three corresponding cadaveric vertebrae (Figure 5.2). The images were fairly clear although some data points were missing at the spinous process area. The reason of the missing data was that both sides of the spinous process were slopes that caused some of the ultrasound beams not to echo back

directly to the transducer; therefore, those portions were not imaged. Although the reconstructed shapes were geometrically reserved and the accuracy of the reconstruction was high, the ultrasound imaging method had limitations due to the reflection characteristic of the ultrasound that was discussed in section 4.3.2. The ultrasound method cannot image and display vertebral body due to the acquisition configuration and the lack of ultrasound energy penetrating through bone (Figure 5.3). According to Equation 5.4, the percentage of the original energy reflected at the interface from water to bone, R_1 , is denoted as the reflection coefficient and calculated

$$R_1 = \frac{I_{r1}}{I} = \left[\frac{Z_2 - Z_1}{Z_2 + Z_1} \right]^2 = \left[\frac{(7.80 - 1.48) \cdot 10^6}{(7.80 + 1.48) \cdot 10^6} \right]^2 = 0.46 \quad (5.4)$$

where $Z_1 = 1.48 \times 10^6$ (Rayls) is the acoustic impedance of water, $Z_2 = 7.80 \times 10^6$ (Rayls) is the acoustic impedance of bone, I_{r1} is the reflection intensity at the first interface, and I is the original intensity pulsing from the transducer.

In theory, 46% of original energy bounces back at the first interface between water and bone. The remaining 54% continues to penetrate through bone until it reaches the second interface between bone and water from the bone side. A portion of this energy reflects at this second interface as shown in Equations (5.5) and (5.6).

$$R_2 = \frac{I_{r2}}{0.54I} = \left[\frac{Z_1 - Z_2}{Z_1 + Z_2} \right]^2 = \left[\frac{(1.48 - 7.80) \cdot 10^6}{(1.48 + 7.80) \cdot 10^6} \right]^2 = 0.46 \quad (5.5)$$

$$I_{r2} = 0.25I \quad (5.6)$$

where R_2 is the reflection coefficient at the second interface from bone to water, and I_{r2} is the reflection intensity at the second interface.

Therefore, only a quarter of the original energy coming back from the second interface at the boundary between vertebral body and water. In the real situation, the amount of the energy returning from the second interface is less than 25% of the original transmitted signal due to the absorption, scattering, and attenuation of signal within the bone and water. The reason why part of the vertebral body interface could be visualized is similar to the vertebral posterior arch. A portion of the original ultrasound beams could go directly through the empty space between the two superior articular processes, hit part of the vertebral body behind, and

bounced back to the probe. The recorded ultrasound signals from this part was strong enough to be reconstructed.

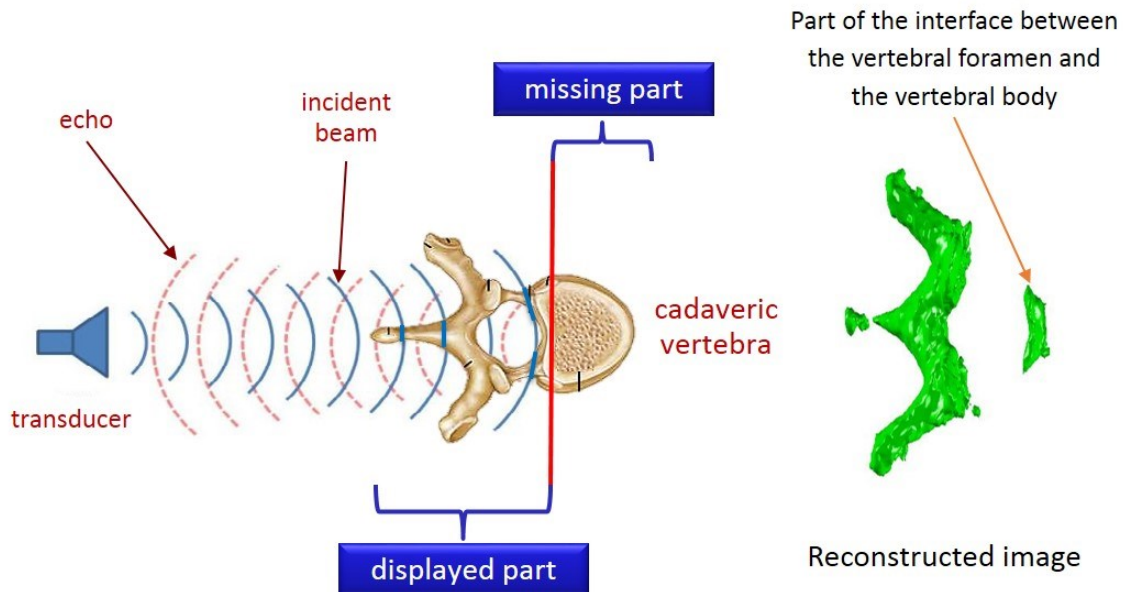


Figure 5.3 The limitation to imaging the vertebral body due to the lack of ultrasound energy penetrating through bone.

5.2.4 Conclusion

This chapter described a complete validation of the reconstruction of three single vertebrae. The accuracy of the reconstruction was high for a variety of vertebrae and the posterior arch of the reconstructed image was similar to that of the cadaver. However, the complete vertebral body could not be reconstructed.

5.3 Measurement of the AVR of cadaveric vertebrae

In the previous section, the measurement of the shape of a cadaveric vertebra was examined. The measurement of the rotation of vertebrae is also of interest in the assessment of scoliosis. This section describes a method to measure the AVR on a cadaveric vertebra. The accuracy of the rotation measurement is also investigated.

5.3.1 Method

The same cadaveric vertebrae T7, L1, and L3 from the previous experiment described in section 5.2 were scanned and the AVR as described in Section 4.4.1 were measured. The axial rotation of each vertebra was adjusted from 0° to 40° with 5° increments by rotating the pivot to the desired angle which was also shown on the protractor. Nine sets of ultrasound data were recorded from each reconstructed vertebra.

Figure 5.4 shows the front view and the top view of the 3D reconstructed vertebra T7. Two methods were proposed to measure the vertebral rotation based on using either the COLs (L-L) or the centres of transverse processes (TP-TP). The COL method was proposed by Chen *et al.* to measure the proxy Cobb angle and the AVR (Chen *et al.*, 2012, Chen *et al.*, 2013, Chen *et al.*, 2016). The user used the computer mouse pointer to locate manually the centres of either landmark on the reconstructed vertebral images according to their knowledge of vertebral anatomy (Figure 5.4a). The program detected the 3D coordinates of these points relative to the transmitter and calculated the AVR. The AVR was automatically determined by the angle between the line going through either the L-L or the TP-TP and a reference vertical plane (the scanning wall of the water tank), in this case plane xz as shown in Figure 5.4b.

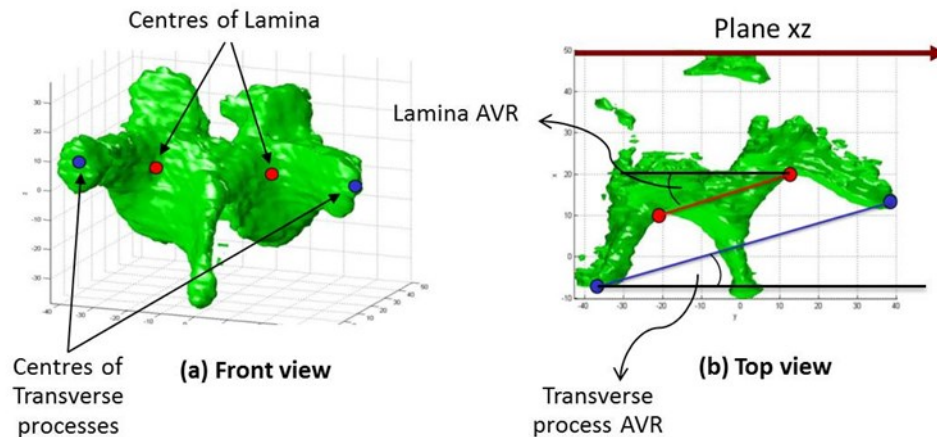


Figure 5.4 (a) - The frontal view (left) and (b) - The transverse view (right) of the 3D reconstructed T7 vertebra for AVR measurement (a) The COLs (red dots) or transverse processes (blue dots) were manually located by using the computer mouse pointer. (b) The rotation of each reconstructed vertebra was automatically determined by the angle between the line going through either the COLs (L-L) or the centres of transverse processes (TP-TP) and a reference vertical plane (xz).

To evaluate the accuracy and reliabilities of the measurement, three raters who had 6 months of scoliosis research experience participated in this study. These three raters, blinded with the rotation information, measured the rotation in two sessions in a one-week interval to minimize memory bias. The intra-class correlation coefficients using the two-way random and absolute agreement (ICC[2,1]) were applied to calculate the intra-reliability and inter-reliability. The accuracy of the measurement was determined based on the mean absolute difference with the standard deviation ($MAD \pm SD$).

5.3.2 Result

Twenty-seven ultrasound datasets (9 datasets/vertebra x 3 vertebrae) were reconstructed into 3D vertebral images. It was found that one of the lamina areas were missing on vertebrae L1 and L3 when the AVR was greater than 30° . Figure 5.5 demonstrates the right lamina of the lumbar vertebra is missing when the rotation is larger than 30° . As a result, the rotation measurement could not be measured on the images when the rotation angle was greater than 30° . However, it was not the case in vertebra T7; laminae could be identified in all T7 cases. Therefore, four cases were excluded out of 27 data sets.

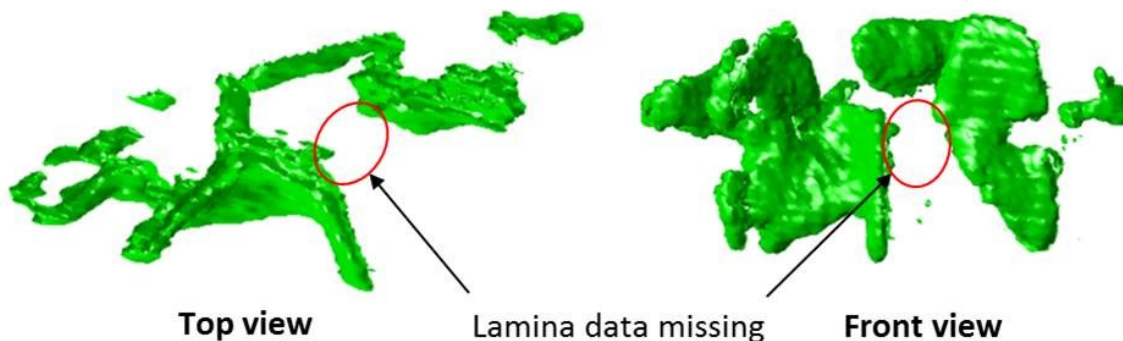


Figure 5.5 The top view (left) and the frontal view (right) of the 3D reconstructed L3 vertebra for the lamina data missing due to ultrasound blocking.

Table 5.2 and Table 5.3 list the intra- and inter-reliability with 95% confidence interval between two measurements of each rater and between raters, respectively. The ICC values of

the intra-reliability and the inter-reliability were greater than 0.98 indicating both methods (L-L and TP-TP) were very reliable. The mean absolute difference (MAD) and the standard deviation (SD) between mean values measured by each rater and the actual values were similar and between 1° and 2° (Table 5.4). The range of absolute difference (RD) between the mean value measured by each rater and the actual value are also illustrated in Table 5.5. Rater 3 shows the maximum difference of 10.9° when measuring the rotation using the laminae. It occurred at the angle of 30° where one of the two laminae was almost missing on vertebra L1 and might be due to a wrong selection of the landmark point. This significant error made the ICC values between rater 3 and rater 1 (0.984) and between rater 3 and rater 2 (0.981) smaller than that between rater 1 and rater 2 (0.992). If this value was excluded, the maximum deviation of the RD was 5.7°, similar to the other L-L ranges. Table 5.6 summarizes the MADs between any two raters, which were approximately 1°.

Table 5.2 *The intra-rater reliabilities for three raters.*

ICC (95% CI)	Rater 1	Rater 2	Rater 3
L-L	0.990 (0.978 - 0.996)	0.992 (0.981 - 0.996)	0.998 (0.996 - 0.999)
TP-TP	0.991 (0.979 - 0.996)	0.999 (0.999 - 1.000)	1.000 (1.000 - 1.000)

Table 5.3 *The inter-rater reliability between two raters.*

ICC (95% CI)	Rater 1 vs. Rater 2	Rater 2 vs. Rater 3	Rater 3 vs Rater 1
L-L	0.992 (0.983 - 0.997)	0.981 (0.955 - 0.992)	0.984 (0.964 - 0.993)
TP-TP	0.990 (0.954 - 0.997)	0.995 (0.986 - 0.998)	0.997 (0.990 - 0.999)

Table 5.4 *The mean absolute difference [absolute (mean measured value - actual value)].*

MAD ± SD	Rater 1	Rater 2	Rater 3
L-L	1.2° ± 1.4°	1.4° ± 1.5°	1.7° ± 2.6°
TP-TP	0.9° ± 1.1°	1.2° ± 1.3°	0.9° ± 0.7°

Table 5.5 *The range of absolute difference [absolute (mean measured value - actual value)].*

RD	Rater 1	Rater 2	Rater 3
L-L	0 – 4.1°	0 – 5.3°	0 – 10.9°
TP-TP	0 – 3.5°	0 – 4.3°	0 – 2.7°

Table 5.6 *The mean absolute difference between two raters.*

MAD ± SD	Rater 1 vs. Rater 2	Rater 2 vs. Rater 3	Rater 1 vs. Rater 3
L-L	1.1 ± 1.0°	1.3 ± 2.1°	1.0 ± 2.0°
TP-TP	1.2 ± 1.1°	0.9 ± 0.7°	0.6 ± 0.7°

It can be seen that all ICC values for TP-TP are slightly higher than that for L-L, whereas all MAD values for TP-TP are slightly lower than that for L-L except for the case between rater 1 and rater 2. The maximum absolute difference between measured values and actual values is 5° for all three raters for both of the L-L and TP-TP methods.

5.3.3 Discussion

Three different cadaveric vertebrae with different structures were used to investigate the accuracy of measuring the AVR from the 3D reconstructed ultrasound images. These three vertebrae represent the most common apical vertebrae in scoliosis for the thoracic, thoracolumbar, and lumbar curves, respectively. The rotation of each vertebra was adjusted in one direction with an assumption that the vertebrae and the experimental setup were symmetric. Rotating the vertebrae in the other direction would provide the same results.

The measurement procedure was simple and measured the AVR directly on the axial plane. The measurements on the reconstructed images were compared to their actual values on the vertebral rotation device. The ICC values, the MAD and RD values of the TP-TP method were slightly higher or better than the L-L method when the rotations of vertebrae L1 and L3 were between 0 and 30° and that of vertebra T7 were from 0 up to 40°. This means that the type of the vertebra and the selection of landmark do not significantly affect the measurement of the rotation. Both the L-L and TP-TP methods could measure the AVR reliably from the 3D ultrasound images.

This study pointed out that if the lumbar vertebra has the rotation greater than 30° one of the laminae cannot be completely identified. Therefore, measurements based on these landmarks could not be performed. However, this does not seem to be a limitation because the vertebral rotation was found in daily routine scoliosis clinics between 15 - 20°, and rarely exceeding 30° or 40° (Weiss, 1995, Barsanti *et al.*, 1990). In this study, the method was verified on three non-deformed cadaveric vertebrae; that is, the laminae and the transverse

processes were assumed symmetric. However, scoliotic vertebrae are not always symmetric; therefore, assuming the symmetry of the vertebra when calculating the rotation may be considered a limitation to some cases.

5.3.4 Conclusion

This study described the method to measure the AVR of the three different vertebrae. The results demonstrated that the accuracy of the AVR was high and that the L-L and TP-TP methods could be used interchangeably to measure the AVR from the 3D ultrasound images without any significant differences. That is, the vertebral laminae are used as landmarks to measure the AVR.

5.4 Accuracy and reliability of the measurement of the AVR, the tilt angle, and the Cobb angle on the spine phantoms

The measurement of the AVR on individual cadaveric vertebra yielded good results. Apart from the AVR, the Cobb angle is also an essential parameter to assess the severity of scoliosis. This section extends the previous study to apply to the spine phantoms to investigate the measurement of the Cobb angle. In this section, the accuracy and the reliability of the *in-vitro* ultrasound measurements of the AVR, the tilt angle (the angle between the vertebral tilt of two vertebrae), and the PA and PMC Cobb angles on the spine phantoms are determined.

5.4.1 The experimental setup and scanning procedures

Two Sawbones spine phantoms (Pacific Research Laboratories, Inc., USA) comprised of 12 vertebrae from thoracic vertebra T6 to lumbar vertebra L5 were used. Figure 5.6 demonstrates the two phantoms and the experimental setup. On the coronal view, one phantom was set to have a moderate scoliotic curve (Figure 5.6a), and the other was designed to be a straight spine (Figure 5.6b). On each phantom, each vertebra was linked to an adjacent vertebra using a plastic rod going through the centres of vertebral bodies. Each phantom was then fixed to an acrylic plate at seven different points and at least 5 cm above the plate. The plastic rod connected the entire spinal column was fused together with vertebrae to form a rigid model to prevent the phantom from changing its shape during experiments and transportation. During experiments, the Sawbones spine phantoms were completely immersed upright in a water-filled tank with 4 mm-thick acrylic walls to mimic the body setting (Figure

5.6c). The spines were scanned starting from the top to the bottom of vertebra so that all of the vertebrae were covered. The ultrasound probe was moved along the curve of the spine while its centre was facing the middle of the spinous process.

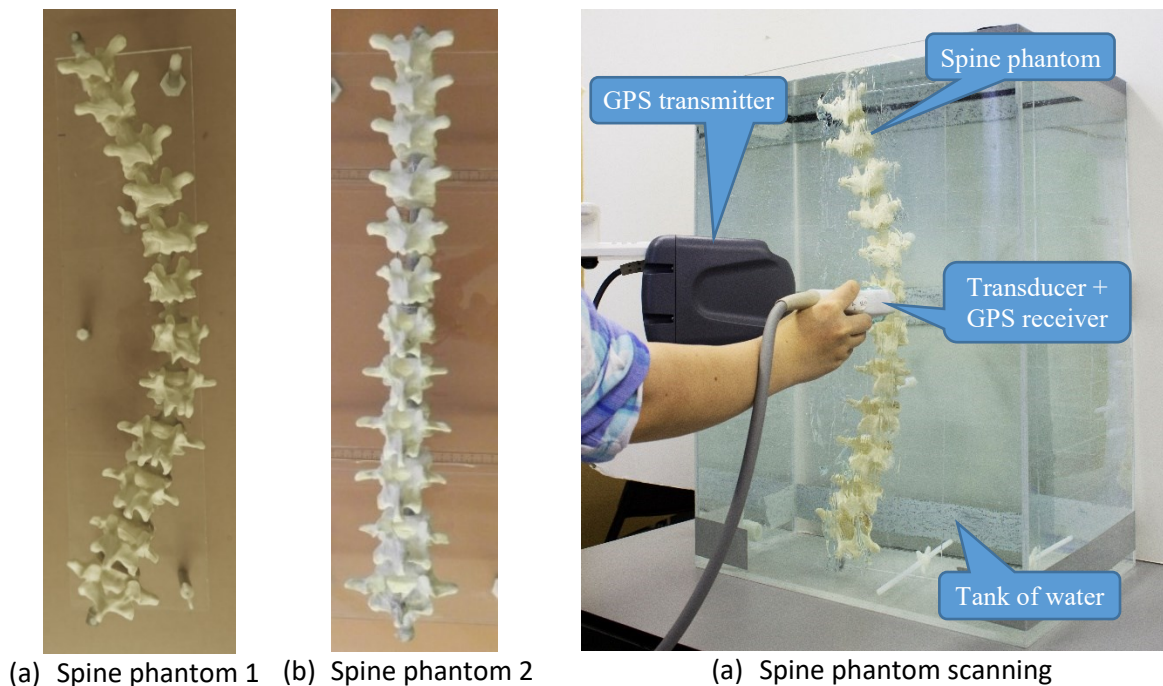


Figure 5.6 The in-vitro experimental setup: (a) Spine phantom 1 (scoliotic); (b) Spine phantom 2 (straight); (c) The spine phantom was immersed into a tank of water that mimicked the body setting.

In order to determine the accuracy of the method, the two spine phantoms were also scanned by the Toshiba Aquilion ONE CT scanner (Toshiba Medical Systems, Japan). Figure 5.7 shows how the spine phantom was scanned similar to a patient laying on a CT scanner's couch. The phantom was secured by a strap to prevent it from vibrating when the couch was moving. Both spine phantoms were scanned with the voltage of 120 KV, the current of 150 mA, and the slice thickness of 0.5 mm. These settings were selected by the CT scanner technologist.

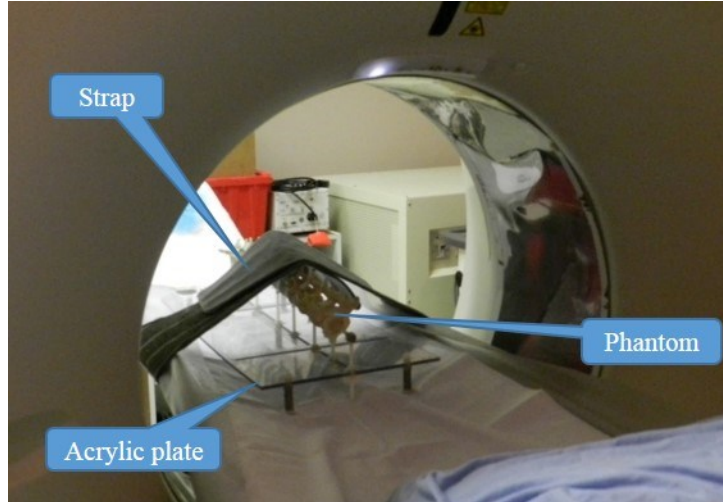


Figure 5.7 The spine phantom was CT scanned in the lying position.

5.4.2 Methods

In this study, the AVR was measured on both 3D ultrasound and CT images. The tilt angle and the Cobb angle were measured on the projected 2D PA plane and the PMC. These two planes were derived from the 3D image, which is described in the following paragraphs.

Determination of the PA plane

To determine the PA plane of the reconstructed spine, two hypotheses were made: (i) the surface of the ultrasound probe was parallel with the PA plane, and (ii) the lumbar vertebra L5 had 0° rotation relative to this PA plane. Therefore, the rotation of the PA plane relative to the reference plane (xz) was equal to the rotation of vertebra L5 with respect to the same xz plane. The L5 rotation was calculated by using the average of rotations of the last twenty B-scans. The estimated 2D PA image view was obtained by projecting the 3D spinal image on the PA plane. In other words, the 3D spinal image was rotated an angle that was estimated from L5 and then projected on the reference plane (xz). The largest voxel value along the projection ray was selected as the value of the corresponding projected pixel. Figure 5.8 illustrates how a pixel of the PA image was determined from a voxel of the 3D spinal volume.

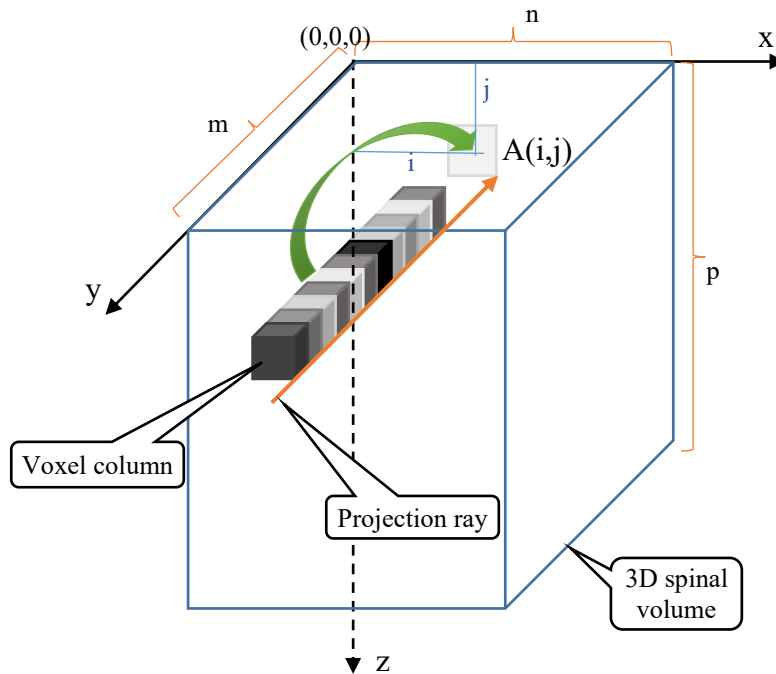


Figure 5.8 The determination of a pixel of the PA image from a voxel of the 3D spinal volume.

That can be explained as follows. Suppose the 3D spinal volume has a size of $m \times n \times p$. The intensity value of pixel $A(i,j)$ of the PA image ($i = 0, 1, \dots, n$; $j = 0, 1, \dots, p$) is the largest value among the values of voxels (i,j,k) in the voxel column along the projection ray when k ranges from 0 to m .

Determination of the plane of maximum curvature

The PMC is defined by the vertical plane that displays the maximum Cobb angle and generally occurs close to the maximum AVR plane. Figure 5.9 illustrates how to determine the PMC from a 3D spinal image and the apical vertebral rotation. To determine the PMC, the apex, and its two adjacent vertebrae were determined, and their AVRs were then measured. Five vertical planes were established and the first one was determined as follows. Suppose these three vertebrae had rotations 18° , 20° , and 17° . The largest AVR among the three (in this case 20°) was used to determine the first vertical plane that formed with reference plane xz . The 3D spine was projected on this PMC to obtain a 2D spinal image on which the Cobb angle was measured.

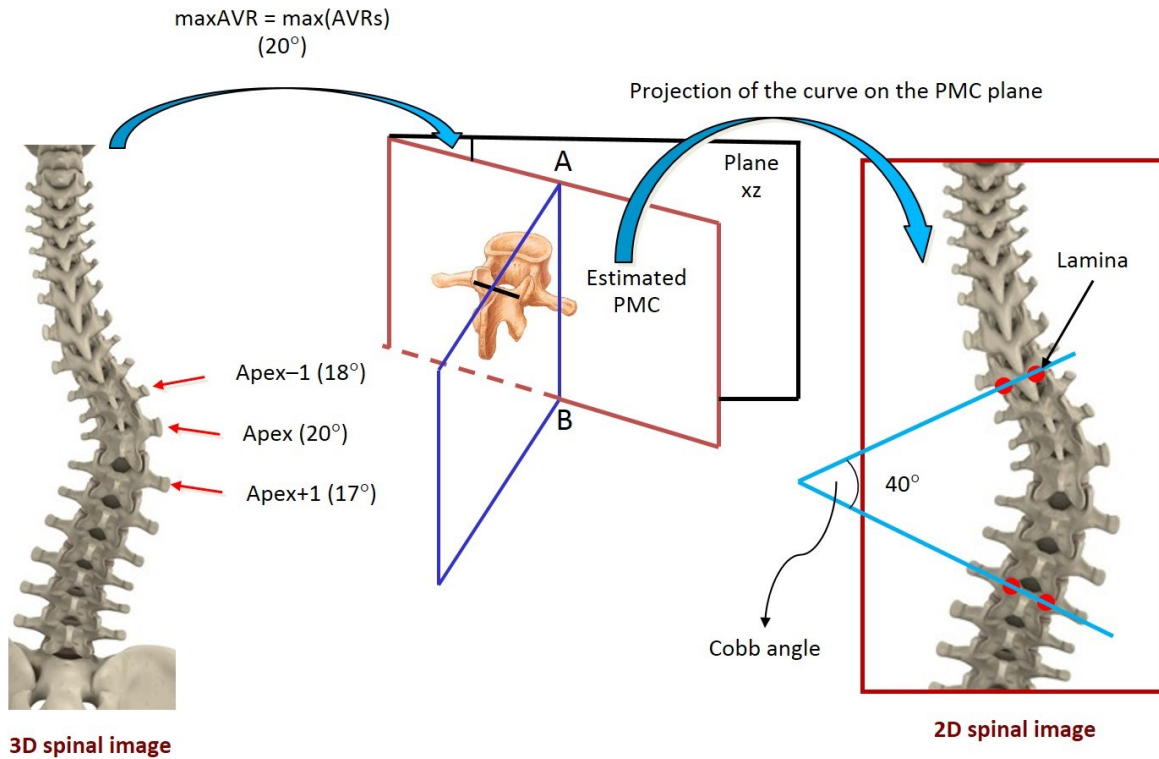


Figure 5.9 The determination of the PMC.

Four other vertical planes were formed with 2° and 4° differences from the line AB on both directions (Figure 5.9). The Cobb angles on these planes were also determined similarly to that on the PA view. The largest Cobb angle among the five values was considered the PMC Cobb angle, and the plane that contained it was the PMC.

Measurement of the AVR, the tilt angle, and the Cobb angle

To determine the accuracy of the 3D construction of the spine phantoms, the AVR, the tilt angle of individual vertebra and the Cobb angle were measured using the developed 3DSA. Another Matlab-based program was developed to reconstruct CT slices into a 3D spinal image to measure the corresponding AVR, the tilt angle of individual vertebra and the Cobb angle. Two raters, a naive rater (Rater 1) and an experienced rater (the software developer) with one-year ultrasound measurement experience (Rater 2), were blinded with information and performed measurements twice in one week apart. Prior to the measurements, the naive rater was trained to use the software to measure the AVR and the Cobb angle on test images until he felt confident to perform the measurements. A statistical analysis including the inter- and

intra-class correlation coefficients (ICC(2,1)), mean absolute difference (MAD), and standard error of measurement (SEM) was calculated to evaluate the accuracy and reliability of measurements. MAD values showed the discrepancies for each measurand between two measurements of each rater, between averaged measurements of the two raters, between ultrasound and CT measurements, and between the PA Cobb angle and PMC Cobb angle.

In this *in-vitro* study, the centres of transverse processes were used instead of the COLs as landmarks for measurement. It was because the spine phantoms were homogenous; hence, their CT images were also homogenous, leading to homogeneity in the projection images. It was therefore more difficult to identify exactly the COLs than that of transverse processes. Furthermore, the previous study demonstrated that there was slight difference in measurements between the L-L and TP-TP methods. Twelve vertebrae of each phantom were measured. The AVRs of 11 lower vertebrae was calculated respective to that of the top one. The vertebra with the largest AVR was considered the apex. Instead of measuring only two Cobb angles from the spine phantoms, the tilt angle of the 12 vertebrae were measured respective to that of the top one. The tilt angle was formed by the line going through two COTPs of the top vertebra and the line connecting those of the other vertebra. The two raters also measured the Cobb angle of the spine on both of the PA and PMC views.

5.4.3 Results

The acquired ultrasound and CT data of the two spine phantoms were reconstructed. Figure 5.10 shows the 3D reconstructed ultrasound and CT images of the two spine phantoms. It can be seen that the image of the straight spine (Spine 2) shows more details than that of the curved one (Spine 1). Furthermore, visually speaking, the ultrasound images display fewer details than the CT image, of which vertebrae have as many features as that of the spine phantoms including the vertebral body. Figure 5.11 shows the PA projection ultrasound and CT images of the two spine phantoms on which the tilt angle and Cobb angle were measured.

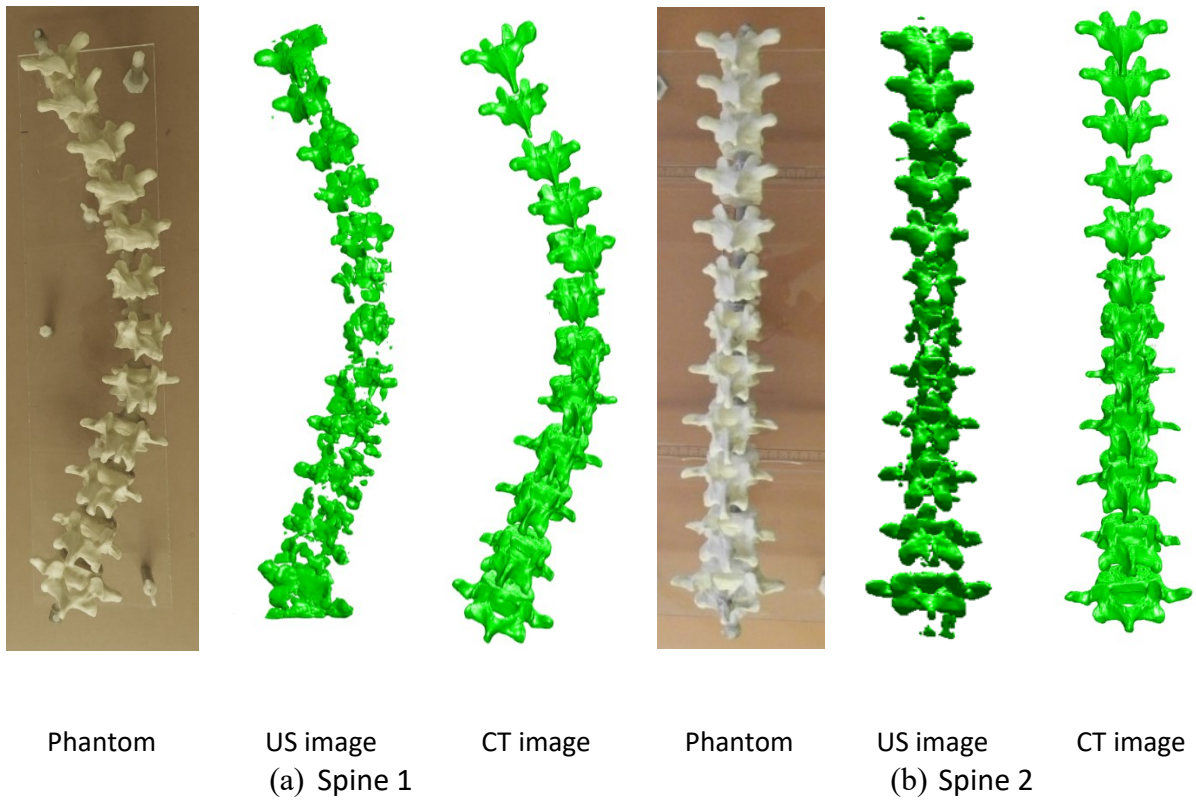


Figure 5.10 The phantom, the ultrasound reconstructed image, and the CT reconstructed image of: (a) Spine 1 (curved), and (b) Spine 2 (straight).

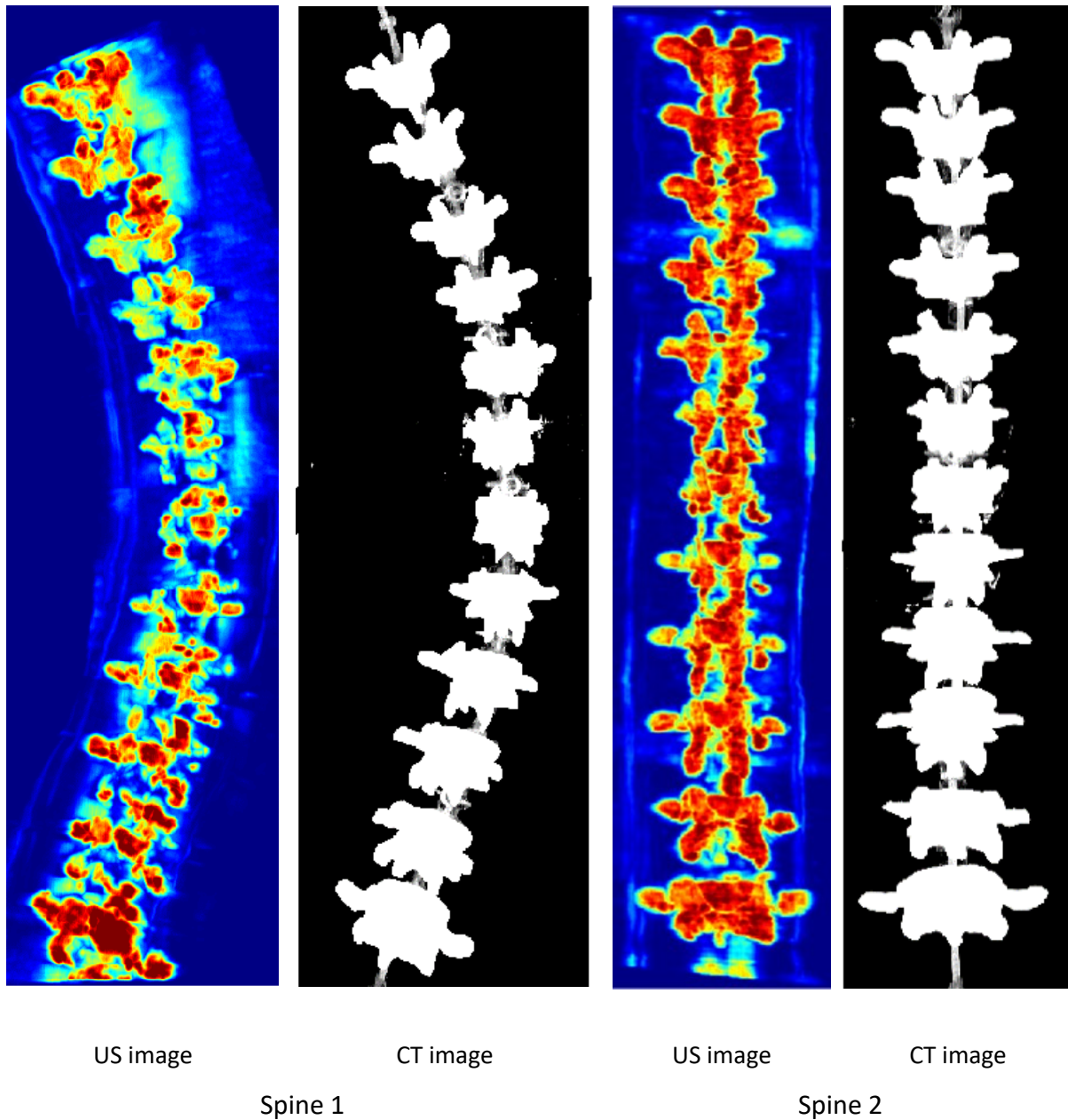


Figure 5.11 The US and CT PA images of the two spine phantoms.

The AVR of 12 vertebrae for each phantom were measured. The PA and PMC Cobb angles were also measured on both spine phantoms. Tables 5.7 - 5.10 summarize the *in-vitro* results. The comparison between the AVR and the tilt angle on the PMC measured on the CT images and their corresponding ultrasound images also shows a strong correlation, reliability and accuracy ($ICC \geq 0.922$, $MAD \leq 1.9^\circ \pm 1.4^\circ$, and $SEM \leq 1.7^\circ$) (Tables 5.7 - 5.8). In

addition, the two raters provided US measurements, which were highly correlated and reliable as shown in Table 5.9. Meanwhile, Table 5.10 reports the Cobb angles measured on the PA and PMC views of the CT and US images by the two raters. In general, the discrepancies between the PA and PMC Cobb angles measured by the two raters for spine 2 are small. Nevertheless, rater 2 provided better measurements than rater 1. While the difference between two raters in the AVR is insignificant, that in the PMC Cobb angle is up to 3.3°.

Table 5.7 Intra-rater reliabilities of the AVR between CT and US measurements for the two raters.

	Rater 1		Rater 2	
	Spine 1	Spine 2	Spine 1	Spine 2
ICC	0.982	0.922	0.985	0.974
MAD ± SD	1.9° ± 1.4°	0.7° ± 0.5°	1.6° ± 1.1°	0.4° ± 0.4°
SEM*	1.7°	0.6°	1.4°	0.4°

*Calculated based on the CT measurements

Table 5.8 Intra-rater reliabilities of the PMC tilt angle between CT and US measurements for the two raters.

	Rater 1		Rater 2	
	Spine 1	Spine 2	Spine 1	Spine 2
ICC	0.951	0.746	0.999	0.931
MAD ± SD	4.2° ± 3.6°	0.8° ± 0.9°	0.9° ± 0.5°	0.6° ± 0.3°
SEM**	3.9°	0.8°	0.6°	0.5°

** Calculated based on the CT measurements

Table 5.9 Inter-rater reliabilities of the ultrasound measurements of the AVR and the PMC tilt angle.

	Spine 1		Spine 2	
	AVR	TAPMC	AVR	TAPMC
ICC	0.980	0.975	0.913	0.760
MAD ± SD	2.1° ± 1.3°	3.5° ± 2.6°	0.6° ± 0.7°	0.8° ± 0.8°
SEM***	1.7°	3.1°	0.6°	0.7°

*** Calculated based on the measurements by Rater 2

Table 5.10 The Cobb angle on the PA and PMC view between CT and US measurements for the two raters.

Cobb angle	Rater 1				Rater 2			
	Spine 1		Spine 2		Spine 1		Spine 2	
	CT	US	CT	US	CT	US	CT	US
On the PA plane	48.4°	54.4°	6.0°	5.1°	55.0°	55.8°	4.3°	5.6°
On the PMC plane	51.7°	56.4°	6.1°	5.8°	59.2°	57.7°	5.3°	5.1°

5.4.4 Discussion

Most of the measurements provided high intra- and inter-rater reliabilities ($ICC > 0.90$) except the PMC tilt angle for Spine 2 (0.746) and between the two raters (0.760). The Spine 2 was designed without rotation on vertebrae and lateral curvature. That means that the AVR and the tilt angle of each vertebra were designed to be zero. Theoretically, the ICC value is affected by the range of measurement and the sample size of measurements. Therefore, Spine 2 had lower ICC values when compared to the Spine 1 measurements. In addition, although Rater 1 supposed to be blinded to the curvature and AVR information on both of the spine phantoms, Rater 1 could recognize that Spine 2 was straight by looking at its images. Thus, the measurement obtained from Spine 2 might be biased. Furthermore, Rater 1 yielded a higher variation in the measurement of the tilt angle on Spine 1 ($4.2^\circ \pm 3.6^\circ$), leading to greater differences of 6° in the measurement of the Cobb angle between the ultrasound and CT images.

As explained in section 5.2.3, only vertebral posterior arches could be imaged and displayed. The AVR and lateral deviation of Spine 1 can also be used to explain why data were missing on some vertebrae. Due to the ultrasound characteristics, the more the vertebra rotates, the higher chance the spinous process blocks the ultrasound signals, which may cause missing lamina data.

Finally, yet importantly, the measurements performed by Rater 2 were more accurate than those by Rater 1 because Rater 2 had more experienced in measuring ultrasound images than Rater 1. This indicates that the accuracy of the measurements was related to user experience.

5.4.5 Conclusion

In this study, the methods to determine the PA plane and the PMC were described. The accuracy and reliability of the measurement of the AVR, the tilt angle, the PA and PMC Cobb angles were also reported, which completed the preliminary investigation of the 3D ultrasound method into imaging scoliosis on the phantoms.

5.5 Summary

In this chapter, the methods to measure the AVR, the Cobb angle and the lateral deviation on the PA plane and the PMC were proposed. It was the first time that the PMC Cobb angle was proposed and measured on the PMC of ultrasound images. The 3D reconstruction of cadaveric vertebrae reported a good accuracy. The intra- and inter-rater ICCs of the *in-vitro* measurements of the AVR and the vertebral tilt angle were high, indicating a high reliability. The *in-vitro* results encourage further studies that are conducted under clinical settings to investigate the repeatability, reliability, and validity of the proposed method. These will be investigated and presented in the next chapter.

***In-vivo* repeatability of the ultrasound method, reliability of the ultrasound measurements, and validity of the PA Cobb angle and AVR measurements**

In this chapter, the repeatability of the ultrasound method and the reliability of the ultrasound measurements under clinical settings are investigated. Section 6.1 reports the methods to measure the AVR, the Cobb angle, and the lateral deviation on ultrasound images and the results of the repeatability study. The intra- and inter-rater reliabilities of the aforementioned ultrasound measurements are reported in section 6.2. Section 6.3 and section 6.4 present the validity studies in which the measurements of the PA Cobb angle and the AVR on the ultrasound images are compared with that on the PA radiographs and EOS images, respectively.

6.1 Repeatability of the 3D ultrasound method in imaging scoliosis

The *in-vitro* studies described in Chapter 5 reported encouraging results such that further studies should be conducted to investigate if the proposed ultrasound method can be applied to *in-vivo* cases. When speaking of measurements, accuracy is most often discussed. However, the repeatability of measurements is equally important. The repeatability of measurements refers to the variation in repeated measurements conducted on the same subject under identical conditions. This can be interpreted that measurements are performed by the same instrument, the same method, and the same rater over a short period of time. To investigate the repeatability of the ultrasound method, AIS patients were scanned twice and their spinal

images were measured. The measurements from the first scan were compared to that from the second scan.

6.1.1 Subject recruitment and scanning procedure

Patients were recruited from the local scoliosis clinics and the inclusions criteria were: i) patients were diagnosed with AIS with the Cobb angle less than 45° , and ii) patients had no in-brace radiographs taken on the same days. In addition, the exclusion criteria were patients who had had spinal surgery. The ethics was approved by the University of Alberta ethics board and all patients signed the consents before participating in the study.

6.1.2 Methods

Twenty-four AIS patients (18 females and 6 males with ages ranging from 10.8 to 17.8 years old) were scanned twice in the standing position similar to the posture that the corresponding standing radiograph was taken as described in section 4.5.1. After the first scan, the patients were requested to stretch and twist their backs, and then walked around the clinic room before returning to have the same posture for the second scan. In the second scan, the same operator who had three years of experience in performing ultrasound scanning scanned the patients.

For each scan set, 24 spinal images were reconstructed from 24 patient datasets using the 3DSA software, but three images were excluded due to poor image quality. Among the remaining 21 images, 28 curves were recognized and measured from the ultrasound images. Five parameters (the AVR, the Cobb angles and the lateral deviations on both of the PA plane and the PMC) on both scans were measured twice in one-week interval by one rater and analyzed. The rater had a one-year experience of reviewing and measuring the Cobb angles and the AVRs on ultrasound images of the spine. For this repeatability study, the second session of measurements from the first scan (scan) was compared with the second session of measurements from the second scan (rescan). For the AVR in particular, for each curve, the rotations of the apex and the two adjacent vertebrae were recorded. Only the measurements of the AVR recorded at the same levels between the scan and the rescan were compared. The difference in vertebral level identification between the scan and the rescan was not accounted for. The ICC was used to investigate the agreement between the two measurement sets. The

Bland-Altman plot was also used to display graphically the agreement between two measurements of the 5 parameters.

Measurement of the AVR

The measurement of the AVR was performed on the PA view and the corresponding transverse view. Figure 6.1a illustrates the PA ultrasound image while Figure 6.1b displays the transverse view of a selected vertebra. Figure 6.1c shows the 3D coordinate system with the directions of the x-, y-, and z-axis. Firstly, the COLs were digitized on the PA image using the computer mouse pointer. For example, as shown in Figure 6.1a, the user selected the COLs of the thoracic vertebra: points A(x_A, y_A, z_A) and B(x_B, y_B, z_B) where (x_A, z_A) and (x_B, z_B) were the coordinates determined from the PA view. The rotation of that vertebra was then calculated on the corresponding transverse view, which was determined by a cross-section of volume V generated by a plane going through line AB and perpendicular to reference plane xz.

On the transverse view, coordinates y of points A and B were automatically determined by using their brightness intensity values. On the column of pixels with coordinate $x = x_A$, the software searched for the highest brightness intensity value of the pixel. Then, the y coordinate of that pixel was y_A . Similarly, the software used the same approach to determine the coordinate of point B (x_B, y_B). The vertebral rotation, α , was the angle between line AB and the referenced horizontal line, and calculated as

$$\tan\alpha = \frac{y_B - y_A}{x_B - x_A} \quad (6.1)$$

$$\alpha = \arctan\left(\frac{y_B - y_A}{x_B - x_A}\right) \quad (6.2)$$

This was an automatic process. In addition, the user could fine-tune the location of points A and B on the transverse view, which might improve the results.

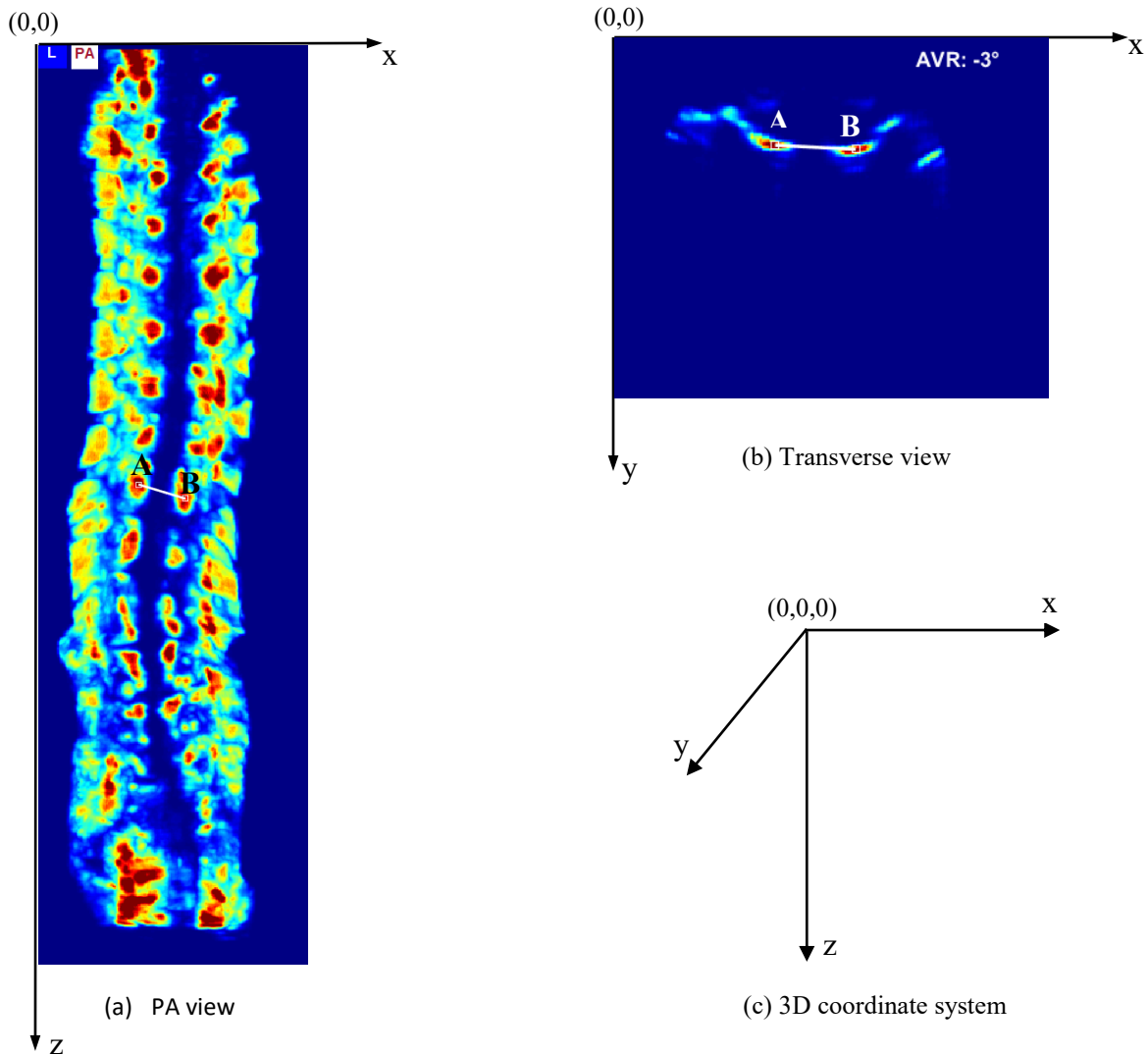


Figure 6.1 Measurement of the AVR: (a) PA view, (b) Transverse view, and (c) 3D coordinate system.

Measurement of the Cobb angle on the PA view

In order to identify the end plates, the apex, and the curve type of each curve, vertebral levels were determined respectively to the level of thoracic vertebra T12. Figure 6.2a illustrates the location of vertebra T12. According to the anatomy of vertebra T12, the identification of T12 on the PA ultrasound image was based on the following characteristics:

- The shadows of T12 laminae are longer than that of the above vertebrae.

- The distance between two laminae of T12 is shorter than that of the above vertebrae.
- Vertebra T12 is the last one that articulates with the ribs.

The proxy Cobb angle of a curve from the ultrasound image is the angle between two lines going through the COLs of two most tilted vertebrae (Chen *et al.*, 2012, Chen *et al.*, 2013). In order to determine the proxy Cobb angle as well as the number of curves, tilt angles of all vertebrae that could be recognized on the PA view were measured. Two points were selected (for example, A and B) on each vertebra on the PA image; the software captured their 2D coordinates, and automatically calculated the vertebral tilt angle. At the same time, the AVR was also measured. The positive sign of the tilt angle was defined when point B was higher than point A ($z_A > z_B$); otherwise, it was negative. The number of curves associated with the change in the sign of the tilt angles. If there was a change from positive to negative, or vice versa, between two adjacent vertebrae, one curve was detected. For each curve, the two most tilted vertebrae were recognized by the largest positive tilt angle and the largest negative tilt angle. Therefore, the Cobb angle was the summation of the largest positive tilt angle and the largest negative tilt angle. Figure 6.2b illustrates the AVR and the Cobb angle: color magenta represents the upper and lower end vertebrae while color yellow represents the apex.

Measurement of the Cobb angle on the PMC view

The Cobb angle on the PMC view was calculated according to the vertebral levels obtained from the PA view. For each curve, the apical rotation was first used to determine the PMC as described in section 5.4.1. Then, the positions of the upper and lower end vertebrae were transferred to the PMC to estimate their corresponding positions on the PMC, from which the Cobb angle on the PMC was calculated. The positions of the upper and lower end vertebrae on the PMC could be fine-tuned by the user to achieve a better result. The PMC Cobb angle was calculated as follows:

Let A, B, C and D be the left and right COL of the upper and lower end vertebra, respectively. The PMC Cobb angle was the angle θ between two vectors AB and CD.

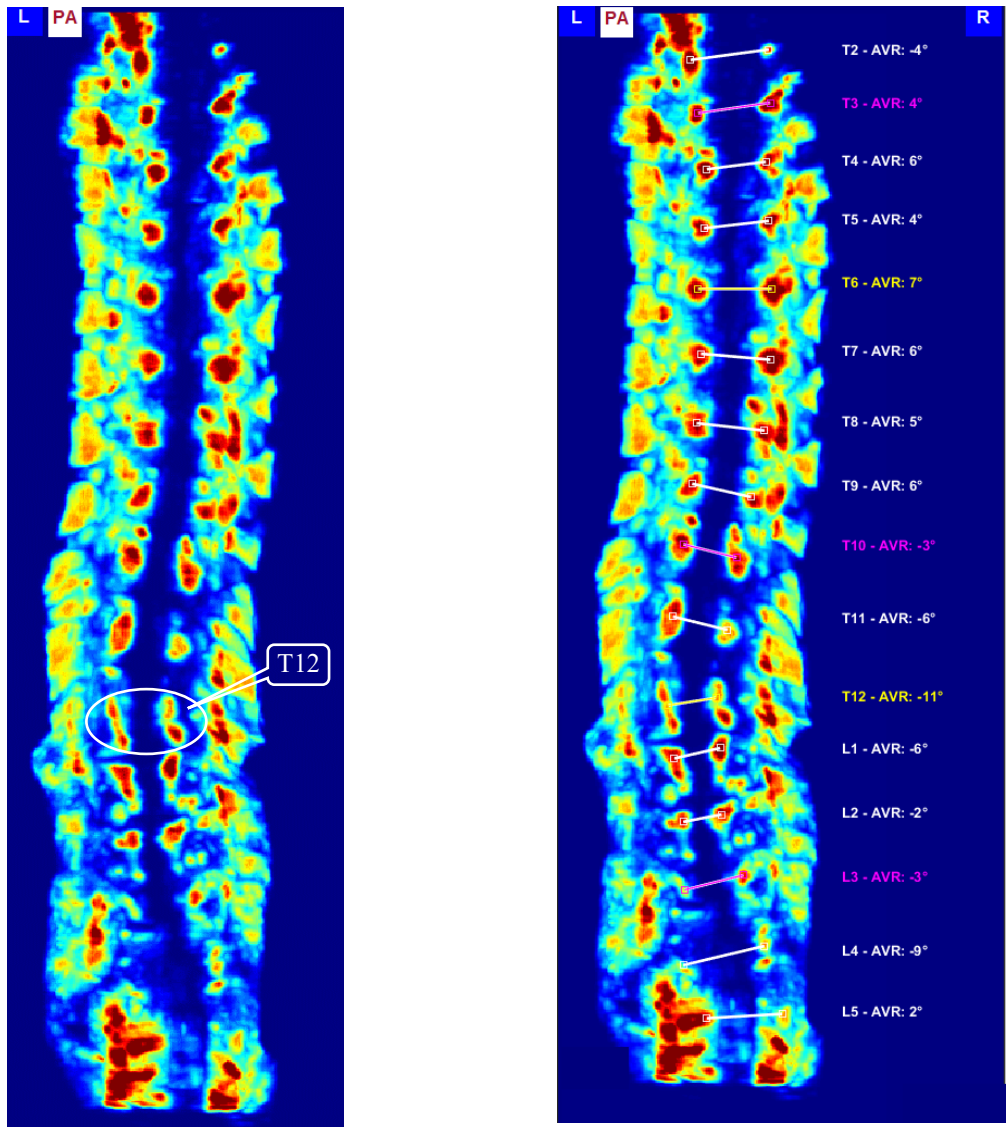
$$\overrightarrow{AB} = (x_B - x_A, y_B - y_A) \quad (6.3)$$

$$\overrightarrow{CD} = (x_D - x_C, y_D - y_C) \quad (6.4)$$

$$\theta = \arccos\left(\frac{\overrightarrow{AB} \cdot \overrightarrow{CD}}{|\overrightarrow{AB}| \cdot |\overrightarrow{CD}|}\right) \quad (6.5)$$

Measurement of the lateral deviation

The lateral deviation in this PhD thesis was defined as the horizontal distance between the centre of the apical vertebra and the vertical line going through the centre of vertebra L5. The centre of a vertebra was identified as the mid-point on the segment connecting two COLs of that vertebra. When the AVR and the Cobb angle were measured, the coordinates of the COLs of the measured vertebrae on the PA image were recorded and saved. The 3DSA software was able to extract the coordinates of the COLs of the apical vertebra and vertebra L5 from the saved data and automatically calculated the lateral deviation on the PA plane. The coordinates of the COLs of the apical vertebra and vertebra L5 were transferred to the PMC and were used to calculate the lateral deviation on the PMC automatically.



(a) Determination of vertebra T12

(b) Determination of the Cobb angle

Figure 6.2 (a) The determination of vertebra T12, and (b) The determination of the AVR and the Cobb angle: color magenta represents the upper and lower end vertebrae while color yellow represents the apex.

6.1.3 Results

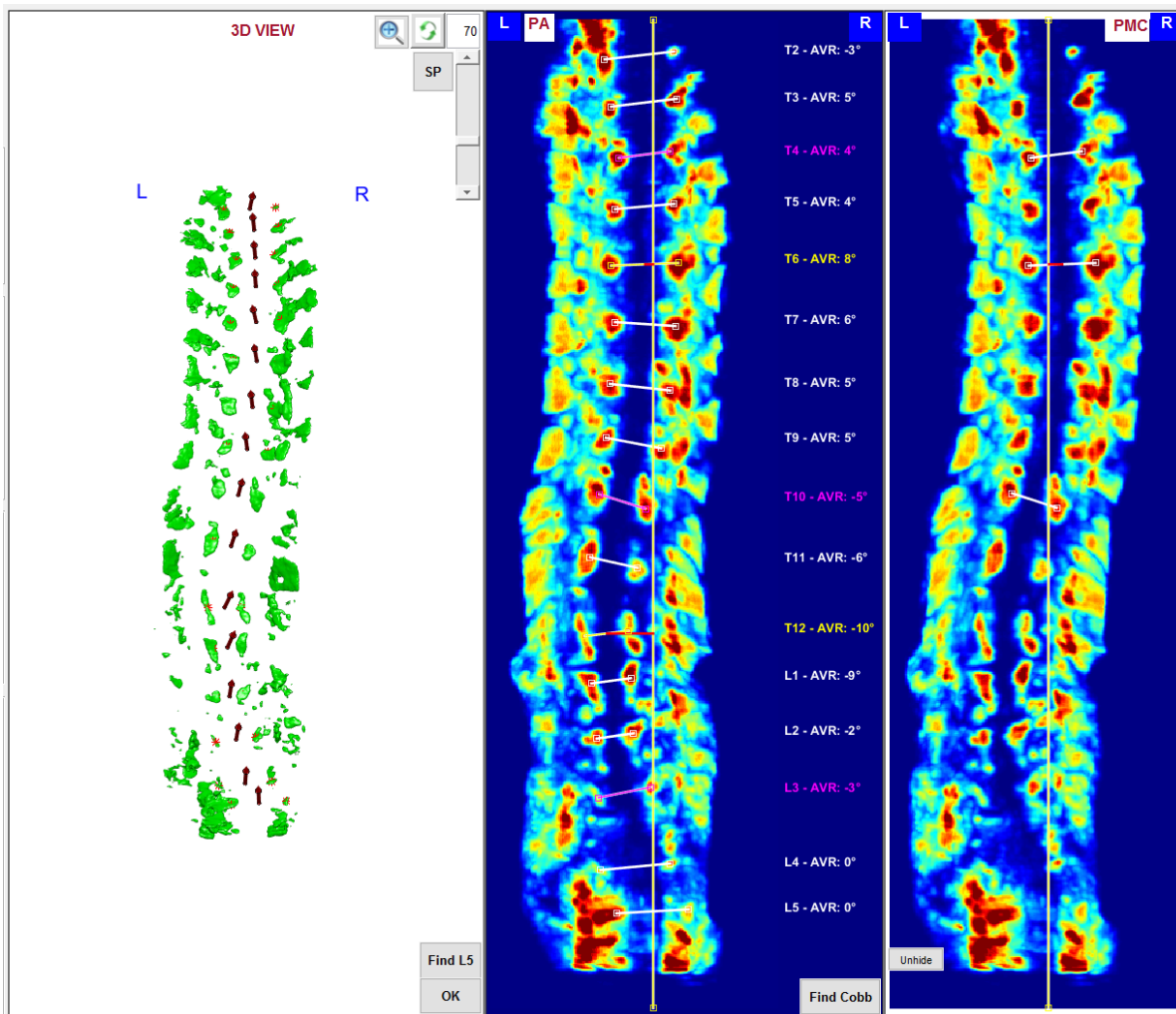
Figure 6.3 shows the reconstructed images from a patient and its PA and PMC images. As can be seen from Figure 6.3a, laminae and transverse processes combined with ribs could be imaged and displayed, but not the spinous processes. The spinous process of each vertebra was then emulated as the arrows based on the coordinates of the COLs of that vertebra

obtained on the PA image. The direction of the arrow represented the direction of rotation of the vertebra. The AVR of each vertebra is displayed on the PA image. The Cobb angle were measured, the end vertebrae and the apex were determined on the PA plane and the PMC. As shown on the PA view (Figure 6.3b), the patient had two curves. The tilt angles on the first four vertebrae from T2 to T6 were positive while on vertebrae T7 - T11 were negative. Since T4 and T10 had the largest positive and negative tilt angles, respectively, they were the upper and lower end vertebrae of the first curve. Since vertebra T6 had the largest lateral deviation and AVR, it was then identified as the apical vertebra. Similarly, T10, L3, and T12 were the upper end, the lower end, and the apical vertebrae of the second curve, respectively. It can also be seen that the curvature of upper curve on the PMC is larger than the corresponding one on the PA view (Figure 6.3c). Twenty-eight curves exhibited mild to moderate scoliosis with the Cobb angles ranging from 11° to 39° with a mean of 24.0° ± 8.9°.

Table 6.1 provides the ICC and MAD values for five measurements of the AVR, the Cobb angles and the lateral deviations on both of the PA and PMC views. A total of 46 vertebrae and 28 curves that were present in both sessions of measurements were compared. All ICC values were greater than 0.9, indicating a high agreement between the two sessions of measurements. The standard deviations of the difference for all five parameters were small (approximately 2° for the AVR and the Cobb angles; less than 6 mm for the lateral deviations).

Table 6.1 Reliabilities of the measurements of the five parameters.

	AVR	PA-Cobb	PMC-Cobb	PA-LD	PMC-LD
ICC	0.949	0.985	0.982	0.903	0.949
95% CI	0.909 - 0.971	0.968 - 0.993	0.961 - 0.992	0.801 - 0.954	0.893 - 0.976
MAD ± SD	2.4° ± 2.3°	1.2° ± 0.9°	1.4° ± 1.1°	7.4 ± 5.2 mm	6.0 ± 5.8 mm



(a) 3D view

(b) PA view

(c) PMC view

Figure 6.3 a) 3D reconstructed spinal image with emulated spinous processes; b) The determination of end vertebrae, apex, the AVR, the Cobb angles, and the lateral deviation on the PA view; c) The determination of end vertebrae, apex, the AVR, the Cobb angles, and the lateral deviation on the PMC view.

The correlations between the measurements of the scan and that of the rescan for these five measurements are also illustrated in Figures 6.4 - 6.8. Most of the measurements for each parameter gather close to each other around and on the linear line with high r^2 values being 0.91, 0.97, 0.96, 0.82, and 0.90 for the AVR, the Cobb angles and the lateral deviations on the PA plane and the PMC, respectively.

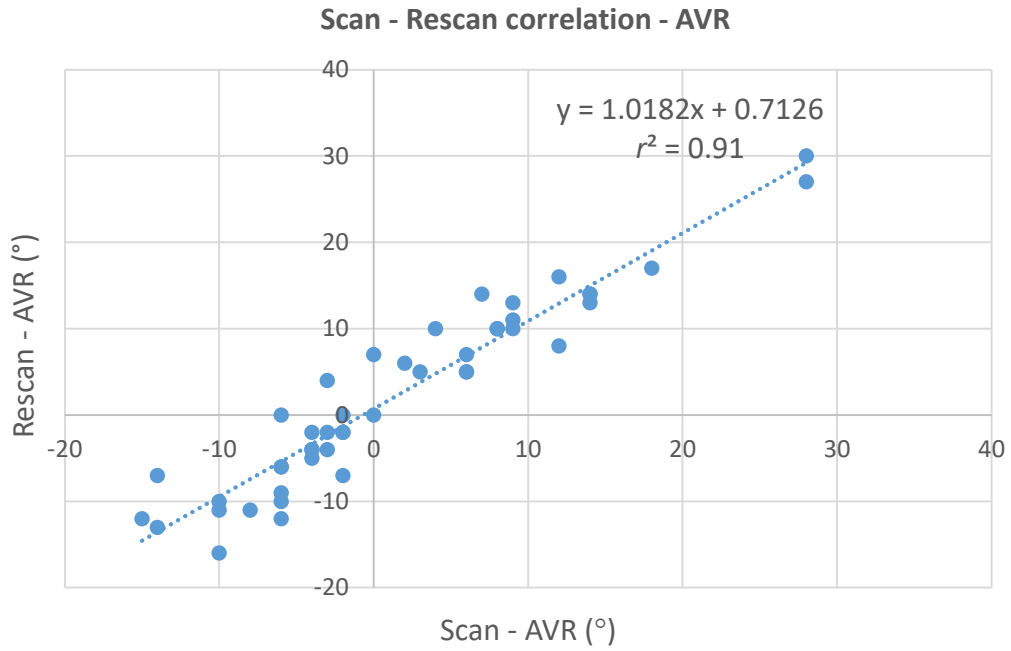


Figure 6.4 The correlation of the AVR measurements between the scan and the rescan.

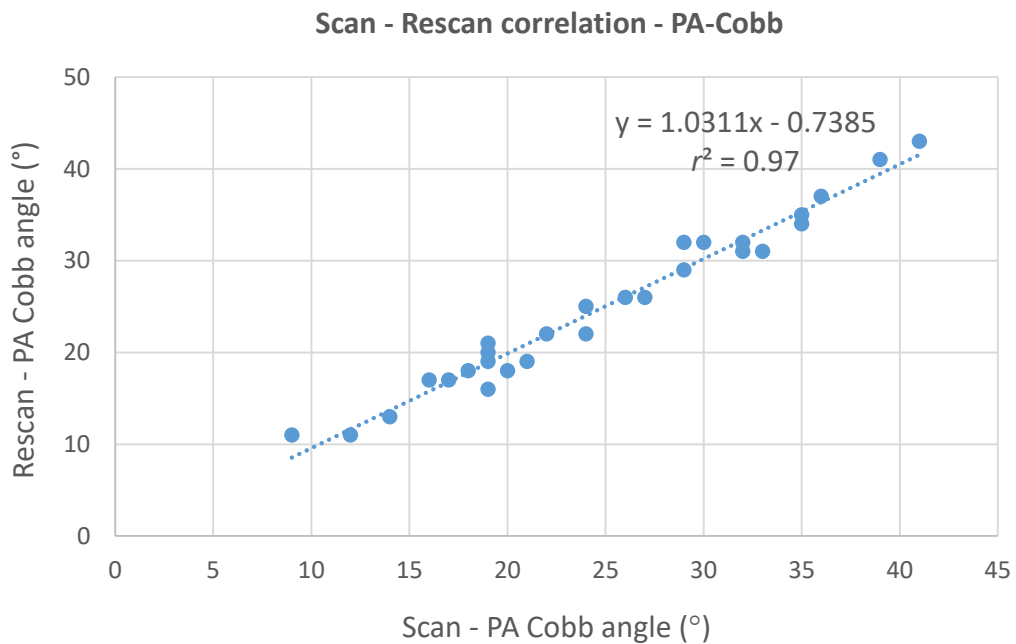


Figure 6.5 The correlation of the PA Cobb angle measurements between the scan and the rescan.

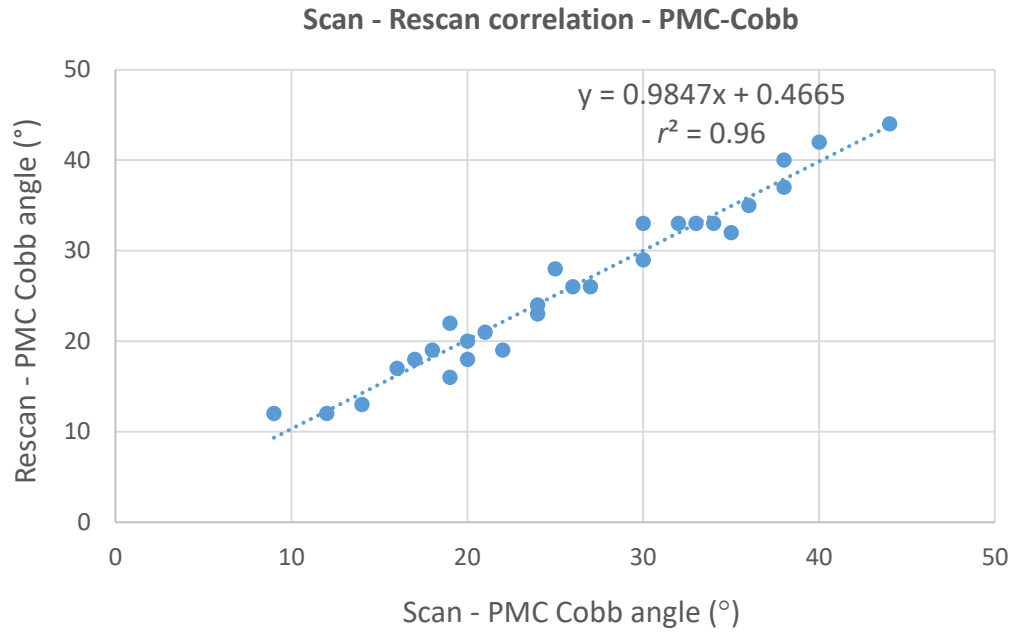


Figure 6.6 The correlation of the PMC Cobb angle measurements between the scan and the rescan.

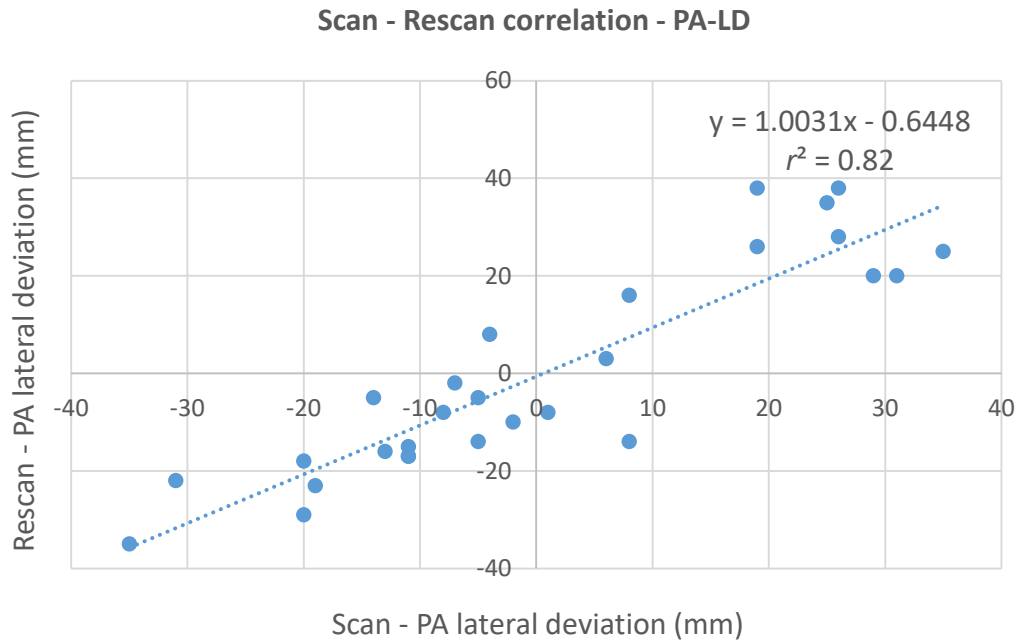


Figure 6.7 The correlation of the PA lateral deviation measurements between the scan and the rescan.

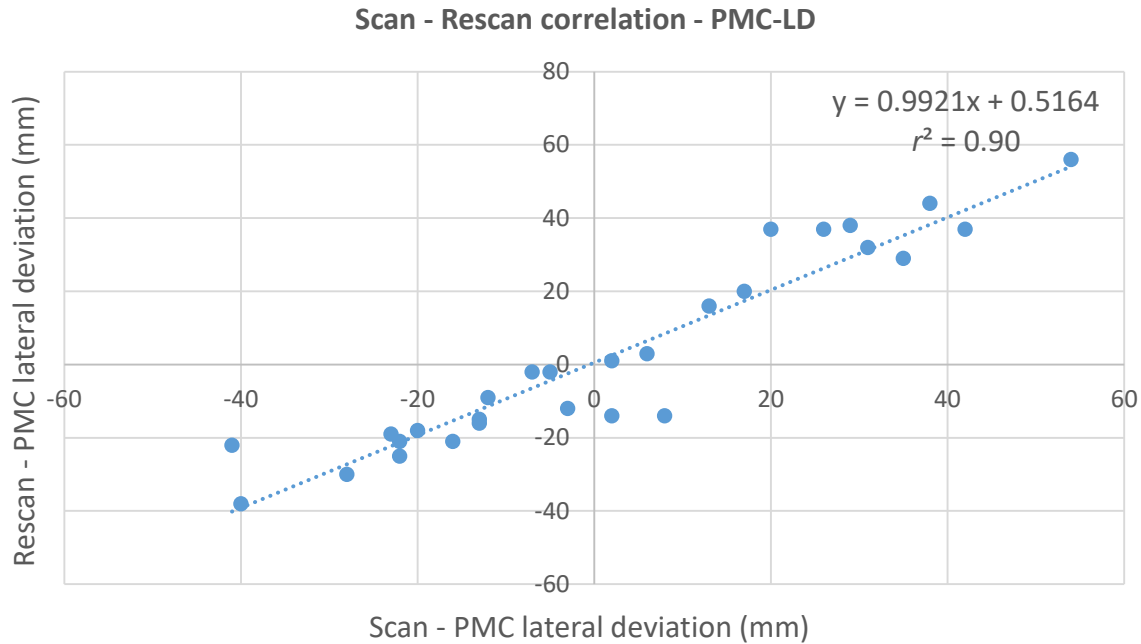


Figure 6.8 The correlation of the PMC lateral deviation measurements between the scan and the rescan.

Figure 6.9 shows the Bland-Altman plot indicating the differences in the AVR measurements between the first scan and the second scan. The AVR measurements had two outliers and 95% of the differences fell within the ranges of $-0.7^\circ \pm 6.6^\circ$ (Mean \pm 2SD). Meanwhile, 100% of the differences in the PA and PMC Cobb angles were within $0.0^\circ \pm 3.1^\circ$ and $-0.1^\circ \pm 3.6^\circ$, respectively, indicating small variations between the two repetitions (Figure 6.10 and Figure 6.11). Figure 6.12 and Figure 6.13 demonstrate the Bland-Altman plots indicating the differences in the PA and PMC lateral deviation measurements between the first scan and the second scan. For each of these two parameters, 26 out of 28 values were within the range of Mean \pm 2SD ($0.6^\circ \pm 18.2^\circ$ and $-0.5^\circ \pm 16.8^\circ$ for the PA and PMC lateral deviations, respectively).

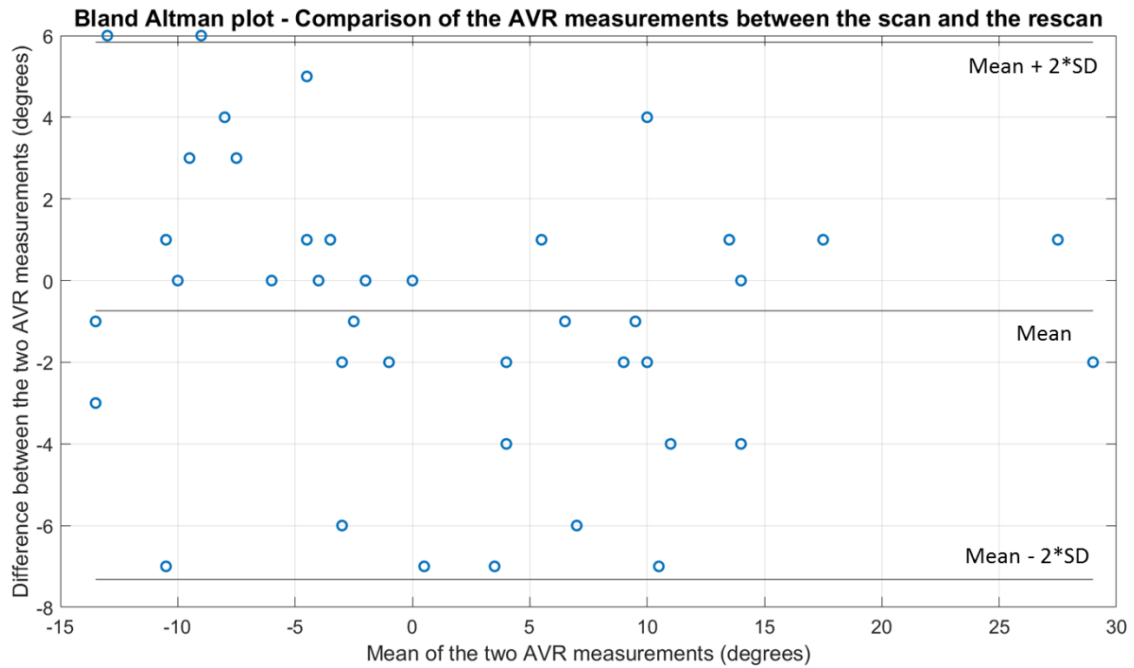


Figure 6.9 The Bland-Altman plot - A comparison of the AVR measurements between the scan and the rescan.

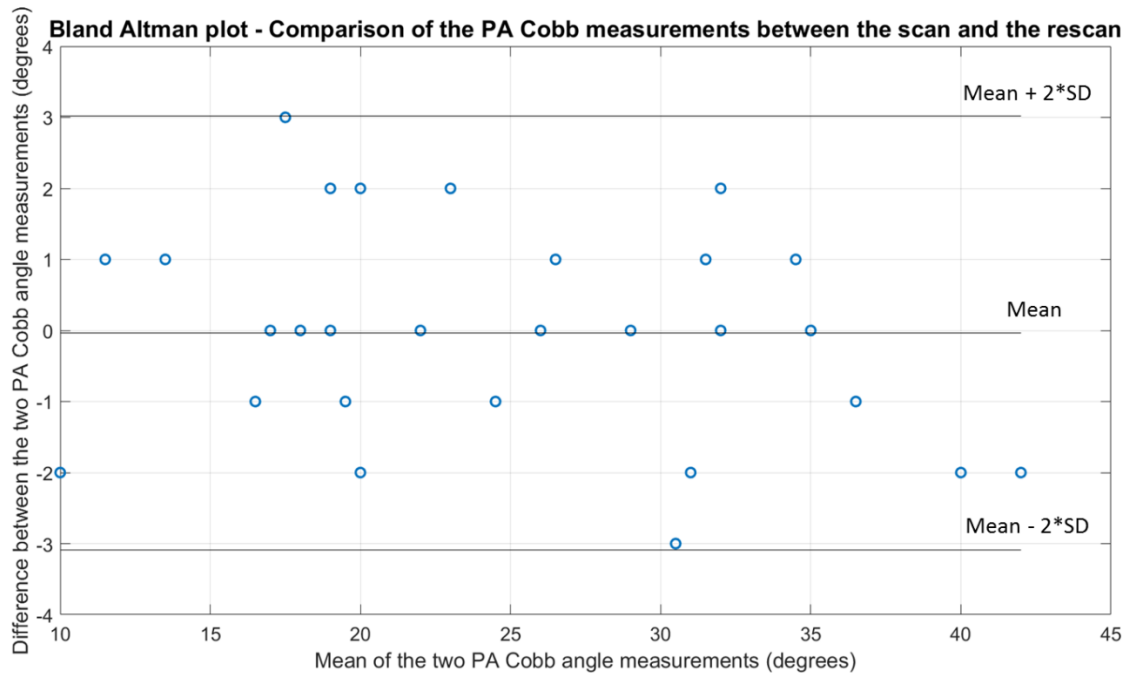


Figure 6.10 The Bland-Altman plot - A comparison of the PA Cobb angle measurements between the scan and the rescan.

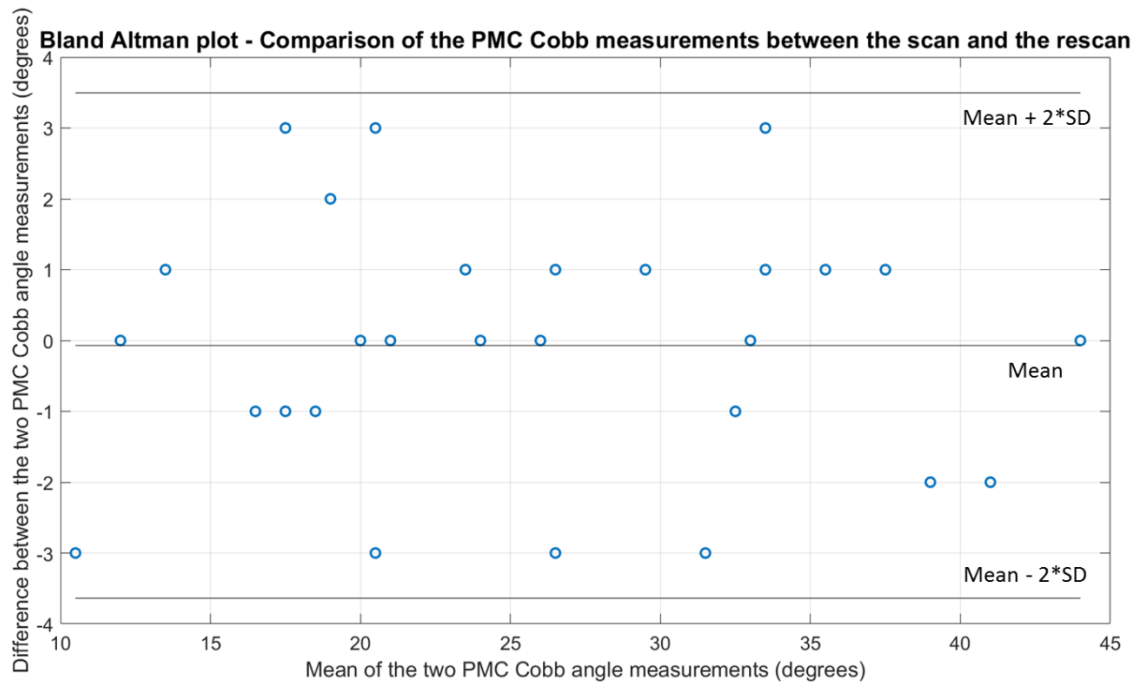


Figure 6.11 The Bland-Altman plot - A comparison of the PMC Cobb angle measurements between the scan and the rescans.

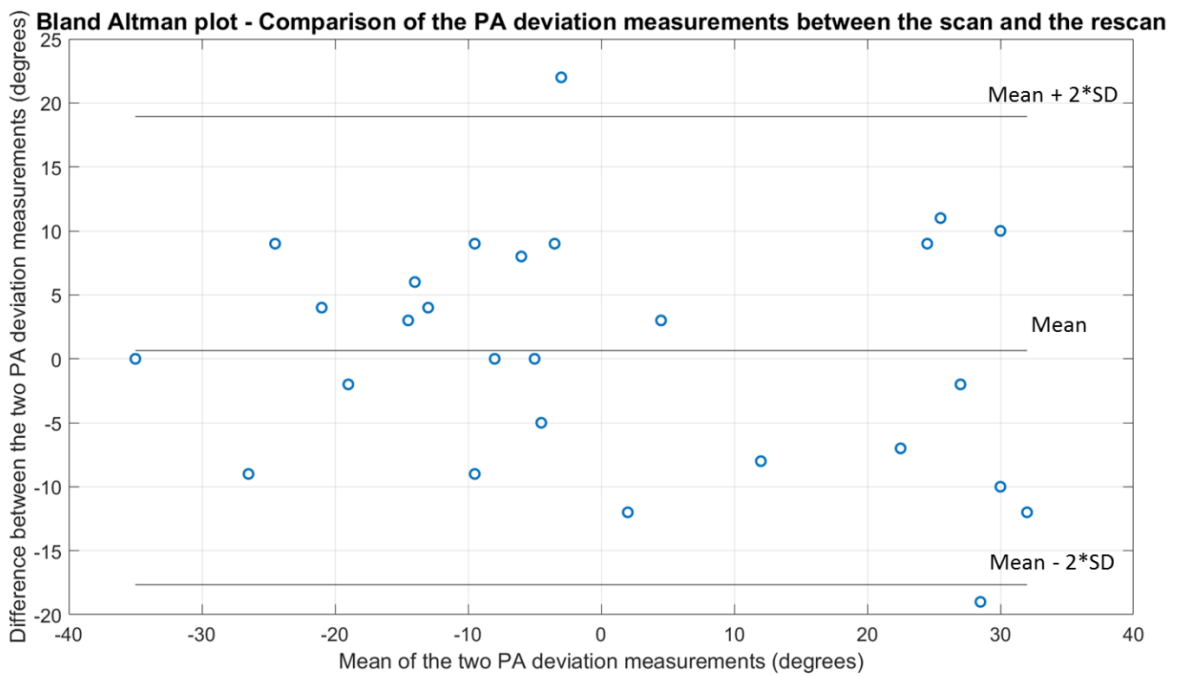


Figure 6.12 The Bland-Altman plot - A comparison of the PA lateral deviation measurements between the scan and the rescans.

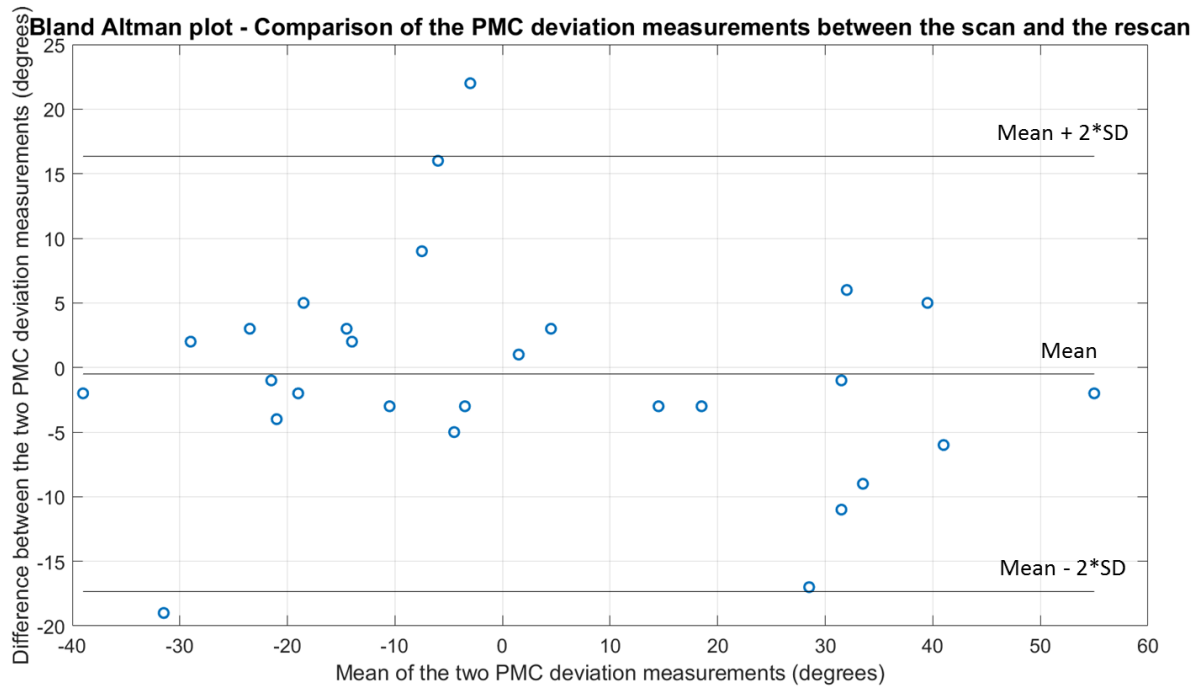


Figure 6.13 The Bland-Altman plot - A comparison of the PMC lateral deviation measurements between the scan and the rescan.

6.1.4 Discussion

The COL method has been previously used to measure the proxy Cobb angle from ultrasound images (Chen *et al.*, 2013). The MAD of the Cobb angle between the COL method and the traditional Cobb method for that pilot study was $0.7^\circ \pm 0.5^\circ$, indicating that the COL method might be appropriate to approximate the proxy Cobb angle. The MAD of the AVR was $2.4^\circ \pm 2.3^\circ$. This value was smaller than the reported values in literature ($5^\circ - 7^\circ$). The MADs in the measurements of the Cobb angle on both PA and PMC views were less than 2° , which was smaller than the clinically acceptance error of 5° . Hence, the measurements of the scan and the rescan agreed well to each other, indicating that the ultrasound method could be repeatable.

In the *in-vitro* study, the AVR was measured on the 3D image. However, in the *in-vivo* study, the measurement of the AVR was based the 2D image because of the following explanation. There was no difference between both AVR measuring methods. In the *in-vitro* study, the phantom was covered by only water, which is a homogeneous material. There was a

strong reflection of the ultrasound energy at the bone interface back to the probe. Therefore, the *in-vitro* 3D image contained two clearly distinguished portions: bone and water. The filtering process easily eliminated the water layer and left the bone in the reconstructed image. As a result, the image was clear, leading to easy and precise identification of the COL. In contrast, vertebrae in *in-vivo* cases were covered by inhomogeneous soft tissues. It was impossible for the filtering process to remove completely the soft tissues, leaving bone structures only. When the COL was selected on the 3D image, the selection point might not fall perfectly on the bone surface, but it might fall on a soft tissue instead. Therefore, an error might occur on the y-coordinate of the lamina, leading to a wrong result of the AVR. To avoid this situation, the COLs were selected on the PA image instead of the 3D image. When a COL was selected on the 2D image, its x- and y-coordinates were known and mapped as x- and z-coordinates of that lamina on the 3D image, respectively. The y-coordinate of the COL on the 3D image was unknown and identified by searching all voxels having the brightest intensity value along the y-axis (x known, y unknown, z known). The y-coordinate could be fine-tuned to obtain a proper position on the transverse view. Thus, the selected COL on the 2D image was mapped to the 3D coordinate system as if it was selected right on the 3D image.

In this ultrasound approach, vertebra L5 was used as a reference for the measurements of the AVR and the lateral deviation. Vertebra L5 is located in the lumbar region, which contains a great deal of noise because of thick muscles; therefore, it is hard to be recognized. The correct selection of vertebra L5 is of importance because it may affect the Cobb angle measurement if the end vertebra is L5, and it directly influences the measurements of the AVR and the lateral deviations on the PA and the PMC. Thus, care should be put into the selection of vertebra L5.

6.1.5 Conclusion

This section described the methods to measure the AVR, the Cobb angle and the maximum lateral deviation on both of the PA plane and the PMC. From the results, it demonstrated that the ultrasound scanning method was repeatable and reliable as the ICC value of all 5 measured parameters between scan and rescan was greater than 0.90.

6.2 Reliability of the measurement of the AVR, the Cobb angles, and the lateral deviations

To determine the reliability of the measurements of the 5 measured parameters, a study that involved 2 raters in measuring the same ultrasound scans (scan + rescan) in 2 different sessions was conducted. The intra- and inter-rater reliabilities and the error indices of selecting end-plate vertebrae were analyzed.

6.2.1 Methods

The same dataset acquired in sections 6.1.1 and 6.1.2 were reused in this reliability study. Two raters, Raters 1 and 2, who both had two years of experience in measuring Cobb angles and AVR on ultrasound spinal images participated in this study. Rater 1 was the 3DSA software developer, who was familiar with the function of the software. Rater 2 was naïve to the software, but she was trained until she felt confident to measure the 5 parameters. Both raters measured the 21 images twice with 1 week apart to obtain 4 sets of measurements from each rater (Figure 6.14). The MS11 was the **M**asurement from the **S**can from Rater **1** on the **1**st session. The MRs11 was the **M**asurement from the **R**escan from Rater **1** on the **1**st session. Similarly,

- The MS12 was the **M**asurement from the **S**can from Rater **1** on the **2**nd session.
- The MRs12 was the **M**asurement from the **R**escan from Rater **1** on the **2**nd session.
- The MS21 was the **M**asurement from the **S**can from Rater **2** on the **1**st session.
- The MS22 was the **M**asurement from the **S**can from Rater **2** on the **2**nd session.
- The MRs21 was the **M**asurement from the **R**escan from Rater **2** on the **1**st session.
- The MRs22 was the **M**asurement from the **R**escan from Rater **2** on the **2**nd session.

Figure 6.14 also illustrates how these datasets were processed to extract measurements that were in common for comparisons. Rater 1 detected 28 curves while Rater 2 identified 29 curves from the ultrasound images. However, only 26 curves that were commonly detected by both raters were extracted and used. Each dataset with apostrophe (MS11', MS12',, MRs22') were extracted from the original dataset (MS11, MS12,, MRs22), respectively, and included 26 common curves. To double the sample size of measurements, the extracted

datasets were combined such that $MS_{11}' + MR_{s11}' = M_{11}$, $MS_{12}' + MR_{s12}' = M_{12}$, $MS_{21}' + MR_{s21}' = M_{21}$, and $MS_{22}' + MR_{s22}' = M_{22}$. These 4 new datasets contained 52 curves.

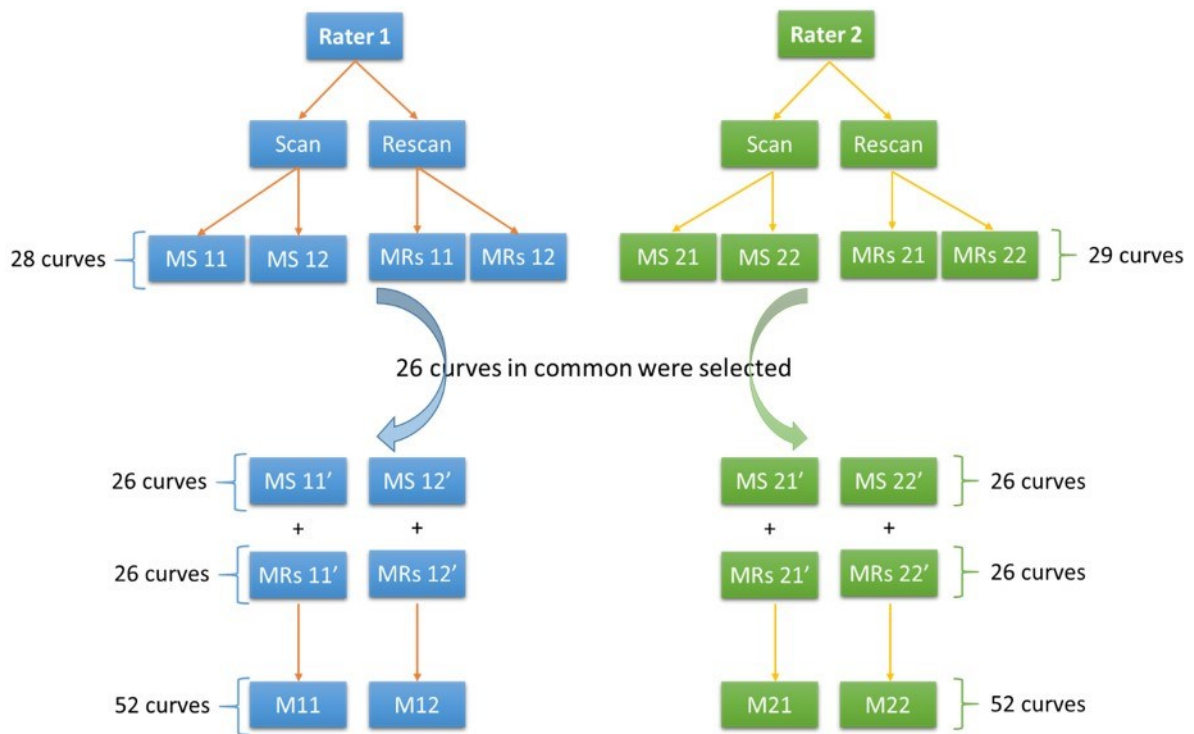


Figure 6.14 A flowchart of the procedure to select the measurements from Rater 1 and Rater 2 for comparisons.

For the intra-rater reliability, the first session of measurements was compared with the second session of measurements on both raters (M11 versus M12, and M21 versus M22). To determine the inter-rater reliability, the second sessions of measurements of both raters were compared (M12 versus M22). To compare the AVR between two sessions of measurement, the rotations of the apical vertebra and its two adjacent vertebrae were recorded. As previously mentioned in section 6.1.2, only the measurements of the AVR recorded at the same levels between the two sessions of measurement were compared. A total of 92 apical vertebrae that appeared in both sets of 26 measurements by both raters were recorded and compared.

The results of comparison were evaluated using the intra-class correlation coefficients with two-way random and absolute agreement ICC(2,1), the mean absolute difference and standard

deviation (MAD ± SD), and the standard error of measurement (SEM). In addition, an error index (EI) that reported a difference in selections of upper and lower end vertebrae between two sessions of measurements was also calculated as follows (Oda *et al.*, 1982):

$$Error\ index = \frac{1}{n} \cdot \sum_{i=1}^n \sqrt{(U_1 - U_2)^2 + (L_1 - L_2)^2}$$

where n is the number of images read by the rater, and U_1 , U_2 , L_1 , L_2 are the first and the second readings of the upper end and the lower end vertebra, respectively. The smaller the error index, the better the result.

Furthermore, the differences of the AVR, the Cobb angle and the lateral deviation on the PA plane and the PMC between the two sessions of measurements were graphically illustrated by the Bland-Altman plots.

6.2.2 Results

Intra-rater reliability

The intra-rater reliabilities of the 5 parameters by Rater 1 and Rater 2 are listed in Table 6.2 and Table 6.3, respectively. The ICC values for all parameters and both raters were greater than 0.90, indicating very high intra-rater reliabilities. There was no significant difference in the measurement of the AVR between Rater 1 and Rater 2 with the MADs, SDs, and SEMs less than 3°. The MADs for the PA and PMC Cobb angles were less than 1.5° while their SDs and SEMs were approximately 1°. The measurement of the lateral deviations on both the PA plane and the PMC for both raters had small MADs of approximately 3.0 mm.

Table 6.2 *Intra-rater reliabilities of the 5 parameters by Rater 1.*

	Apical AVR	PA-Cobb	PMC-Cobb	PA-LD	PMC-LD
ICC	0.935	0.989	0.986	0.980	0.985
95% CI	0.903 - 0.957	0.980 - 0.993	0.976 - 0.992	0.966 - 0.989	0.974 - 0.991
MAD ± SD	2.6° ± 2.7°	0.9° ± 0.9°	1.1° ± 1.1°	3.0 ± 2.8 mm	3.0 ± 3.5 mm
SEM*	2.6°	0.9°	1.1°	3.0 mm	3.2 mm

* Calculated using the standard deviation of the second session of measurements (M12).

Table 6.3 Intra-rater reliabilities of the 5 parameters by Rater 2.

	Apical AVR	PA-Cobb	PMC-Cobb	PA-LD	PMC-LD
ICC	0.929	0.973	0.975	0.990	0.991
95% CI	0.894 - 0.952	0.953 - 0.984	0.956 - 0.985	0.982 - 0.994	0.984 - 0.995
MAD ± SD	2.8° ± 2.7°	1.5° ± 1.2°	1.5° ± 1.3°	2.2 ± 2.5 mm	2.8 ± 2.4 mm
SEM*	2.8°	1.3°	1.4°	2.1 mm	2.5 mm

* Calculated using the standard deviation of the second session of measurements (M22).

Figures 6.15 - 6.19 show the scatter plots depicting correlations of the 5 parameters measured by Rater 1. All the r^2 values were high at 0.88, 0.98, 0.97, 0.96, and 0.97 for the AVR, the PA and PMC Cobb angles, the PA and PMC lateral deviations, respectively. Meanwhile, Figures 6.20 - 6.24 show the correlations between the two sessions of measurements of these five parameters from Rater 2. All r^2 values were greater than 0.90 except for the AVR where the $r^2 = 0.86$, indicating high correlations between the two sessions of measurements.

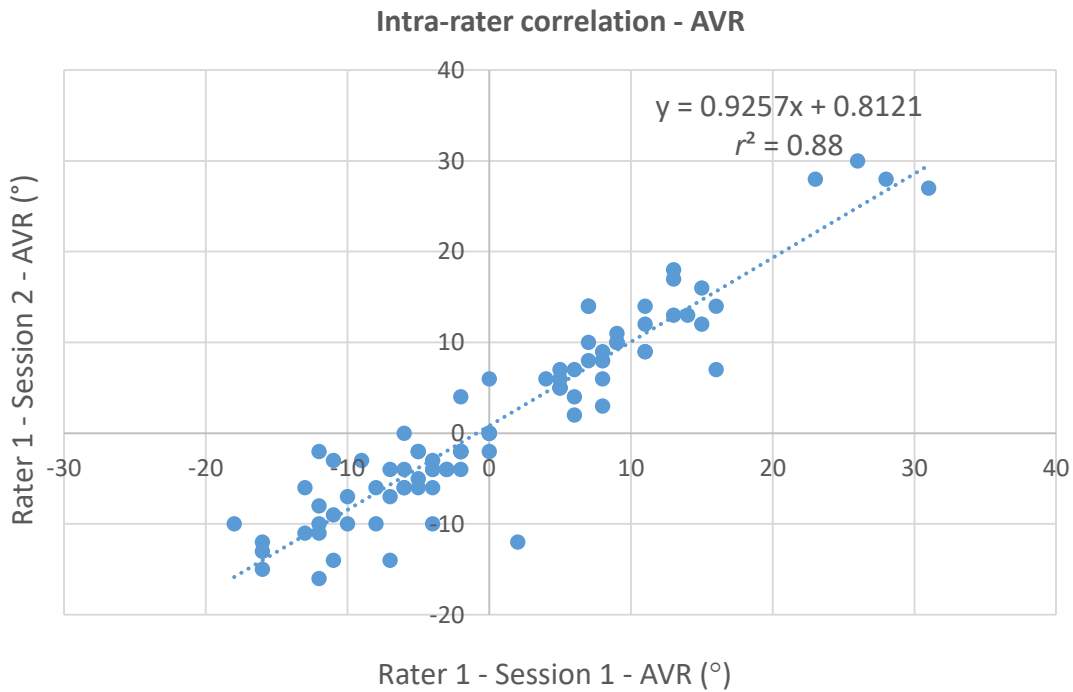


Figure 6.15 The intra-rater correlation of the AVR measurements (Rater 1).

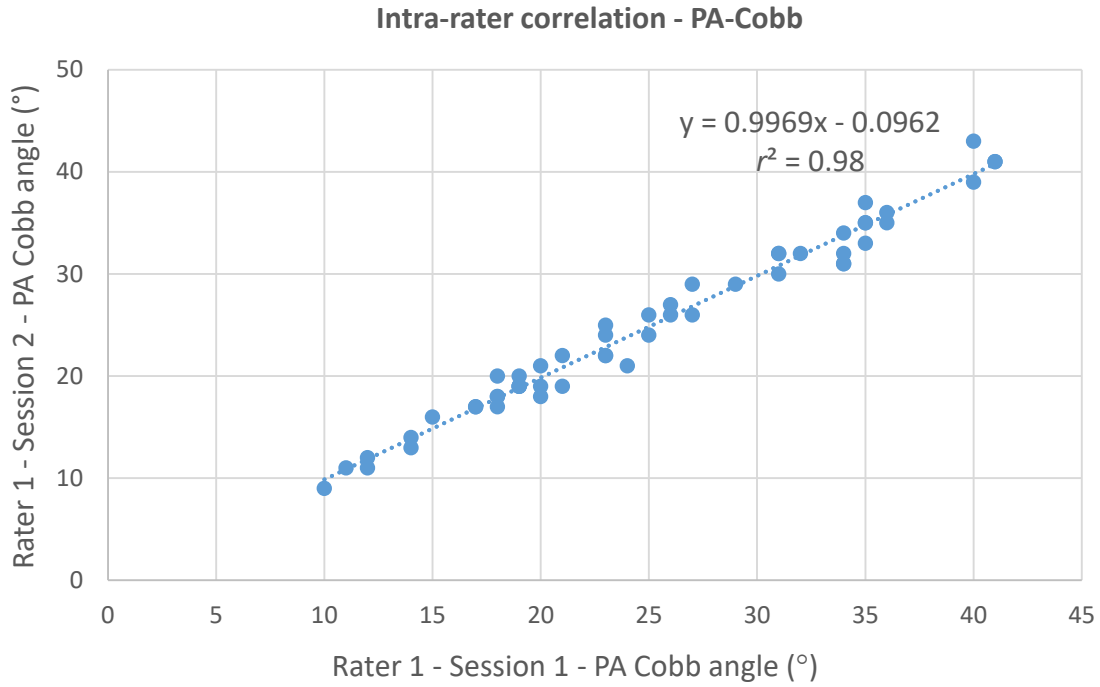


Figure 6.16 The intra-rater correlation of the PA Cobb angle measurements (Rater 1).

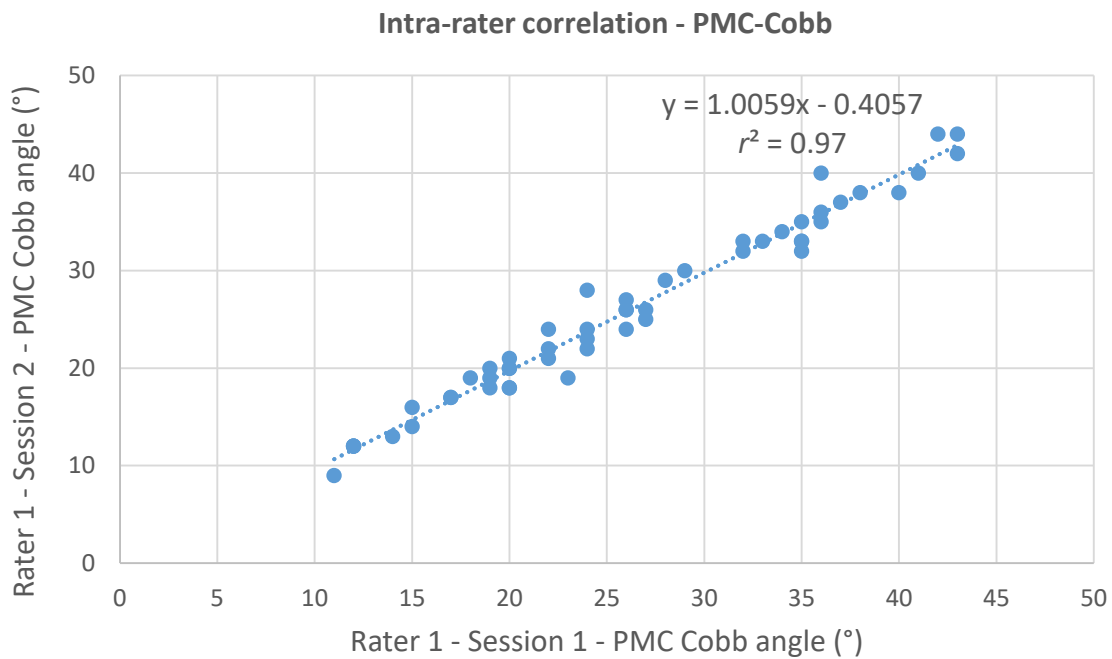


Figure 6.17 The intra-rater correlation of the PMC Cobb angle measurements (Rater 1).

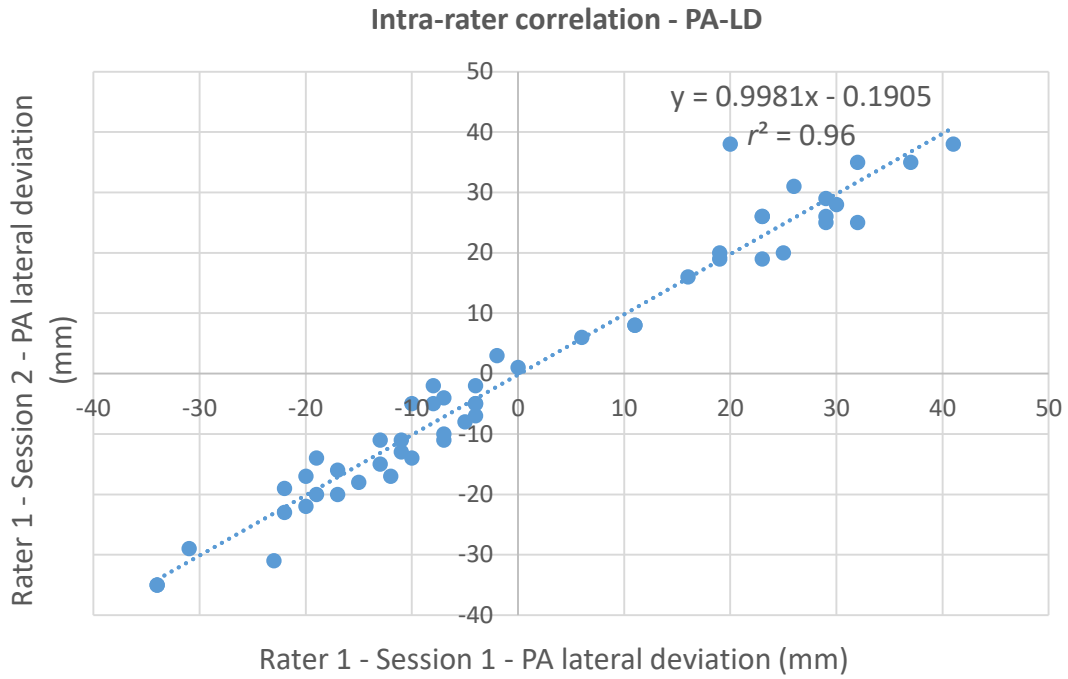


Figure 6.18 The intra-rater correlation of the PA lateral deviation measurements (Rater 1).

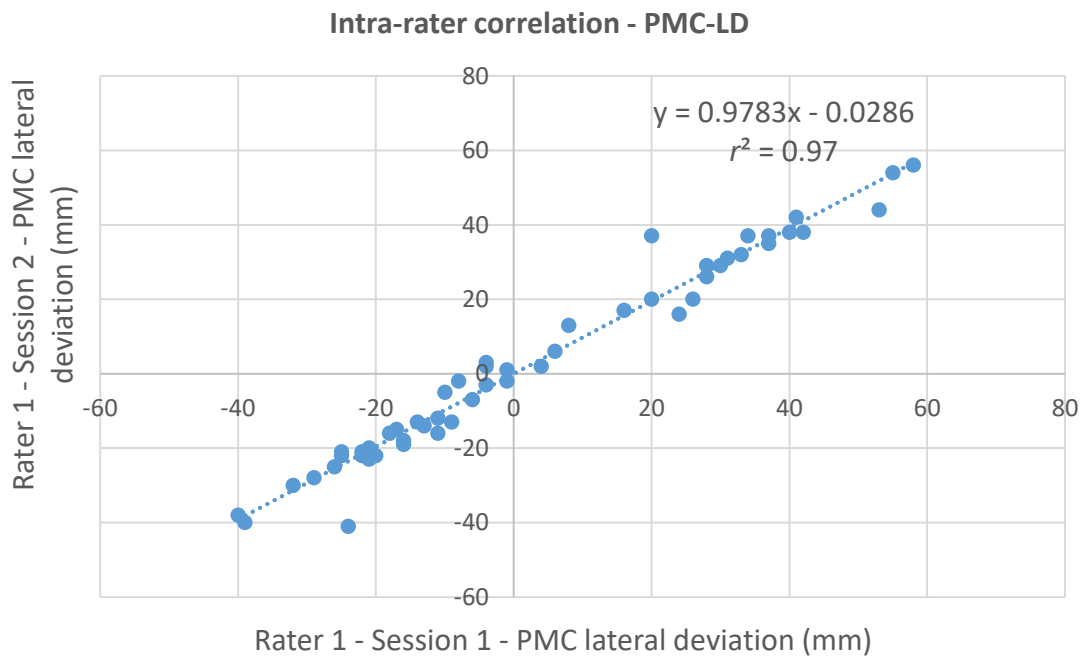


Figure 6.19 The intra-rater correlation of the PMC lateral deviation measurements (Rater 1).

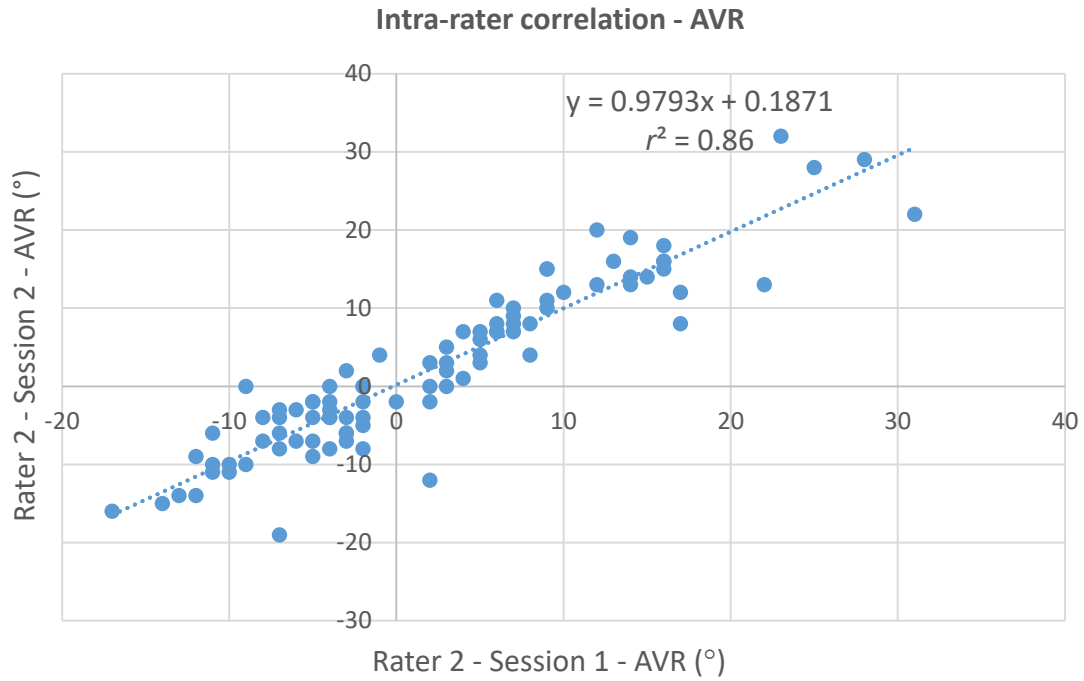


Figure 6.20 The intra-rater correlation of the AVR measurements (Rater 2).

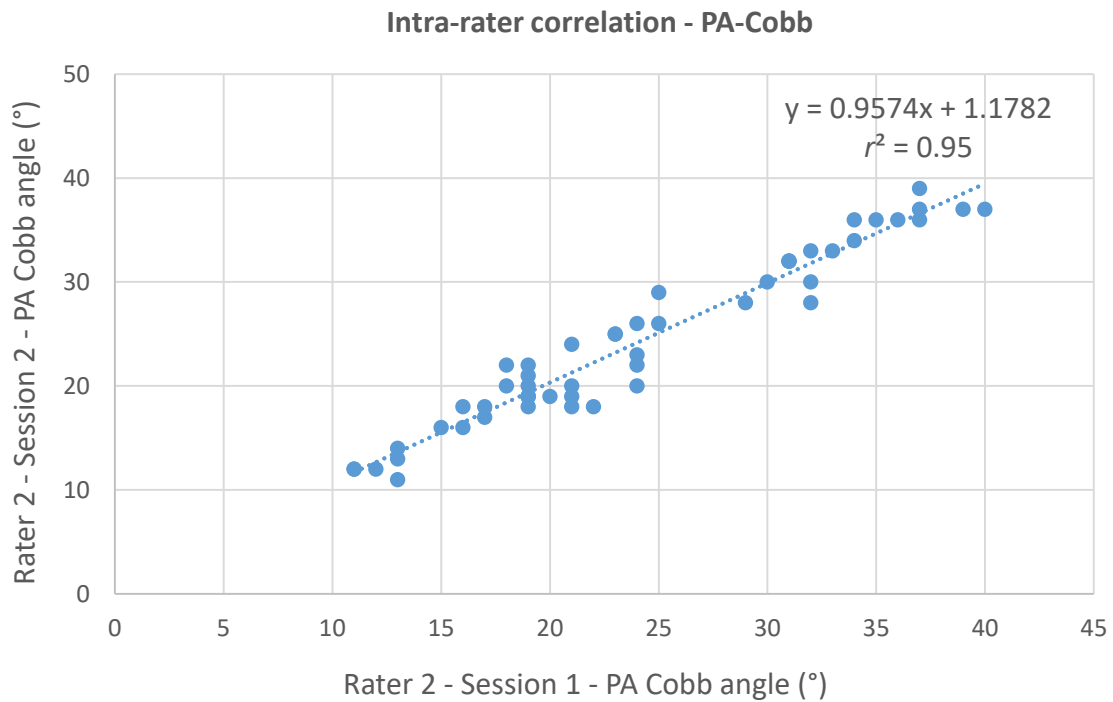


Figure 6.21 The intra-rater correlation of the PA Cobb angle measurements (Rater 2).

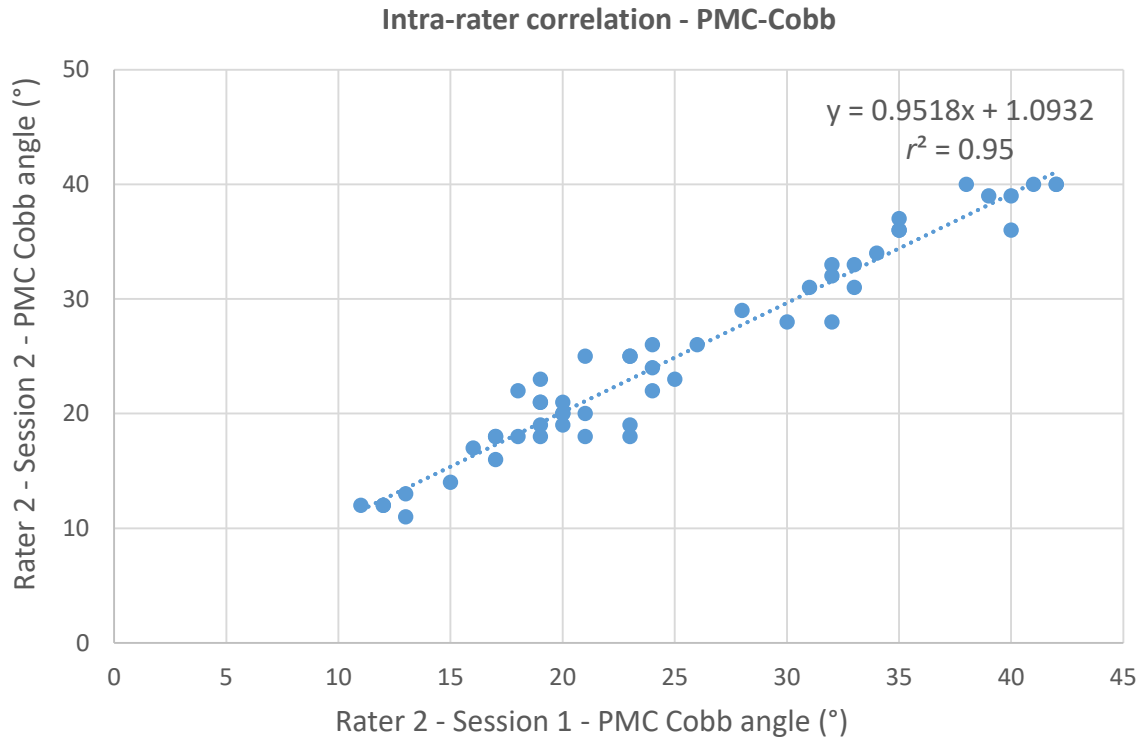


Figure 6.22 The intra-rater correlation of the PMC Cobb angle measurements (Rater 2).

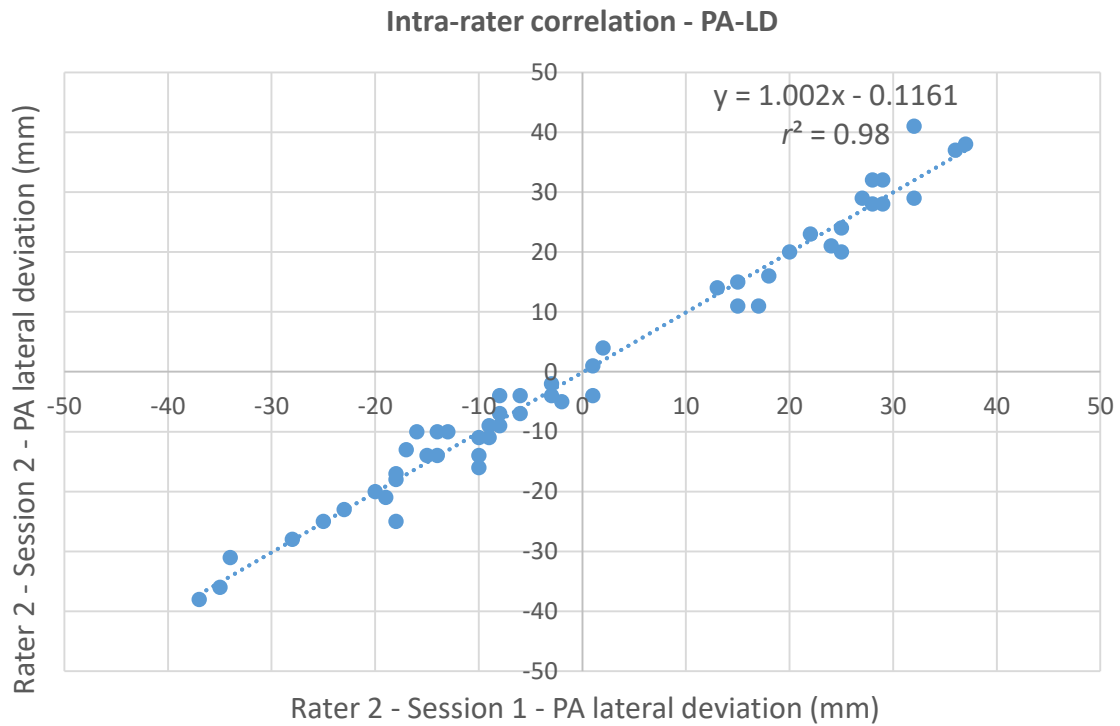


Figure 6.23 The intra-rater correlation of the PA lateral deviation measurements (Rater 2).

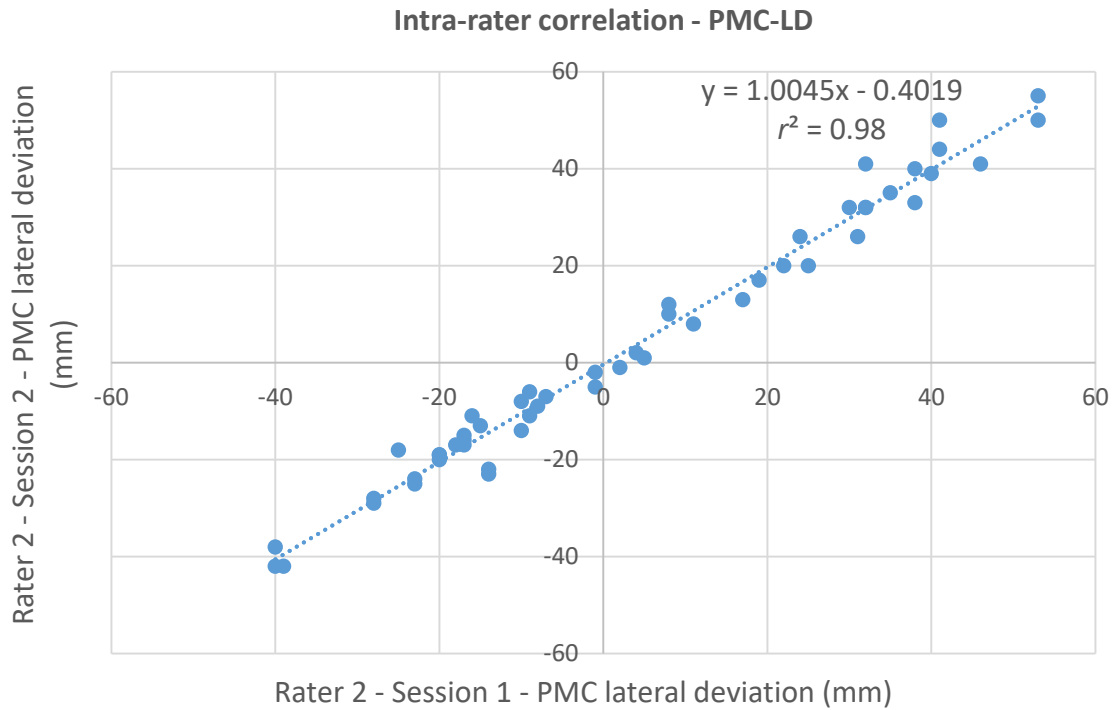


Figure 6.24 The intra-rater correlation of the PMC lateral deviation measurements (Rater 2).

Table 6.4 reports the Pearson's r and the difference between the PA and PMC Cobb angles by Rater 1 and Rater 2. All the correlation coefficients were greater than 0.99, indicating a high correlation between the PA and PMC Cobb angles measured by both raters. The differences between the two Cobb angles were positive, indicating that in all cases, the PMC Cobb angles were always equal to or greater than the PA Cobb angles. On average, the PMC Cobb angle were 1° larger than the PA Cobb angle.

Table 6.4 The Pearson's r and the difference between the PA and PMC Cobb angles by Rater 1 and Rater 2.

	Rater 1		Rater 2	
	M11	M12	M21	M22
r	0.994	0.996	0.992	0.991
MAD \pm SD	$1.0^\circ \pm 1.1^\circ$	$0.9^\circ \pm 0.9^\circ$	$1.0^\circ \pm 1.3^\circ$	$0.8^\circ \pm 1.3^\circ$
Difference*	0 - 5°	0 - 3°	0 - 6°	0 - 7°

*Difference = the PMC Cobb angle - the PA Cobb angle

Inter-rater reliability

Table 6.5 summarizes the inter-rater reliability of the 5 parameter between Rater 1 and Rater 2. All the ICC[2,1] values showed high inter-rater reliability (> 0.93). The MAD \pm SD value of the AVR measurements were $2.5^\circ \pm 2.6^\circ$ while MAD \pm SD values were $1.9^\circ \pm 2.4^\circ$ and $2.2^\circ \pm 2.5^\circ$ for the PA and PMC Cobb angles, respectively. Meanwhile, these values varied between 2.7 ± 2.0 mm and 3.3 ± 2.8 mm for the PA and PMC lateral deviations, respectively.

Table 6.5 *Inter-rater reliability of the 5 parameter between Rater 1 and Rater 2.*

	AVR	PA-Cobb	PMC-Cobb	PA-LD	PMC-LD
ICC	0.939	0.935	0.932	0.987	0.987
95% CI	0.910 - 0.959	0.888 - 0.963	0.880 - 0.961	0.978 - 0.993	0.978 - 0.993
MAD \pm SD	$2.5^\circ \pm 2.6^\circ$	$1.9^\circ \pm 2.4^\circ$	$2.2^\circ \pm 2.5^\circ$	2.7 ± 2.0 mm	3.3 ± 2.8 mm
SEM*	2.6°	2.0°	2.3°	2.4 mm	3.0 mm

* Calculated using the standard deviation of the measurements by Rater 2

Figures 6.25 - 6.29 illustrate the inter-rater correlations of the AVR, the Cobb angles and the lateral deviations on the PA plane and the PMC between Rater 1 and Rater 2. It can be seen that the inter-rater correlations were not as linear as the intra-rater correlations with the r^2 values being 0.88, 0.89, 0.88, 0.98, and 0.97 for the AVR, the PA and PMC Cobb angles, the PA and PMC lateral deviations, respectively. More points are offset from the linear line in the graphs of the AVR, the PA and PMC Cobb angles.

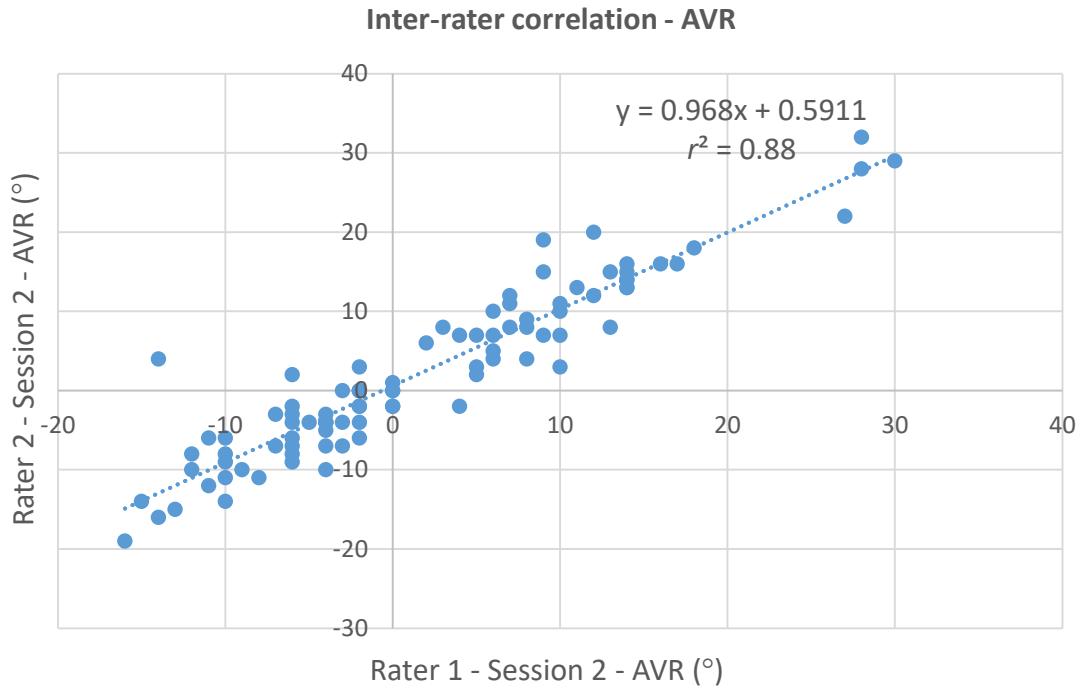


Figure 6.25 The inter-rater correlation of the AVR measurements between Rater 1 and Rater 2.

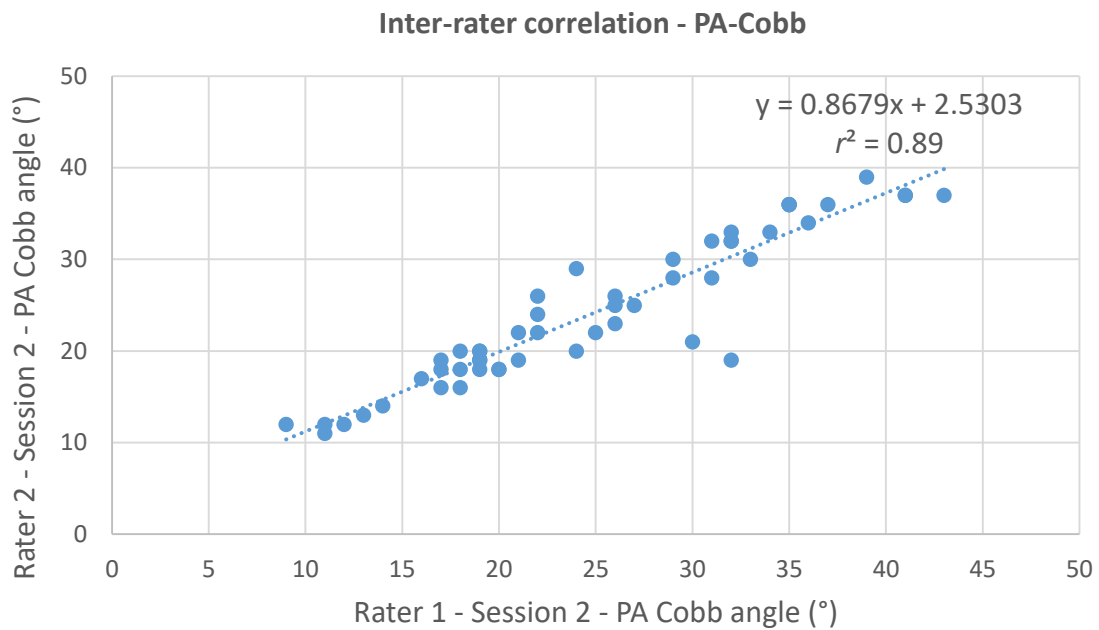


Figure 6.26 The inter-rater correlation of the PA Cobb angle measurements between Rater 1 and Rater 2.

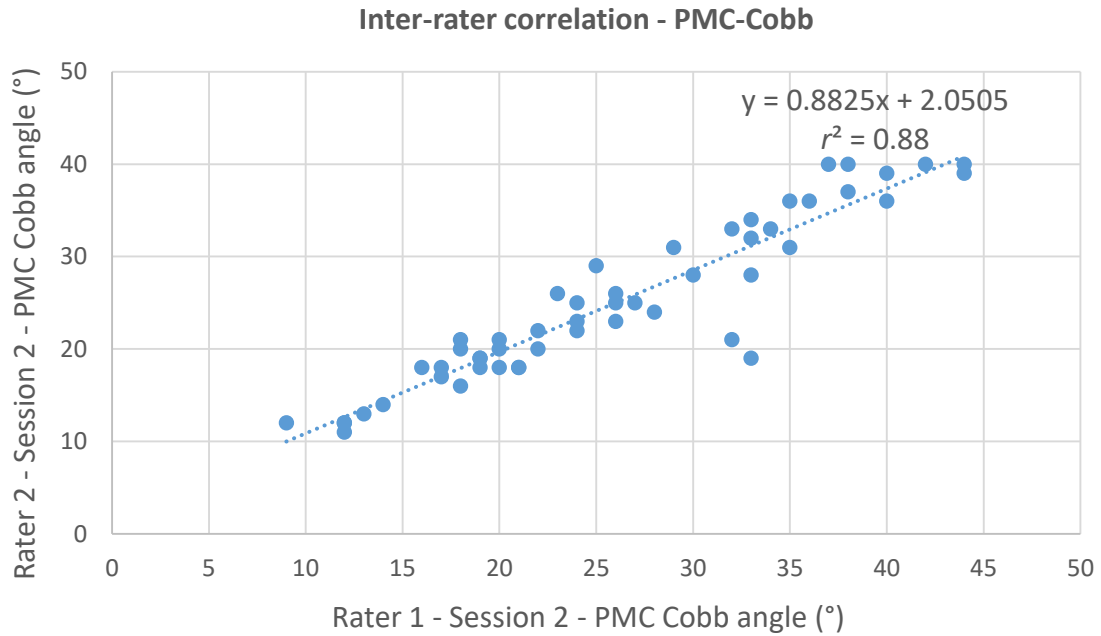


Figure 6.27 The inter-rater correlation of the PMC Cobb angle measurements between Rater 1 and Rater 2.

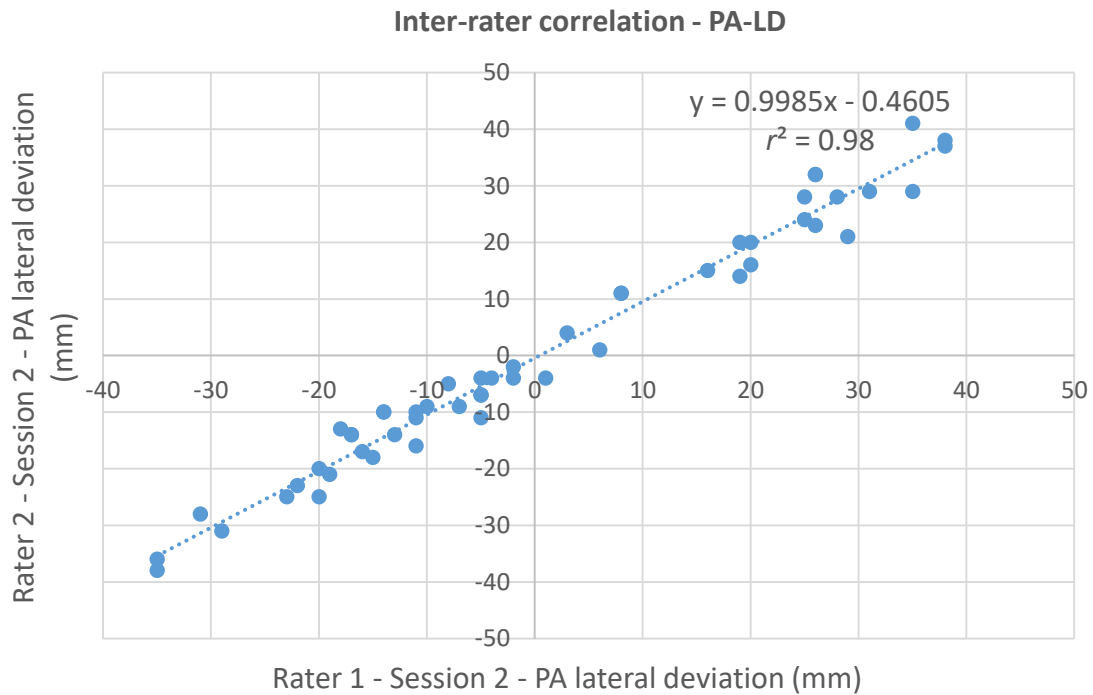


Figure 6.28 The inter-rater correlation of the PA lateral deviation measurements between Rater 1 and Rater 2.

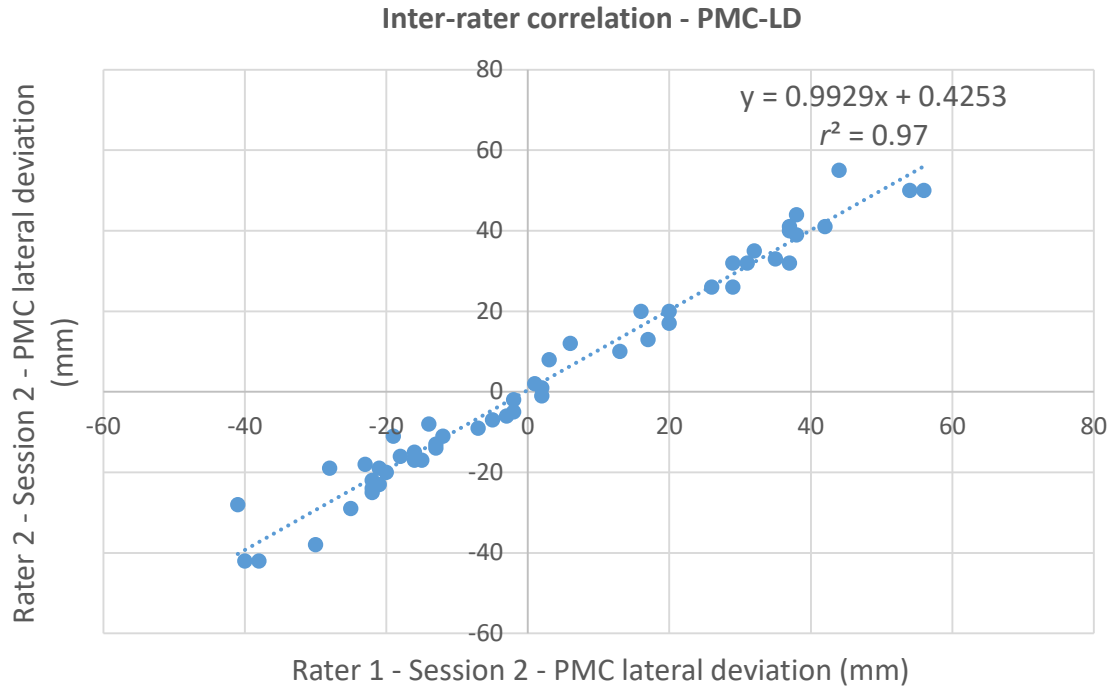


Figure 6.29 The inter-rater correlation of the PMC lateral deviation measurements between Rater 1 and Rater 2.

Figures 6.30 - 6.34 show the Bland-Altman Plots demonstrating the discrepancies in the measurements of the AVR, the PA and PMC Cobb angles, and the PA and PMC lateral deviations between the two raters, respectively. Eighty-seven of 92 AVR values were within the 95% confident interval of $-0.5^\circ \pm 7.2^\circ$ (Mean \pm 2SD). Fifty of 52 PA Cobb angles and the same number for the PMC Cobb angles fell within the ranges of $0.8^\circ \pm 5.8^\circ$ and $1.0^\circ \pm 6.4^\circ$, respectively. Meanwhile, over 95% of the values of the PA and PMC lateral deviations fell within the ranges of 0.5 ± 6.6 mm and -0.4 mm \pm 8.6 mm, respectively.

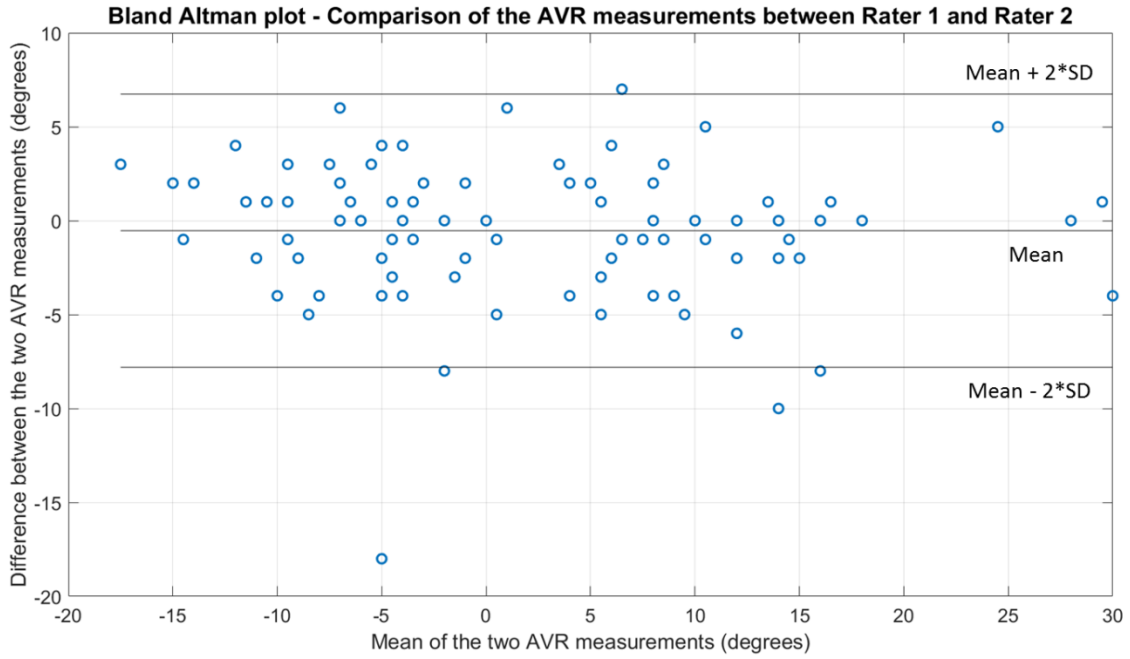


Figure 6.30 The Bland-Altman plot - A comparison of the AVR measurements between Rater 1 and Rater 2.

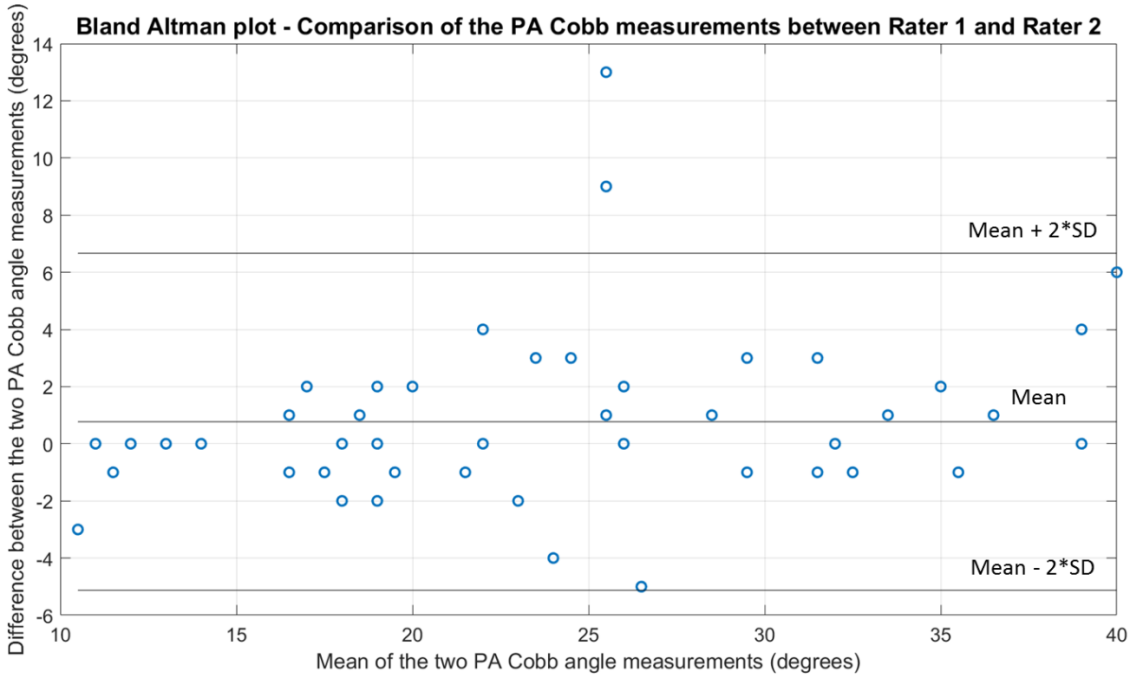


Figure 6.31 The Bland-Altman plot - A comparison of the PA Cobb angle measurements between Rater 1 and Rater 2.

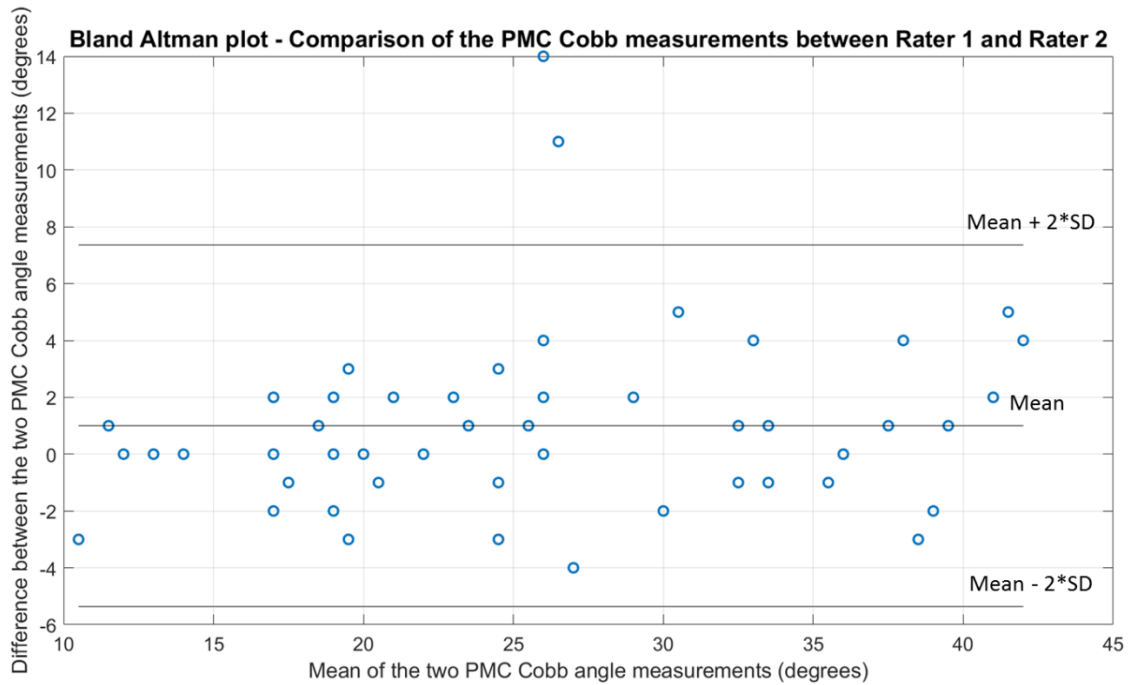


Figure 6.32 The Bland-Altman plot - A comparison of the PMC Cobb angle measurements between Rater 1 and Rater 2.

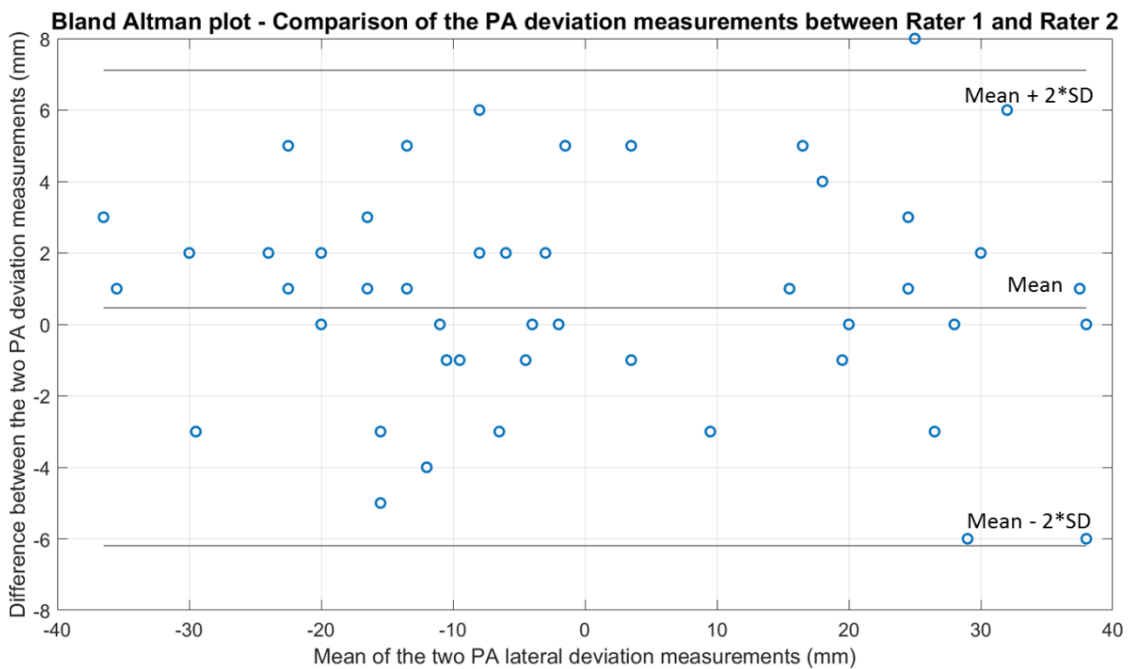


Figure 6.33 The Bland-Altman plot - A comparison of the PA lateral deviation measurements between Rater 1 and Rater 2.

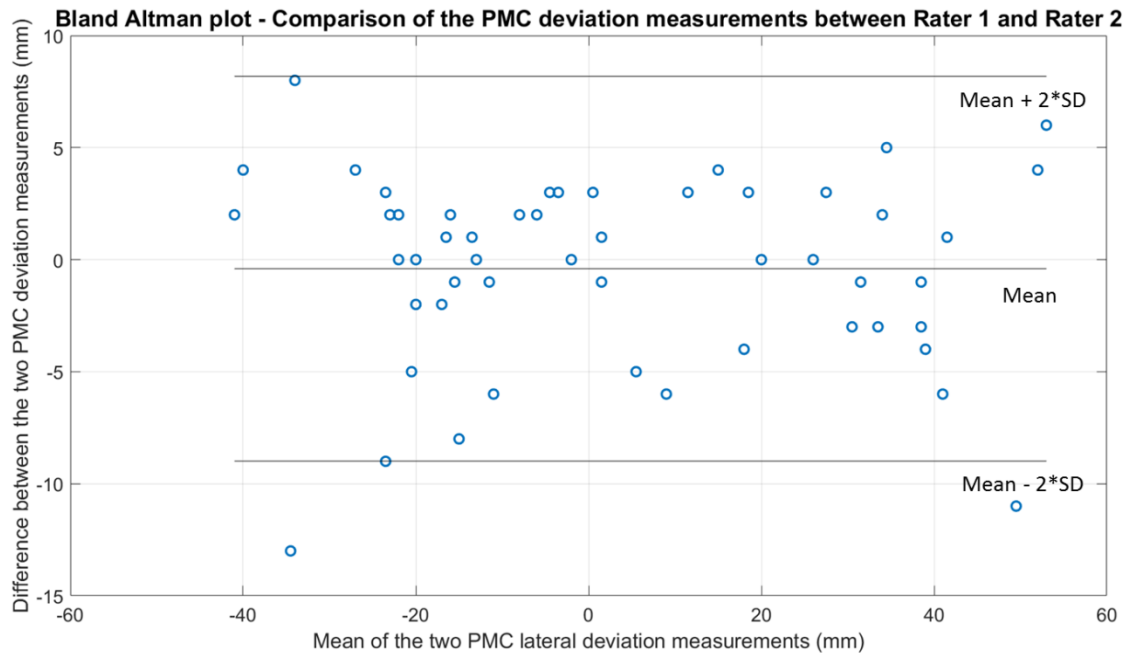


Figure 6.34 The Bland-Altman plot - A comparison of the PMC lateral deviation measurements between Rater 1 and Rater 2.

Error index

Table 6.6 summarizes the error indices indicating the differences in selecting end vertebrae between two sessions of measurements of each rater and between two raters. Rater 1 showed higher agreement in selecting end vertebrae (EI = 0.41) than Rater 2 (EI = 1.05). Rater 1 had only one end vertebra differing by equal or more than two levels. Meanwhile, Rater 2 had 13 end vertebrae differing by equal or more than 2 levels. The EI between the two raters was 1.48.

Table 6.6 End vertebrae difference between individual raters and between Rater 1 and Rater 2.

Session	0		± 1		± 2		> 2		EI
	UEV ^a	LEV ^b	UEV	LEV	UEV	LEV	UEV	LEV	
Rater 1	39	44	13	7	0	1	0	0	0.41
Rater 2	26	31	15	19	10	2	1	0	1.05
Rater 1 - Rater 2	19	20	22	24	11	6	0	2	1.48

^a Upper End Vertebrae

^b Lower End Vertebrae

6.2.3 Discussion

The AVR was quantitatively measured on the transverse view through the selection of the COLs on the PA plane. The measurement of the AVR was done simultaneously with that of the PA Cobb angle, thus reducing the implementation time. This AVR-measuring procedure was simple, requiring only two points to calculate the AVR directly on the axial plane. Many methods were proposed and used to measure the AVR such as radiography (Cobb, 1948, Drerup, 1984, Nash and Moe, 1969, Stokes *et al.*, 1986, Chi *et al.*, 2006, Weiss, 1995, Cerny *et al.*, 2014), CT (Aaro *et al.*, 1978, Ho *et al.*, 1993), MRI methods (Birchall *et al.*, 1997) and ultrasound (Suzuki *et al.*, 1989, Chen *et al.*, 2016). However, most of these radiographic methods are limited to the 2D PA radiographs. The measurement on the PA plane provides an estimation of the AVR, not the actual value. Furthermore, most of these methods require more points and parameters to calculate the AVR. The CT examination exposes patients to harmful ionizing radiation. MRI is expensive, time-consuming, and requires patients in supine position. This lying position may alter the severity of scoliosis, and an underestimate may occur. The reliabilities and variations of the 2D and 3D methods to measure the AVR were summarized (Vrtovec *et al.*, 2009).

This study measured the AVR on the transverse image; the rotation of one vertebra was relative to that of vertebra L5, which was in turn relative to the reference plan xz. Therefore, the accuracy of the rotation of the other vertebrae highly depended on the actual rotation of vertebra L5. The intra-rater reliabilities (ICCs [2,1]) for the two raters were 0.935 and 0.929, respectively, while the inter-rater reliability (ICC[2,1]) was 0.939. The MAD \pm SD of the AVR measurements from Rater 1, Rater 2 and Rater vs Rater 2 were less than 3° (Rater 1: 2.6° \pm 2.7°; Rater 2: 2.8° \pm 2.7°; Rater 1 vs Rater 2: 2.5° \pm 2.6°). This study shows similar results compared to the methods reported in literature that measured the AVR on the transverse images. Ho proposed a method to measure the AVR on a CT transverse image (Ho *et al.*, 1993), which is considered a gold standard. Ho's method reported small intra- and inter-rater variations between 1.2° and 3.3°, and between 1.9° and 3.0°, respectively. However, this CT-based approach is less suitable due to additional radiation exposure to patients. Chen *et al.* proposed the COL method to measure the AVR on the ultrasound transverse image (Chen *et al.*, 2016). Chen's method showed good results with the intra- and inter-rater reliability of

0.95 - 0.99 and 0.91, respectively, and maximum intra- and inter-rater variation of $0.7^\circ \pm 0.7^\circ$ and $0.9^\circ \pm 1.1^\circ$, respectively. Wang *et al.* (Wang *et al.*, 2016) compared the AVR measured by the COL method on ultrasound images with that by the Aaro-Dahlborn method on MRI images. Their study reported the MAD between these two methods were $0.3^\circ \pm 0.3^\circ$, $0.5^\circ \pm 0.3^\circ$, and $1.0^\circ \pm 1.1^\circ$ for the AVR of $0.0^\circ - 5.0^\circ$, $5.0^\circ - 10.0^\circ$, and $> 10.0^\circ$, respectively. Nevertheless, Wang *et al.* had the 3D ultrasound and MRI scans performed in the supine position, which may underestimate the severity of scoliosis. The results of the present study indicated that the 3D ultrasound could measure the AVR reliably for the patients with AIS.

It was reported in the literature that the intra- and inter-rater reliabilities of the Cobb angle measurements from radiographs ranged between 0.87 and 0.99 and 0.87 to 0.98, respectively, (Mok *et al.*, 2008, Kuklo *et al.*, 2005, Gstoettner *et al.*, 2007, Wills *et al.*, 2007). Similarly, the intra- and inter-rater reliabilities of the Cobb angle measurements from ultrasound images ranged between 0.84 to 0.99 (Chen *et al.*, 2013, Cheung *et al.*, 2015, Zheng *et al.*, 2015, Young *et al.*, 2015, Wang *et al.*, 2015). This study showed the intra- and inter-rater reliabilities were within the ranges from the literature (Intra-rater: 0.97 to 0.99 and Inter-rater: 0.93. In addition, the intra-rater and inter-rater variations of the Cobb angle measurement on radiographs were $3^\circ - 5^\circ$ and $6^\circ - 9^\circ$, respectively (Morrissy *et al.*, 1990, Carman *et al.*, 1990, Pruijs *et al.*, 1994). This study showed a much better result on using 3D ultrasound images in which the maximum intra- and inter-rater measurements variation were 1.5° and 2.2° , respectively.

Furthermore, it was the first time that the Cobb angle was measured on the ultrasound PMC and reported. On average, the PMC Cobb angles were 1° larger than the PA Cobb angles for both the thoracic and lumbar regions. This value was smaller than the reported values in literature. Delorme *et al.* (Delorme *et al.*, 2000) reported the differences between the PA and PMC Cobb angles of $3^\circ - 5^\circ$ on radiographs for the thoracic and lumbar regions. Meanwhile, the Cobb angle measured on the radio plane and the patient plane of 3D EOS images were $2^\circ - 4^\circ$ and $4^\circ - 6^\circ$ larger than the Cobb angle on the frontal radiograph for the thoracic and lumbar regions, respectively (Pasha *et al.*, 2016). The smaller differences between the PMC Cobb angle and the PA Cobb angle from this ultrasound study might be because the recruited patients only had a small range of the Cobb angle (10° to 45° only). In addition, in literature,

the Cobb angle on the PMC was usually obtained by rotating the spine around the vertical axis at 1° intervals until the largest Cobb angle was obtained on the projected plane (Delorme *et al.*, 2000). Although the reported method could provide a high degree of accuracy on the PMC Cobb angle, it was a very time-consuming process. In order to minimize the computational time in the ultrasound method, only 5 estimated PMC which were around the maximum AVR was used to calculate the largest Cobb angle. Although the accuracy was reduced, the processing time was also reduced significantly.

Lastly, the error indices EI reported in this study (Rater 1: 0.41, Rater 2: 1.05, Rater 1 vs Rater 2: 1.48) were almost similar to the results from another ultrasound study (Chen *et al.*, 2013). Chen *et al.* reported slightly higher intra-rater error indices between 0.57 and 1.16, but lower inter-rater error indices between 0.94 and 1.14.

6.2.4 Conclusion

In this study, reliabilities of the *in-vivo* measurement of the AVR, the Cobb angles and the lateral deviations on the PA plane and the PMC were calculated. All the ICC values were high (> 0.90), and the MAD values were all within the ranges reported in literature. Although the accuracy of the PMC Cobb angle measured from the ultrasound had not been validated, this was the first reported method to measure the Cobb angle on the PMC from ultrasound images. In order to apply the proposed method in scoliosis clinics, the accuracy of the *in-vivo* AVR and PMC Cobb angle measurements must be validated.

6.3 Validity of the measurements of the PA Cobb angle

To investigate the agreement of the PA Cobb angle measurements from the 3D ultrasound images, the PA Cobb angle measurements obtained from the previous section (section 6.2) were compared with the clinical records, which were measured by experienced health professional. The inter-method reliabilities were calculated to evaluate the validity.

6.3.1 Methods

The ultrasound PA Cobb angle measurements from the second measurement sessions from both raters (M12 and M22) were used to compare with the recorded Cobb angles from the

scoliosis clinics. In the clinical record, only 50 Cobb angles were recorded, therefore, the corresponding 50 measurements from the ultrasound images were used for comparison.

6.3.2 Results

Table 6.7 provides a comparison of the PA radiograph and ultrasound Cobb angle measurements from both raters. Both Pearson's r values were higher than 0.92, indicating strong correlations between the ultrasound and radiograph measurements. Rater 1 yielded a lower correlation with the radiograph measurements, which was not statistically significant ($p = 0.17$) compared to Rater 2. Rater 1 also showed higher MAD and SD ($2.2^\circ \pm 2.7^\circ$) than Rater 2 ($1.7^\circ \pm 1.6^\circ$). The SEM values between the ultrasound and the radiograph measurements ranged from 1.7° to 2.4° . All differences between the ultrasound and radiograph measurements by Rater 1 were within 15° , with 96% of measurements within 5° . This was inferior to Rater 2 who had the maximum difference of 6° with 96% of measurements within 5° .

Table 6.7 Comparison of the PA Cobb angle measurements between the radiograph and ultrasound methods by two raters.

Rater	Pearson's r	MAD \pm SD ($^\circ$)	Max. Diff. ($^\circ$)	% within 5°	SEM*
Rater 1	0.930	$2.2^\circ \pm 2.7^\circ$	15	96	2.4°
Rater 2	0.967	$1.7^\circ \pm 1.6^\circ$	6	96	1.7°

* Calculated using the standard deviation of radiograph measurements

Figure 6.35 and Figure 6.36 show the measurement differences between the PA Cobb angle from the ultrasound images and radiographs by Rater 1 and Rater 2, respectively. Rater 1 yielded two outliers ($> 2SD$), and the differences were greater than 13° . Meanwhile, Rater 2 produced 2 outliers and both of them were 6° different from the radiographic measurements. Hence, Rater 1 had lower ICC values and higher average of MAD difference than Rater 2.

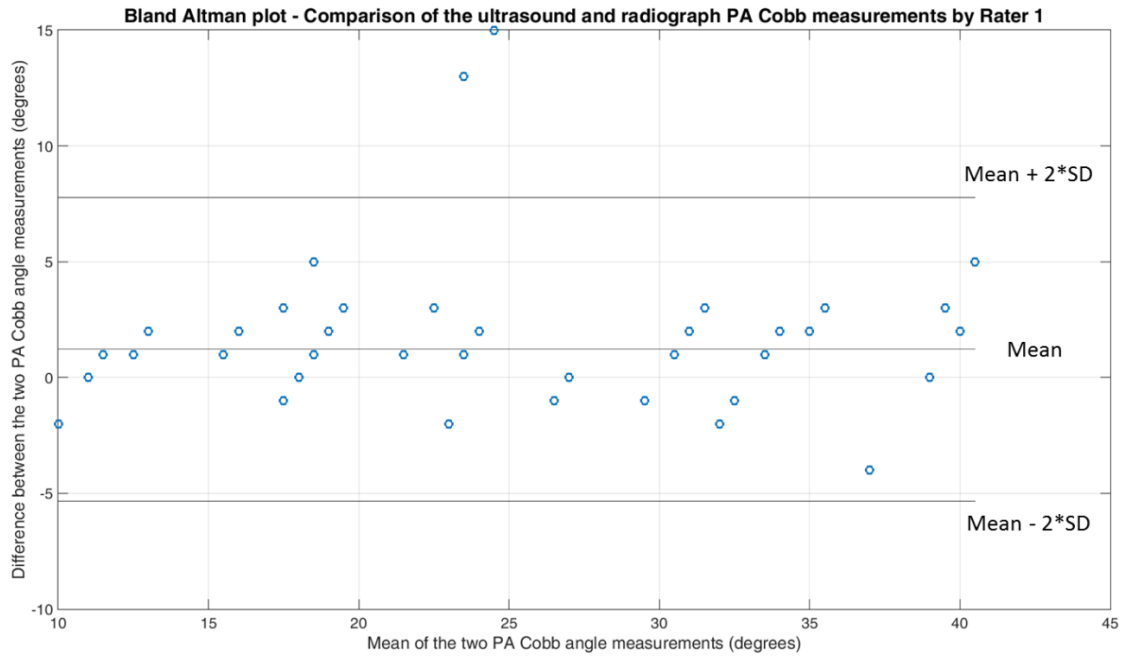


Figure 6.35 The Bland-Altman plot - A comparison of the ultrasound and radiograph PA Cobb angle measurements by Rater 1.

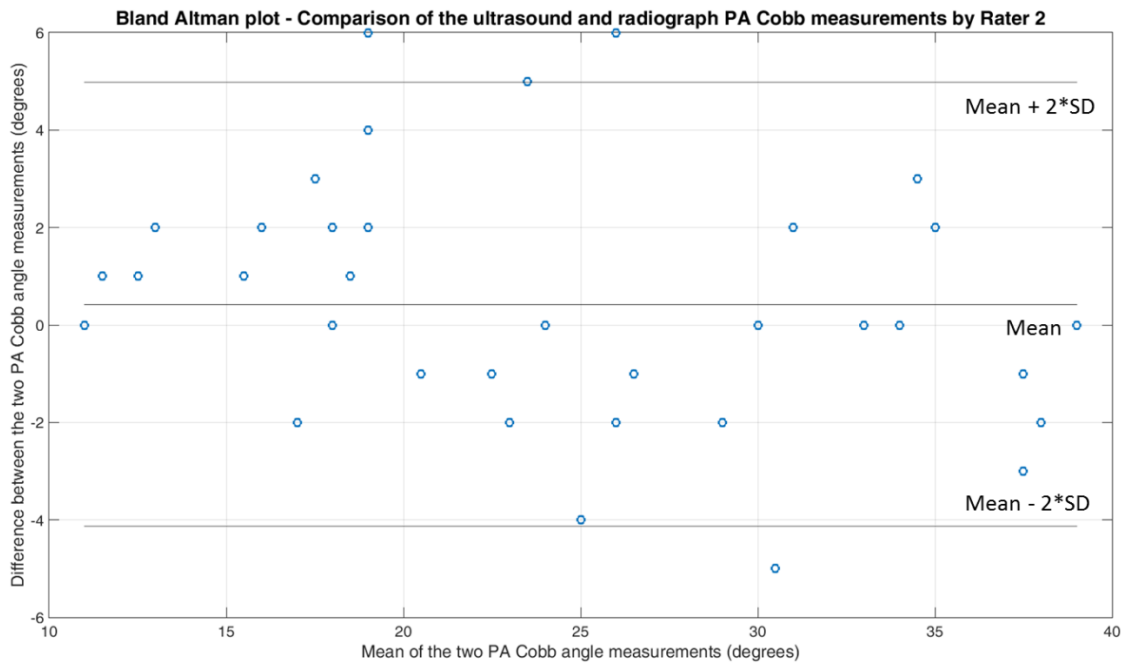


Figure 6.36 The Bland-Altman plot - A comparison of the ultrasound and radiograph PA Cobb angle measurements by Rater 2.

Table 6.8 reports the differences in selecting the end vertebrae between ultrasound images and radiographs for the two raters. The EIs for Rater 1 and Rater 2 were 1.22 and 1.28, respectively, which were similar. Rater 1 had 88 out of 100 end-vertebra differing within one level whereas Rater 2 reported 87 in 100 end-vertebra differing within one level.

Table 6.8 End vertebrae difference between ultrasound images and radiographs by both raters.

	0		± 1		± 2		> 2		EI
	UEV	LEV	UEV	LEV	UEV	LEV	UEV	LEV	
Rater 1	23	35	18	12	6	1	3	2	1.22
Rater 2	19	20	22	26	6	4	3	0	1.28

6.3.3 Discussion

This validity study showed high intra-rater reliabilities between ultrasound and radiographic measurements ($ICC > 0.92$) for both raters. The average $MAD \pm SD$ were $2.2^\circ \pm 2.7^\circ$ and $1.7^\circ \pm 1.6^\circ$ for Rater 1 and Rater 2, respectively. The reported ICC and MAD were slightly better than that from the literature (Zheng *et al.*, 2015, Young *et al.*, 2015). From Zheng *et al.* (Zheng *et al.*, 2015) study, they reported the correlation coefficient between the ultrasound and radiographic methods ranged between 0.78 and 0.83 among 3 raters and the minimum $MAD \pm SD$ was $3.3^\circ \pm 2.3^\circ$ for 3 raters. Meanwhile, Young *et al.* (Young *et al.*, 2015) reported the comparison of radiograph and ultrasound curvature measurements yielded ICC values ranging from 0.70 to 0.86 for 4 raters and MADs ranging from $2.6^\circ \pm 2.0^\circ$ to $4.1^\circ \pm 2.6^\circ$. They also reported larger end-vertebra differences between ultrasound and radiograph measurements with the error indices ranging from 1.30 to 2.36. The more experienced raters in this present study may contribute to the better results.

There was a difference of approximate 2.5° in the PA Cobb angle between the radiograph and the sonograph. The possible reasons are: 1) patients' posture for data acquisition between the radiography and the ultrasound methods might be different; 2) the landmarks used for the determination of the Cobb angle were not the same: the end plate of vertebrae in radiography but the COL in ultrasonography.

6.3.4 Conclusion

In this validity study, the reliability and the accuracy of the PA Cobb measurements from the 3D ultrasound images was high (ICC > 0.92 and the maximum MAD \pm SD = $2.2^\circ \pm 2.7^\circ$). The 3D ultrasound image method should be further investigated so that it can apply to scoliosis clinics to reduce radiation exposure to children who have AIS.

6.4 Validity of the measurement of the AVR

To validate the AVR measurements from the ultrasound image, a study to compare the measurements from the EOS[®] imaging system and ultrasound was conducted.

6.4.1 EOS imaging system

Figure 6.37 illustrates the EOS[®] imaging system and its working principle. The EOS[®] X-ray machine is capable of slot scanning the whole body in an upright, weight-bearing position with two X-ray sources and provides the lateral and PA radiographs simultaneously. The 3D reconstruction of the spine is based on the digitization of vertebral points and a database of vertebral anatomy. For the EOS[®], the scale of the subject and the image is 1:1, thus spinal and vertebral parameters can be very precisely measured and calculated. Visualization of 3D reconstructed models in various views by sterEOS 3D software enables presentation of top view images to help analyze rotational conditions of lower limbs, joints and spine deformities in the horizontal plane, providing revolutionary novel possibilities in orthopedic surgery, especially in spine surgery.

The dedicated EOS software SterEOS (version 1.6) was used to reconstruct the 3D spinal image. After the reconstruction, the Cobb angle, the sagittal balance, and the AVR on the patient plane and the radio plane could be generated. Glaser *et al.* (Glaser *et al.*, 2012) investigated the accuracy of the AVR measurement from EOS images compared to CT images. They reported that the root-mean-square accuracy of the AVR measurement was 1.9° with a maximum error of 5.8° .

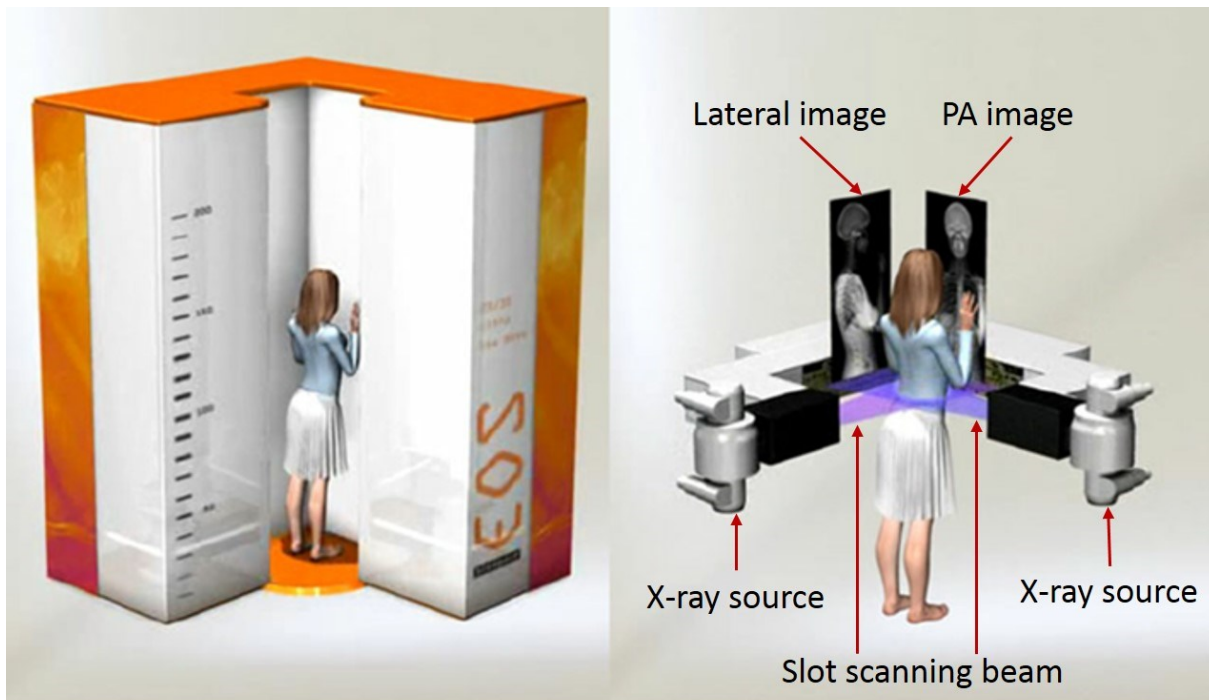


Figure 6.37 The EOS imaging system and its working principle (modified from (Illes and Somoskeoy, 2012)).

6.4.2 Methods

Recruitment of patient data

Nine patients who were diagnosed with AIS (Gender: 7 females and 2 males; Age: 13.2 ± 1.0 years, Cobb angle: $21.5^\circ \pm 6.3^\circ$) and initial visit were recruited from the local scoliosis clinic. The ethics approval was granted from the University of Alberta's ethics board and all patients signed the consent forms before participating in the study. The inclusion criterion was patients who had both PA and lateral radiographs from the EOS system. The exclusion criteria were patients who had spine surgery.

Measurement of the AVR

Rater 1 and Rater 2 described in the reliability study in section 6.2.1 had two to three years of experience in measuring the Cobb angles and the AVR on ultrasound spinal images. They both measured the AVR of all vertebral levels on nine ultrasound images twice in one week apart using the 3DSA software. Meanwhile, Rater 3 measured the rotation of each vertebral level twice in a one-week interval using the dedicated sterEOS software. Rater 3 who had over

20 years of experience in the domain of scoliosis had just completed a training course on using the sterEOS software.

To eliminate the effect of the reference plane that may be different in measuring the AVR between the ultrasound and EOS software, axial intervertebral rotations (AIR) were used. To compare the AVR between two sessions of measurement, the rotations of the apical vertebra and its two adjacent vertebrae were recorded. Thus, for each curve, two AIR measurements were calculated and compared: the first AIR between the superior adjacent vertebra and the apex, and the second AIR between the apex and the inferior adjacent vertebra. The second measurements by Rater 1 and Rater 2 were compared with the second measurement by Rater 3. Only the measurements of the AIR recorded at the same levels between the ultrasound and EOS images were compared. The difference in vertebral level identification was not accounted for.

6.4.3 Results

Nine subjects were measured and 13 curves were detected. The AVR of 39 vertebrae were measured, and 26 AIR were calculated and recorded. The Pearson's r values for both raters were close to zero, indicating weak correlations between the ultrasound measurements and the EOS measurement. However, the differences between the ultrasound and the EOS measurements were small, being $3.3^\circ \pm 3.3^\circ$ and $4.1^\circ \pm 3.0^\circ$ for Rater 1 and Rater 2, respectively.

Figure 6.38 and Figure 6.39 demonstrate the differences in the AIR at the apical regions between the ultrasound and EOS measurements by Rater 1 and Rater 2, respectively. Rater 1 and Rater 2 yielded one outlier and the remaining values lay within $-0.1^\circ \pm 9.4^\circ$ and $-1.1^\circ \pm 10.2^\circ$ (Mean \pm 2SD), respectively.

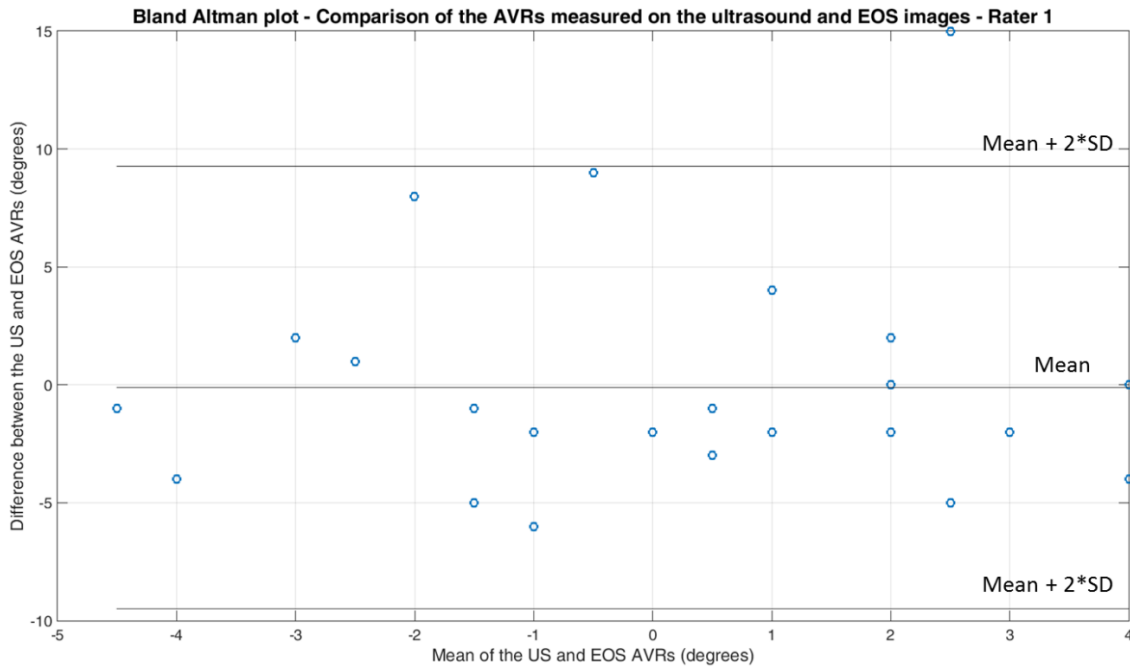


Figure 6.38 The Bland-Altman plot - A comparison of the AIR measurements between the ultrasound and the EOS images by Rater 1.

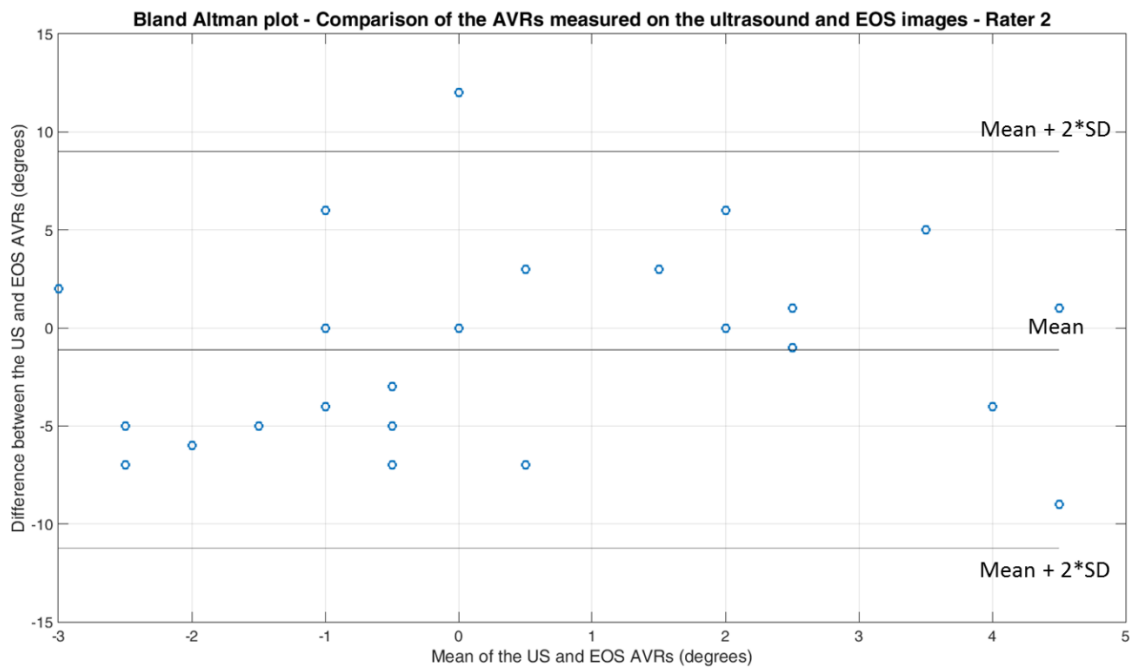


Figure 6.39 The Bland-Altman plot - A comparison of the AIR measurements between the ultrasound and EOS images by Rater 2.

6.4.4 Discussion

In this validity study, the measurement of the AIR on EOS images were used as reference. Computed tomography can be used to obtain 3D spinal images, but it requires a large number of slices to reconstruct the entire vertebral column. High effective radiation dose of CT limits its use to a short segment of the spine in pediatric spine examinations. In addition, this CT examination requires patients in the supine position, which changes the curvature of the vertebral column compared with the standing position.

The measurement of the AVR that was performed on both standing ultrasound and EOS images was focused on the apical vertebra and its two adjacent vertebrae as their values are maximal at these respective levels. There was almost no correlation between the ultrasound and EOS measurements. This may be because of the following reasons. The first reason may be due to the difference in the reconstruction of 3D images between the ultrasound and EOS methods. Ultrasound images were obtained on an individual basis. That means the 3D ultrasound spinal image of a patient was reconstructed based on the data acquired from that person. In contrast, the 3D EOS image of a patient was reconstructed based on the digitization of vertebral points on the lateral and PA images and *a priori* database of vertebral anatomy. That means more data that were not acquired from that person were added to complete the surface of the reconstructed image. Therefore, the EOS reconstructed image did not reflect the real image of the spine. Another potential reason was that the selection of vertebral landmarks for measuring the AVR was different between the two methods. The ultrasound method used the COLs to measure the AVR while it was unknown that which vertebral landmarks were used in the EOS method. Last but not least, the uncorrelation may be because of variations between raters. Due to a limited time, the ultrasound and EOS measurements were performed by different raters. Two raters measured the AVR on the ultrasound images while the other rater measured the AVR on the EOS images.

This study involved 9 AIS patients with 13 curves. It is recommended that more AIS patients be recruited and each raters measure the AVR on both ultrasound and EOS images.

6.4.5 Conclusion

In this validity study, the measurement of the AVR on ultrasound images was validated with that on EOS images. The Pearson's correlation coefficients were close to zero, indicating there was almost no correlation between the ultrasound and EOS measurements.

6.5 Summary

In this chapter, the methods to measure the AVR, the Cobb angle and the lateral deviation on the PA plane and the PMC under clinical settings were proposed. It was the first time that the PMC Cobb angle was proposed and measured on the PMC of ultrasound images. The *in-vivo* studies were performed to investigate the repeatability and reliability of the proposed method. The intra- and inter-rater ICCs and the MADs of the measurements showed that the proposed approach could be repeatable and reliable. The comparison of the PA Cobb angle between the ultrasound and radiographic methods showed good results with high correlations and small differences. However, the validity study of the AVR yielded the Pearson's correlation coefficients approximately zero, indicating that there was almost no correlation in the measurements of the AVR between ultrasound and EOS methods.

The correlation of 3D ultrasound parameters with the progression of AIS: A pilot study

In clinical practice, a good prediction of curve progression may assist the treating orthopedic surgeon to provide better management to children who have scoliosis. A curve is considered progressed or reduced when there is an increase or reduction of 6° or more in the Cobb angle, respectively, between two consecutive clinical visits. In this chapter, a retrospective study is performed to investigate the correlation of 3D ultrasound parameters with the progression of AIS using a preliminary developed predictive model. This model can estimate the future PMC Cobb angle from the current ultrasound measurements using multiple linear regression.

7.1 Introduction

The pathogenesis of spinal deformity progression is poorly understood. Current clinical practice routinely monitors the progression of scoliosis at all patients with a series of full spinal X-rays. This routine procedure exposes patients to ionizing radiation, which increases cancer risk in growing adolescents. Reducing ionizing radiation can be achieved if the future spinal curvature can be predicted within the clinic based on the current measurement. Prediction of spinal curvature has been investigated by many scoliosis researchers as reported in section 3.2 (Lonstein and Carlson, 1984, Duval-Beaupere and Lamireau, 1985, Weinstein and Ponseti, 1983, Duval-Beaupere, 1992, Duval-Beaupere, 1996, Yamauchi *et al.*, 1988, Wu *et al.*, 2005, Wu *et al.*, 2010, Wu *et al.*, 2011, Tan *et al.*, 2009, Lam *et al.*, 2012, Peterson and Nachemson, 1995, Soucacos *et al.*, 1998, Escalada *et al.*, 2009, Nault *et al.*, 2013, Nault *et al.*, 2014). Scoliosis is a 3D deformity of the spine; therefore, 3D parameters obtained from the spine should be included in the prediction of AIS progression. Several 3D predictive models

utilize ionizing radiation (Wu *et al.*, 2005, Wu *et al.*, 2010, Wu *et al.*, 2011, Nault *et al.*, 2013, Nault *et al.*, 2014). However, prediction of spinal curvature using 3D ultrasound measurements has not been reported. The following sections present a pilot study that develops a model to predict the progression of scoliosis using measurements obtained from 3D spinal images.

7.2 Methods

7.2.1 Recruitment of patient data

To build a predictive model, patient data were obtained from the local scoliosis clinic's database with ethics approval from the University of Alberta's ethics board. Records were extracted from patients who (i) were diagnosed with AIS; (ii) had no prior treatment; (iii) had Cobb angles between 10° and 45°; (iii) had at least two consecutive clinical visits with ultrasound scans at each visit; and (iv) had an elapsed time between two clinical visits between 6 months to 12 months. Twenty-nine patients (26 females, 3 males, aged 14.4 ± 1.5 years old) met the inclusion criteria and their records were extracted from the database between April 2013 (when 3D ultrasound scanning started) and April 2016. The acquired number was small because most of the patients who visited the clinic during this period were follow-up patients and had prior treatment.

Initially, there were two groups of predictors of interest. The first group included ultrasound parameters that were measured and recorded from the reconstructed 3D ultrasound images: the PMC Cobb angle, the PMC lateral deviation, the apical AVR, the number of curve, the number of vertebrae within the curve, the curve location (thoracic, thoraco-lumbar, lumbar), and the torsion. Most of these parameters had been used in X-ray based models (Lonstein and Carlson, 1984, Duval-Beaupere and Lamireau, 1985, Weinstein and Ponseti, 1983, Duval-Beaupere, 1992, Duval-Beaupere, 1996, Wu *et al.*, 2005, Tan *et al.*, 2009, Wu *et al.*, 2010, Wu *et al.*, 2011, Lam *et al.*, 2012, Peterson and Nachemson, 1995, Yamauchi *et al.*, 1988, Soucacos *et al.*, 1998). All these ultrasound measurements were performed by the same Rater 1 who was in the reliability study described in section 6.2.1 of this thesis. The torsion was the average rotation of each vertebra within a curve. It was calculated by using the apical AVR divided by the number of vertebrae within the curve. The second group, which was obtained from the clinical record, consisted of the elapsed time between two clinical visits (in

days), the patient gender, the patient body mass index (BMI), and the patient age. All the predictors had numeric values except for the patient gender and the curve location. The patient gender was coded as 0 for female and 1 for male while the curve location at the thoracic, thoraco-lumbar, and lumbar regions was coded as 1, 2, and 3, respectively. Initially, each observation contained all eleven parameters that were mentioned above. If a patient developed multiple curves, the major curve was used for the model development.

In this pilot study, 29 pairs of spinal images were reconstructed. These pairs were randomly split into two portions: 23 pairs for the training data and 6 pairs for the test data. The full lists of the training data (Appendix Table 1) and the test data (Appendix Table 2) can be found in the Appendices.

7.2.2 Elimination of outliers

An outlier is defined as an observation that deviates significantly from the other observations as to arouse suspicions that it does not fit with the majority of a data set. If the outlier is not removed, it can affect the result significantly, especially when the sample size is small.

In order to detect outliers in the dataset, the squared Mahalanobis distance was used (Mahalanobis, 1936). In statistics, the Mahalanobis distance is a measure of the distance between a point P and a distribution D . It is a multi-dimensional generalization of the idea of measuring how many standard deviations away P is from the mean of D . In this PhD thesis, the outliers of the training data (observations) were detected using the Matlab-based function created by Professor A. Trujillo-Ortiz *et al.* (Facultad de Ciencias Marinas, Universidad Autonoma de Baja California, Mexico, 2006).

7.2.3 Selection of predictors (independent variables)

Developing a regression model using irrelevant or redundant independent variables can lead to model overfitting. An over-fitted model could affect clinical decision-making because it tends to underestimate the probability of an event in low-risk patients and overestimate it in high-risk patients (Pavlou *et al.*, 2015). In addition, when multiple linear regression is performed with multi-collinear independent variables, coefficient estimation can be wrong.

Therefore, the predictors for the model must be selected and validated carefully so that only independent variables that contribute significantly to the model are included.

Not all initially suggested predictors could be used at the end. The selection of significant predictors was done using the backward selection method by applying the linear regression function in Microsoft Excel. A significant predictor appeared in the regression model with a p -value smaller than 0.05. Figure 7.1 illustrates the flowchart of the predictor selection process. To start with, all initial predictors were first put into the multiple linear regression to find their p -values. If all p -values were smaller than 0.05, then the final predictive model was established with all initial predictors. Otherwise, the predictor with the highest p -value was eliminated from the initial predictors. The remaining predictors were put into the multiple linear regression function again. The same procedure was repeated until all predictors contributed significantly to the model.

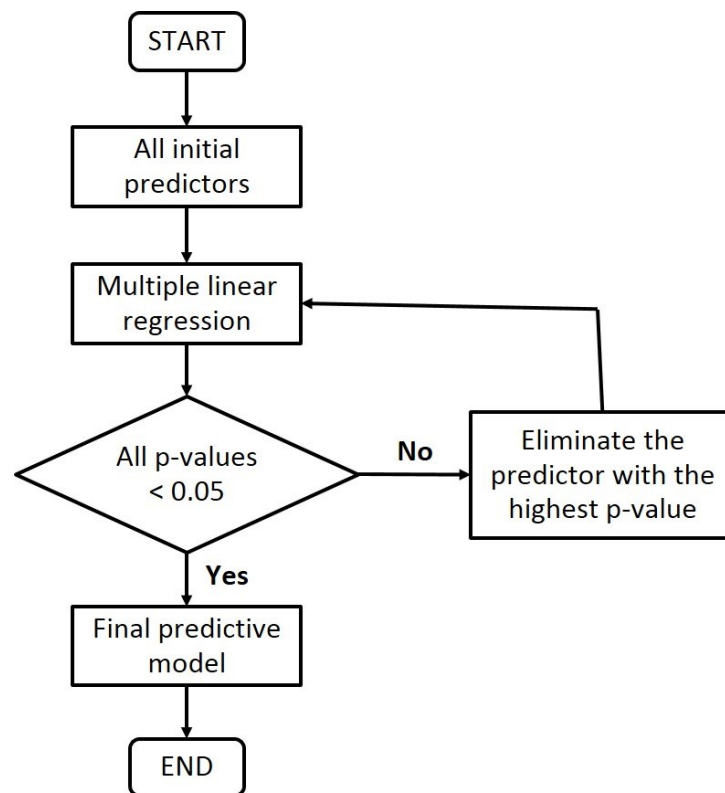


Figure 7.1 The flowchart of selecting the significant predictors.

7.2.4 Development of the PMC Cobb angle predictive model

A linear regression model was trained and developed to estimate the future PMC Cobb angle after a given period based on the measurements of the current clinical visit. A curve is considered progressed if its Cobb angle increases more than 5°.

The linear regression model can be written as:

$$y = \alpha + \sum_{i=1}^p \beta_i * x_i + \varepsilon \quad (7.1)$$

where y is the predicted outcome (dependent variable), α is the intercept, x_i is the i^{th} predictor (independent variable), β_i is the i^{th} regression coefficient, and ε is the error between the observed and predicted y . If $p = 1$, Equation 7.1 becomes a single linear regression model. If $p \geq 2$, Equation 7.1 becomes the multiple linear regression model.

7.2.5 Validation method

The 6 pairs of the test data were used to validate the final predictive model. The measurements from the first visit were used to calculate the predicted PMC Cobb angle while the PMC Cobb angle from the second visit was used to validate the results. In statistics, the coefficient of determination, r^2 , indicates how well measured data fit a statistical model. If r^2 is equal to 1, it indicates that the regression line perfectly fits the data, while $r^2 = 0$ indicates that the line does not fit into any of the data. The coefficient of multiple correlation, r , is the Pearson correlation coefficient between the predicted and the measured values of the PMC Cobb angle. Normally, the value of r^2 tends to increase as additional predictors are included in the model. Thus, increasing the number of predictors in the model can artificially lead to a higher r^2 even when the extra predictors are irrelevant. To penalize this effect, and to take the number of predictors and the sample size into account, the adjusted coefficient of determination, \bar{r}^2 , is used and defined as

$$\bar{r}^2 = 1 - (1 - r^2) * \frac{n - 1}{n - p - 1}, \quad n - p - 1 \neq 0 \quad (7.2)$$

where p is the number of predictors, and n is the sample size. The adjusted r^2 is calculated to justify the performance of the model on the test data and is less than r^2 . The adjusted r^2 can be negative if r^2 is small. This occurs when there are unnecessary predictors in the model but the sample size is small or the data has collinearity problem. Negative adjusted r^2 values can be reported and interpreted as 0.

7.3 Results

With a given significant level of 0.05, there was no observation detected as an outlier. Table 7.1 reports the collinearity among all initial predictors. A correlation of 1 means two variables are perfectly correlated while a correlation of 0 means there is absolutely no correlation. There were strong correlations between the lateral deviation (LD) and the torsion, between the LD and the AVR, and between the torsion and the AVR. These three predictors were considered removing in the selection of significant predictors. If multicollinearity exists in multiple regression, coefficient estimation could be wrong.

Table 7.1 Collinearity among all initial predictors.

	2 nd PMC Cobb	1 st PMC Cobb	AVR	LD	# of curve	# of vertebrae	Torsion	Location	Elapsed time	Gender	BMI	Age
2 nd PMC Cobb	1											
1 st PMC Cobb	0.94	1										
AVR	0.12	0.10	1									
LD	0.35	0.33	0.83	1								
# of curve	0.59	0.58	0.09	0.11	1							
# of vertebrae	0.34	0.19	0.19	0.48	0.19	1						
Torsion	0.07	0.04	0.98	0.77	0.03	0.14	1					
Location	-0.31	-0.28	-0.36	-0.23	-0.27	-0.21	-0.36	1				
Elapsed time	-0.12	-0.04	0.04	-0.16	0.24	-0.18	0.06	-0.09	1			
Gender	-0.19	-0.29	-0.31	-0.46	-0.22	0.01	-0.29	-0.43	0.00	1		
BMI	0.06	0.08	0.34	0.34	-0.13	0.06	0.29	-0.09	0.37	-0.11	1	
Age	0.28	0.39	-0.09	-0.04	0.15	-0.44	-0.08	0.04	0.23	-0.21	0.06	1

Table 7.2 summarizes a statistical analysis when all initial predictors were input into the multiple linear regression model. The LD contributed most insignificantly to the model because its p -value (0.94) was the greatest. This predictor was first eliminated from the initial set of predictors. Similarly, the remaining predictors were put into a new multiple linear

regression model. The backward selection left the 1st PMC Cobb angle and the number of vertebrae with *p*-values smaller than 0.05.

Table 7.3 shows the distributions of each predictors used in the multiple linear regression. The range of the 1st PMC Cobb angle was from 12° to 50° while the number of vertebrae consisted on the major curve ranged from 4 to 9. In addition, the discrepancies between the 2nd and the 1st PMC Cobb angle ranged between -6° and 10° ($0.4^\circ \pm 3.9^\circ$). Four out of 23 cases (17.4%) showed curve progression or reduction.

Table 7.2 Statistical analysis for all initial predictors.

	<i>Coefficients</i>	<i>Standard Error</i>	<i>t Stat</i>	<i>p-value</i>	<i>Lower 95%</i>	<i>Upper 95%</i>
<i>Intercept</i>	-23.12	16.56	-1.40	0.19	-59.58	13.34
<i>1st PMC Cobb</i>	0.84	0.12	6.86	0.00	0.57	1.12
<i>AVR</i>	-1.04	0.84	-1.24	0.24	-2.90	0.81
<i>LD</i>	0.01	0.13	0.07	0.94	-0.27	0.29
<i># of curve</i>	5.12	2.98	1.72	0.11	-1.45	11.68
<i># of vertebrae</i>	1.32	1.09	1.20	0.25	-1.09	3.73
<i>Torsion</i>	6.78	4.42	1.53	0.15	-2.94	16.51
<i>Location</i>	0.47	0.44	1.07	0.31	-0.49	1.43
<i>Elapsed time</i>	-0.02	0.01	-1.63	0.13	-0.05	0.01
<i>Gender</i>	6.25	4.46	1.40	0.19	-3.58	16.07
<i>BMI</i>	0.45	0.36	1.27	0.23	-0.33	1.24
<i>Age</i>	0.18	0.74	0.25	0.81	-1.45	1.82

Table 7.3 Measurements considered as selected predictors in the multiple linear regression.

	2 nd PMC Cobb (°)	1 st PMC Cobb (°)	Number of vertebrae
Range (min. - max.)	11° - 47°	12° - 50°	4 - 9
Mean ± Standard deviation	26° ± 11°	26° ± 11°	6 ± 1

Table 7.4 reports the statistical analysis generated by the final predictive model with two final predictors: the 1st PMC Cobb and the number of vertebrae consisted on the major curve. The adjusted r^2 in this case was 0.90 greater than 0.80, which means there was a good fit of data to the model. The adjusted r^2 of 0.90 also meant that 90.0% of the variation in the 2nd PMC Cobb angle could be explained by the 1st PMC Cobb angle and the number of vertebrae. Furthermore, the significance F less than 0.1 indicated that there was a correlation among the

three variables. This relation was presented in Equation 7.3 in which the regression coefficients were -4.92, 0.87, and 1.39 for the projection line intercept, the 1st PMC Cobb angle, and the number of vertebrae, respectively. There was a 95% probability that the true value of the coefficient fell between the Lower 95% and Upper 95% values. The probability was 2.5% that it lay below the lower value, and 2.5% that it lay above the upper value.

Table 7.4 Statistical analysis for the two final predictors.

<i>Regression Statistics</i>	
Multiple <i>r</i>	0.95
<i>r</i> square	0.91
Adjusted <i>r</i> square	0.90
Standard Error	3.40
Observations	23

ANOVA

	<i>df</i>	<i>SS</i>	<i>MS</i>	<i>F</i>	<i>Significance F</i>
Regression	2	2217.08	1108.54	95.62	5.79035E-11
Residual	20	231.87	11.59		
Total	22	2448.96			

	<i>Coefficients</i>	<i>Standard Error</i>	<i>t Stat</i>	<i>P-value</i>	<i>Lower 95%</i>	<i>Upper 95%</i>
Intercept	-4.92	3.75	-1.31	0.20	-12.75	2.91
1 st PMC Cobb	0.87	0.07	12.91	0.00	0.73	1.01
# of vertebrae	1.39	0.57	2.44	0.02	0.20	2.58

Predicted PMC Cobb

$$= -4.92 + 0.87 * (1\text{st PMC Cobb}) + 1.39 * (\text{Number of vertebrae}) \quad (7.3)$$

where the 1st Cobb angle ranged between 12° and 50°, and the number of vertebrae varied from 4 to 9. Figure 7.2 depicts the model's output as the function of the 1st PMC Cobb angle and the number of vertebrae.

Figure 7.3 demonstrates the normal probability plot of the residuals that was used to investigate whether the process data exhibited the normal distribution. Visually speaking, all

the data points were plotted closely along the fitted normal line. Therefore, the process data was closely normally distributed.

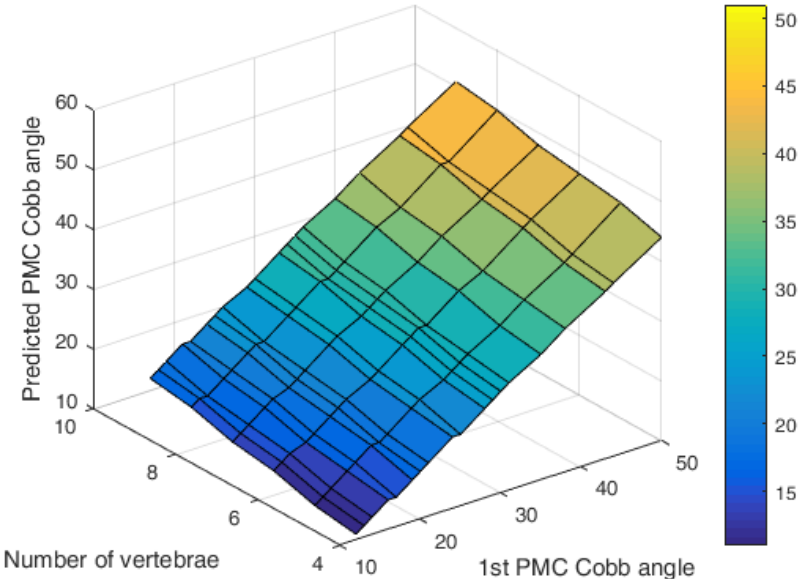


Figure 7.2 Multiple linear regression output shown for the range of the 1st PMC Cobb angle and the number of vertebrae. The color map indicates the magnitude of the predicted PMC Cobb angle (degrees).

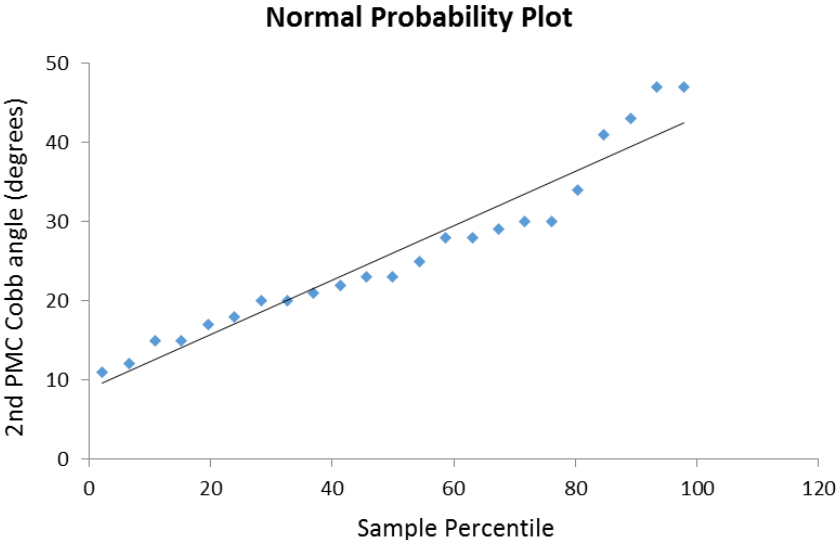


Figure 7.3 The normal probability plot of the residuals.

Table 7.5 illustrates the distribution of the ultrasound measurements of the test data. The 1st PMC Cobb angle range between 15° and 49° indicated the severity of scoliosis from mild to moderate.

Table 7.5 Measurements of selected predictors used to validate multiple linear regression.

	1 st PMC Cobb (°)	Number of vertebrae
Range (min. - max.)	15° - 49°	5 - 8
Mean ± SD	31° ± 12°	6 ± 1

Table 7.6 shows the two predictors' values from the first clinic visit, the measured and predicted PMC Cobb angles at the second clinical visit and the difference between them. All the 6 subjects had no expected curve progression or reduction. The differences in the PMC Cobb angles between the measured and predicted outcomes confirmed this trend. They are demonstrated in Figure 7.4.

Table 7.6 The measurements of the first clinical visit and the predicted Cobb angle.

Subject	1 st PMC Cobb (°)	Number of vertebrae	Measured 2 nd PMC Cobb (°)	Predicted 2 nd PMC Cobb (°)	Diff. in 2 nd PMC Cobbs (°)
1	19	5	23	19	-4
2	33	6	31	32	1
3	38	7	35	38	3
4	15	8	15	19	4
5	49	7	50	47	-3
6	32	5	32	30	-2

Diff. in the 2nd Cobb = Predicted 2nd PMC Cobb – Measured 2nd PMC Cobb

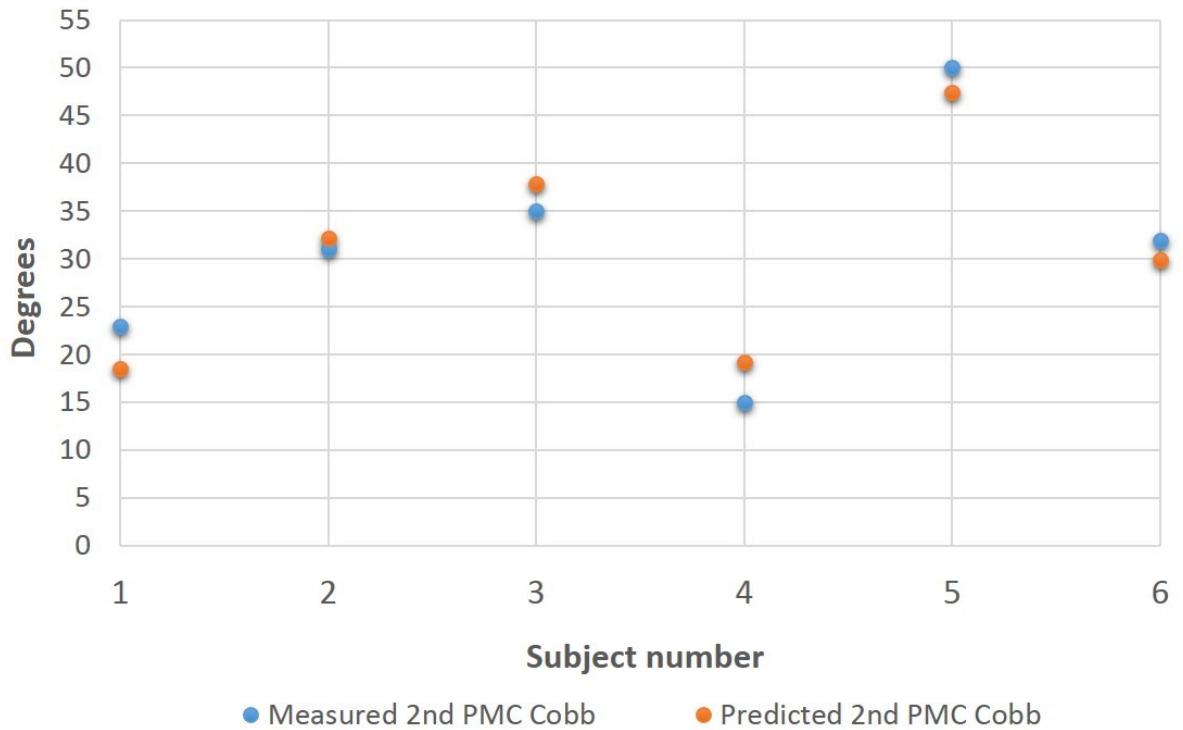


Figure 7.4 The difference between the measured and predicted Cobb angles.

Table 7.7 reports the statistical analysis of the validation. The mean absolute difference and its standard deviation between the measured and predicted Cobb angles was $2.9^\circ \pm 1.3^\circ$. The adjusted r^2 was 0.87 (> 0.80), indicating a good fit of data to the model.

Table 7.7 The statistical analysis of the validation.

r^2	0.92
Adjusted r^2	0.87
MAD \pm SD	$2.9^\circ \pm 1.3^\circ$

Figure 7.5 illustrates the Bland-Altman plot to compare the predicted and measured PMC Cobb angles. The mean of the differences between the two PMC Cobb angles was -0.1° , indicating that the predicted and measured values were close. In addition, 100% of the differences lies between the Mean $\pm 2 \times$ SD ($-0.1^\circ \pm 6.8^\circ$).

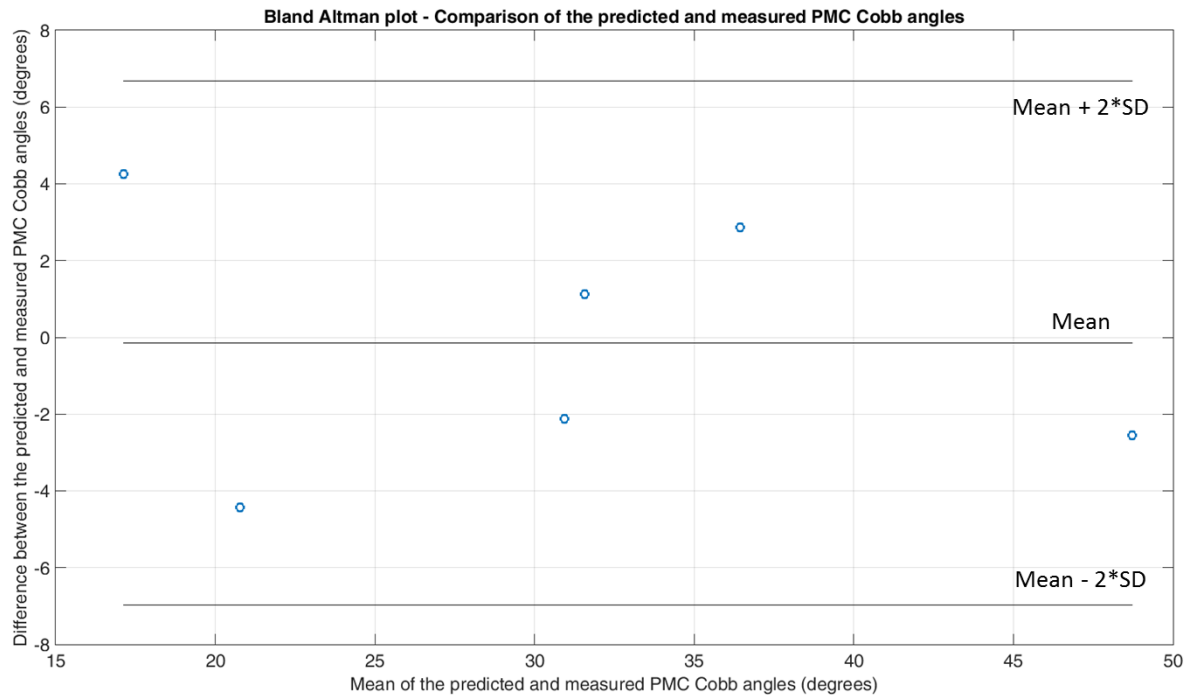


Figure 7.5 Bland-Altman plot – A comparison of the predicted and measured PMC Cobb angles

7.4 Discussion

The preliminary predictive model was built using 23 subjects (observations) and 2 predictors (variables), which is equivalent to 11.5 subjects per variable (SPV). The minimum SPV in regression varies among researchers. Schmidt determined that the minimum number of SPV should be between 15 and 20 (Schmidt, 1971). However, some authors proposed some rules of thumb supported by simulation studies. A minimum SPV of 10 was suggested to ensure accurate prediction in subsequent subjects (Harrell *et al.*, 1984, Peduzzi *et al.*, 1995, Peduzzi *et al.*, 1996). In addition, Austin and Steyerberg found by a simulation that a SPV of 2 was required for adequate estimation of regression coefficients, standard errors, and confidence intervals in linear regression models (Austin and Steyerberg, 2015).

As shown from Table 7.3 and Table 7.5, the test data range was within the training data range. That is, the predicted PMC Cobb angles were interpolated from the predictive model. Predicted outcomes can be interpolated or extrapolated. Of the two methods, interpolation is

preferred because it provides a greater likelihood of obtaining a valid estimate. Otherwise, extrapolation assumes that the observed trend continues for values outside the range used to build the predictive model. In addition, the differences between the predicted and the 1st PMC Cobb angle of the training data ranged between -6° and 10° ($0.4^{\circ} \pm 3.9^{\circ}$), indicating that three cases were covered: reduced, stable, and progressive. For the test data illustrated in Table 7.6, a comparison between the predicted PMC Cobb angle and the 1st PMC Cobb angle shows that there is no progression for all 6 tested cases. For the first time, the Cobb angle on the PMC of a 3D ultrasound image was used to determine which curve would progress or reduce and which curve would stabilize.

There are many studies about the prediction of scoliosis progression as mentioned in section 3.2. However, few of them are quantitative studies, that is, most of them dealt with the incidence of progression. Yamauchi *et al.* ((Yamauchi *et al.*, 1988) used roentgenologic parameters to determine the rate of progression. A quantitative prediction could be obtained within $\pm 10^{\circ}$ accuracy. Wu *et al.* (Wu *et al.*, 2005) proposed a 3D radiographic method in which the predicted Cobb angle was extrapolated from three successive previous values of computed Cobb angles. The accuracy of the prediction that was developed from 11 subjects was $4.40^{\circ} \pm 1.86^{\circ}$ and the linear regression *r*-value was 0.97 ($r^2 = 0.94$). In a later study, Wu *et al.* (Wu *et al.*, 2010) used three or four previous spinal curves obtained in 6-month intervals to construct an artificial progression surface. The predictive model was developed based on data acquired from 11 subjects. The spinal curvature at the next 6-month interval was extrapolated from the progression surface, which could yield the prediction accuracy of $4.1^{\circ} \pm 3.3^{\circ}$ and the *r*-value of 0.95 ($r^2 = 0.90$). The prediction at the next 12-month interval was less accurate at $6.2^{\circ} \pm 8.5^{\circ}$ and the predicted data did not correlate well with the actual data ($r \geq 0.36$). In another study, Parent *et al.* (Parent *et al.*, 2014) stated that that curve prediction at skeletal maturity based on 3D parameters measured at the first visit is possible with a coefficient of determination of 0.715.

In the present study, the accuracy of the prediction was higher ($2.9^{\circ} \pm 1.3^{\circ}$) than Wu *et al.* studies, but the coefficient of determination r^2 was equal or slightly smaller. However, in Wu *et al.* studies, patients with bracing were included, indicating unnatural progression that might affect the result of the prediction. In addition, those studies required three or four previous

records to predict the next 6- or 12-month outcomes. That means those studies required a number of clinical visits with a number of radiographs already taken before the prediction could start. The predictive model of the present study only deployed the current 3D ultrasound measurements from untreated patients; therefore, the natural progression of a curve was preserved. Moreover, the progression of scoliosis could be predicted at the initial presentation.

This preliminary study reported a promising result; however, it had limitations. Firstly, due to a limited number of participants, elapsed time between two clinical visits ranged between 6 months to 12 months. Therefore, the predicted outcome was within the time range of next 6 to 12 months. Secondly, only two predictors were involved in the predictive model, which might not truly reflect the complexity of AIS progression. As a result, this preliminary study demonstrated the 3D ultrasound morphologic parameters might had correlation to predict the progression of AIS. A larger cohort training data is required so that a more accurate model that may include more predictors can be developed. Furthermore, the performance of the future developed predictive model should be validated with a larger sample before it can apply to a clinical setting.

7.5 Conclusion

In this pilot study, a multiple linear regression method was used to investigate the correlation of the 3D ultrasound parameters with the progression of AIS. This non-ionizing method reduces the accumulated ionizing radiation exposure to patients and provides a strong correlation between the 1st PMC Cobb angle, the number of vertebrae within the largest curve, and the predicted PMC Cobb angle. The preliminary results are promising that the curve progression may be able to predict using 3D ultrasound measurements. More patients' data are needed to widen the range of scoliotic curves and to include more predictors.

Conclusions, limitations, and recommendations

In this chapter, a brief recapitulation and the major contributions of the work are provided. In addition, limitations of the work in this thesis are discussed, and recommendations for future research expanding from this work are presented.

8.1 Summary of the work

AIS is a complex 3D deformity of the spine with the coronal curvature of greater than 10° . Due to the associated axial vertebral rotation, the current standard 2D radiography recommended by the Scoliosis Research Society cannot reflect the 3D nature of scoliosis. The PMC provides a more accurate measurement in severe scoliosis cases as they have larger AVR. Recent studies have shown that ultrasound is feasible for imaging patients with AIS. This imaging modality is cost effective and free of ionizing radiation; therefore, it is safe to patients. The limitation of all those ultrasound studies was the PMC Cobb angle had not been identified and reported.

In this research work, the 3DSA software was developed to reconstruct 3D spinal images. This software was able to measure the coronal curvature and the lateral deviation on both the PA plane and the PMC, and the AVR. After the data acquisition of ultrasound data, the ultrasound intensity data and the position tracking information of B-scans were obtained. Speckle noise was first removed by applying the median filter. The contrast of a B-scan image depends on reflection of ultrasound energy at the interface between two media. When images are obtained using the pulse-echo technique, bone features normally have higher image intensity values than their surrounding tissues. Therefore, contrast stretching was applied to compress the values of darker pixels while expanding the higher-level values. This function

aimed to enhance vertebral features, separated them from surrounding tissues to make the segmentation of vertebral features easier in the automatic fuzzy segmentation process. The vertebral features were finally reconstructed into the 3D spinal image using the voxel-based reconstruction method with bi-linear interpolation. In order to accelerate the 3D reconstruction process, the target spinal volume was divided into 8 equal sections along its length to take advantage of the 8-core CPU in the computer. In addition, in the voxel-based 2D/3D conversion process, the search region of the two closest B-scans for each target voxel was limited to a certain number of B-scans instead of the entire B-scans data.

To investigate the effect of the reconstruction configuration on the quality of the reconstructed images, both the convex and linear ultrasound probes were used to scan a cadaveric vertebra T7 and few volunteers' spine. From both *in-vitro* and *in-vivo* studies, it was identified that the 2.5 MHz frequency from the convex probe, the 0.2 mm spacing, and the 0.6 reconstruction resolution constituted the optimal configuration and was used throughout the rest of the thesis. The *in-vitro* experiment demonstrated that the dimensional errors between the reconstructed images and the cadavers were quite small (1.5 ± 1.1 mm, 1.8 ± 0.5 mm, and 2.9 ± 1.5 mm for vertebrae T7, L1, and L3, respectively).

The COL landmark was applied to measure the Cobb angle and the lateral deviation on the PA plane and the PMC, and the AVR on the transverse plane. The PA plane and the PMC, and the transverse view for each vertebra were first identified and five aforementioned parameters were then measured. The repeatability study was performed to investigate if the ultrasound scanning method could be repeatable. Each patient was scanned twice in a similar manner and high agreement in the measurements of five parameters between the two scans was reported. Similarly, the reliability study was conducted to determine the reliability of the measurement method. The results of this study showed high intra- and inter-rater reliabilities for all five parameters. In addition, the Cobb angle measurements from the PA ultrasound images agreed well with the clinical standard Cobb angle measurements with a small variation ($MAD < 3^\circ$). Furthermore, the PMC Cobb angle was equal to or greater than the PA Cobb angle with 7° being the maximum differences between the two Cobb angles, respectively.

To investigate which ultrasound parameters could be used to predict the progression of AIS, a predictive model was developed using multiple linear regression. The results of

regression left 2 predictors from the 11 initial predictors in the model: the PMC Cobb angle and the number of vertebrae within the largest curve. This non-ionizing method reduces ionizing radiation exposure to patients. The preliminary results are promising that the curve progression may be able to predict using 3D ultrasound measurements. More patients' data are necessary to widen the range of scoliotic curves.

In conclusion, 3D freehand ultrasonography with the tracking system was able to image the scoliotic spine in AIS. The proposed ultrasound method could measure the spinal curvature, the lateral deviation, and the AVR reliability and accurately within a scoliosis clinic. Ultrasound parameters might be able to apply to predict quantitatively the progression of AIS.

8.2 Contributions

The research work described in this thesis used freehand 3D ultrasound to image the scoliotic spine. A fast and innovative imaging technique was developed to reconstruct 3D ultrasound spine images. From this image, the AVR, the Cobb angles and the lateral deviations on the PA plane and the PMC could be measured. It was the first time that the coronal curvature and the lateral deviation were measured on the PMC of a 3D ultrasound image of the spine.

A strong correlation was found between the PMC Cobb angle, the number of vertebrae within the major curve and the progression of AIS. These two parameters were obtained from pre-treatment clinical measurements so that the natural progression of AIS was preserved. It was the first time that the 3D ultrasound parameters were used to predict the progression of AIS.

8.3 Limitations and recommendations for future work

Due to the characteristics of ultrasound imaging to bone, the vertebral body could not be imaged, leading to an incomplete reconstruction of the spine. Thus, the Cobb method could not be applied to measure the Cobb angle. In addition, users need to imagine the complete shape of each vertebra. In the future study, *a priori* database may be considered to reconstruct the full vertebra so that the entire spine can be displayed.

Another limitation is that the AVR of all levels were measured relative to the AVR of vertebra L5. There was a challenge to locate vertebra L5 on an ultrasound image because of a

higher noise level in the lumbar region when compared to the thoracic area. Hence, it was more difficult to identify the laminae on lumbar vertebrae. In the future research, the fuzzy segmentation technique should account for the region of the vertebra so that the laminae of the lumbar vertebrae can be exposed clearly.

Currently, the sterEOS software does not calculate the Cobb angle measurement on the PMC; therefore, other imaging methods should be explored to validate this measurement.

The predictive model of AIS progression was developed in the retrospective study. Although this retrospective study was of relatively low costs because patient records could often easily be searched, its results could be affected by confounding. Confounding is a phenomenon in which a mediator variable or a confounding variable can adversely affect the relation between the predictors (independent variables) and the outcome (dependent variable). This may cause an incorrect analysis of the results. The next step of this pilot study is to develop a predictive model based on a prospective cohort study. Furthermore, in this pilot study, two predictors were involved in the prediction of the AIS progression, which may not reflect fully its complexity. In order to be able to include as many predictors as possible in the predictive model, the sample size should be large enough to satisfy the rule of thumb of at least 10 subjects per predictor. However, the sample size acquired from the local scoliosis clinic was limited, which was a limitation in prediction research. To accelerate the recruitment of AIS patients, multi-centre and collaborative studies that can address this issue should be considered.

References

1. AARO, S. & DAHLBORN, M. 1981. Estimation of vertebral rotation and the spinal and rib cage deformity in scoliosis by computer tomography. *Spine (Phila Pa 1976)*, 6, 460-7.
2. AARO, S., DAHLBORN, M. & SVENSSON, L. 1978. Estimation of vertebral rotation in structural scoliosis by computer tomography. *Acta Radiol Diagn (Stockh)*, 19, 990-2.
3. ADAIR, I. V., VAN WIJK, M. C. & ARMSTRONG, G. W. 1977. Moiré Topography in Scoliosis Screening. *Clin Orthop Relat Res*, 165 - 171.
4. ADAMS, W. 1882. *Lectures on the pathology and treatment of lateral and other forms of curvature of the spine*, J.& A. Churchill, New Burlington Street.
5. ALDEN, K. J., MAROSY, B., NZEGWU, N., JUSTICE, C. M., WILSON, A. F. & MILLER, N. H. 2006. Idiopathic scoliosis: identification of candidate regions on chromosome 19p13. *Spine (Phila Pa 1976)*, 31, 1815-9.
6. ANDRE, B., TROCHU, F. & DANSEREAU, J. 1996. Approach for the smoothing of three-dimensional reconstructions of the human spine using dual Kriging interpolation. *Med Biol Eng Comput*, 34, 185-191.
7. ASHER, M. A. & BURTON, D. C. 2006. Adolescent idiopathic scoliosis: natural history and long term treatment effects. *Scoliosis*, 1, 2.
8. AUBIN, C. E., DANSEREAU, J., PARENT, F., LABELLE, H. & DE GUISE, J. A. 1997. Morphometric evaluations of personalised 3D reconstructions and geometric models of the human spine. *Med Biol Eng Comput*, 35, 611-8.
9. AUSTIN, P. C. & STEYERBERG, E. W. 2015. The number of subjects per variable required in linear regression analyses. *J Clin Epidemiol*, 68, 627-36.
10. AZIZ, A. & KARARA, H. M. Direct linear transformation into object space coordinates in close-range photogrammetry. Proc. of the Symposium on Close-Range Photogrammetry, 1971. 1-18.
11. BARSANTI, C. M., DEBARI, A. & COVINO, B. M. 1990. The torsion meter: a critical review. *J Pediatr Orthop*, 10, 527-31.

12. BAUMGARTNER, T. A. 1969. Estimating Reliability When all Test Trials are Administered on the Same Day. *American Association for Health, Physical Education and Recreation*, 40, 222-225.
13. BENAMEUR, S., MIGNOTTE, M., LABELLE, H. & DE GUISE, J. A. 2005. A hierarchical statistical modeling approach for the unsupervised 3-D biplanar reconstruction of the scoliotic spine. *IEEE Trans Biomed Eng*, 52, 2041-57.
14. BENAMEUR, S., MIGNOTTE, M., PARENT, S., LABELLE, H., SKALLI, W. & DE GUISE, J. A. 2003. 3D/2D registration and segmentation of scoliotic vertebrae using statistical models. *Comput Med Imag Grap*, 27, 321-337.
15. BERRYMAN, F., PYNSENT, P., FAIRBANK, J. & DISNEY, S. 2008. A new system for measuring three-dimensional back shape in scoliosis. *Eur Spine J*, 17, 663-72.
16. BIRCHALL, D., HUGHES, D. G., HINDLE, J., ROBINSON, L. & WILLIAMSON, J. B. 1997. Measurement of vertebral rotation in adolescent idiopathic scoliosis using three-dimensional magnetic resonance imaging. *Spine*, 22, 2403-2407.
17. BLANCHARD, B. & ELBAROUDI, F. 2008. Imaging process for a computerized three-dimensional reconstruction from two-dimensional radiographic images; device implementation.
18. BLAND, J. M. & ALTMAN, D. G. 1999. Measuring agreement in method comparison studies. *Stat Methods Med Res*, 8, 135-60.
19. BOISVERT, J., CHERIET, F., PENNEC, X., LABELLE, H. & AYACHE, N. 2008. Articulated spine models for 3-D reconstruction from partial radiographic data. *IEEE Trans Biomed Eng*, 55, 2565-74.
20. BRENNAN, S. C., REDD, W. H., JACOBSEN, P. B., SCHORR, O., HEELAN, R. T., SZE, G. K., KROL, G., PETERS, B. E. & MORRISSEY, J. K. 1988. Anxiety and panic during magnetic resonance scans. *Lancet*, 2, 512.
21. BRENNER, D., ELLISTON, C., HALL, E. & BERDON, W. 2001. Estimated risks of radiation-induced fatal cancer from pediatric CT. *AJR Am J Roentgenol*, 176, 289-96.
22. BRENNER, D., ELLISTON, C., HALL, E. & BERDON, W. 2001. Estimated risks of radiation-induced fatal cancer from pediatric CT. *AJR Am J Roentgenol*, 176, 289-96.
23. BUNNELL, W. P. 1984. An objective criterion for scoliosis screening. *J Bone Joint Surg Am*, 66, 1381-7.

24. BUNNELL, W. P. 1993. Outcome of spinal screening. *Spine (Phila Pa 1976)*, 18, 1572-80.
25. BUNNELL, W. P. 2005. Selective Screening for Scoliosis. *Clin Orthop Relat Res*, 434, 40-45 10.1097/01.blo.0000163242.92733.66.
26. BURWELL, R. G., AUJLA, R. K., COLE, A. A., KIRBY, A. S., PRATT, R. K., WEBB, J. K. & MOULTON, A. 2002. Preliminary study of a new real-time ultrasound method for measuring spinal and rib rotation in preoperative patients with adolescent idiopathic scoliosis. *Stud Health Technol Inform*, 91, 262-6.
27. BUSHBERG, J. T., SEIBERT, A. J., LEIDHOLDT, E. M. & BOONE, J. M. 2012. The essential physics of medical imaging, Philadelphia.
28. CANAVESE, F. & KAELIN, A. 2011. Adolescent idiopathic scoliosis: Indications and efficacy of nonoperative treatment. *Indian J Orthop*, 45, 7-14.
29. CARMAN, D. L., BROWNE, R. H. & BIRCH, J. G. 1990. Measurement of scoliosis and kyphosis radiographs. Intraobserver and interobserver variation. *J Bone Joint Surg Am*, 72, 328-33.
30. CARPINETA, L. & LABELLE, H. 2003. Evidence of three-dimensional variability in scoliotic curves. *Clin Orthop Relat Res*, 139-48.
31. CERNY, P., MARIK, I. & PALLOVA, I. 2014. The radiographic method for evaluation of axial vertebral rotation - presentation of the new method. *Scoliosis*, 9, 11.
32. CHAMBERLAIN, C. C., HUDA, W., HOJNOWSKI, L. S., PERKINS, A. & SCARAMUZZINO, A. 2000. Radiation doses to patients undergoing scoliosis radiography. *Br J Radiol*, 73, 847-53.
33. CHAZONO, M., TANAKA, T., MARUMO, K., KONO, K. & SUZUKI, N. 2015. Significance of peak height velocity as a predictive factor for curve progression in patients with idiopathic scoliosis. *Scoliosis*, 10, 1-4.
34. CHEN, W., LE, L. H. & LOU, E. H. 2016. Reliability of the axial vertebral rotation measurements of adolescent idiopathic scoliosis using the center of lamina method on ultrasound images: in vitro and in vivo study. *Eur Spine J*.
35. CHEN, W., LOU, E. H. M. & LE, L. H. 2012. Ultrasound Imaging of Spinal Vertebrae to Study Scoliosis. *Open Journal of Acoustics*, 02, 95-103.

36. CHEN, W., LOU, E. H., ZHANG, P. Q., LE, L. H. & HILL, D. 2013. Reliability of assessing the coronal curvature of children with scoliosis by using ultrasound images. *J Child Orthop*, 7, 521-9.
37. CHERIET, F., DELORME, S., DANSEREAU, J., AUBIN, C. E., DE GUISE, J. A. & LABELLE, H. 1999. Intraoperative 3D reconstruction of the scoliotic spine from radiographs. *Annales de Chirurgie*, 53, 808-815.
38. CHERIET, F., JIANG, D. & STEWART, N. F. 2007a. Modelling of Scoliotic Deformities. *International Journal of Modelling and Simulation*, 27.
39. CHERIET, F., LAPORTE, C., KADOURY, S., LABELLE, H. & DANSEREAU, J. 2007b. A novel system for the 3-D reconstruction of the human spine and rib cage from biplanar X-ray images. *IEEE Trans Biomed Eng*, 54, 1356-8.
40. CHEUNG, C. W., LAW, S. Y. & ZHENG, Y. P. 2013. Development of 3-D ultrasound system for assessment of adolescent idiopathic scoliosis (AIS): and system validation. *Conf Proc IEEE Eng Med Biol Soc*, 2013, 6474-7.
41. CHEUNG, C. W., ZHOU, G. Q., LAW, S. Y., MAK, T. M., LAI, K. L. & ZHENG, Y. P. 2015b. Ultrasound Volume Projection Imaging for Assessment of Scoliosis. *IEEE Trans Med Imaging*.
42. CHEUNG, C.-W. J., ZHOU, G.-Q., LAW, S.-Y., LAI, K.-L., JIANG, W.-W. & ZHENG, Y.-P. 2015a. Freehand three-dimensional ultrasound system for assessment of scoliosis. *Journal of Orthopaedic Translation*, 3, 123-133.
43. CHI, W. M., CHENG, C. W., YE, W. C., CHUANG, S. C., CHANG, T. S. & CHEN, J. H. 2006. Vertebral axial rotation measurement method. *Comput Methods Programs Biomed*, 81, 8-17.
44. CHUNG, M., DAHABREH, I. J., HADAR, N., RATICHEK, S. J., GAYLOR, J. M., TRIKALINOS, T. A. & LAU, J. 2011. Emerging MRI Technologies for Imaging Musculoskeletal Disorders Under Loading Stress. USA: Agency for Healthcare Research and Quality.
45. CINQUIN, P., BAINVILLE, E., BARBE, C., BITTAR, E. & BOUCHARD, V. 1995. Computer Assisted Medical Interventions. *IEEE Eng Med Biol*, 14, 254-263.

46. CLIN, J., AUBIN, C. E., LALONDE, N., PARENT, S. & LABELLE, H. 2011. A new method to include the gravitational forces in a finite element model of the scoliotic spine. *Med Biol Eng Comput*, 49, 967-77.
47. COBB, J. 1948. Outline for the study of scoliosis. *Instructional Course Lectures*, 5, 261-275.
48. CONVERSANO, F., FRANCHINI, R., GRECO, A., SOLOPERTO, G., CHIRIACO, F., CASCIARO, E., AVENTAGGIATO, M., RENNA, M. D., PISANI, P., DI PAOLA, M., GRIMALDI, A., QUARTA, L., QUARTA, E., MURATORE, M., LAUGIER, P. & CASCIARO, S. 2015. A novel ultrasound methodology for estimating spine mineral density. *Ultrasound Med Biol*, 41, 281-300.
49. COOK, L. T., DE SMET, A. A., TARLTON, M. A. & FRITZ, S. L. 1981. Assessment of scoliosis using three-dimensional analysis. *IEEE Trans Biomed Eng*, 28, 366-371.
50. COUPE, P., HELLIER, P., AZZABOU, N. & BARILLOT, C. 2005. 3D freehand ultrasound reconstruction based on probe trajectory. *Med Image Comput Comput Assist Interv*, 8, 597-604.
51. CURRIER, D. P. 1984. *Elements of research in physical therapy*, Baltimore, Williams & Wilkins.
52. DANSEREAU, J. & STOKES, I. A. 1988. Measurements of the three-dimensional shape of the rib cage. *J Biomech*, 21, 893-901.
53. DANSEREAU, J., BEAUCHAMP, A., DE GUISE, J. A. & LABELLE, H. 3-D reconstruction of the spine and rib cage from stereoradiographic and imaging techniques. *Proceedings of The Canadian Society of Mechanical Engineers*, 1990. 58-79.
54. DARUWALLA, J. S. & BALASUBRAMANIAM, P. 1985. Moire topography in scoliosis. Its accuracy in detecting the site and size of the curve. *J Bone Joint Surg Br*, 67, 211-3.
55. DE SMET, A. A., TARLTON, M. A., COOK, L. T., BERRIDGE, A. S. & ASHER, M. A. 1983. The top view for analysis of scoliosis progression. *Radiology*, 147, 369-72.
56. DE SMET, A. A., TARLTON, M. A., COOK, L. T., FRITZ, S. L. & DWYER, S. J., 3RD 1980. A radiographic method for three-dimensional analysis of spinal configuration. *Radiology*, 137, 343-8.

57. DEACON, P., FLOOD, B. M. & DICKSON, R. A. 1984. Idiopathic scoliosis in three dimensions: A radiographic and morphometric analysis. *J Bone Joint Surg Br.* , 66, 509-12.
58. DELORME, S., LABELLE, H., AUBIN, C. E., DE GUISE, J. A., RIVARD, C. H., POITRAS, B. & DANSEREAU, J. 2000. A Three-Dimensional Radiographic Comparison of Cotrel–Dubousset and Colorado Instrumentations for the Correction of Idiopathic Scoliosis. *Spine*, 25, 205-210.
59. DESCHENES, S., CHARRON, G., BEAUDOIN, G., LABELLE, H., DUBOIS, J., MIRON, M. C. & PARENT, S. 2010. Diagnostic imaging of spinal deformities: Reducing patients radiation dose with a new slot-scanning X-ray imager. *Spine*, 35, 989-994.
60. DESCHENES, S., GODBOUT, B., POMERO, V., SKALLI, W. & DE GUISE, J. A. 2004. Vertebral pose estimation using edge-based pattern matching and stereoradiographic 3D reconstruction of the spine. *International Congress Series*, 1268, 237-242.
61. DEWEY, M., SCHINK, T. & DEWEY, C. F. 2007. Claustrophobia during magnetic resonance imaging: cohort study in over 55,000 patients. *J Magn Reson Imaging*, 26, 1322-7.
62. DEWI, D. E. O., WILKINSON, M. H. F., MENGKO, T. L. R., PURNAMA, I. K. E., VAN OOIJEN, P. M. A., VELDHUIZEN, A. G., MAURITS, N. M. & VERKERKE, G. J. 2009. 3D ultrasound reconstruction of spinal images using an improved Olympic Hole-filling method. *2009 International Conference on Instrumentation, Communications, Information Technology, and Biomedical Engineering (ICICI-BME)*. Bandung, Indonesia: IEEE.
63. DEWI, D. E. O., WILKINSON, M. H. F., MENGKO, T. L. R., PURNAMA, I. K. E., VAN OOIJEN, P. M. A., VELDHUIZEN, A. G., MAURITS, N. M. & VERKERKE, G. J. 2009. 3D ultrasound reconstruction of spinal images using an improved Olympic Hole-filling method. *2009 International Conference on Instrumentation, Communications, Information Technology, and Biomedical Engineering (ICICI-BME)*. Bandung, Indonesia: IEEE.

64. DOBBS, M. B., LENKE, L. G., SZYMANSKI, D. A., MORCUENDE, J. A., WEINSTEIN, S. L., BRIDWELL, K. H. & SPONSELLER, P. D. 2002. Prevalence of neural axis abnormalities in patients with infantile idiopathic scoliosis. *The Journal of Bone and Joint Surgery*, 84-A, 2230 - 2234.
65. DOODY, M. M., LONSTEIN, J. E., STOVALL, M., HACKER, D. G., LUCKYANOV, N. & LAND, C. E. 2000. Breast cancer mortality after diagnostic radiography: Findings from the U.S. scoliosis cohort study. *Spine*, 25, 2052-63.
66. DRERUP, B. & HIERHOLZER, E. 1994. Back shape measurement using videorasterstereography and three-dimensional reconstruction of spinal shape. *Clin. Biomech.*, 9, 28 - 36.
67. DRERUP, B. 1984. Principles of measurement of vertebral rotation from frontal projections of the pedicles. *J Biomech*, 17, 923-35.
68. DRISCOLL, C. R., AUBIN, C. E., CANET, F., LABELLE, H. & DANSEREAU, J. 2012. Impact of prone surgical positioning on the scoliotic spine. *J Spinal Disord Tech*, 25, 173-81.
69. DUBOUSSET, J., CHARPAK, G., DORION, I., SKALLI, W., LAVASTE, F., DEGUISE, J., KALIFA, G. & FERREY, S. 2005. A new 2D and 3D imaging approach to musculoskeletal physiology and pathology with low-dose radiation and the standing position: the EOS system. *Bull Acad Natl Med*, 189, 287-297.
70. DUMAS, R., BLANCHARD, B., CARLIER, R., DE LOUBRESSE, C. G., LE HUEC, J. C., MARTY, C., MOINARD, M. & VITAL, J. M. 2008. A semi-automated method using interpolation and optimisation for the 3D reconstruction of the spine from bi-planar radiography: a precision and accuracy study. *Med Biol Eng Comput*, 46, 85-92.
71. DUMAS, R., LE BRAS, A., CHAMPAIN, N., SAVIDAN, M., MITTON, D., KALIFA, G., STEIB, J. P., DE GUISE, J. A. & SKALLI, W. 2004. Validation of the relative 3D orientation of vertebrae reconstructed by bi-planar radiography. *Med Eng Phys*, 26, 415-22.
72. DUMAS, R., STEIB, J. P., MITTON, D., LAVASTE, F. & SKALLI, W. 2003. Three-dimensional quantitative segmental analysis of scoliosis corrected by the in situ contouring technique. *Spine (Phila Pa 1976)*, 28, 1158-62.

73. DUVAL-BEAUPERE, G. & LAMIREAU, T. H. 1985. Scoliosis at less than 30 degrees: Properties of the evolutivity (risk of progression). *Spine*, 10, 421-424.
74. DUVAL-BEAUPERE, G. 1992. Rib hump and supine angle as prognostic factors for mild scoliosis. *Spine*, 17, 103-107.
75. DUVAL-BEAUPERE, G. 1996. Threshold values for supine and standing Cobb angles and rib hump measurements: prognostic factors for scoliosis. *Eur Spine J*, 5, 79-84.
76. ESCALADA, F., MARCO, E., DUARTE, E., MA MUNIESA, J., BOZA, R., TEJERO, M. & CACERES, E. 2009. Assessment of angle velocity in girls with adolescent idiopathic scoliosis. *Scoliosis*, 4, 20.
77. FENSTER, A., DOWNEY, D. B. & CARDINAL, H. N. 2001. Three-dimensional ultrasound imaging. *Phys Med Biol*, 46, R67-99.
78. FORSBERG, D., LUNDSTROM, C., ANDERSSON, M., VAVRUCH, L., TROPP, H. & KNUTSSON, H. 2013. Fully automatic measurements of axial vertebral rotation for assessment of spinal deformity in idiopathic scoliosis. *Phys Med Biol*, 58, 1775-87.
79. FROBIN, W. & HIERHOLZER, E. 1981. Rasterstereography : A photogrammetric method for measurement of body surfaces. *Photogrammetric Engineering and Remote Sensing*, 47, 1717 - 1724.
80. FROBIN, W. & HIERHOLZER, E. 1982. Analysis of human back shape using surface curvatures. *I. Biomechanics*, 15, 379 - 390.
81. GLASER, D. A., DOAN, J. & NEWTON, P. O. 2012. Comparison of 3-dimensional spinal reconstruction accuracy: biplanar radiographs with EOS versus computed tomography. *Spine (Phila Pa 1976)*, 37, 1391-7.
82. GOBBI, D. G. & PETERS, T. M. 2002. Interactive intra-operative 3D ultrasound reconstruction and visualization. In: DOHI, T. & KIKINIS, R. (eds.) *5th International Conference on Medical Image Computing and Computer-Assisted Intervention - MICCAI 2002*. Tokyo, Japan: Springer-Verlag Berlin Heidelberg.
83. GOCEN, S. & HAVITCIOGLU, H. 2001. Effect of rotation on frontal plane deformity in idiopathic scoliosis. *Orthopedics*, 24, 265-8.
84. GOCEN, S., AKSU, M. G., BAKTIROGLU, L. & OZCAN, O. 1998. Evaluation of computed tomographic method to measure vertebral rotation in adolescent idiopathic

- scoliosis: An intraobserver and interobserver analysis. *Journal of Spinal Disorders*, 11, 210 - 214.
85. GSTOETTNER, M., SEKYRA, K., WALOCHNIK, N., WINTER, P., WACHTER, R. & BACH, C. M. 2007. Inter- and intraobserver reliability assessment of the Cobb angle: manual versus digital measurement tools. *Eur Spine J*, 16, 1587-92.
 86. GUO, X., CHAU, W. W., CHAN, Y. L. & CHENG, J. C. 2003. Relative anterior spinal overgrowth in adolescent idiopathic scoliosis. Results of disproportionate endochondral-membranous bone growth. *J Bone Joint Surg Br*, 85, 1026-31.
 87. GUPTA, P., LENKE, L. G. & BRIDWELL, K. H. 1998. Incidence of neural axis abnormalities in infantile and juvenile patients with spinal deformity. *Spine*, 23, 206 - 210.
 88. HARRELL, F. E., JR., LEE, K. L., CALIFF, R. M., PRYOR, D. B. & ROSATI, R. A. 1984. Regression modelling strategies for improved prognostic prediction. *Stat Med*, 3, 143-52.
 89. HIERHOLZER, E. & FROBIN, W. 1982. Automatic Measurement of Body Surfaces Using Rasterstereography. In: VON BALLY, G. & GREGUSS, P. (eds.) *Optics in Biomedical Sciences: Proceedings of the International Conference, Graz, Austria, September 7-11, 1981*. Berlin, Heidelberg: Springer Berlin Heidelberg.
 90. HIPPOCRATES 1927. Hippocrates. On Joints. In: PAGE, T. E., CAPPS, E., ROUSE, W. H. D., POST, L. A. & WARMINGTON, E. H. (eds.). London: W. Heinemann.
 91. HO, E. K. W., CHAN, F. L. & LEONG, J. C. Y. 1993. New methods of measuring vertebral rotation from computed tomographic scan. *Spine*, 18, 1173-1177.
 92. HRESKO, M. T. 2013. Clinical practice. Idiopathic scoliosis in adolescents. *N Engl J Med*, 368, 834-41.
 93. ILLES, T. & SOMOSKEOY, S. 2012. The EOS imaging system and its uses in daily orthopaedic practice. *Int Orthop*, 36, 1325-31.
 94. ILLES, T., TUNYOGI-CSAPO, M. & SOMOSKEOY, S. 2011. Breakthrough in three-dimensional scoliosis diagnosis: significance of horizontal plane view and vertebra vectors. *Eur Spine J*, 20, 135-43.

95. IMAGAMA, S., KAWAKAMI, N. & ISHIGURO, N. 2011. Three-dimensional CT analysis of congenital scoliosis and kyphosis: A new classification. *In: SUBBURAJ, K. (ed.) CT Scanning – Techniques and Applications*. InTech.
96. INTERACTIVE BIOLOGY. <http://www.interactive-biology.com/wp-content/uploads/2011/08/AnatomicalPlanes.png>. Accessed on July 21, 2016.
97. JAREMKO, J., DELORME, S., DANSEREAU, J., LABELLE, H., RONSKY, J., PONCET, P., HARDER, J., DEWAR, R. & ZERNICKE, R. F. 2000. Use of neural networks to correlate spine and rib deformity in scoliosis. *Comput Methods Biomech Biomed Engin*, 3, 203-213.
98. KADOURY, S., CHERIET, F. & LABELLE, H. A statistical image-based approach for the 3D reconstruction of the scoliotic spine from biplanar radiographs. *IEEE International Symposium on Biomedical Imaging: From Nano to Macro, ISBI 2008*, 14-17 May 2008 2008 Paris, France. IEEE, 660-663.
99. KADOURY, S., CHERIET, F., LAPORTE, C. & LABELLE, H. 2007. A versatile 3D reconstruction system of the spine and pelvis for clinical assessment of spinal deformities. *Med Biol Eng Comput*, 45, 591-602.
100. KALRA, M. K., QUICK, P., SINGH, S., SANDBORG, M. & PERSSON, A. 2013. Whole spine CT for evaluation of scoliosis in children: feasibility of sub-milliSievert scanning protocol. *Acta Radiol*, 54, 226-30.
101. KASPIRIS, A., GRIVAS, T. B., WEISS, H. R. & TURNBULL, D. 2011. Surgical and conservative treatment of patients with congenital scoliosis: alpha search for long-term results. *Scoliosis*, 6, 12.
102. KATZ, D. E., HERRING, J. A., BROWNE, R. H., KELLY, D. M. & BIRCH, J. G. 2010. Brace wear control of curve progression in adolescent idiopathic scoliosis. *J Bone Joint Surg Am*, 92, 1343-52.
103. KIM, H. S., ISHIKAWA, S., OHTSUKA, Y., SHIMIZU, H., SHINOMIYA, T. & VIERGEVER, M. A. 2001. Automatic scoliosis detection based on local centroids evaluation on moire topographic images of human backs. *IEEE Trans Med Imaging*, 20, 1314-20.

104. KIM, H., KIM, H. S., MOON, E. S., YOON, C. S., CHUNG, T. S., SONG, H. T., SUH, J. S., LEE, Y. H. & KIM, S. 2010. Scoliosis imaging: What radiologists should know. *RadioGraphics*, 30, 1823–1842.
105. KONIECZNY, M. R., SENYURT, H. & KRAUSPE, R. 2013. Epidemiology of adolescent idiopathic scoliosis. *J Child Orthop*, 7, 3-9.
106. KUKLO, T. R., POTTER, B. K., O'BRIEN, M. F., SCHROEDER, T. M., LENKE, L. G., POLLY, D. W., JR. & SPINAL DEFORMITY STUDY, G. 2005. Reliability analysis for digital adolescent idiopathic scoliosis measurements. *J Spinal Disord Tech*, 18, 152-9.
107. LAM, G. C., HILL, D. L., LE, L. H., RASO, J. V. & LOU, E. H. 2008. Vertebral rotation measurement: a summary and comparison of common radiographic and CT methods. *Scoliosis*, 3, 16.
108. LAM, T. P., HUNG, V. W., YEUNG, H. Y., CHU, W. C., NG, B. K., LEE, K. M., QIN, L. & CHENG, J. C. 2012. Quantitative ultrasound for predicting curve progression in adolescent idiopathic scoliosis: a prospective cohort study of 294 cases followed-up beyond skeletal maturity. *Ultrasound Med Biol*, 39, 381-7.
109. LAM, T. P., HUNG, V. W., YEUNG, H. Y., CHU, W. C., NG, B. K., LEE, K. M., QIN, L. & CHENG, J. C. 2012. Quantitative ultrasound for predicting curve progression in adolescent idiopathic scoliosis: a prospective cohort study of 294 cases followed-up beyond skeletal maturity. *Ultrasound Med Biol*, 39, 381-7.
110. LE, L. H., GU, Y. J., LI, Y. & ZHANG, C. 2010. Probing long bones with ultrasonic body waves. *Applied Physics Letters* 96, 114-122.
111. LIU, X. C., THOMETZ, J. G., TASSONE, J. C., PAULSEN, L. C. & LYON, R. M. 2013. Historical review and experience with the use of surface topographic systems in children with idiopathic scoliosis. *OA Musculoskeletal Medicine*, 1, 1 - 8.
112. LONSTEIN, J. E. & CARLSON, J. M. 1984. The prediction of curve progression in untreated idiopathic scoliosis during growth. *J Bone Joint Surg Am*, 66, 1061-71.
113. LONSTEIN, J. E. 1994. Adolescent Idiopathic Scoliosis. *Lancet*, 344, 1407-1412.
114. LUDVIGSEN, H. 2010. *Real-time GPU-based 3D ultrasound reconstruction and visualization*. Master Dissertation, Norwegian University of Science and Technology.

115. MAHALANOBIS, P. C. On the generalized distance in statistics. National Institute of Science, 1936 India. 49 - 55.
116. MALFAIR, D., FLEMMING, A. K., DVORAK, M. F., MUNK, P. L., VERTINSKY, A. T., HERAN, M. K. & GRAEB, D. A. 2010. Radiographic evaluation of scoliosis: review. *AJR Am J Roentgenol*, 194, S8-22.
117. MARCIL, E., DANSEREAU, J., LABELLE, H. & DE GUISE, J. A. Incorporation of patient displacement into a trunk reconstruction technique *In: ROBERGE, F. A. & KEARNEY, R. E.*, eds. IEEE 17th Annual Conference on Engineering in Medicine and Biology Society, 1995., 1995 Montreal, Quebec, Canada. IEEE, 385-386.
118. MARKETOS, S. G. & SKIADAS, P. S. 1999. Historical perspective. Hippocrates: The father of spine surgery. *Spine*, 24, 1381 - 1387.
119. MARTINI, F. H., TIMMONS, M. J. & TALLITSCH, R. B. 2003. *Human anatomy*, USA, Pearson.
120. MARUYAMA, T., KOBAYASHI, Y., MIURA, M. & NAKAO, Y. 2015. Effectiveness of brace treatment for adolescent idiopathic scoliosis. *Scoliosis*, 10, S12.
121. MARZAN, G. T. 1976. *Rational design for close-range photogrammetry*. PhD Dissertation, University of Illinois at Urbana-Champaign.
122. MCCANN, H. A., SHARP, J. C., KINTER, T. M., MCEWAN, C. N., BARILLOT, C. & GREENLEAF, J. F. Multidimensional ultrasonic imaging for cardiology. IEEE, 1988. 1063-1073.
123. MCKENNA, C., WADE, R., FARIA, R., YANG, H., STIRK, L., GUMMERSON, N., SCULPHER, M. & WOOLACOTT, N. 2012. EOS 2D/3D X-ray imaging system: a systematic review and economic evaluation. *Health Technol Assess*, 16.
124. MEHLMAN, C. T., ARAGHI, A. & ROY, D. R. 1997. Hyphenated history: the Hueter-Volkman law. *Am J Orthop (Belle Mead NJ)*, 26, 798-800.
125. MERCIER, L., LANGO, T., LINDSETH, F. & COLLINS, D. L. 2005. A review of calibration techniques for freehand 3_d ultrasound systems. *Ultrasound Med Biol*, 31, 449-471.
126. MILLER, N. H. 1999. Cause and natural history of adolescent idiopathic scoliosis. *Orthop Clin North Am*, 30, 343-52, vii.

127. MITTON, D., LANDRY, C., VERON, S., SKALLI, W., LAVASTE, F. & DE GUISE, J. A. 2000. 3D reconstruction method from biplanar radiography using nonstereocorresponding points and elastic deformable meshes. *Med Biol Eng Comput*, 38, 133-139.
128. MITULESCU, A., SEMAAN, I., DE GUISE, J. A., LEBORGNE, P., ADAMSBAUM, C. & SKALLI, W. 2001. Validation of the non-stereo corresponding points stereoradiographic 3D reconstruction technique. *Med Biol Eng Comput*, 39, 152-8.
129. MOK, J. M., BERVEN, S. H., DIAB, M., HACKBARTH, M., HU, S. S. & DEVIREN, V. 2008. Comparison of observer variation in conventional and three digital radiographic methods used in the evaluation of patients with adolescent idiopathic scoliosis. *Spine (Phila Pa 1976)*, 33, 681-6.
130. MORRISSY, R. T., GOLDSMITH, G. S., HALL, E. C., KEHL, D. & COWIE, G. H. 1990. Measurement of the Cobb angle on radiographs of patients who have scoliosis. Evaluation of intrinsic error. *J Bone Joint Surg Am*, 72, 320-327.
131. MORTON, A., RIDDLE, R., BUCHANAN, R., KATZ, D. & BIRCH, J. 2008. Accuracy in the Prediction and Estimation of Adherence to Bracewear Before and During Treatment of Adolescent Idiopathic Scoliosis. *J Pediatr Orthop*, 28, 336 - 341.
132. MOURA, D. C. 2010. *Three-dimensional biplanar reconstruction of the scoliotic spine for standard clinical setup*. PhD Dissertation, University of Porto.
133. MOURA, D. C., BOISVERT, J., BARBOSA, J. G., LABELLE, H. & TAVARES, J. M. 2011. Fast 3D reconstruction of the spine from biplanar radiographs using a deformable articulated model. *Med Eng Phys*, 33, 924-33.
134. NASH, C. L., JR. & MOE, J. H. 1969. A study of vertebral rotation. *J Bone Joint Surg Am*, 51, 223-9.
135. NAULT, M. L., MAC-THIONG, J. M., ROY-BEAUDRY, M., DE GUISE, J. A., LABELLE, H. & PARENT, S. 2013. Three-dimensional Spine Parameters Can Differentiate Between Progressive and Nonprogressive Patients With AIS at the Initial Visit: A Retrospective Analysis. *J Pediatr Orthop*, 33, 617-622.
136. NAULT, M. L., MAC-THIONG, J. M., ROY-BEAUDRY, M., TURGEON, I., DE GUISE, J. A., LABELLE, H. & PARENT, S. 2014. Three-Dimensional Spinal

- Morphology Can Differentiate Between Progressive and Nonprogressive Patients With Adolescent Idiopathic Scoliosis at the Initial Presentation. *Spine*, 39, 601-606.
137. NELSON, T. R. & PRETORIUS, D. H. 1997. Interactive acquisition, analysis and visualization of sonographic volume data. *Int J Imag Systems Technol*, 8, 26-37.
 138. NGUYEN, D. V., VO, Q. N., LE, L. H. & LOU, E. H. M. 2015. Validation of 3D surface reconstruction of vertebrae and spinal column using 3D ultrasound data – A pilot study. *Medical Engineering and Physics*, 37, 239-244.
 139. NGUYEN, D. V., VO, Q. N., LE, L. H. & LOU, E. H. M. 2015. Validation of 3D surface reconstruction of vertebrae and spinal column using 3D ultrasound data – A pilot study. *Medical Engineering and Physics*, 37, 239-244.
 140. NGUYEN, K. C., LE, L. H., TRAN, N. H. T. T., SACCHI, M. D. & LOU, E. 2013. Excitation of ultrasonic Lamb waves using a phased array system with two array probes: Phantom and in vitro bone studies. *Ultrasonics*, 54, 1178-1185.
 141. NOVOSAD, J., CHERIET, F., PETIT, Y. & LABELLE, H. 2004. Three-dimensional (3-D) reconstruction of the spine from a single X-ray image and prior vertebra models. *IEEE Trans Biomed Eng*, 51, 1628-39.
 142. NYSTRÖM, L., SÖDERKVIST, I. & WEDIN, P.-Å. 1994. A note on some identification problems arising in roentgen stereo photogrammetric analysis. *J Biomech*, 27, 1291-1294.
 143. ODA, M., RAUH, S., GREGORY, P. B., SILVERMAN, F. N. & BLECK, E. E. 1982. The significance of roentgenographic measurement in scoliosis. *J Pediatr Orthop*, 2, 378-82.
 144. OHBUCHI, R., CHEN, D. & FUCHS, H. Incremental volume reconstruction and rendering for 3D ultrasound imaging. In: ROBB, R. A., ed. *Visualization in Biomedical Computing '92*, 1992 Chapel Hill, NC, USA. SPIE, 312–323
 145. OMEROĞLU, H., OZEKIN, O. & BIÇIMOĞLU, A. 1996. Measurement of vertebral rotation in idiopathic scoliosis using the Perdriolle torsion meter: a clinical study on intraobserver and interobserver error. *European Spine*, 5, 167-171.
 146. OTSU, N. 1979. A threshold selection method from gray-level histograms. *IEEE Transactions on systems, man, and cybernetics*, 9, 62-66.

147. OTTO, C. M. Principles of echocardiographic image acquisition and Doppler analysis. Textbook of Clinical Ecocardiography, 2000 Philadelphia. WB Saunders, 1-29.
148. PARENT, E., WATKINS, E., EMRANI, M. & HILL, D. 2010. Differences in measures of full-torso surface topography among healthy teenagers are independent of growth indicators. *Scoliosis*, 5.
149. PARENT, S., NAULT, M. L., MAC-THIONG, J. M., LABELLE, H. & DE, G. J. 2014. System and method for predicting scoliosis progression. Google Patents.
150. PASHA, S., CAHILL, P. J., DORMANS, J. P. & FLYNN, J. M. 2016. Characterizing the differences between the 2D and 3D measurements of spine in adolescent idiopathic scoliosis. *Eur Spine J*.
151. PATIAS, P., GRIVAS, T. B., KASPIRIS, A., AGGOURIS, C. & DRAKOUTOS, E. 2010. A review of the trunk surface metrics used as Scoliosis and other deformities evaluation indices. *Scoliosis*, 5, 12.
152. PAVLOU, M., AMBLER, G., SEAMAN, S. R., GUTTMANN, O., ELLIOTT, P., KING, M. & OMAR, R. Z. 2015. How to develop a more accurate risk prediction model when there are few events. *BMJ*, 351, h3868.
153. PAZOS, V., CHERIET, F., SONG, L., LABELLE, H. & DANSEREAU, J. 2005. Accuracy assessment of human trunk surface 3D reconstructions from an optical digitising system. *Med Biol Eng Comput*, 43, 11-5.
154. PEARCY, M. J. 1985. Stereo radiography of lumbar spine motion. *Acta Orthop Scand Suppl*, 212, 1-45.
155. PEDUZZI, P., CONCATO, J., FEINSTEIN, A. R. & HOLFORD, T. R. 1995. Importance of events per independent variable in proportional hazards regression analysis. II. Accuracy and precision of regression estimates. *J Clin Epidemiol*, 48, 1503-10.
156. PEDUZZI, P., CONCATO, J., KEMPER, E., HOLFORD, T. R. & FEINSTEIN, A. R. 1996. A simulation study of the number of events per variable in logistic regression analysis. *J Clin Epidemiol*, 49, 1373-9.
157. PERDRIOLLE, R. & VIDAL, J. 1985. Thoracic idiopathic scoliosis curve evolution and prognosis. *Spine (Phila Pa 1976)*, 10, 785-91.

158. PETERSON, L. E. & NACHEMSON, A. L. 1995. Prediction of progression of the curve in girls who have adolescent idiopathic scoliosis of moderate severity. Logistic regression analysis based on data from The Brace Study of the Scoliosis Research Society. *J Bone Joint Surg Am*, 77, 823-827.
159. POMERO, V., MITTON, D., LAPORTE, S., DE GUISE, J. A. & SKALLI, W. 2004. Fast accurate stereoradiographic 3D-reconstruction of the spine using a combined geometric and statistic model. *Clin Biomech* 19, 240-7.
160. PRAGER, R. W., IJAZ, U. Z., GEE, A. H. & TREECE, G. M. 2010. Three-dimensional ultrasound imaging. *Proc Inst Mech Eng H*, 224, 193-223.
161. PRUIJS, J. E., HAGEMAN, M. A., KEESSEN, W., VAN DER MEER, R. & VAN WIERINGEN, J. C. 1994. Variation in Cobb angle measurements in scoliosis. *Skeletal Radiol*, 23, 517-20.
162. PURNAMA, K. E., WILKINSON, M. H., VELDHUIZEN, A. G., VAN OOIJEN, P. M., LUBBERS, J., SARDJONO, T. A. & VERKERKE, G. J. Ultrasound for human spine: vertebral features enhancement using length attribute filter. *Int J CARS*, 2007a. 464-465.
163. PURNAMA, K. E., WILKINSON, M. H., VELDHUIZEN, A. G., VAN OOIJEN, P. M., LUBBERS, J., SARDJONO, T. A. & VERKERKE, G. J. 2007b. Ultrasound imaging for human spine: imaging and analysis. *Int J CARS*, 2, S114-S116.
164. PURNAMA, K. E., WILKINSON, M. H., VELDHUIZEN, A. G., VAN OOIJEN, P. M., LUBBERS, J., SARDJONO, T. A. & VERKERKE, G. J. Following scoliosis progression in the spine using ultrasound imaging. In: DÖSSEL, O. & SCHLEGEL, W. C., eds. IFMBE, 2009. Springer, 600-602.
165. RELEASE, E. P. 2013. EOS imaging introduces breakthrough Micro Dose feature at JFR 2013. *EOS Imaging*.
166. ROHLING, R., GEE, A. & BERMAN, L. 1999. A comparison of freehand three-dimensional ultrasound reconstruction techniques. *Med Image Anal*, 3, 339-59.
167. RONCKERS, C. M., LAND, C. E., MILLER, J. S., STOVALL, M., LONSTEIN, J. E. & DOODY, M. M. 2010. Cancer mortality among women frequently exposed to radiographic examinations for spinal disorders. *Radiat Res*, 174, 83-90.

168. RUGGERONE, M. & AUSTIN, J. H. M. 1986. Moiré Topography in Scoliosis: Correlations with Vertebral Lateral Curvature as Determined by Radiography. *Phy Ther*, 66, 1072 -1077.
169. SAHLSTRAND, T. 1986. The clinical value of Moire topography in the management of scoliosis. *Spine (Phila Pa 1976)*, 11, 409-17.
170. SAKKA, S. A. & MEHTA, M. H. 1997. The use of Quantec scanner in longitudinal follow up of patients with scoliosis. *Research Into Spinal Deformaties*, 1, 355-360.
171. SARJI, S. A., ABDULLAH, B. J. J., KUMAR, G., TAN, A. H. & NARAYANAN, P. 1998. Failed magnetic resonance imaging examinations due to claustrophobia. *Australasian Radiology*, 42, 293-295.
172. SCHMIDT, F. L. 1971. The Relative Efficiency of Regression and Simple Unit Predictor Weights in Applied Differential Psychology. *Educational and Psychological Measurement*, 31, 699-714.
173. SHEREBRIN, S., FENSTER, A., RANKIN, R. N. & SPENCE, D. Freehand three-dimensional ultrasound: Implementation and applications. *In: METTER, R. L. V. & BEUTEL, J., eds. Physics of Medical Imaging, 1996 Newport Beach, CA, USA. SPIE*, 296 –303.
174. SOCIETY, S. R. 1986. *Scoliosis. A handbook for patients.*, Park Ridge Illinois.
175. SOLBERG, O. V., LINDSETH, F., BO, L. E., MULLER, S., BAKENG, J. B., TANGEN, G. A. & HERNES, T. A. 2011. 3D ultrasound reconstruction algorithms from analog and digital data. *Ultrasonics*, 51, 405-19.
176. SOLBERG, O. V., LINDSETH, F., TORP, H., BLAKE, R. E. & NAGELHUS HERNES, T. A. 2007. Freehand 3D ultrasound reconstruction algorithms--a review. *Ultrasound Med Biol*, 33, 991-1009.
177. SOUCACOS, P. N., ZACHARIS, K., GELALIS, J., SOULTANIS, K., KALOS, N., BERIS, A., XENAKIS, T. & JOHNSON, E. O. 1998. Assessment of curve progression in idiopathic scoliosis. *Eur Spine J*, 7, 270-7.
178. STAGNARA, P., FAUCHET, R. & PELOUX , J. 1965. The plan of choice for the radiologic examination of kyphoscolioses. *Rev Chir Orthop Reparatrice Appar Mot*, 51, 517-524.

179. STOKES, I. A. & WINDISCH, L. 2006. Vertebral height growth predominates over intervertebral disc height growth in adolescents with scoliosis. *Spine (Phila Pa 1976)*, 31, 1600-4.
180. STOKES, I. A. 2002. Mechanical effects on skeletal growth. *J Musculoskelet Neuronal Interact*, 2, 277-80.
181. STOKES, I. A., ARMSTRONG, J. G. & MORELAND, M. S. 1988. Spinal deformity and back surface asymmetry in idiopathic scoliosis. *J Orthop Res*, 6, 129-37.
182. STOKES, I. A., BIGALOW, L. C. & MORELAND, M. S. 1986. Measurement of axial rotation of vertebrae in scoliosis. *Spine (Phila Pa 1976)*, 11, 213-8.
183. SUZUKI, S., YAMAMURO, T., SHIKATA, J., SHIMIZU, K. & IIDA, H. 1989. Ultrasound measurement of vertebral rotation in idiopathic scoliosis. *J Bone Joint Surg Br*, 71, 252-5.
184. TAKASAKI, H. 1970. Moire topography. *Appl Opt*, 9, 1467-72.
185. TAN, K. J., MOE, M. M., VAITHINATHAN, R. & WONG, H. K. 2009. Curve progression in idiopathic scoliosis: follow-up study to skeletal maturity. *Spine (Phila Pa 1976)*, 34, 697-700.
186. THEOLOGIS, T. N., FAIRBANK, J. C., TURNER-SMITH, A. R. & PANTAZOPOULOS, T. 1997. Early detection of progression in adolescent idiopathic scoliosis by measurement of changes in back shape with the Integrated Shape Imaging System scanner. *Spine (Phila Pa 1976)*, 22, 1223-7; discussion 1228.
187. TORELL, G., NACHEMSON, A., HADERSPECK-GRIB, K. & SCHULTZ, A. 1985. Standing and supine Cobb measures in girls with idiopathic scoliosis. *Spine (Phila Pa 1976)*, 10, 425-7.
188. TRAN, N. H. T. T., NGUYEN, K. C., SACCHI, M. D. & LE, L. H. 2014. Imaging ultrasonic dispersive guidedwave energy in long bones using linear radon transform. *Ultrasound in Med & Biol*, 40, 2715-2727.
189. TRAN, N. H. T. T., STIEGLITZ, L., GU, Y. J. & LE, L. H. 2013. Analysis of ultrasonic waves propagating in a bone plate over a water half-space with and without overlying soft tissue. *Ultrasound in Med. & Biol.*, 39, 2422-2430.

190. TROBAUGH, J. W., TROBAUGH, D. J. & RICHARD, W. D. 1994. Three-dimensional imaging with stereotactic ultrasonography. *Comput Med Imaging Graph*, 18, 315-23.
191. TROCHU, F. 1993. A contouring program based on dual kriging interpolation. *Engineering with Computers*, 9.
192. TURNER-SMITH, A. R., HARRIS, J. D., HOUGHTON, G. R. & JEFFERSON, R. J. 1988. A method for analysis of back shape in scoliosis. *J Biomech*, 21, 497-509.
193. UNGI, T., KING, F., KEMPSTON, M., KERI, Z., LASSO, A., MOUSAVI, P., RUDAN, J., BORSCHNECK, D. P. & FICHTINGER, G. 2014. Spinal curvature measurement by tracked ultrasound snapshots. *Ultrasound Med Biol*, 40, 447-54.
194. VAN GOETHEM, J., VAN CAMPENHOUT, A., VAN DEN HAUWE, L. & PARIZEL, P. M. 2007. Scoliosis. *Neuroimaging Clin N Am*, 17, 105-15.
195. VASILIADIS, E. S., GRIVAS, T. B. & KASPIRIS, A. 2009. Historical overview of spinal deformities in ancient Greece. *Scoliosis*, 4, 6.
196. VO, Q. N., LOU, E. H. & LE, L. H. 2015. 3D ultrasound imaging method to assess the true spinal deformity. *Conf Proc IEEE Eng Med Biol Soc*, 2015, 1540-3.
197. VO, Q. N., LOU, E. H. & LE, L. H. 2015. 3D ultrasound imaging method to assess the true spinal deformity. *Conf Proc IEEE Eng Med Biol Soc*, 2015, 1540-3.
198. VO, Q. N., LOU, E. H. M. & LE, L. H. 2014. Measurement of axial vertebral rotation using three-dimensional ultrasound images. *Scoliosis*, 10, 1-4.
199. VRTOVEC, T., PERNUS, F. & LIKAR, B. 2009. A review of methods for quantitative evaluation of axial vertebral rotation. *Eur Spine J*, 18, 1079-90.
200. WADE, R., YANG, H., MCKENNA, C., FARIA, R., GUMMERSON, N. & WOOLACOTT, N. 2013. A systematic review of the clinical effectiveness of EOS 2D/3D X-ray imaging system. *Eur Spine J*, 22, 296-304.
201. WANG, Q., LI, M., LOU, E. H. & WONG, M. S. 2015. Reliability and Validity Study of Clinical Ultrasound Imaging on Lateral Curvature of Adolescent Idiopathic Scoliosis. *PLoS One*, 10, e0135264.
202. WANG, Q., LI, M., LOU, E. H., CHU, W. C., LAM, T. P., CHENG, J. C. & WONG, M. S. 2016. Validity Study of Vertebral Rotation Measurement Using 3-D Ultrasound in Adolescent Idiopathic Scoliosis. *Ultrasound Med Biol*.

203. WEINSTEIN, S. L. & PONSETI, I. V. 1983. Curve progression in idiopathic scoliosis. *J Bone Joint Surg Am*, 65, 447-55.
204. WEINSTEIN, S. L., DOLAN, L. A., CHENG, J. C., DANIELSSON, A. & MORCUENDE, J. A. 2008. Adolescent idiopathic scoliosis. *Lancet*, 371, 1527-37.
205. WEINSTEIN, S. L., DOLAN, L. A., WRIGHT, J. G. & DOBBS, M. B. 2013. Effects of bracing in adolescents with idiopathic scoliosis. *N Engl J Med*, 369, 1512-21.
206. WEIR, J. P. 2005. Quantifying test-retest reliability using the intraclass correlation coefficient and the SEM. *J Strength Cond Res*, 19, 231-40.
207. WEISS, H. R. 1995. Measurement of vertebral rotation: Perdriolle versus Raimondi. *Eur Spine J*, 4, 34-8.
208. WEISZ, I., JEFFERSON, R. J., TURNER-SMITH, A. R., HOUGHTON, G. R. & HARRIS, J. D. 1988. ISIS scanning: a useful assessment technique in the management of scoliosis. *Spine (Phila Pa 1976)*, 13, 405-8.
209. WILLNER, S. 1979a. Moire topography--a method for school screening of scoliosis. *Arch Orthop Trauma Surg*, 95, 181-5.
210. WILLNER, S. 1979b. Moire topography for the diagnosis and documentation of scoliosis. *Acta Orthop Scand*, 50, 295-302.
211. WILLS, B. P., AUERBACH, J. D., ZHU, X., CAIRD, M. S., HORN, B. D., FLYNN, J. M., DRUMMOND, D. S., DORMANS, J. P. & ECKER, M. L. 2007. Comparison of Cobb angle measurement of scoliosis radiographs with preselected end vertebrae: traditional versus digital acquisition. *Spine (Phila Pa 1976)*, 32, 98-105.
212. WU, H., RONSKY, J. L., CHERIET, F., HARDER, J., KUPPER, J. C. & ZERNICKE, R. F. 2011. Time series spinal radiographs as prognostic factors for scoliosis and progression of spinal deformities. *Eur Spine J*, 20, 112-117.
213. WU, H., RONSKY, J. L., CHERIET, F., KUPPER, J., HARDER, J., XUE, D. & ZERNICKE, R. F. 2010. Prediction of scoliosis progression with serial three-dimensional spinal curves and the artificial progression surface technique. *Med Biol Eng Comput*, 48, 1065-75.
214. WU, H., RONSKY, J. L., PONCET, P., CHERIET, F., XUE, D., HARDER, J. A. & ZERNICKE, R. F. Prediction of scoliosis progression in time series using a hybrid

- learning technique. Engineering in Medicine and Biology 27th Annual Conference, September 1-4, 2005 2005 Shanghai, China. IEEE, 6452-6455.
215. YAMAUCHI, Y., YAMAGUCHI, T. & ASAKA, Y. 1988. Prediction of curve progression in idiopathic scoliosis based on initial roentgenograms. A proposal of an equation. *Spine (Phila Pa 1976)*, 13, 1258-61.
 216. YAZICI, M., ACAROGLU, E. R., ALANAY, A., DEVIREN, V., CILA, A. & SURAT, A. 2001. Measurement of vertebral rotation in standing versus supine position in adolescent idiopathic scoliosis. *J Pediatr Orthop*, 21, 252-6.
 217. YOUNG, M., HILL, D. L., ZHENG, R. & LOU, E. 2015. Reliability and accuracy of ultrasound measurements with and without the aid of previous radiographs in adolescent idiopathic scoliosis (AIS). *Eur Spine J*, 24, 1427-33.
 218. ZHANG, J., SHI, X., WANG, Y., LV, L., WU, J. & ZHAO, Z. 2010. Three-dimensional vertebrae reconstruction from stereoradiography based on epipolar geometry. In: MUCHIN, V. E. & HU, Z. (eds.) *2010 International Conference on Biomedical Engineering and Computer Science (ICBECS)*. Wuhan, China.
 219. ZHENG, R., CHAN, A. C. Y., CHEN, W., HILL, D. L., LE, L. H., HEDDEN, D., MOREAU, M., MAHOOD, J., SOUTHON, S. & LOU, E. 2015. Intra- and Inter-rater Reliability of Coronal Curvature Measurement for Adolescent Idiopathic Scoliosis Using Ultrasonic Imaging Method - A Pilot Study. *Spine Deformity*, 3, 151-158.
 220. ZHENG, R., LE, L. H., SACCHI, M. D., TA, D. & LOU, E. 2007. Spectral ratio method to estimate broadband ultrasound attenuation of cortical bones in vitro using multiple reflections. *Phys Med Biol*, 52, 5855-5869.
 221. ZHENG, R., YOUNG, M., HILL, D., LE, L. H., HEDDEN, D., MOREAU, M., MAHOOD, J., SOUTHON, S. & LOU, E. 2016. Improvement on the Accuracy and Reliability of Ultrasound Coronal Curvature Measurement on Adolescent Idiopathic Scoliosis With the Aid of Previous Radiographs. *Spine (Phila Pa 1976)*, 41, 404-11.

Appendices

Appendix Table 1 Training data

Subject	2 nd PMC Cobb	1 st PMC Cobb	AVR	LD	# of curve	# of vertebrae	Torsion	Location	Elapsed time (days)	Gender	BMI	Age
1	11	12	4	4	1	5	0.80	2	301	0	20.6	14.5
2	17	14	-4	-8	2	7	-0.57	2	217	0	15.5	11.5
3	20	16	-4	-10	1	5	-0.80	3	182	0	23.0	14.8
4	34	30	8	26	2	8	1.00	1	217	0	20.1	13.8
5	28	31	-11	-25	2	5	-2.20	3	453	0	22.7	15.3
6	47	44	6	38	2	7	0.86	1	189	0	18.7	16.3
7	15	19	7	13	1	5	1.40	3	217	0	19.2	15.3
8	47	50	11	40	2	8	1.38	1	217	0	19.5	14.4
9	18	20	5	13	2	7	0.71	1	364	0	22.1	14.3
10	25	21	17	17	2	6	2.83	3	238	0	19.4	12.6
11	41	38	12	28	2	7	1.71	1	196	0	20.5	11.8
12	28	29	7	-11	2	4	1.75	1	392	0	18.6	17.2
13	22	12	-5	-16	1	7	-0.71	2	224	1	20.0	14.0
14	23	29	-13	-16	2	5	-2.60	2	189	0	16.7	15.8
15	20	25	2	-17	1	4	0.50	3	245	0	17.9	14.9
16	23	24	18	37	2	7	2.57	1	322	0	17.5	16.0
17	29	28	-12	-46	2	6	-2.00	1	190	1	15.5	14.6
18	12	13	3	-4	1	6	0.50	1	383	1	21.8	12.3
19	30	28	16	25	2	7	2.29	1	406	0	29.2	15.0
20	30	35	8	36	1	7	1.14	1	182	0	26.2	14.9
21	15	12	-3	-1	1	9	-0.33	2	236	0	17.5	11.8
22	43	43	-13	-17	2	7	-1.86	2	350	0	18.7	16.2
23	21	17	3	15	1	6	0.50	1	196	0	18.1	15.0

Appendix Table 2 Test data

Subject	2 nd PMC Cobb	1 st PMC Cobb	AVR	LD	# of curve	# of vertebrae	Torsion	Location	Elapsed time (days)	Gender	BMI	Age
1	23	19	-4	-10	2	5	-0.8	3	196	0	18.6	13.3
2	31	33	-10	-16	2	6	-1.67	3	147	0	20.8	16.6
3	35	38	8	6	2	7	1.14	1	231	0	18.7	14.1
4	15	15	2	17	1	8	0.25	1	154	0	17.9	12.0
5	50	49	12	40	2	7	1.71	1	189	0	19.5	13.8
6	32	32	18	21	3	5	3.60	2	434	0	37.3	15.7